



TECHNISCHE
UNIVERSITÄT
WIEN

DISSERTATION

Selective Oxidation of Ethanol on Modified Supported Au Catalysts: From Fundamental Understanding to Improved Performance

ausgeführt zum Zwecke der Erlangung des akademischen Grades eines Doktors der
technischen Wissenschaften unter der Leitung von

Associate Prof. Dipl.-Ing. Dr.techn. Karin Föttinger

E165

Institut für Materialchemie

eingereicht an der Technischen Universität Wien

Fakultät für Technische Chemie

von

DI Andreas Nagl, BSc.

Matrikelnummer: 00825178

Kahlenberger Straße 1F/4, 1190 Wien

Wien, am 2.5.2019

Statement of Authorship

Hereby I declare that this PhD is the result of my own scientific research work conducted during my PhD study at the Institute of Materials Chemistry, Technische Universität Wien, from October 2015 to April 2019, unless otherwise acknowledged in the text. The chapters represent papers that were published or are being prepared for submission to international peer-reviewed journals. All references and verbatim extracts have been quoted, and all sources of information have been specifically acknowledged. This thesis has not been submitted for any other degree.

Vienna, 2nd May 2019

Andreas Nagl

Zusammenfassung

Der Wechsel von Rohöl als primären Rohstoff für die chemische Industrie hin zu erneuerbaren Ressourcen ist von größter Bedeutung. Bioethanol, mit einer jährlichen Produktion von über 100 Mrd. Litern, ist einer der vielversprechendsten Kandidaten für neue Rohstoffquellen. Selektive Oxidation von Ethanol eröffnet einen Weg zu Acetaldehyd, Ethylacetat und Essigsäure.

In dieser Dissertation wurde die selektive Oxidation von Ethanol auf (bimetallischen) Goldkatalysatoren untersucht. Zuerst wurde ein grundlegender Einblick in den Mechanismus von geträgerten Gold-Katalysatoren gegeben. Verschiedene Trägermaterialien wurden getestet, TiO₂ in der Rutil- und Anatase-Modifikation (sowie Mischungen), ZnO und Al₂O₃. Dabei wies der Au-Katalysator auf Rutil die höchste Aktivität und hohe Selektivität hinsichtlich Acetaldehyd (> 97%) zwischen 200 und 300°C auf. Das wichtigste Nebenprodukt war Ethylacetat, eine Folge der Kopplung von Acetaldehyd mit Ethoxy-Spezies. Die Totaloxidation zu CO₂ war vernachlässigbar.

Bimetallische Katalysatoren sind im Fokus von breiterem Interesse, da sie durch die Wahl der zweiten Metallkomponente vielfältige Möglichkeiten zum Anpassen der katalytischen Eigenschaften bieten. Für die Herstellung von bimetallicen Katalysatoren wurden verschiedene Promotor-Metalle getestet (Ag, Ru, Pt), wobei sich Silber als das geeignetste Element mit klar promotierendem Effekt auf die Reaktionsrate erwies. Als Nichtoxid-Referenz wurde Au und AuAg auf Aktivkohleträger verwendet. Kinetische Studien an Au/Rutile, AuAg/Rutile sowie den Aktivkohle-basierten Referenzen gaben Einblick in den Reaktionsmechanismus, und wurden mit den DFT Ergebnissen von J.E. de Vrieze in der Gruppe von M. Saeys, Universität Gent, Belgien verglichen. Mit guter Übereinstimmung zwischen Au/C und den theoretischen Ergebnissen, wurden verschiedene Reaktionsschritte (Protonentransfer von Ethanol zu atomarem Sauerstoff, Oberflächen-Hydroxyl-Spezies und molekularem Sauerstoff und bei höheren Temperaturen β -H Elimination) als ratenbestimmend identifiziert (im Gegensatz zu einer dominanten Route).

STEM-HAADF Messungen zeigten vergleichbare Partikelgrößenverteilungen für alle Katalysatoren mit durchschnittlichen Partikelgrößen von 2.7-3.5 nm. STEM-EDX zeigte die bimetalliche Natur der AuAg Partikel, sowohl auf Aktivkohle als auch auf Rutil (jeweils nach der Vorbehandlung).

Eine Reihe von *operando*-Spektroskopie-Methoden wurde angewandt, DRIFTS (Diffuse Reflectance Infrared Fourier Transform Spectroscopy), NAP-XPS (Near Ambient Pressure-XPS) und XAS (X-Ray Absorption Spectroscopy). Sowohl für Au/Rutil und AuAg/Rutil zeigte *operando* DRIFTS Ethoxy-Spezies und, abhängig vom Umsatz, COO als dominierende Intermediate an der Oberfläche.

XAS an der Au LIII-Kante zeigte, dass Gold unter allen Reaktionsbedingungen auf Au/Rutil und AuAg/Rutil metallisch bleibt, was NAP-XPS-Resultate wie auch theoretische Rechnungen bestätigen, nach denen Au⁰ in der Lage ist, molekularen Sauerstoff zu aktivieren. XAS-Messungen an der Ag K-Kante zeigen, dass ein relevanter Anteil von Silber, etwa 50% auf Au/Rutil und ca. 40% auf Ag/Rutil unter Reaktionsbedingungen oxidiert sind, möglicherweise innerhalb des Rutilträgers und zu weit von der Oberfläche entfernt, um für NAP-XPS zugänglich zu sein. Diese Beobachtung widerspricht der verbreiteten Hypothese der Ag₂O-Segregation an der Nanopartikel-Oberfläche. Für AuAg/C wird Legierungsbildung und keine Silber-Abreicherung angenommen, was unterschiedliche Kinetik-Resultate erklärt.

NAP-XPS zeigte weiters einen erhöhten Anteil von Ti³⁺-Spezies unter Dehydrogenierungsbedingungen (ohne Sauerstoff), was eine mögliche Erklärung für die unterschiedlichen Reaktionsordnungen auf den aktivekohlebasierten Katalysatoren darstellt.

Des Weiteren wurde der Einfluss von Wasser im Reaktionsfeed untersucht und mit Daten aus wässriger Lösung, zur Verfügung gestellt von S. Mostrou-Moser in der Gruppe von van Bokhoven, verglichen. Ein umgekehrter Trend wurde hinsichtlich der Katalysatoraktivität gefunden mit folgendem Trend in der Flüssigphase (wo das Hauptprodukt Essigsäure ist): AuPt > Au > AuRu > AuAg (wobei Au durch die höhere Selektivität interessanter ist). Überraschenderweise ist AuAg/Rutil, obwohl am aktivsten in der Gasphase, in der Flüssigphase am wenigsten aktiv (Gasphase: AuAg > Au > AuRu > AuPt). Gasphasenexperimente mit Wasser im Feed zeigten, dass Wasser einen aktivierenden Effekt auf Au/Rutil und im Gesamten nur geringe Auswirkungen auf Ag/Rutil hat. Interessanterweise ist der promotierende Effekt des Wassers von der Anwesenheit von Rutil abhängig und konnte für Au/C nicht beobachtet werden. Daher wurde gezeigt, dass die Ergebnisse in der wässrigen Phase in der Gasphase durch eine Wasserzugabe nicht reproduziert werden konnten, der Unterschied im Verhalten also in der

Flüssigphase und dem dort unterschiedlichen Mechanismus angenommen werden muss. In der Gasphase konnten mittels NAP-XPS keine elektronischen Änderungen, die durch Wasser herbeigeführt wurden, beobachtet werden, und auch DRIFTS zeigte keine anderen Spezies an der Katalysatoroberfläche, sodass ein rein kinetischer Effekt des Wassers angenommen wird.

Zusammenfassend ist AuAg/Rutil ein vielversprechendes System für die Ethanoloxidation zu Acetaldehyd. In dieser Dissertation konnte die verbreitete Hypothese, nach der Ag an der Gold-Oberfläche zu erhöhter Katalysator-Performance führen, widerlegt werden. Die Ag-Atome migrieren in den Rutil-Support, und verursachen dort einen promotierenden Effekt. Der spezifische Mechanismus hinter dem Effekt bleibt umstritten und benötigt weitere Untersuchungen.

Abstract

The transition from crude oil as primary feedstock for the chemical industry towards renewable sources is of paramount importance. Bioethanol is one of the most promising candidates for new raw materials, with an annual production over 100 billion liters. Selective oxidation of ethanol opens the pathway to acetaldehyde, ethyl acetate and acetic acid.

In this thesis, the selective oxidation of ethanol on (bimetallic) gold catalysts was investigated. First, a fundamental insight is given into the mechanism of supported gold catalysts. Different support materials were tested, TiO₂ both in the rutile and anatase modification (and mixtures), ZnO and Al₂O₃, whereas the rutile-supported Au catalyst exhibited the highest activity with high selectivity towards acetaldehyde (> 97%) between 200 and 300°C. The main by-product was ethyl-acetate, a result of the coupling of acetaldehyde with ethoxy species. Total oxidation to CO₂ was negligible.

Bimetallic catalysts, however, have attracted lots of interest as they offer a wide range of possibilities to tune catalytic properties by the choice of the second metal component. For the preparation of bimetallic Au catalysts, different promoter metals were screened (Ag, Ru, Pt), and silver was proven the best suited showing a clear promoting effect on reaction rates. As a non-oxide reference carbon-supported Au and AuAg were used. Thus, kinetic studies performed on Au/rutile, AuAg/rutile as well as the carbon-supported references gave insight into the reaction mechanism and were compared to computational DFT results obtained by J. E. de Vrieze in M. Saeys' group, Ghent University, Belgium. With good agreement between the Au/C and theoretical results, different reaction steps (proton transfer of ethanol to atomic oxygen, surface hydroxyl species and molecular oxygen and at higher temperatures ethoxy β -H elimination) were identified as rate limiting rather than one dominant route.

STEM-HAADF measurements showed comparable particle size distributions for all catalysts with mean particles sizes between 2.7 and 3.5 nm. STEM-EDX revealed bimetallic nature of the AuAg particles on both carbon and rutile after the pretreatment.

A range of *operando* spectroscopy techniques was employed, DRIFTS (Diffuse Reflectance Infrared Fourier Transform Spectroscopy), NAP-XPS (Near Ambient Pressure-XPS) and XAS (X-Ray Absorption Spectroscopy). For both Au/rutile and

AuAg/rutile *operando* DRIFTS revealed ethoxy species as the dominant intermediate on the surface as well as bands of surface acetate that are dependent on conversion.

XAS at the Au LIII-edge reveals that the gold remains metallic under all reaction conditions on both Au/rutile and AuAg/rutile, confirming results from the NAP-XPS and computational results that predict the ability of Au⁰ to activate molecular oxygen. XAS measurements at the Ag K-edge revealed a significant proportion of silver, approximately 50% for AuAg/rutile and ca. 40% for Ag/rutile, to be oxidized under reaction conditions, possibly located within the rutile support and too far away from the surface to be accessible for NAP-XPS: The latter showed a massive depletion from the surface. This observation contradicts the generally accepted hypothesis of Ag₂O segregation on the nanoparticle surface. For the AuAg/C, an alloying and no Ag depletion from the surface is hypothesized, explaining the different kinetic results. Thus, under reaction conditions the nanoparticle surface is strongly enriched in Au.

NAP-XPS further revealed an increased amount of Ti³⁺ species under ethanol dehydrogenation conditions, without oxygen, as compared to ethanol oxidation, thus possibly explaining different reaction orders on carbon-supported catalysts.

The influence of water was investigated and differences between the gas-phase and the aqueous phase, the latter of which was investigated by partners at the ETH Zurich, were discussed.

Finally, the influence of water in the reaction feed was investigated and compared to data from aqueous-phase reaction, the latter performed by S. Mostrou-Moser in the van Bokhoven group. A reversed trend of active catalysts was found, with the catalyst activity ordered as follows in the liquid-phase (where the main product is acetic acid): AuPt > Au > AuRu > AuAg (with Au being the more interesting catalyst as it shows higher selectivity). Surprisingly, the AuAg/rutile, favored in the gas-phase reaction, is the least active one in the liquid phase (gas phase: AuAg > Au > AuRu > AuPt). Gas-phase experiments with water in the feed revealed that water has an activating effect on Au/rutile and overall just minor effects on Ag/rutile. For the bimetallic AuAg, a mixed effect of Au and Ag was shown. Interestingly, the promotional effect was dependent on the presence of rutile and could not be observed for Au/C for the investigated temperatures. Thus, it could be proved that the results of the liquid-phase could not be reproduced in the gas-phase by water introduction, showing that the different behavior must be attributed to the liquid-phase and

a different reaction mechanism must be assumed. Also, for the gas-phase, NAP-XPS involving a water feed could not show any water-induced electronical changes and DRIFTS did not reveal any different species on the catalyst surface leading to the conclusion that the effect is a merely kinetic one.

In conclusion, the rutile supported AuAg catalyst is a very promising system for ethanol oxidation to acetaldehyde. In this thesis, the common believe that Ag atoms dispersed in the Au surface are responsible for the increased catalyst performance has been disproved. The Ag atoms migrate into the rutile support and in doing so, cause a promotion effect. The specific mechanism behind this effect, however, remains strongly debated and will require further investigation.

Acknowledgements

I would like to express my gratitude to **Prof. Dr. Karin Föttinger** for welcoming me to her group and the inspiring atmosphere. I am also very thankful for sharing your experimental skills, knowledge and correcting this thesis, countless (synchrotron) proposals, abstracts and manuscripts. Thank you for your patience, feedback and supporting also unusual ideas.

I am grateful to **Prof. Dr. van Jeroen A. van Bokhoven** for the fruitful collaboration, his time, feedback and patience during the project meetings in Vienna and Zürich. Thank you for the valuable discussions and scientific guidance.

Many thanks also to **Prof. Dr. Mark Saeys** for the enriching collaboration and the productive (Skype) meetings. Thank you for the interesting discussions, the feedback and the insight into the big world of DFT.

I am grateful to **Prof. Dr. Pintar** for the great collaboration, his time and efforts to advance my project and most of all his welcoming atmosphere during my stays in his lab. Thank you for the valuable discussions, the access to instruments and arranging STEM measurement time. Thanks to **Dr. Groan Dražić** for the Cs-corrected STEM imaging for my samples.

I am also thankful to **Prof. Dr. Günther Rupprechter** for providing such a productive atmosphere at the institute as well as discussions and the feedback in the group meeting. Thank you also for the entertaining time when were stuck at various airports on our way to the Operando Conference.

I would like to highlight my gratitude to **Dr. Annette Foelske** and **Dr. Markus Sauer** from the Analytical Instrumentation Center, TU Wien, for providing me exceptional support in everything connected with XPS. Thank you for your patience, the many discussions and the huge amount of time invested in the data evaluation. Thank you for joining me at BESSY at ALBA, and special thanks to Markus for doing the nightshifts with me.

I am especially grateful to **Sotiria Mostrou-Moser** for the great collaboration and being more than just a colleague: Thank you for being a true friend and thank you for the discussions, the feedback and valuable comments as a chemical engineer. Thank you for the great time we had at the Swiss Light Source and the Diamond Light Source.

Many thanks to **Jenoff de Vrieze** for the awesome cooperation and being a great friend: Thank you for the great discussions, proof-reading this thesis, giving me insight into the mechanism of my reaction. Thank you for the great time we had at the ALBA synchrotron and showing the best ribs place on earth.

Special thanks to **Janvit Teržan** for the inspiring collaboration, the TPD measurements, the many discussions and mental support during my PhD time. Thank you for the amazing time in Ljubljana that I will never forget. Thank you for the countless times we had fun.

I would like to thank all my colleagues in my research group: Endless thanks to **Nevzat Yigit** for welcoming me in the group, getting me started with my project, the many discussions, the countless occasions of fun and simply being friend. Thanks for all the great time at all the synchrotrons, starting at the MAX lab and ending at the Diamond Light Source. Many thanks to **Klaus Dobrezberger** for the discussions, the help at the ALBA synchrotron, the many literally dark hours at the TEM where you more often than not walked the extra mile to help me with my sample, the countless laughs and last but not least thanks for being a friend. Thanks also to **Gernot Pacholik** for choosing me as your supervisor for your Master thesis and giving me the opportunity to learn about industrially relevant research. Thanks for becoming more than colleague by being a true friend, thanks for the many discussions, the enthusiastic support at BESSY, ALBA and the Diamond Light Source. I would like to thank especially **Markus Latschka** for being an exceptionally committed Bachelor student. I am happy that you chose to stay in our research group and thank you for the discussions and the dedicated support at ALBA and the Diamond Light Source, for the many opportunities of fun and for being a great friend. I am grateful to **Ging, Kosri Chanokbhorn**, for the support as a Master student with exceptional motivation and drive. Thank you also to **Nathalie Schmölder** for being a creative, hard-working and dedicated Bachelor student.

Many thanks for **Rainald Rosner** for awaking the DIY'ler sleeping in me. Thanks for helping me automatize my kinetic setup, all the discussions, the mental support and being my fellow nerd at the institute.

I am also thankful to **Dr. Klaudia Hradil** for her time, patience and support regarding matters of XRD and the Pair Distribution Function analysis. Thanks to **Werner Artner** for all the support in measuring XRD and never losing patience when I had troubles with a Rietveld refinement.

Thanks also to the USTEM team for supporting me with the (S)TEM measurements. Special thanks to **Dr. Stefan Löffler** and **Thomas Schachinger** for patiently helping us out when we were stuck.

Thanks to **Prof. Dr. Limbeck** and **Felix Horak** for performing LA-ICP-MS measurements for my catalysts.

Thanks to **Prof. Dr. Wesley Browne** and his team for giving me access to your excellent Raman equipment in Groningen.

Also, I would like to thank the beamline scientists from the following beamlines for the kind and thoughtful support: BESSY ISISS, ALBA BL22 – CLÆSS, ALBA BL24 – CIRCE and DLS B18.

I would like to express my gratitude to the **Lions Club Wien St. Stephan** for choosing me for the Lions Sonderpreis 2018 and thus funding synchrotron measurements as well as a short research stay in the group of Prof. Dr. Mark Saeys as well as in the group Prof. Dr. Wesley Browne.

I would like to thank Venator for supporting my research by providing rutile and Evonik/Grolman Chemikalien for providing P25.

Finally, I'd like to address special thanks to my **family** and my girlfriend **Adrienn** for their love and constant encouragement during this sometimes very challenging time.

This project was also financially supported by the Austrian Science Fund (FWF) by project [I2158-N28].

Abbreviations

B.E.	Binding Energy
BET	Brunauer–Emmett–Teller
DFT	Density Functional Theory
DRIFTS	Diffuse Reflectance Infrared Fourier Transform Spectroscopy
DP	Deposition Precipitation
EDX	Energy-Dispersive X-ray spectroscopy
EELS	Electron Energy Loss Spectroscopy
EXAFS	Extended X-ray Absorption Fine Structure
FID	Flame Ionization Detector
FTIR	Fourier-Transform Infrared
FWHM	Full Width at Half Maximum
GDP	Gross Domestic Product
GC	Gas Chromatograph
HAADF	High-Angle Annular Dark Field
IWI	Incipient Wetness Impregnation
K.E.	Kinetic Energy
LCF	Linear Combination Fit
MCT	Mercury Cadmium Telluride
MFC	Mass Flow Controller
NAP-XPS	Near Ambient Pressure X-ray Photoelectron Spectroscopy
PID	Proportional-Integral-Derivative
RT	Room Temperature
TCD	Thermal Conductivity Detector

TEM	Transmission Electron Microscopy
TOF	Turnover Frequency
TPD	Temperature Programmed Desorption
STEM	Scanning Transmission Electron Microscopy
UHV	Ultra High Vacuum
UV	Ultraviolet
VB	Valence Band
XANES	X-ray Absorption Near-Edge Structure Spectroscopy
XAS	X-ray Absorption Spectroscopy
XPS	X-ray Photoelectron Spectroscopy
XRD	X-ray Diffraction

Table of Contents

Statement of Authorship	2
Zusammenfassung.....	3
Abstract.....	6
Acknowledgements.....	9
Abbreviations.....	12
1. Introduction.....	17
1.1. The Importance of Bioethanol as Feedstock.....	17
1.2. State-of-the-Art of Gold Catalysis in Ethanol Oxidation.....	18
1.3. Supported Bimetallic Gold Catalysts for Oxidation Reactions.....	21
1.4. Synthesis of Bimetallic Gold Catalysts.....	23
1.5. About this Work.....	25
2. Experimental.....	27
2.1. Catalyst Preparation	27
2.2. Catalyst Characterization	29
2.3. Kinetic Measurements.....	30
2.4. Operando DRIFTS Measurements	33
2.5. Operando XAS Measurements.....	33
2.6. Operando NAP-XPS Measurements	34
3. Titania-supported Gold Catalysts	37
3.1. Catalyst Characterization	37
3.2. Kinetic Measurements and Mechanistic Considerations	41
3.3. TPD and <i>Operando</i> DRIFTS Studies.....	45
3.4. The Choice of the Catalyst Support	51
3.5. Computational Mechanistic Considerations.....	56
3.5.1. Computational Methods	56
3.5.2. Ethanol Oxidation Pathways	57

3.5.3.	Simulation of Ethanol Oxidation with a Coverage Dependent First Principles Microkinetic Model	61
3.6.	Conclusion.....	69
4.	Bimetallic Catalysts: Choice of the Promoter.....	72
5.	Bimetallic Supported Gold-Silver Catalysts.....	78
5.1.	Catalyst Characterization	78
5.2.	Kinetic Measurements and Mechanistic Considerations	89
5.3.	Operando Studies	98
5.3.1.	DRIFTS.....	98
5.3.2.	NAP-XPS at ISSS/BESSY II	107
5.3.3.	NAP-XPS at CIRCE/ALBA	113
5.3.4.	Operando XAS.....	127
5.4.	Conclusion.....	137
6.	The Influence of Water and Comparison with the Liquid Phase Reaction.....	139
6.1.	Catalyst Characterization	139
6.2.	Liquid Phase Results (ETH Zurich).....	139
6.3.	Influence of Water in the Gas-Phase Reaction.....	141
6.3.1.	Kinetic Results	141
6.3.2.	Operando Spectroscopy	147
6.4.	Conclusion.....	154
7.	General Conclusions	156
8.	References.....	160
9.	Appendix.....	171
9.1.	Catalyst Synthesis	171
9.2.	XRD Analysis of Catalysts	172
9.3.	Detailed LA-ICP-MS Parameters for the Determination of Metal Loadings ...	179
9.4.	Details for Kinetic Measurements.....	180

9.4.1. GC Settings	180
9.4.2. Exact Flow Settings for Reaction Order Measurements	181
9.4.3. Exact Flow Settings for the Measurement of the Water Influence	182
9.5. Details for DRIFTS Measurements	182
9.6. Additional STEM Data	183
9.6.1. Additional STEM-EDX Data	183
9.6.2. STEM-HAADF	183
9.7. NAP-XPS	185
9.7.1. BESSY II	185
9.7.2. ALBA	188
9.8. Additional Information for the First Principles Microkinetic Model	191
Publications	196
Peer-Reviewed Papers	196
In Preparation	196
Talks and Poster Presentations	196
Scientific Reports	198
Resume	200

1. Introduction

1.1. The Importance of Bioethanol as Feedstock

Enabling chemical reactions, catalysis plays a vital role in our modern world with 95% of products (by volume) involving a catalytic step and 80% of added value in chemical industry based on catalysis¹. As the most important technology in chemical industry, according to estimates, catalysis contributes to >35% of the world's GDP and for every US\$ 1 spent on a catalyst, up to US\$ 1000 worth of product can be generated¹.

Owing to the need to replace crude oil as primary feedstock for the chemical industry, chemicals from renewable sources, such as biomass, have moved into focus²⁻⁴. With a production of 104 billion liters in 2017⁵, bioethanol is one of the most promising raw materials. Due to competition with food production, second-generation ethanol production, i.e. from agricultural waste or lignocellulosic biomass is preferred⁶⁻⁹. However, apart from the most important usage as biofuel, also the pulp-and-paper industries have conflicting interests¹⁰. One example of a commercialized process for bioethanol from lignocellulosic sources is the sunliquid® process from Clariant, with a plant with a 50.000 tons/a production capacity under construction in Romania^{11,12}.

The selective oxidation of ethanol opens the pathway to acetaldehyde and acetic acid, both of which are platform chemicals produced in the million tons scale. Although the importance of acetaldehyde is declining¹³, in 2009 the capacity of installed plants exceeded 2 million tons per year¹⁴. It is an important intermediate in the production of many chemicals, i.e. acetic acid, acetic anhydride, ethyl acetate, peracetic acid, butanol, 2-ethylhexanol, pentaerythritol, chlorinated acetaldehydes (chloral), glyoxal, alkyl amines, pyridines. Acetic acid (primary uses are the production of vinyl acetate, acetic anhydride, acetate esters, terephthalic acid, monochloroacetic acid) is, even though several technologies were commercialized, nowadays primarily produced by the Monsanto (based on a homogenous Rh-complex catalyst) and Cativa processes (based on an Ir complex)¹⁵, both of which require HI as corrosive co-catalyst. Thus, a green chemistry process taking advantage of renewable feedstock and using molecular oxygen as oxidant is highly desirable.

Selective oxidation using gold has been shown to be active and selective for a number of (selective) oxidation reactions, e.g. propene epoxidation, oxidation of ethene to vinyl acetate, oxidation of higher alkenes, alkanes, alcohols and polyols, aldehydes and sugars,

amines¹⁶. Despite the price of Au, there are efforts to use Au in industrial processes: (1) Production of methyl glycolate from ethylene glycol (with Nippon Shokubai operating a pilot plant of 50 tons per year in 2004), (2) propene to propene oxide epoxidation and (3) oxidation carbohydrates to aldonic acids¹⁷. Research at DuPont by Provine et al. shows that addition of Au to Pd silica-supported catalysts for the production of vinyl acetate monomers (VAM) significantly increases the rate of production and space time yield¹⁸.

Due to the high activity with an excellent selectivity towards acetaldehyde and acetic acid, Au is the primary choice in ethanol-based production of chemicals.

1.2. State-of-the-Art of Gold Catalysis in Ethanol Oxidation^I

Selective oxidation of alcohols is an increasingly important reaction that provides a sustainable, solvent-free alternative for the production of ketones, aldehydes and esters¹⁹. Ever since Haruta et al.^{20,21} demonstrated the, rather surprising, high activity of gold nanoparticles in CO oxidation, gold based catalysts have received increasing attention in alcohol oxidation^{16,22–25}. Wittstock and coworkers observed a high activity of nanoporous gold for methanol oxidation at low temperatures²⁶, with a competition between formation of formaldehyde, the primary oxidation product, and methyl formate, the coupling product²⁷. Based on TPR and HREEL measurements on pre-covered O/Au(111), Xu et al.²⁸ proposed a potential oxidation mechanism. In the first step, methanol is dehydrogenated via proton transfer to adsorbed oxygen, forming a methoxy intermediate. Subsequent β -H elimination, which is proposed to be the rate-limiting step, results in formaldehyde. This kinetic role of oxygen was confirmed using *ab initio* calculations²⁹. The barrier for methanol activation decreases from 152 kJmol⁻¹ for direct O-H scission, to 40 kJmol⁻¹ for proton transfer to surface oxygen. Surprisingly, the barrier for β -H elimination also shows a significant decrease when the hydrogen atom is transferred to surface oxygen, from 62 kJmol⁻¹ to 44 kJmol⁻¹²⁹. Significant decreases in activation barrier were observed for methanol oxidation with surface hydroxyl groups (OH^{*})³⁰, molecular oxygen (O₂^{*}) and surface hydroperoxyl species (OOH^{*})³¹. As a result, there's a wide variety

^I This chapter is based on the manuscript “Complex Kinetics for a Simple Reaction: Oxidative Dehydrogenation of Ethanol on Gold” by J. E. De Vrieze, A. Nagl, M. Latschka, S. Mostrou-Moser, J. Teržan, P. Djinović, F. Horak, A. Limbeck, A. Pintar, J. A. van Bokhoven, J. W. Thybaut, K. Föttinger, M. Saeys.

of possible surface reactions and, to date, the dominant reaction mechanism, as well as the rate-determining step, remains unknown.

A similar kinetic puzzle exists surrounding the high activity of ethanol oxidation on gold catalysts^{32–35}. The main difference from methanol, however, is the higher selectivity to its corresponding aldehyde when the reaction is performed in gas phase³⁶. Interestingly, this selectivity shifts to acetic acid when the reaction is performed in liquid phase³⁷. Starting from ethanol two main pathways are available depending on which hydrogen atom in ethanol is eliminated first. When the O-H bond is broken in the first step, an alkoxy intermediate (ethoxy) is obtained, i.e. the alkoxy pathway. Alternatively, when the first step is the β -H elimination, an alkyl intermediate (1-hydroxyethyl) is formed, i.e. the alkyl pathway. In each of those 4 reaction steps, oxidation can occur via hydrogen transfer to the surface, adsorbed oxygen, surface hydroxyl species, molecular oxygen and surface hydroxyperoxyl species³⁸.

In addition to the ethanol oxidation mechanism itself, the activation of oxygen also remains an interesting question as it is often stated that gold has a very low activity for O₂ activation^{39–41}. The ability to activate oxygen is often ascribed to the presence of a metal oxide support⁴², such as TiO₂^{43,44}, CeO₂⁴⁵ or Al₂O₃⁴⁶, which contradicts the high oxidation activity observed for unsupported gold catalysts^{26,32}. As such, the species formed during oxidation might open alternative pathways and facilitate O₂ activation^{47,48}. This lack of fundamental insight in dominant mechanism, rate-limiting step(s) and role of the support severely hampers the design and optimization of gold-based oxidation catalysts, something especially important in gold catalysis due to the high material cost.

Reducible supports lead to more active Au-catalysts⁴⁹, however deviations from this trend are known with TiO₂ and Al₂O₃ showing better performance than ZnO and ZrO₂⁵⁰, a result that was partially confirmed in this thesis, chapter 3.4. Widmann et al. report indications for the involvement of lattice oxygen for Au/TiO₂ catalysts in CO oxidation^{51,52} and Abad et al. show a collaborative effect between Au and the support with CeO₂⁴².

In liquid phase, for the oxidation of alcohols, diols and polyols (such as sugars), Prati et al. reported the necessity of presence of a strong base, e.g. NaOH, for the first hydrogen abstraction step^{24,53}. The selective oxidation of ethanol in liquid-phase yielded mainly acetaldehyde with acetic acid as secondary product as well as ethyl acetate as further by-product⁵⁴, whereas others report acetic acid as the main product^{17,37}. Also in the liquid

phase, using Au/ MgAl₂O₄, Christensen showed the ethanol oxidation to acetic acid⁵⁵. Further investigation into the liquid-phase reaction, also yielding mainly acetic acid, by S. Mostrou-Moser⁵⁶ et al. (this work, focusing on gas-phase, results from a joint project with S. Mostrou-Moser and J. A. van Bokhoven at the ETH Zürich, where the liquid-phase reaction was investigated) showed improved catalytic performance when switching from a batch reactor to a flow setup for Au/TiO₂. Unlike in gas-phase, in aqueous phase both solution-mediated and metal-catalyzed elementary steps seem to be involved in the reaction, also shown experimentally (for ethanol and glycerol oxidation) by isotope experiments with ¹⁸O₂ and H₂¹⁸O which proves oxygen atoms of hydroxyl groups rather than from molecular oxygen are incorporated into the product³⁰. Ab initio calculations from Muñoz-Santiburcio et al.⁵⁷ suggest active participation of water molecules by stepwise charge transfer in the liquid-phase, as opposed to concerted charge transfer to oxygen splitting and abstraction of protonic and hydridic hydrogen atoms in the gas-phase reaction. Due to the fact that bioethanol contains only 4-12 wt.% EtOH after fermentation, and purification is an energy and thus costly process, the liquid-phase oxidation in an aqueous solution is of particular interest⁵⁸.

In gas-phase, Au/TiO₂ also proved a promising catalyst for the oxidation of ethanol^{59,60}. The influence of water, however, is also an interesting and open question in gas-phase. Mullen et al.⁴⁵ reported an enhancement of the acetaldehyde formation on Au/CeO₂ upon addition of water to the reaction feed and it decreased the ethanol reaction order of ethyl acetate production, decreasing the reaction rate. Introduction of D₂O/D-ethanol suggested that breaking of an OH-bond could be connected to the rate-determining step. For CO oxidation, Fujitani et al.⁶¹ also reported a promoting role of H₂O associated with maintaining the cationic state of Au, involvement of H₂O and OH⁻ groups in the oxidation, the activation of O₂ (by facilitating the oxygen dissociation on the surfaces of gold nanoparticles) as well as the transformation of catalytic intermediates and inhibitors. They claim that these factors depend on the metal oxide support resulting in oxygen activation by water on catalysts with the semiconductive metal oxide supports: Au/TiO₂, Au/MnO₂, Au/Fe₂O₃, Au/Co₃O₄, Au/NiO. In contrast to that, for Au/Mg(OH)₂ and Au/La(OH)₃, H₂O is directly involved in the reaction. Saavedra et al.⁴³ identified the changing of number of active sites due to coverage of weakly adsorbed water on Au/TiO₂ as the primary factor for catalyst activity (DFT calculations suggest proton transfer at the metal-support interface

and formation of Au-COOH intermediates, the decomposition of which is supposed to be rate-limiting).

1.3. Supported Bimetallic Gold Catalysts for Oxidation Reactions

Bimetallic Au-catalysts have gained widespread attention over the past few years due to their unique properties, as they both address several issues of their monometallic counterparts as well as often show a synergistic effect of the two metal components leading to new properties and potential tunability (composition, choice of second metal, etc.):

Durability (as required for industrial use), particularly in liquid phase oxidations with O₂, and the apparent need for a base are major drawbacks for monometallic gold catalysts⁶²⁻⁶⁴. Aggregation upon heat treatment and activity for nanoparticles with sizes < 5 nm, sensitivity to moisture (leading to poor reproducibility) as well as inertia toward oxygen and hydrogen⁶⁵ without an oxide support or another metal are further drawbacks of gold. The latter however, is controversially disputed in literature⁶⁶ as intrinsic ability to activate molecular oxygen under oxidation conditions^{44,67} as well as reaction paths proposed involving Au only^{44,68,69} is reported. This was also experimentally confirmed by van Bokhoven et al.⁴⁹ with time-resolved XAS showing charge transfer from the Au d band to the 2p* orbital of oxygen (thus indicating partially oxidized gold as short-lived species under oxidizing conditions) as well as Weiher et al. for Au/TiO₂⁷⁰.

Bimetallic Au-catalysts can overcome these limitations as well as show superior properties due to synergistic effects. Improved activity, selectivity, and stability have been reported in conjunction with other metals such as Pd^{62,65,71,72}, Pt^{62,65}, Ru⁶², Cu^{65,73}, Ag⁷⁴⁻⁷⁷.

Numerous reactions, such as CO oxidation (AuPd⁷⁸⁻⁸⁰, AuAg^{74,76,77}, AuNi⁸¹), preferential oxidation of CO (AuAg⁷³, AuCu⁷³) the selective oxidation of alcohols to aldehydes (AuPd^{65,71,72,82,83}, AuIr⁸⁴⁻⁸⁶, AuAg⁸⁷), partial and complete oxidation of methanol (AuRu^{88,89}), alcohol dehydrogenation (AuAg⁹⁰), oxidations of sugars (AuAg⁹¹), water-gas-shift (AuRu⁹²) show this superior performance with bimetallic catalysts.

However, the nature and origin of the synergistic effect of two metals are often poorly understood⁶². In a bimetallic Au-catalyst, the second metal might be prone to oxidation in O₂-containing atmosphere, leading to segregation and enrichment at the surface and providing reactive oxygen in oxidation reactions. Prevention of sintering is another benefit

of many bimetallic systems, either by the higher melting point as of Au (for PGMs as second metal) or by interaction with the support in the oxidized state⁶⁵. For example, for AuIr/TiO₂, the presence of Ir near the TiO₂ surface increases the adhesion energy of nanoparticles and the attraction between Ir and TiO₂ lead to reduced sintering⁸⁶.

In this work, after a first screening of different promoters (Pd, Pt, Ru, Ag, section 4), AuRu and AuAg have been selected as the most promising catalysts. Both Ru and Ag are known to have a high affinity to O₂:

The interaction between Ru and oxygen resulted in dynamic non-stoichiometric surface oxides RuO_x during methanol oxidation⁹³. Yamaguchi et al. applied a Ru/Al₂O₃ catalyst for alcohol oxidation with molecular O₂⁹⁴. While Au and Ru Au/Ru immiscible in the bulk, in the dispersed state they undergo interactions⁹⁵. Venugopal et al. reported a synergistic effect based on gold-ruthenium interactions for the low-temperature water-gas-shift reaction⁹².

Ag, on the other hand, is a well-known catalyst for dehydrogenation and oxidation, also offering a wide range of oxide chemistry at/near the surface^{96,97}. The AuAg system, historically known as “Electrum”, was investigated by G. Guisbeers et al.⁹⁸: In the bulk, following the Hume-Rothery rules (similar atomic radius, crystal structure, valence, and electronegativity) silver and gold are miscible in every ratio and alloy formation is favored. On the nanoscale, however, thermodynamically driven by minimizing the free energy of the nanoparticle, segregation of Ag is expected (and was proven by HAADF-STEM for nanoparticles of approx. 9 nm of size). Various Au-Ag systems have been used in catalysis, e.g. Liu et al. reported outstanding properties for CO oxidation with large AuAg particles⁷⁴ (in contrast, monometallic Au is most active between 2-5 nm⁷⁴) and also Wang et al. found reduced size-dependency of catalytic activity⁶⁵. However, the influence of size, is controversially discussed in literature. Zheng et al. report that nanoparticles of 6 nm size show higher activity than those with 3.5 nm and 8 nm size⁹⁹. They attributed the enhanced activity to the ability of silver to activate O₂^{77,100}: CO is activated on low-coordinated gold atoms, while active oxygen will be provided by the AgO_x patches present. AuAg/CeO₂ was used for VOC oxidation and preferential CO oxidation and improved performance of AuAg was attributed to the Ag enhancing of surface ceria oxygen mobility⁷⁵. It is often hypothesized that the presence of Ag in the Au surface, reduces the barrier for O₂ activation

either via direct dissociation or through formation of the hydroperoxide species, which has a low dissociation barrier³¹.

1.4. Synthesis of Bimetallic Gold Catalysts

For the synthesis of the catalysts, there are several ways: Deposition-precipitation (DP) as reported by Zanella et al.^{101–104} as well as others^{105–107} is certainly the most popular route¹⁰⁸. However, for oxide supports with low points of zero charge (PZC < 5), e.g. silica, silica-alumina or activated carbons, this method is not applicable¹⁰⁸. Preparation of AuAg catalysts is also a challenge due to the formation of AgCl, however co-deposition-precipitation with ammonia yielded bimetallic AuAg nanoparticles with decreasing size as the Ag/Au ratio increased^{108,109}. Another possibility is a two-step synthesis as reported for AuIr¹⁰⁸.

Bimetallic catalysts can also be prepared by co-impregnation¹⁰⁸ as was demonstrated for AuPd, AuCu, AuIr and AuPt. Homogenous metal nanoparticles are not guaranteed even if the respective metals are miscible at every ratio, e.g. for AuPd where smaller particles were reported to be Pd-rich and the larger ones (≥ 50 nm) contained more gold¹⁰⁸.

By using a one-pot colloidal preparation method, chemical composition, particle size and particle shape can be controlled⁶⁵, however subsequent deposition on a support and removal of the stabilizing agent can change these parameters significantly. One example is the preparation of AuAg on mesoporous MCM-41 with CTAB (hexadecyltrimethylammonium bromide) as surfactant, with the disadvantage of sintering (resulting in particles of 20-50 nm of size) due to AgBr formation⁶⁵. This problem can be circumvented by using other stabilizing agents such as P123 or surfactant removal by O₂ plasma⁶⁵. Two-step methods involving deposition of two metal precursors on a support followed by co-reduction or sequential reduction, is governed more by the metal–metal and metal–support interactions making the preparation of uniform size and composition difficult⁶⁵. Silica-supported AuAg catalysts were prepared by (I) functionalizing the support with amine groups, (II) adsorption of a gold precursor on the amine-functionalized support, (III) reduction with NaBH₄, (IV) adsorption of the second metal precursor and (V) again reduction with NaBH₄⁶⁵. For this procedure, washing to remove the chloride to avoid AgCl formation (which would lead to sintering) is essential⁶⁵. This approach was successful for various silica and alumina supports, but failed for titania and carbon⁶⁵.

The colloidal synthesis route, sol immobilization, offers the advantage of a narrow particle size distribution obtained by reduction of the metal precursor in the presence of various stabilizing or capping agents (CO, citrate, thiol, or amines as well as polymers such as poly-vinylpyrrolidone, PVP, and poly-vinylalcohol, PVA)¹⁰⁸. Stabilizers avoid aggregation and precipitation and control particle growth during reduction, which is induced by sodium borohydride, hydrazine, amine-borane complexes, methanol or glucose and can be assisted by heating, sonication, radiolysis, UV or microwave¹⁰⁸.

A one-pot chemical reduction, deposition of a metal salt and its reduction, followed by the same procedure for the second metal component was shown for AuCu as well as AuAg on silica (a thermal treatment with H₂ being essential for the alloy formation)¹⁰⁸. On SBA-15, gold-silver alloy core and a silver nanoshell was reported¹⁰⁸. Other interesting synthesis techniques are the photo-deposition by UV light as well as the reaction via support, e.g. graphite oxide¹⁰⁸. Using sequential adsorption–reduction method with NaBH₄, Zheng et al. showed surface etching to improve Au–Ag catalysts for benzyl alcohol dehydrogen-ation without oxidant or hydrogen acceptor¹¹⁰.

Also combinations of different synthesis techniques are possible, e.g. for the synthesis of AuRu/CeO₂-ZrO₂ with DP of Au followed by impregnation with Ru(NO)(NO₃)₃. A similar approach was used in this work (see section 2.1) to add silver by incipient wetness impregnation (IWI) to a monometallic gold catalyst (after washing steps to remove the chloride).

Core-shell particles offer further tunability of a bimetallic system, Miao et al. reported AgPd shells on Au nanoparticles of 8.9 nm size for the electrocatalytic EtOH oxidation¹¹¹. Enhanced catalytic activity for the reaction of 4-nitrophenol (4-NP) to 4-aminophenol (4-AP) with NaBH₄ was reported for bimetallic AuAg core-shell particles with varying core sizes from 10 to 100 nm¹¹². Similarly, AuAg core-shell nanocomposites show increased activity (with respect to their monometallic counterparts) for the reduction of nitrobenzene (NB) and 1,3-dinitrobenzene (DNB)¹¹³. Also for oxygen reduction gold-based core-shell particles, AuCu₄₀Pd₆₀ showed higher activity than a commercial Pt catalyst¹¹⁴.

1.5. About this Work

This thesis is on the topic of supported bimetallic gold catalysts for the selective ethanol oxidation in the gas phase. The research goals of this projects were: (I) Understanding the monometallic gold system for the selective ethanol oxidation, including the choice of a suitable support. (II) Finding a suitable bimetallic system by introducing a second metal component as promoter for the reaction. (III) Detailed investigation of the most suitable bimetallic catalyst including mechanistic studies by state-of-the-art *operando* spectroscopy (DRIFTS, NAP-XPS, XAS). (IV) Comparison of the liquid-phase reaction, as performed by the project partners (S. Mostrou-Moser in the van Bokhoven group) at the ETH Zürich: Is the same bimetallic system the most active under both conditions? Are there meaningful differences in the selectivity, reaction mechanism? (V) Investigation of the influence of water in the gas-phase. This is motivated by several factors such as the general importance of H₂O in catalytic reaction mechanisms, understanding the differences to the liquid-phase where, due to process-requirements, always an aqueous solution of ethanol is used as educt. And, finally, given the (costly and energy-consuming) effort to purify/dehydrogenate ethanol, the water tolerance of the reaction in gas-phase is an interesting question. Thus, this thesis is structured as follows:

After presenting the state-of-the-art in this chapter and introducing the experimental methods (chapter 2), first a study of the monometallic gold catalyst is given. For the Au/rutile as well as the Au/C system, a combined experimental and computational kinetics study is given in order to investigate potential support effects. The experimentally measured reaction orders are subsequently compared to a first principles microkinetic model, combining all the possible reaction steps proposed in recent literature, allowing the identification of the dominant reaction mechanism as well as the rate-limiting step(s).

After having gained thorough understanding of that system, chapters 4 and 5 deal with bimetallic systems, first exploring different promoters and then focusing on the AuAg system. Chapter 6 explores the difference between the ethanol oxidation in gas-phase and the liquid-phase and sheds light onto the effect of water introduction to the gas phase.

Selected parts of a joint manuscript^{II} with J. E. de Vrieze in M. Saeys' group, Ghent University, Belgium, are reprinted in this work. In addition to the shared literature study (section 1.2), the experimental data and the joint conclusion based on theory and experiment (section 3.6), also results of the microkinetic first principles modelling are shown to provide deeper understanding of the reaction mechanism. These microkinetic results are reprinted with permission from J. E. de Vrieze and M. Saeys and do not originate from my own work.

Likewise, this thesis was carried out in cooperation with S. Mostrou-Moser from J. A. van Bokhoven's group, ETH Zürich, Switzerland. Whereas my own experimental work covers the gas-phase reaction, S. Mostrou-Moser worked in liquid-phase: These results are reprinted with permission from S. Mostrou-Moser and J. A. van Bokhoven and do not originate from my own work.

Some TPD experiments were undertaken by J. Teržan in A. Pintar's group and Cs-corrected STEM imaging was performed in cooperation with G. Dražić and A. Pintar during a research stay at the Department for Environmental Sciences and Engineering, National Institute of Chemistry, Ljubljana, Slovenia.

NAP-XPS experiments were performed at the ISISS beamline at BESSY, Berlin, as well as at the CIRCE beamline, ALBA, Barcelona. Significant amounts of the XPS evaluation were performed in cooperation with A. Foelske and M. Sauer from the, Analytical Instrumentation Center, TU Wien.

Also, other (experimental) results by other colleagues are clearly acknowledged throughout this work.

^{II}“Complex Kinetics for a Simple Reaction: Oxidative Dehydrogenation of Ethanol on Gold” by J. E. de Vrieze, A. Nagl, M. Latschka, S. Mostrou-Moser, J. Teržan, P. Djinović, F. Horak, A. Limbeck, A. Pintar, J. A. van Bokhoven, J. W. Thybaut, K. Föttinger, M. Saeys.

2. Experimental

2.1. Catalyst Preparation

The TiO₂-supported catalysts (nominal metal loadings: 5 wt.% Au) were prepared by deposition-precipitation with urea^{101,104–107,115}. Rutile (TP Hombikat Mikrorutil, Venator, BET surface area 105 m²/g) was added to an aqueous solution of HAuCl₄ (purchased from Sigma Aldrich) and urea (Merck) with a pH of 7. During vigorous stirring at 80°C for 4 h, the pH changed from acidic to basic and an orange precipitate was deposited on the support material. The catalyst was washed 5x with DI water (to achieve a chloride-free catalyst) and dried at 100°C.

Several TiO₂-based catalysts were prepared, Au/rutile using TP Hombikat Mikrorutil (Venator, BET surface area 105 m²/g), Au/anatase with anatase nanopowder (Sigma Aldrich, 45-55 m²/g), Au/P25 with AEROXIDE® P25 TiO₂ (35-65 m²/g with an anatase/rutile ratio of approximately 80/20, Evonik Industries) as well as Au/anatase₈₀rutile₂₀ a mixture of 80% anatase (Sigma Aldrich, 45-55 m²/g) and 20% rutile (Venator, BET surface area 105 m²/g). The nominal metal loading was 5 wt.% Au for all catalysts.

Bimetallic catalysts (AuRu/Rutile, AuPt/Rutile) were prepared from Au/rutile using Platinum(IV)chloride (Sigma Aldrich) with urea (same ratio as for the monometallic catalyst) and Ruthenium(III)chloride hydrate (Sigma-Aldrich), respectively. The monometallic reference catalysts for Pt and Ru were prepared the same way on pure rutile.

Silver-promoted catalysts (AuAg/rutile as well as AuAg/C) were prepared from the monometallic Au catalysts using incipient wetness impregnation (IWI) with a silver nitrate solution (approx. 1.5 mL was needed for 1 g rutile powder). An Ag/rutile reference sample was prepared using the same protocol (with rutile as starting material instead of Au/rutile).

For the second metal component/promoter was added yielding a metal loading of 1 wt.%, except for Pt, where 2 wt.% were used to preserve the approximate molar Au/promoter ratio: The atomic mass of Pt of 195.08 is roughly twice as high as the respective atomic masses of Ag, 107.87 g/mol, and Ru, 101.07 g/mol.

The reason for this was the high atomic mass of Pt of 195.08, which is roughly twice as high as the respective atomic masses of Ag (107.87 g/mol) and Ru (101.07 g/mol).

All samples were stored with without any calcination step in the dark avoiding light exposure.

Several batches of catalysts were prepared: (I) Batch 1 for the first kinetic screening and choice of the ideal promotor (section 4). (II) Batch 2 for further experiments. However, due to a higher drying temperature, these samples resulted in a larger particle size and no further experiments were performed for this thesis. (III) Batch 3 for all the reaction order measurements presented in chapter 3 (investigation Au/rutile), chapter 5 (investigation of AuAg/rutile), section 6.3 (investigation of the influence of H₂O in gas-phase) as well as all the DRIFTS measurements presented in this work. (IV) Batch 4 for the synchrotron beamtimes presented in section 5.3.

The Au/C sample was purchased from Strem Chemicals (CAS number: 7440-57-5, synthesized by laser ablation) with a loading of 1 wt.% Au. AUROLite/TiO₂ (0.8 wt.% metal loading), AUROLite/ZnO as well as AUROLite/Al₂O₃ (both 1 wt.% metal loading) are commercial samples obtained from Strem Chemicals (CAS number: 7440-57-5, extrudates). For all measurements, the extrudates were grinded to a fine powder.

On overview of all the different batches prepared for this thesis is given in the following table:

Table 1. Overview of the samples investigated in this thesis.

	Samples	Usage
Batch 1	Au/rutile, AuAg/rutile, AuPt/rutile, AuRu/rutile	Section 4, section 6.2
Batch 2	Au/rutile, AuAg/rutile, AuRu/rutile	Not used after quick kinetic screening.
Batch 3	Au/rutile, AuAg/rutile	All measurements in section 3, section 5 and section 6, except for synchrotron measurements.
Batch 4		Synchrotron measurements in section 5.3 and 6.3.2.
Anatase/Rutile	Au/P25, Au/anatase, Au/anatase ₈₀ rutile ₂₀	Section 3.4, investigation of different TiO ₂ modifications.

Commercial Catalysts	Au/C and AuAg/C, AUROLite/TiO ₂ , AUROLite/ZnO, AUROLite/Al ₂ O ₃	The Au/C and AuAg/C (prepared from Au/C) were used as reference in this whole work. The AUROLite samples were used as references in section 3.4.
-----------------------------	---	--

The exact weights used are listed in the annex, section 9.1.

2.2. Catalyst Characterization

The particle size distributions of the catalysts were established by STEM-HAADF imaging using a FEI Tecnai F20 FEG-TEM instrument (operated at 200 kV): Samples were imaged after the pretreatment process of the catalyst (oxidative treatment in 20% O₂ at 400°C followed by reductive treatment in 5% H₂ at 300°C – see Kinetic measurements section) on lacey carbon grids.

Additional HR-STEM and HR-STEM-EDX images for the bimetallic AuAg/rutile sample were performed with a probe Cs-corrected Scanning Transmission Electron Microscope, model ARM 200 CF (Jeol Ltd.). For the EDX measurements, a Jeol Centurio with 100 mm² SDD detector with a declared solid angle of 1 sr was used. Imaging was done at 200 keV and 80 keV (to avoid beam damage). These measurements were undertaken in cooperation with G. Dražić and A. Pintar, Department for Environmental Sciences and Engineering, National Institute of Chemistry, Ljubljana, Slovenia.

XRD measurements were undertaken after synthesis as well as after the pretreatment using a PANalytical X'Pert (PANalytical) PRO powder diffractometer in Bragg-Brentano geometry (see annex for detailed parameters).

BET surface area was established using an ASAP 2020 instrument (Micromeritics). The pretreated samples were degassed under vacuum at 100°C for 180 min (heating ramp: 10°C/min) prior to measurement.

Samples were imaged after the pretreatment process of the catalyst (oxidative treatment in 20% O₂ at 400°C followed by reductive treatment in 5% H₂ at 300°C) on lacey carbon grids as well as for (selected samples) after the reaction.

Temperature programmed desorption (TPD) experiments were performed for H₂, O₂ and ethanol (EtOH) using a Autochem 2920 apparatus (Micromeritics) coupled to a mass spectrometer (Thermo Star, Pfeiffer Vacuum). The samples (50 mg on a flock of quartz wool inside a quartz reactor) were pretreated in 20 % O₂/N₂ for 30 min at 400 °C followed by 5% H₂/Ar at 300 °C for an additional 30 min. After cooling to 0°C, saturation was reached with 5% H₂/Ar or 20% O₂/N₂, respectively. For the EtOH-TPD experiments, saturation was reached with 10 pulses of EtOH vapor after cooling to -30 °C followed by degassing with Ar for 30 minutes at 25°C. Samples were heated with a 5°C/min. ramp to 600°C. The following m/z fragments were recorded: 32 for O₂, 2 for H₂ and 18 for H₂O. For the EtOH-TPD, 31 and 45 for EtOH, 44 for CO₂ and 29 for acetaldehyde were monitored. Desorption energies are determined by Redhead analysis.

Au loadings were determined using Laser Ablation-Inductively Coupled Plasma-Mass Spectrometry (LA-ICP-MS). A NWR213 (ESI) ns-Laser ablation (LA) system was hyphenated to an iCAP Q (Thermo Fisher Scientific) quadrupole inductively coupled plasma mass spectrometer (Q-ICP-MS). The particles were dispersed in ethanol and pipetted on a polycarbonate disk and individual particle clusters, as identified in the LA system, were subsequently ablated and analyzed in the ICP (detailed parameters in annex, section 9.3). The LA-ICP-MS experiments were carried out and evaluated by F. Horak in the group of A. Limbeck, Institute of Chemical Technologies and Analytics, Technische Universität Wien, Vienna, Austria. For the Ag-content, due the absence of any washing step, the nominal silver content was assumed to be correct.

2.3. Kinetic Measurements

Kinetic measurements were performed in a continuous-flow fixed-bed quartz reactor under atmospheric pressure. Ethanol was introduced by bubbling He through a liquid-vapor saturator kept at different temperatures. A flow diagram of the setup is shown in Figure 1. The mass flow controllers, mks 247 (MKS Instruments), were controlled by an microcontroller Arduino Leonardo ETH (Arduino) in combination with a 16 bit AD5696 DAC (Analog Devices) with a custom software (using Arduino C/C++ for the

microcontroller and a .net-based windows program written in C#) allowing automated programming of the gas flows, thus resulting in highly reproducible measurements. The programming of the custom software was done as part of this thesis whereas the hardware was assembled by R. Rosner. The oven was controlled by a Eurotherm 3216 PID (Eurotherm/Schneider Electric) controller, with the thermocouple placed inside the reactor. Prior to reaction, the catalyst was pretreated in 20% O₂ (all gases used for kinetic measurements were diluted in He) with a heating to 400°C at 10°C/min and after a holding period of 30 minutes, a reduction step followed at 300°C in 5% H₂ for another 30 minutes. Quantitative analysis of the effluent gas stream was conducted using an Agilent 7890A GC (equipped with an FID and a TCD detector) setup for two column-use (Agilent HP PLOT-Q and an HP-PLOT Molsieve). Selected reactions were also monitored by mass spectrometry (Pfeiffer Vacuum OmniStar GSD 320 O mass spectrometer). Turnover frequency (TOF) was determined by normalizing the reaction rate for acetaldehyde and ethyl acetate to the number of surface gold atoms, which was estimated from the average size obtained from the particle size distribution (from STEM-HAADF imaging), and from the gold content as measured via LA-ICP-MS. The gold nanoparticles were assumed to be of hemispherical form on the support.

Unless more sample was used (e.g. for the measurements of reaction orders at low temperatures with low conversion), the catalyst was diluted with quartz sand to avoid mass and heat transfer limitations.

Catalytic activity evaluation was done under the following conditions: The catalysts were diluted with quartz sand to a total gold loading of the catalyst bed of 0.5 wt.%. A total flow of 51.2 mL with 1.1 mL/min. EtOH and O₂, a 1:1 ratio of the educts (resulting in a partial pressure of 2.2 kPa each) was applied at temperatures between 200 and 300°C (in steps of 25°C).

The influence of water on the reaction rate was measured under three conditions, (I) 1.1 kPa EtOH/O₂ (no water), (II) 1.1 kPa EtOH/O₂ and 0.6 kPa H₂O and (III) 1.1 kPa EtOH/O₂ and 2.0 kPa H₂O To see the reversibility of the water additoin effect, the measurement was concluded with applying conditions (I), without water, again. The flow was kept as close as possible to 50.5 mL/min (see annex, section 9.4.3, for the exact gas flows) and the temperature was kept constantly at 250°C.

Samples were measured in a conversion regime below 20% (unless stated otherwise) to ensure that the system was in the differential conversion regime (diluted with quartz sand as necessary). Reaction order measurements were performed as follows: (1) For the O₂ reaction order, the O₂ partial pressure was varied between 1.1 kPa and 5.3 kPa whereas the EtOH partial pressure was kept constant at 2.2 kPa. (2) The EtOH reaction order was established with EtOH partial pressures from 0.5 kPa to 4.5 kPa with a constant O₂ partial pressure of 10.1 kPa. For both (1) and (2) the total flow was kept constant at approx. 50 mL/min. The exact experimental parameters are listed in the annex section 9.3.

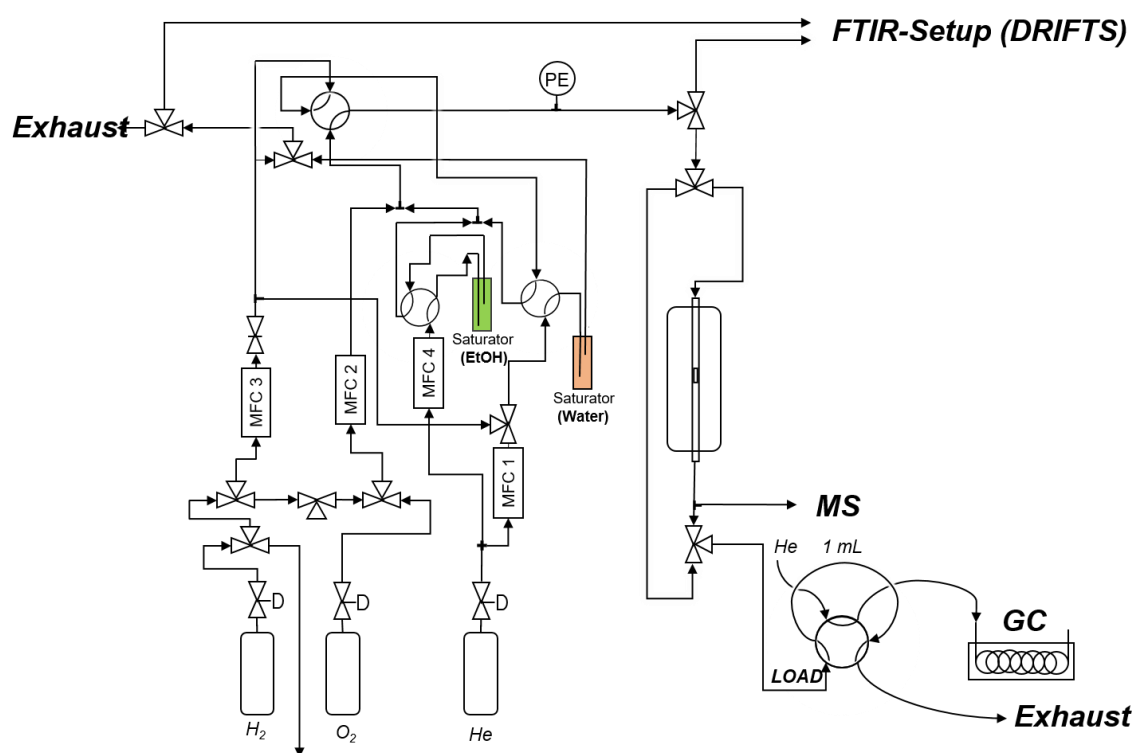


Figure 1. Flow diagram of the kinetic setup. Four mass flow controllers, two for He, one for H₂ and one for O₂ allow the dosage of the gases at the defined flow rates. Two saturators allow dosing of liquids (as vapors). For the reactions, one was used for EtOH whereas the other one was used for H₂O. Effluent gases are analyzed by an Agilent 7890A GC (equipped with an FID and a TCD detector) with two columns (Agilent HP PLOT-Q and an HP-PLOT Molsieve). Selected reactions were also monitored by mass spectrometry (Pfeiffer Vacuum OmniStar GSD 320 O mass spectrometer). Gas-flows can be directed to the FTIR setup to conduct DRIFTS measurements. A piezoelectric pressure sensor (PE) monitors the pressure of the reaction.

Measurements in the aqueous phase were performed S. Mostrou-Moser at the ETH Zürich as follows: The experiments were conducted in a batch reactor system consisting of a series of parallel autoclaves (Berghof BR-25). The catalyst (50 mg and 90-125 µm grain size) and 10 ± 0.03 mL of a 5 ± 0.3 vol. % EtOH solution (Fluka, >99.8%) were added to the Teflon®-

lined reactor, which was sealed. Thereafter, oxygen (PanGas, 99.999%) was introduced ($p = 15$ bar). Each reactor was stirred and heated with a Heidolph MR3002 apparatus, which was controlled by a BTC-3000 Berghof controller. At the end of the reaction, the autoclaves were cooled below 7°C and the remaining pressure was released.

The liquid products were analyzed off-line with an Agilent 7890A gas chromatograph (GC) equipped with a flame ionization detector (FID, 30 mL/min H_2 flow mixed in 400 mL/min air at 300 K) and a DB-WAX column. During the analysis, 0.5 μL of sample was injected at 70 K and a carrier gas flow of 2 mL/min He was applied through the column DB-WAX. The temperature of the column was constant at 40°C for 2 min and was then heated at $8^{\circ}\text{C}/\text{min}$ to 135°C . The molar concentration of each component was determined using linear regression of calibration standards.

2.4. Operando DRIFTS Measurements

Operando diffuse reflectance infrared Fourier transform spectroscopy (DRIFTS) measurements were performed with a Bruker Vertex 70 FTIR equipped with an MCT detector and a Pike DiffusIR (including a heatable environmental chamber with gas-flow capabilities and a CaF_2 window). Measurements were undertaken with undiluted samples in the sample cup with the same flows as for the catalytic activity evaluation as described in section 2.3, with EtOH and/or O_2 partial pressures of 2.2 kPa = 1.1 mL/min at a total flow of approx. 50.5 mL/min (see annex section 9.4. for exact flows). Spectra were taken during the pretreatment as well as at 150°C and 250°C under the conditions: (I) EtOH only, (II) EtOH and O_2 , (III) EtOH only and (IV) O_2 only (He was always used to balance the total flow.). The influence of water was investigated under two conditions, (I) 1.1 kPa EtOH/ O_2 (no water) and (II) 1.1 kPa EtOH/ O_2 and 2.0 kPa H_2O .

As background, the cell equipped with an Al-alignment mirror purged with He, was used. Spectra are shown after Kubelka-Munk (KM) transformation. Spectra were taken from 4000 to 900 cm^{-1} with a resolution of 4 cm^{-1} .

2.5. Operando XAS Measurements

Operando X-ray absorption spectroscopy studies at the Au LIII-edge (11.9187 keV) were measured in transmission mode, ALBA Synchrotron, Barcelona, Spain¹¹⁶. The solid-gas

reactor (“multipurpose cell”) developed by Simonelli et al. in cooperation with the Instituto de Tecnología Química (ITQ-UPV) was used¹¹⁶. For the measurement of the Ag K-edge an undiluted pellet with 100 mg sample was used whereas for the Au LIII edge 20 mg sample were diluted with BN to a total weight of 100 mg. The gas stream outlet was monitored by an OmniStar GSD 320 O mass spectrometer (Pfeiffer Vacuum).

Pretreatment was carried out at a total flow of 50 mL/min, starting with 20% O₂ with a heating from RT to 400°C (holding time ~ 2 hours) and > 30 min 5% H₂ at 300°C (holding time ~ 2 hours). The reaction was performed at a total flow of 68 mL/min. (ca. 1 mL/min. O₂/EtOH) at 250°C and 300°C.

The Al₂O₃ ex-situ reference spectrum was obtained at a shared beamtime with S. Mostrou-Moser at the superXAS beamline, Swiss Light Source, and used for the linear combination fits (LCFs).

The Ag K-edge was measured at the B18 beamline, Diamond Light Source, Didcot, UK¹¹⁷. Experiments were performed using the “Industrial Group Micro-Reactor”, a capillary-based flow cell heated by a hot air blower. Whereas the references, the Ag foil and Ag₂O were measured in transmission mode, all the operando experiments were done with fluorescence detection. The effluent gas was monitored by on-line mass spectrometry.

Pretreatment was performed with 20% O₂ under heating from RT to 400°C, holding for 30 minutes followed by a reduction step with 5% H₂ at 300°C for another 30 minutes. Both conditions applied at a total flow of 50 mL/min. Operando experiments were undertaken under the following conditions: (I) 1.1 mL/min EtOH/O₂, (II) 1.1 mL/min EtOH, (III) 0.6 mL/min H₂O and (IV) 0.17 mL/min EtOH + 0.5 mL/min H₂O + 0.25 mL/min O₂. All operando experiments were carried out at a total flow of 50 mL/min and 250°C.

For both beamtimes, data processing and evaluation was performed with the PrestoPronto software package by Prestipino¹¹⁸, version b.1.0.0. Data reduction of all XAS spectra involved energy calibration, background subtraction and normalization. Au and Ag metal foils were used for energy calibration.

2.6. Operando NAP-XPS Measurements

Operando near ambient pressure X-ray photoelectron spectroscopy, NAP-XPS, measurements were performed at two beamtimes: The first was taking place at the ISSS

beamline, BESSY II of the Helmholtz-Zentrum Berlin, which is described elsewhere in detail^{119,120}. The setup consists of differentially pumped electrostatic lenses with a Phoibos 150 Plus (SPECS) analyzer. Samples were pressed as a pellet with a K-type were pressed into a Ta-grid (Unique Wire Weaving, NJ, USA) together with a K-type thermocouple and, mixed with graphite (Alfa Aesar) to reduce charging effects. It was mounted on a sapphire sample holder placed in front of the electrostatic nozzle. Heating was performed using an infrared laser. In this flow cell equipped with MFCs, all experiments were performed at a total pressure of 0.5 mbar, except for the reducing step of the pretreatment where only 0.33 mbar could be reached (due to limitations of the available mass flow controllers).

Pretreatment carried out under oxidative conditions with an O₂ flow of 5 mL/min. during heating to 400°C with 10°C/min followed by reduction at 300°C under 5 mL/min H₂ flow. In contrast to kinetic experiments (section 2.3), however, temperatures were held for approx. 3 hours to take the XPS spectra. *Operando* experiments were performed under the following conditions: (I) 2.5 mL/min EtOH/O₂ at 250°C, (II) 2.5 mL/min EtOH at 250°C, (III) again 2.5 mL/min EtOH/O₂ at 250°C as well as at 300°C and 350°C and again 250°C (to investigate, possibly irreversible, temperature effects), (IV) 2.5 mL/min EtOH and 5 mL/min H₂O (to examine the, again possibly irreversible, influence of water) at 250°C and finally (V) again 2.5 mL/min EtOH/O₂ at 250°C. This beamtime focused on depth profiling at kinetic energies of 310 and 700 eV in order to investigate the surface composition and find out whether a surface segregation of AgO_x on the bimetallic AuAg nanoparticle surface occurs in an oxygen-containing atmosphere.

Further questions of interests were investigation of temperature effects, the effect of water addition to the reaction feed as well as possible changes of the oxidations state of Au, Ag and Ti.

The energy calibration was performed using the carbon C 1s peak which was omnipresent due to the graphite added to the pellet.

The second NAP-XPS experiment was carried out at the CIRCE beamline at the ALBA Synchrotron, Barcelona, Spain¹²¹ taking advantage of a differential pumping system (equipped with a Phoibos NAP150 from SPECS hemispherical electron energy analyzer)¹²². Samples were pressed into a Ta-grid (Unique Wire Weaving, NJ, USA) together with a K-type thermocouple and, and where necessary, mixed with graphite (Alfa

Aesar) to reduce charging effects. Heating was carried out with a heatable sample holder (with an encapsulated filament). All experiments were performed at a pressure of 0.5 mbar.

The pretreatment was carried out as described above for the ISIS beamtime experiment. *Operando* measurements, under reaction conditions, were conducted under three different EtOH/O₂ conditions, (I) 1.6 mL/min EtOH and 2.5 mL/min O₂, (II) 2.5 mL/min for both EtOH/O₂ as well as (III) 2.5 mL/min EtOH only and (IV) again 2.5 mL/min EtOH/O₂. The gas composition at the exit of the flow cell was monitored by mass spectroscopy.

The main interest of this beamtime was the verification of the results of the depth profiling obtained at BESSY II and obtain the oxidation state of Ag. Depth profiling was performed at three different kinetic energies (100, 310 and 670 eV).

For AuAg/rutile, the energy calibration was performed using the Au 4f, whereas for Ag/rutile the added graphite was used.

XPS spectra were analyzed using the CasaXPS package. For the Ag 3d and Au 4f signals, a linear background was assumed, whereas for any other signals, a Shirley-type function was applied. Atomic ratios of Au/Ag (and Ag/Au, respectively) were calculated using cross-sections as published by Yeh and Linau¹²³. A correction using the known photon flux characteristics of the beamlines/monochromators was used to account for differences in the photon flux at different energies.

3. Titania-supported Gold Catalysts^{III}

3.1. Catalyst Characterization

The gold nanoparticles are highly dispersed in a nanocrystalline state as shown by STEM-HAADF imaging in Figure 2 a) with a mean size 3.3 ± 1.0 nm on Au/rutile (see annex section 9.2 for the XRD), whereas on the carbon-supported particles are considerably larger with a mean size of 14.5 ± 0.5 nm.

STEM-HAADF micrographs and size distributions comparing different TiO₂ supports to Au/rutile are shown in Figure 3. Also, the commercial catalysts AUROLite/TiO₂ and AURLite/ZnO were characterized by STEM-HAADF, Figure 4. The corresponding mean particle sizes are summarized in For batch 4 of Au/rutile, used for the synchrotron measurements, a loading of 4.41 wt.% was determined.

Table 3. Due to the low catalytic activity of AUROLite/Al₂O₃, no STEM-HAADF study was conducted on this sample (average particle size, as given by the manufacturer, Strem Chemicals, is 2-3 nm).

The measured BET surface areas of the catalysts (Table 4), 28 m²/g for Au/rutile and 210 m²/g for Au/C, reflect the washing steps during synthesis (rutile: 103 m²/g) on the one hand and the typical high surface area of activated carbon on the other hand. Also, BET surface areas of selected catalysts discussed in section 3.4, are listed in Table 4.

The metal loadings, as determined by LA-ICP-MS are listed in Table 2:

Table 2 Metal loadings as determined by LA-ICP-MS. Starred values are provided by the manufacturer, not measured.

Sample	Metal Loading (wt.%)
Au/rutile	2.82 ± 0.12
Au/C	1*
Au/anatase	2.75 ± 0.18
Au/P25	3.02 ± 0.10
Au/anatase ₃₀ rutile ₂₀	3.30 ± 0.23

^{III} This chapter is based on the manuscript “Complex Kinetics for a Simple Reaction: Oxidative Dehydrogenation of Ethanol on Gold” by J. E. de Vrieze, A. Nagl, M. Latschka, S. Mostrou-Moser, J. Teržan, P. Djinović, F. Horak, A. Limbeck, A. Pintar, J. A. van Bokhoven, J. W. Thybaut, K. Föttinger, M. Saeys. The first principles microkinetics model by J. E. de Vrieze in the group of M. Saeys was reprinted here with permission to discuss the experimental results.

AUROLite/TiO₂	0.8*
AUROLite/ZnO	1*

For batch 4 of Au/rutile, used for the synchrotron measurements, a loading of 4.41 wt.% was determined.

Table 3. Size distributions of the catalysts covered in chapter 3.

Sample	Mean Particle Size (nm)
Au/rutile	3.3 ± 1.0
Au/C	14.5 ± 0.5
Au/anatase	3.4 ± 0.6
Au/P25	3.6 ± 1.2
Au/anatase₃₀rutile₂₀	3.9 ± 1.1
AUROLite/TiO₂	3.2 ± 0.6
AUROLite/ZnO	2.1 ± 0.4

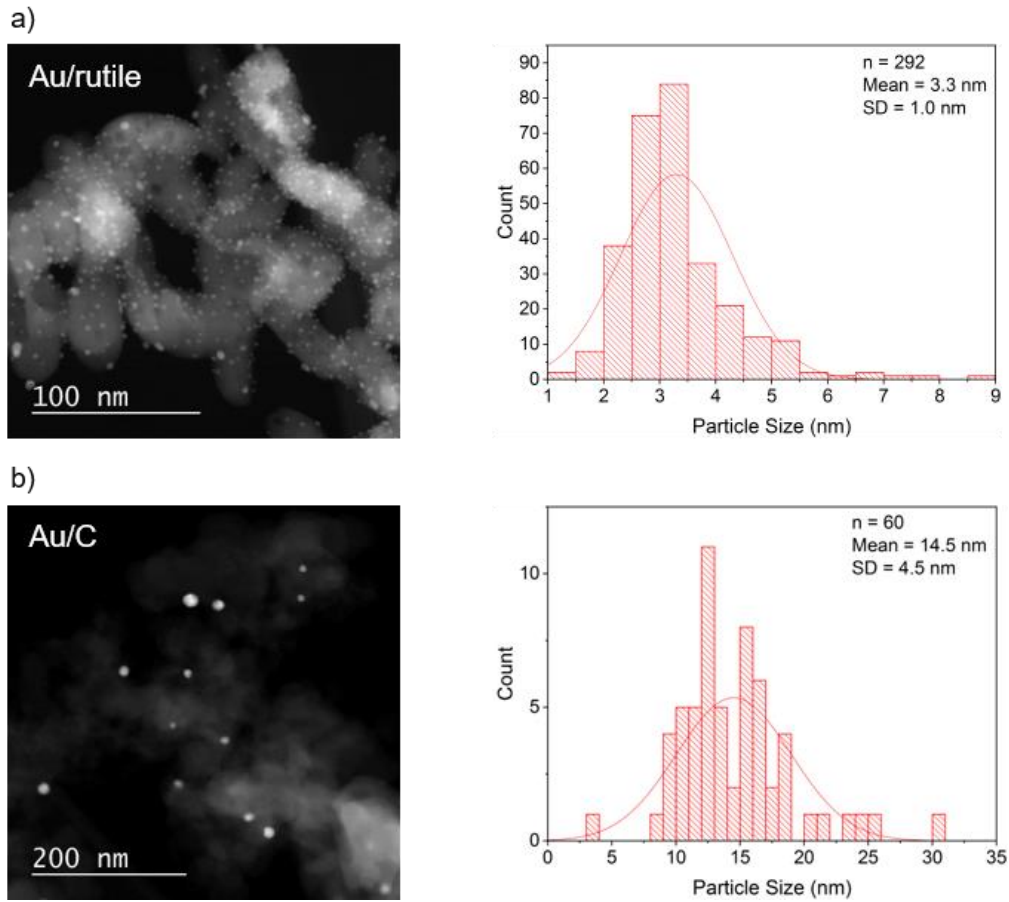


Figure 2. STEM-HAADF images of Au/rutile (a) and Au/C (b) and their respective size distributions. Au/rutile has a mean particle size of 3.3 ± 1.0 nm (representative sample of 292 particles counted) whereas Au/C has a considerably larger mean particle size of 14.5 ± 4.5 nm (60 particles).

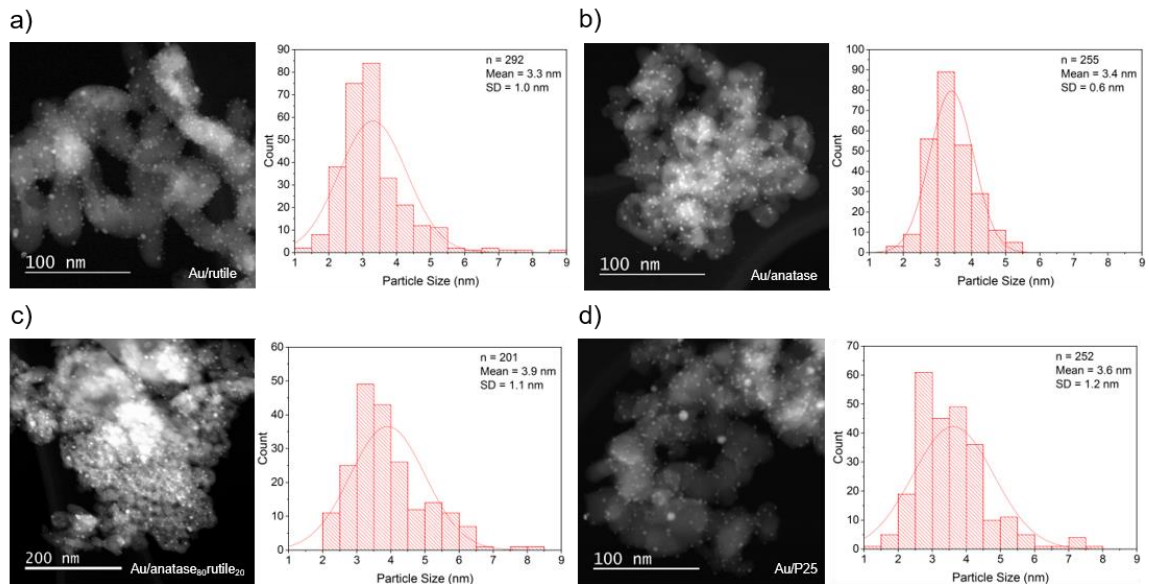


Figure 3. STEM-HAADF images and size distributions for (a) Au/rutile, (b) Au/Anatase, (c) Au/anatase₈₀rutile₂₀ and (d) Au/P25. Information on the AUROLite/TiO₂ sample is given in Figure 4.

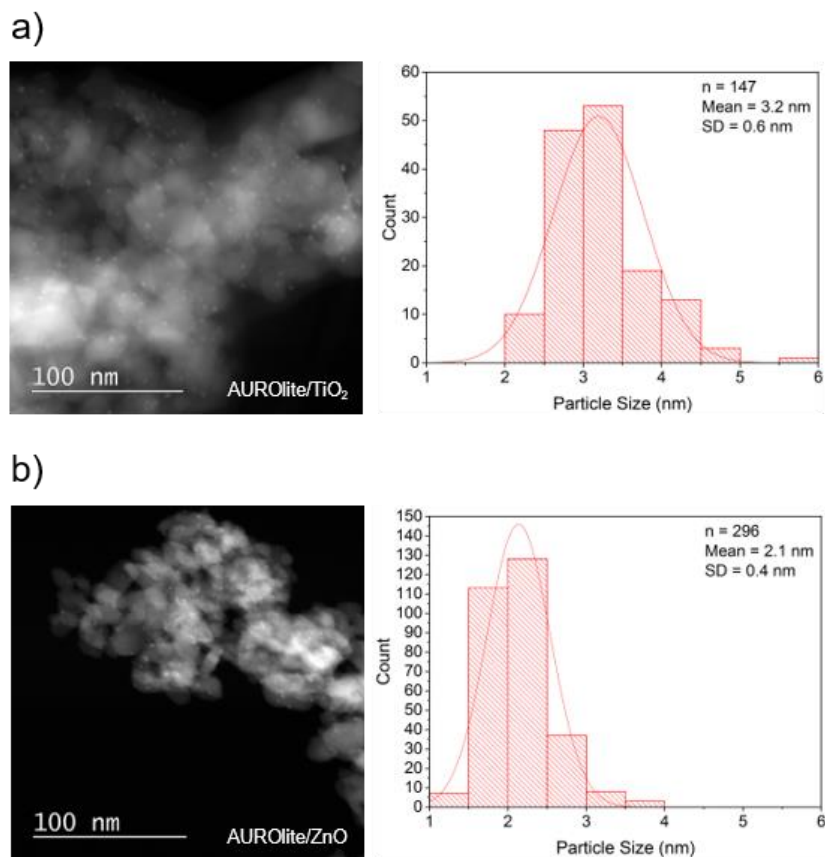


Figure 4 STEM-HAADF images and size distributions for (a) AUROLite/TiO₂, (b) AUROLite/ZnO.

Table 4. BET surface areas of the catalysts.

Sample	BET surface area (m ² /g)
Rutile	103 (manufacturer: 105)
Au/rutile	28
Au/C	210
Anatase	68
Au/Anatase	33
AUROLite/TiO ₂	20
AUROLite/ZnO	38

The Au/rutile and Au/C are discussed in detail in section 3.2 (kinetic measurements), 3.3 (TPD experiments and *operando* DRIFTS measurements) and 3.5 (computational results). Differences in TiO₂ supports, rutile, anatase and mixtures of the both, as well as ZnO and Al₂O₃ are discussed in 3.4.

3.2. Kinetic Measurements and Mechanistic Considerations

Reaction rates for Au/rutile and Au/C are depicted in Figure 5, normalized to the catalyst mass as well as the metal loading. In both cases, Au/rutile showed superior activity, partly owing to the much smaller particle sizes. Turnover frequencies were determined using the mean particle size and metal loading as determined previously, Figure 6. Au/rutile and Au/C showed very similar intrinsic activity at 200°C with a TOF of 0.18s⁻¹. However, Au/rutile shows a stronger dependence on the reaction temperature than Au/C with a slope of 1.83 compared to 1.04, Figure 6. Surprisingly, this indicates that Au/rutile has a higher apparent activation than Au/C. For both samples, high selectivity towards acetaldehyde (> 97%) with ethyl acetate as the main side product was observed (at 300°C very small amounts of acetic acid were seen for Au/rutile).

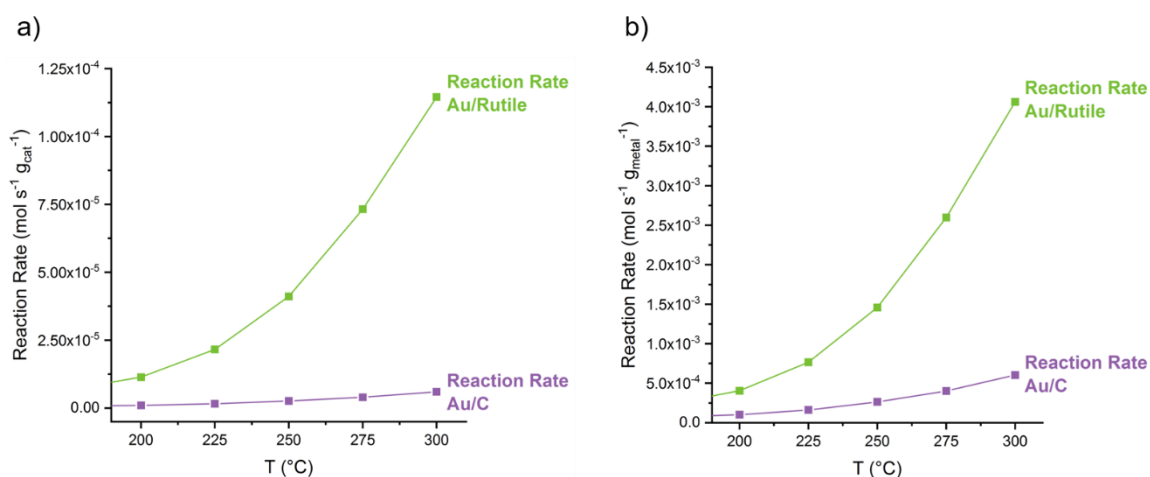


Figure 5. Reaction rates per (a) catalyst mass in gram and (b) metal loading in gram metal for Au/rutile and Au/C. A total flow of approx. 51.2 mL, with 1.1 mL/min. EtOH and O₂, a 1:1 ratio of the educts (resulting in a partial pressure of 2.2 kPa) was used.

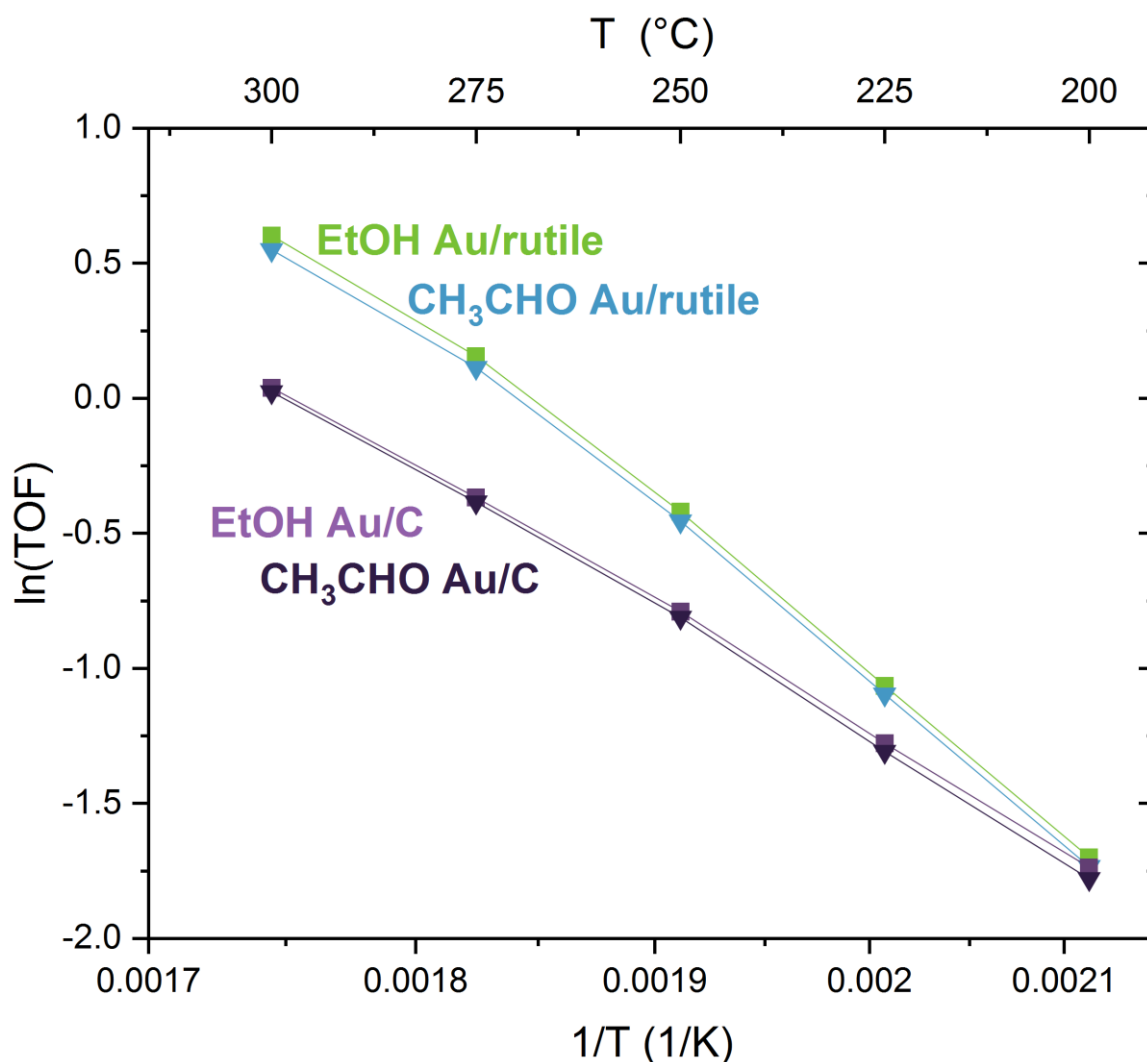


Figure 6. $\ln(\text{TOF})$ against $1/T$ are plotted for the EtOH TOF of Au/rutile (green) and the CH_3CHO TOF of Au/rutile as well as for the Au/C (light and dark purple), respectively. TOFs are similar for both catalysts at low temperature and considerably larger for Au/rutile at higher temperature (numerical TOFs are listed in Table 2).

The TOFs of the different reaction products are shown in Table 5. The TOFs for ethyl acetate and acetic acid are a few orders of magnitude lower than production of acetaldehyde. The formation of acetic acid was even below the detection limit at temperatures below 300°C and is therefore not displayed in Table 5. This large difference in production rates results in a high selectivity towards acetaldehyde, Figure 7.

Table 5. TOF obtained for acetaldehyde, ethyl acetate and acetic acid production.

TOF Acetaldehyde (s^{-1})					
	200°C	225°C	250°C	275°C	300°C
Au/rutile	0.18	0.33	0.64	1.12	1.73
Au/C	0.17	0.27	0.44	0.68	1.02
TOF Ethyl acetate (s^{-1})					

	200°C	225°C	250°C	275°C	300°C
Au/rutile	3.1×10^{-3}	5.4×10^{-3}	1.1×10^{-2}	2.4×10^{-2}	4.7×10^{-2}
Au/C	3.7×10^{-3}	4.1×10^{-3}	5.0×10^{-3}	6.0×10^{-3}	7.9×10^{-3}
TOF Acetic acid (s^{-1})					
	200°C	225°C	250°C	275°C	300°C
Au/rutile					8.5×10^{-4}
Au/C					

As shown in Figure 7, the main product is acetaldehyde with a selectivity over 97% for all measured temperatures. The main side product is ethyl acetate with a selectivity of around 3%, depending on the temperature, consistent with previous measurements³⁶. When the temperature was increased, the ethyl acetate selectivity slight decreased. This is mainly a result of the reaction mechanism, ethyl acetate is formed by coupling of an ethoxy species with acetaldehyde³³. As the temperature increased, both the ethoxy as well as the acetaldehyde coverage will decrease, reducing the coupling probability. However, an opposite trend is observed on Au/rutile, which indicates potentially different kinetics for ethyl acetate formation. In addition, acetic acid formation is observed on Au/rutile at 300 °C. Under all conditions, the total oxidation of ethanol, i.e. CO₂ formation, was below the detection limit for both catalysts.

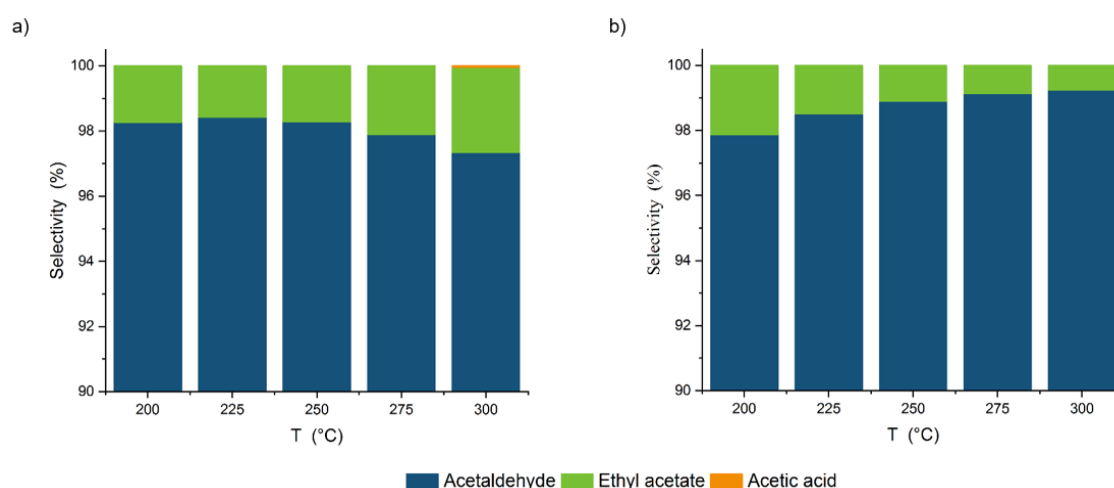


Figure 7. Selectivities of the investigated catalysts, (a) Au/rutile and (b) Au/C, for both of which a selectivity > 98% towards acetaldehyde was observed. Only for Au/rutile, small amounts (< 1%) of acetic acid were observed at 300°C.

To characterize the kinetics of ethanol oxidation on Au/C and Au/rutile, reaction orders were determined. By varying the O₂ and ethanol partial pressures at different temperatures, Figure 8, the reaction orders could be calculated via linear regression. As shown in Figure 8, a good fit is observed between the logarithm of the partial pressure and the logarithm of the acetaldehyde formation rate for both Au/rutile and Au/C at all measured temperatures.

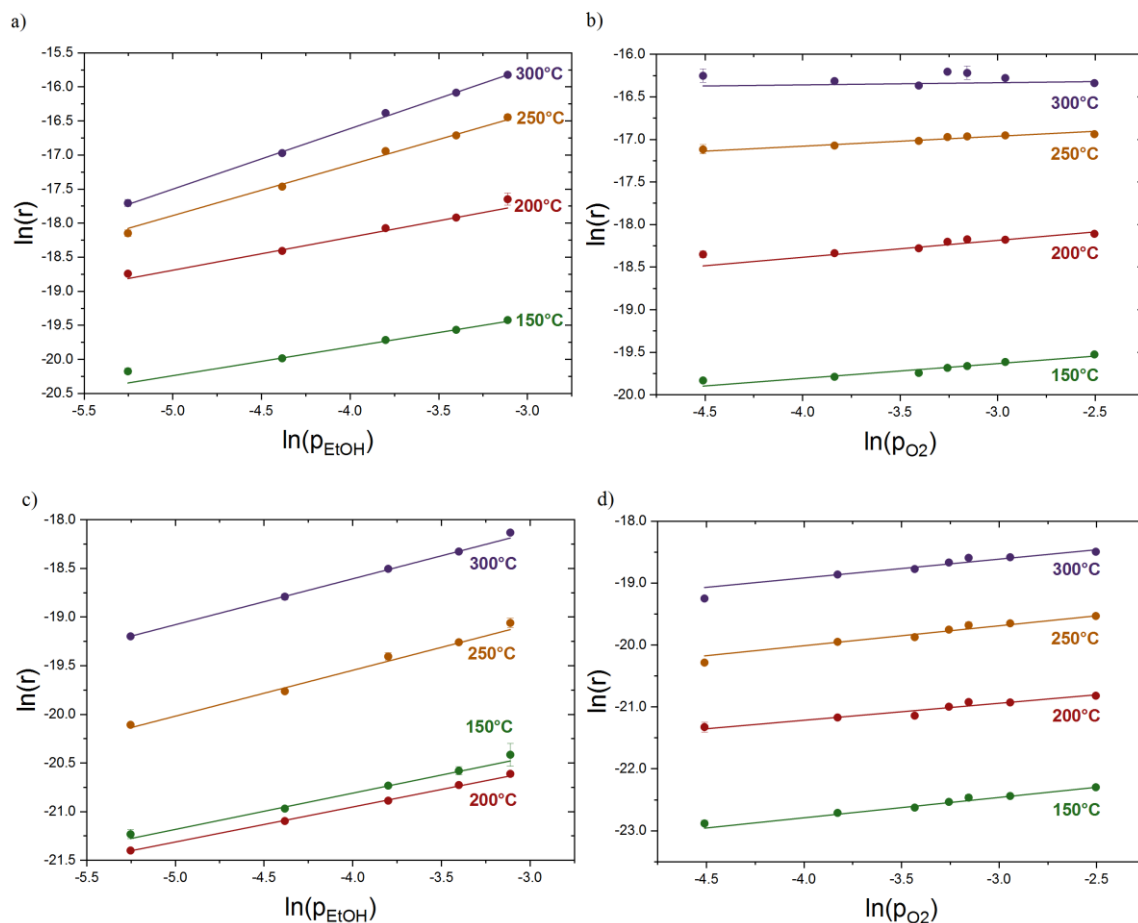


Figure 8. Reaction orders of EtOH (a) and O₂ (b) for Au/rutile and for the Au/C (c,d), respectively. The values of the respective reaction orders are listed in Table 6.

An overview of how the reaction orders change with temperature is shown in Table 6. At 150°C, the ethanol reaction order is similar on Au/rutile and Au/C, 0.42 and 0.38 respectively. When the temperature increased, however, the ethanol order doubled on Au/rutile, amounting to 0.89 at 300°C, while the order only increased to 0.47 on Au/C. The oxygen order is also similar at 150°C, 0.37 and 0.33 for the Au on rutile and carbon support respectively. While the oxygen order decreases on Au/rutile with increasing temperature (indicating higher availability of oxygen, eventually through activation at the rutile/Au interface at higher temperatures), to 0.03 at 300 °C, the oxygen order is practically constant on Au/C. Carbon can generally be assumed to be inert under these conditions, as such it

provides a good model to study the kinetics of gold itself, eliminating the possible support effects. The observed difference in reaction kinetics between rutile and carbon supported gold indicates a catalytic effect of rutile, either by providing an active site, through strong metal support interactions or charge transfer, or the Au-support interface plays a role in the mechanism. It is remarkable, however, that the oxygen reaction order on Au/C is lower than the ethanol reaction order at all the studied temperatures. This shows that even for ‘unsupported’ gold, oxygen activation is kinetically less important than ethanol activation, confirming the observations by Abad et al.⁶⁷ that gold is intrinsically able to activate molecular oxygen under oxidation conditions. To gain insight in the trends observed on the Au/C catalyst and further elaborate on its difference with Au/rutile, a first principles microkinetic model is required.

Table 6. Obtained reaction orders for O₂ and EtOH.

	Au/rutile		Au/C	
	EtOH Order	O ₂ Order	EtOH Order	O ₂ Order
150°C	0.42 ± 0.02	0.18 ± 0.02	0.37 ± 0.02	0.33 ± 0.01
200°C	0.48 ± 0.02	0.20 ± 0.02	0.36 ± 0.01	0.27 ± 0.03
250°C	0.75 ± 0.05	0.12 ± 0.02	0.47 ± 0.02	0.32 ± 0.02
300°C	0.89 ± 0.02	0.03 ± 0.06	0.47 ± 0.00	0.30 ± 0.03

3.3. TPD and *Operando* DRIFTS Studies

For the H₂- and O₂-TPD experiments, neither H₂ nor O₂ desorption was observed (desorption temperature below adsorption temperature). EtOH-TPD profiles for Au/C and Au/rutile, on the other hand, show distinctive differences (see Figure 9). Using the Redhead equation, peak temperatures were converted to adsorption energies.

For Au/C one single peak at 62.7°C, corresponding to the desorption of ethoxy species from the surface is observed (ethanol desorption temperature is below the adsorption temperature). Taking into account computational results, section 3.5, the E_{ads} of 95 kJmol⁻¹ obtained by Redhead analysis is consistent with calculations for the β-H elimination in the ethoxy species, 88 kJmol⁻¹, on the Au(111) surface. Thus, EtOH shows dissociative adsorption under β-H elimination, which is highly activated. Upon temperature increase, dehydrogenation of the ethoxy species starts to occur. The barrier of 95 kJmol⁻¹ is also very close for the β-H elimination in the ethoxy species, 88 kJmol⁻¹ whereas the hydrogenation

of the ethoxy species back to EtOH has a lower barrier of 34 kJmol⁻¹. As a result, all hydrogen that is produced will be instantly consumed to hydrogenate ethoxy species, making the desorption peaks of ethanol and acetaldehyde coincide.

In fact, only the fragmentation pattern shows that some of the ethanol is desorbed as acetaldehyde, as all the observed patterns, 29, 31 and 45 are both present in the MS of acetaldehyde and ethanol. Apart from this single peak, only above 400°C ($E_{\text{ads}} = 230 \text{ kJmol}^{-1}$), CO₂ formation is observed (The 44 fragment is common to both CO₂ and acetaldehyde, however CO₂ lacks the 29 fragment.), which is probably due to the decomposition of activated carbon or of functional groups of the activated carbon.

For Au/rutile, however, a different picture presents itself: The desorption peaks and their respective adsorption energies are listed in Table 7. At 65.9 °C (69 kJmol⁻¹), the same ethanol and acetaldehyde peak is observed, however also some total oxidation of CO₂ is already observed. Practically all the ethanol adsorbed is indeed desorbed as acetaldehyde or CO₂. Amounts desorbed are by an order of magnitude lower than for the Au/C due to the high surface area of activated carbon (whereas the number of Au surface atoms in this sample is only approx. 47% of the Au/rutile). Due to the presence of oxygen (from rutile), a clear peak is also observed for a COO species at 365.0 °C (184 kJmol⁻¹), indicating the presence of a strongly bound acetate-like species. This desorption energy corresponds to the calculated barrier for acetate dissociation into CO₂ and CH₃*, 169 kJmol⁻¹.

For the rutile reference, two peaks are observed, acetaldehyde desorbing at 323.5°C, 173 kJmol⁻¹, and CO₂ desorbing at 430.3°C, 204 kJmol⁻¹. Thus, already the rutile facilitates the oxidation of EtOH by providing sites for the β-H elimination of ethoxy species and providing oxygen, although at much higher temperatures.

The huge differences in the TPDs reflect the influence of rutile onto the reaction as demonstrated by the reaction order measurements in section 3.2. These TPD experiments were performed by J. Teržan in A. Pintar's group, Department for Environmental Sciences and Engineering, National Institute of Chemistry, Ljubljana, Slovenia.

Table 7 Results of the Redhead analysis for Au/rutile.

Compound	T (°C)	E_{ads} (kJmol ⁻¹)
Acetaldehyde/Ethanol	65.9	96
Acetaldehyde	137.9	128

Acetaldehyde	365.0	184
CO₂	375.8	187
CO₂	583.0	242

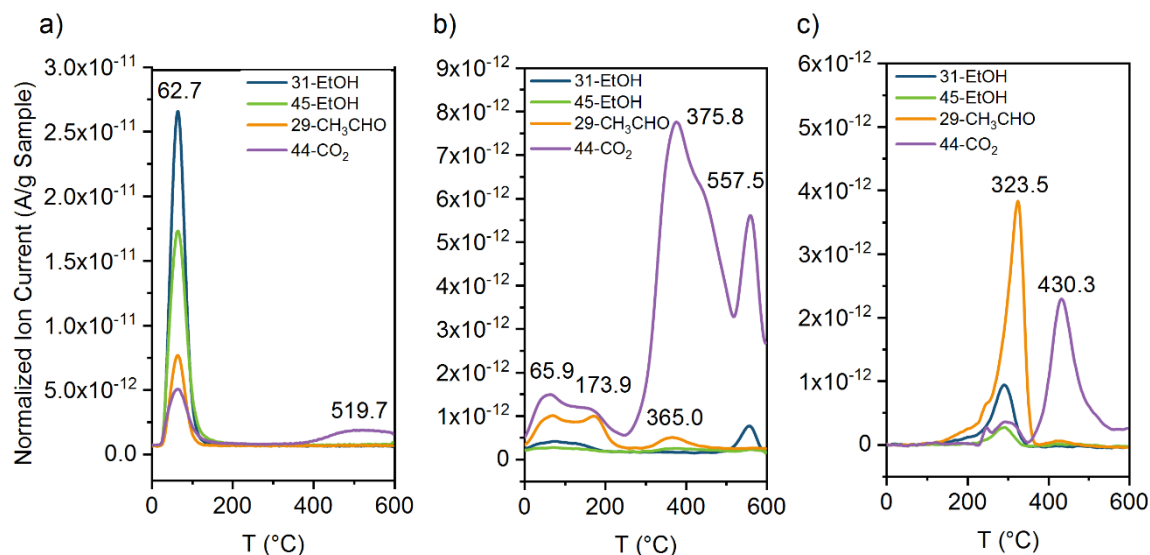


Figure 9. Ethanol TPD experiments for (a) Au/C, (b) Au/rutile (c) rutile reference sample. *m/z* signals of 31 and 45 were used for the EtOH detection, whereas 29 was used for acetaldehyde (CH₃CHO) and 44 for CO₂. These TPD experiments were performed by J. Teržan in A. Pintar's group, Department for Environmental Sciences and Engineering, National Institute of Chemistry, Ljubljana, Slovenia.

Operando DRIFTS measurements reveal the surface species present on the catalysts under reaction conditions (see Figure 10 for steady-state conditions at 250°C, EtOH/O₂ ratio = 1/1, and Figure 11 for the complete measurement series).

Figure 10 a) shows the region between 4000 – 2500 cm⁻¹ at 250°C (EtOH/O₂ ratio = 1/1) where for both Au/rutile and rutile the broad band at 3417 cm⁻¹ is affiliated to adsorbed EtOH¹²⁴ which can be also adsorbed in multilayers¹²⁴ and interact with remaining hydroxyl groups (3690, 3660 and 3629 cm⁻¹) of the rutile on the surface^{125,126} (and form ethoxy species¹²⁶). Whereas these OH-groups cannot be seen in Figure 10, this replacement on the surface^{126,127} can be observed in Figure 11. The peak at 3417 cm⁻¹ is much more pronounced for the rutile in contrast to the Au/Rutile sample, presumably due to the higher surface area of rutile and higher conversion and desorption of acetaldehyde on the Au/rutile, and thus less ethanol coverage on the latter.

Bands at 2976 cm^{-1} , 2935 cm^{-1} and 2873 cm^{-1} were assigned to $\nu_a(\text{CH}_3)$, $\nu_s(\text{CH}_3)$, $\nu_a(\text{CH}_2)$ and $\nu_s(\text{CH}_2)$ ^{124-126,128-131} of ethanol, ethoxy and, possibly, also acetaldehyde¹²⁷ (see Figure 10 a) and appear only after the pretreatment upon ethanol addition (see Figure 11 a)).

The Au/C sample shows bands with very low intensity (very dark powder with – as shown by TPD – ethanol adsorption only at low temperatures with a very low metal loading of 1 wt.% and low particle surface area due to the large particle size). Between 4000 – 2500 cm^{-1} , the $\nu_{s/a}$ band of adsorbed ethanol (in contrast to rutile and Au/rutile) is absent, but the presence of ethanol can be seen through the C-H stretching bonds (not all three peaks are clearly resolved).

Figure 10 b), on the other hand, shows the region of 1900-1100 cm^{-1} . The band at 1731 cm^{-1} can be assigned to the $\nu(\text{CO})$ of adsorbed acetaldehyde¹²⁹ (and possibly also in the gas-phase¹²⁶) and is much more clearly visible at the Au/rutile sample due to the higher conversion. On rutile, the broad 1435 cm^{-1} signal can be attributed to adsorbed acetate^{124,131} (1438 cm^{-1} and 1443 cm^{-1} in literature^{124,131}), $\nu_{ip}(\text{C-O})$ of η_2 -acetaldehyde¹³⁰ or η_2 -acetyl¹³⁰ (1432 cm^{-1} in literature) and $\delta_{as}(\text{CH}_3)$ of acetaldehyde/ethoxy^{126,127} (1444 cm^{-1} in literature^{126,127}). On Au/rutile two bands, at 1450 and 1435 cm^{-1} are seen whereas on rutile, only 1435 cm^{-1} is observed. The 1379 cm^{-1} band is assigned to $\delta_s(\text{CH}_3)$ of ethoxy species^{126,129} whereas 1344 cm^{-1} can be attributed to $\omega(\text{CH}_3)/\delta(\text{CH}_3)$ of ethoxy, acetyl and η -acetaldehyde¹³⁰ (1344 cm^{-1} is the band maximum on Au/rutile, on pure rutile the band is shifted to a slightly higher wavenumber of 1354 cm^{-1}) or adsorbed acetate¹²⁴ (1340 cm^{-1}).

For the Au/rutile sample, a significantly different situation can be observed: The $\delta_s(\text{CH}_3)$ band of ethoxy species disappeared and the prominent bands at 1520 cm^{-1} and 1450 cm^{-1} appeared, both of which can be attributed to $\nu(\text{COO})$ ^{126,128,129,131}, thus showing the presence of acetate species. For Au/C, ethoxy species can be observed at 1379 cm^{-1} and, possible also $\nu(\text{COO})$ at higher wavenumbers in the same broad peak. Two small peaks at approx. 1257 and 1226 cm^{-1} are attributed to $\delta(\text{OH})$, possibly ethanol^{60,128,131,132} or acetaldehyde¹²⁷.

At both 150°C and 250°C, measurements were undertaken under the conditions (I) EtOH, (II) EtOH + O₂, (III) EtOH, (IV) O₂, In Figure 11 a), during the pretreatment, decrease of water can be observed. Upon switching to reaction conditions, the adsorbed ethanol appears (as can be seen by the corresponding C-H bands, which quickly decrease under O₂-only flow) and the rutile's OH-groups are replaced by adsorbed ethoxy species.

Figure 11 b) shows the dynamic behavior of the COO species on the Au/rutile catalyst. Starting with the pretreatment under oxidative conditions (20% O₂, heating from RT to 400°C with a holding time of 30 min), the COO intensity (1520/1450 cm⁻¹) of residual organic components from the sample synthesis as also observed by Tan et al.¹²⁹ is decreasing only to reappear under reductive conditions (5% H₂ at 300°C for 30 min). At 150°C and 250°C, a dynamic behavior of the COO species, now attributed to the acetate coverage on Au(111) was observed: After pretreatment, the 1450/1520 cm⁻¹ bands drop in intensity (to approx. 75% for 1520 cm⁻¹ and 50% for 1450 cm⁻¹). Under reaction conditions, the COO bands are higher as the conversion increases, thus increasing upon switching from condition (I) to (II), EtOH only, and upon heating from 150°C to 250°C. Afterwards, under condition (III), EtOH, and (IV), O₂, the bands are decreasing again. The dynamic behavior of the COO band was investigated using first principles kinetic modeling. The oxidation of acetaldehyde to acetate was included in the model and showed a significant acetate coverage, >10%. However, including this acetate formation had no significant effect on the predicted reaction orders or the reaction path analysis, indicating that this species has a spectating role.

For Au/C, no changes in the bands shown in Figure 10 were observed over time and under different reaction conditions. A complete list of the assigned bands can be found in Table 8.

Further discussion of DRIFTS, especially the comparison the AuAg samples can be found in 5.3.1.

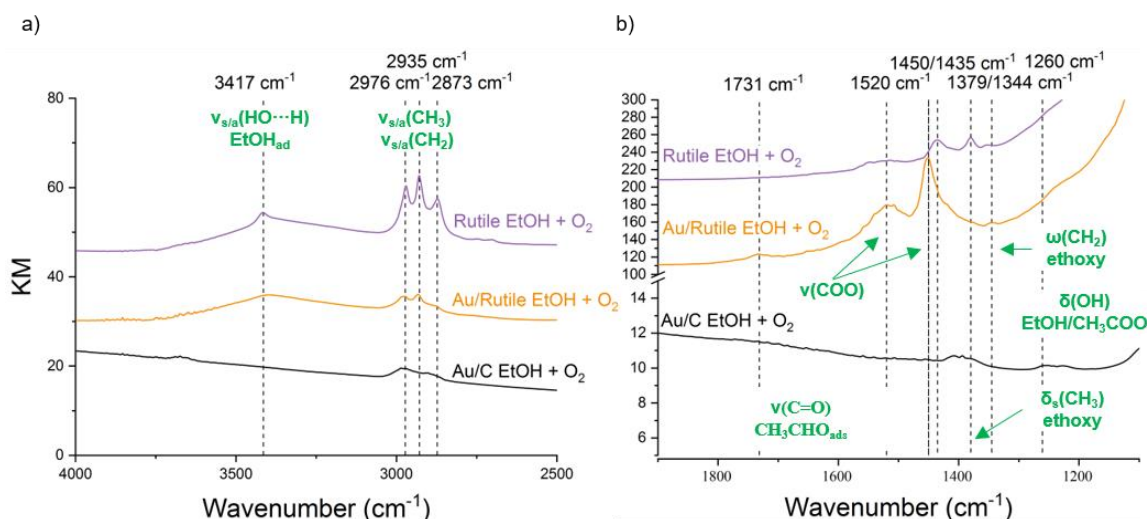


Figure 10. DRIFTS spectra (transformed to Kubelka-Munk) under operando conditions (250°C, total flow of approx. 51.2 mL, with 1.1 mL/min. EtOH and O₂: partial pressure of 2.2 kPa) of the region between (a) 4000 – 2500 cm⁻¹ and (b) 1900-1100 cm⁻¹.

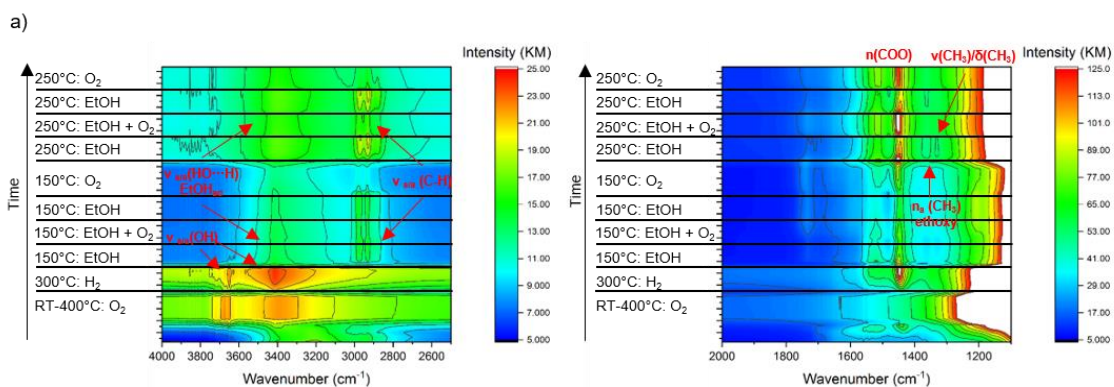


Figure 11. Time-resolved operando DRIFTS measurements for the Au/rutile sample, regions between (a) 4000 – 2500 cm⁻¹ and (b) 1900-1100 cm⁻¹. The measurement series started with the pretreatment under oxidative conditions (RT-400°C under 20% O₂ with 10°C/min, holding for 30 minutes) followed by a reducing step (300°C for 30 min under 5% H₂). Operando measurements were performed at EtOH and/or O₂ partial pressures of 2.2 kPa = 1.1 mL/min (each). For the whole measurement, the total flow was at approx. 50 mL/min (for exact flows see annex). (a) Shows the replacement of hydroxy groups of the rutile with ethoxy groups whereas (b) shows the dynamic behavior of COO species: During pretreatment, they can be attributed to residual organic species from the sample synthesis¹²⁹ and during reaction conditions they reflect the coverage of acetate species on the Au(111).

Table 8. Complete list of assigned bands and their adsorbates (including references).

Wavenumber in this work (cm ⁻¹)	Wavenumber in literature	Assignment	Adsorbate
1260	1260 ⁶⁰ , 1264 ^{128,1} 31,132 / 1274 ¹²⁸ , 1261 ¹²⁷	δ(OH) ^{60,128,131} , 132 δ(OH) ¹²⁷	Ethanol Acetaldehyde

1344/1354	1348 ¹³⁰	$\omega(\text{CH}_2)^{130}$	Ethoxy, acetyl ¹³⁰
	1346 ¹³⁰	$\delta(\text{CH}_3)^{130}$	Ethoxy ¹³⁰ , η -acetaldehyde ¹³⁰ bidentate acetate, secondary and tertiary ethanol derivative ¹³⁰
	1340 ¹²⁴	$\delta_s(\text{CH}_3)^{124}$	adsorbed acetate ¹²⁴
1379	1379 ^{126,129}	$\delta_s(\text{CH}_3)^{126,129}$	Ethoxy ^{126,129}
1435	1438, 1443 ^{124,131}	$\nu_s(\text{COO})$	Acetate ^{124,131}
1450/1520	1443 ¹²⁹ /1553 ¹²⁹ ,	$\nu(\text{COO})^{126,128,129,131}$,	Acetate ^{126,128,129,131}
	1453 ¹³¹ /1535 ¹³¹		
	1415 ¹²⁸ , 1437 ¹²⁸ ,		
	1441 ¹²⁸ /1527 ¹²⁸ ,		
	1540 ¹²⁸ , 1583 ¹²⁸		
	1580 ¹²⁶ , 1456 ¹²⁶ ,		
1496 ¹²⁶			
1731	1731 ¹²⁶	$\nu(\text{CO})^{126,129}$	Acetaledehyde (gas-phase) ¹²⁶
	1735 ¹²⁹		Acetaldehyde adsorbed on TiO ₂ ¹²⁹

3.4. The Choice of the Catalyst Support

Different TiO₂ supports, anatase and rutile as well as mixtures were tested, Figure 12. All catalysts were prepared in the same way with the same Au loading. The Au/rutile is clearly the most active catalyst, showing the highest activity at all measured temperatures, suggesting rutile to be the best TiO₂ modification for this reaction. Au supported on pure anatase is the second-best catalyst, however only slightly better than the mixtures of anatase and rutile. P25 is a commercially available TiO₂ consisting of approximately 80% anatase and 20% rutile (as specified by the manufacturer). Using powder XRD and Rietveld analysis, 87% anatase and 13% rutile were determined (see annex section 9.2). A catalyst supported on an artificial mixture of 80% anatase, Au/anatase₈₀rutile₂₀, and 20% rutile yields nearly the same catalytic activity, proving that indeed the rutile/anatase mixture is the most dominant factor for the catalytic activity. Interestingly, the mixtures of anatase and rutile show lower activity than anatase, given the fact that rutile leads to higher catalytic activity than anatase. The exact reason for this phenomenon remains unclear, maybe

significant numbers of Au nanoparticles at rutile-anatase interface play a role, as observed in photocatalysis²³. Another possible reason is that the Au nanoparticles are not equally distributed on anatase/rutile, possibly due to preferential nucleation at one of the two modifications during the deposition-precipitation process. Efforts to prove on of these hypotheses by STEM-EELS, however, failed to the low statistical relevance (quantifying the number of nanoparticles on anatase particles and rutile particles).

Considering the reaction rate normalized to the catalyst mass, AUROLite/TiO₂ shows the lowest catalytic activity of all the Au-catalysts, Figure 12 a), however this can be attributed to the low metal loading of 0.8 wt.% as opposed to 5 wt.% for all the other samples. Normalizing the reaction rate to the metal mass shows that the catalyst is indeed close to the other catalysts with an anatase/rutile mixture as support. The rutile is not only the most potent support, it also exhibits a higher catalytic activity than anatase, however, even at 300°C, on a low level of $3.0 \cdot 10^{-6} \text{ mol s}^{-1} \text{ g}_{\text{cat}}^{-1}$ at a conversion of 5.9% (Figure 14) as opposed to $1.1 \cdot 10^{-6} \text{ mol s}^{-1} \text{ g}_{\text{cat}}^{-1}$ at a conversion of 2.2% (Figure 14).

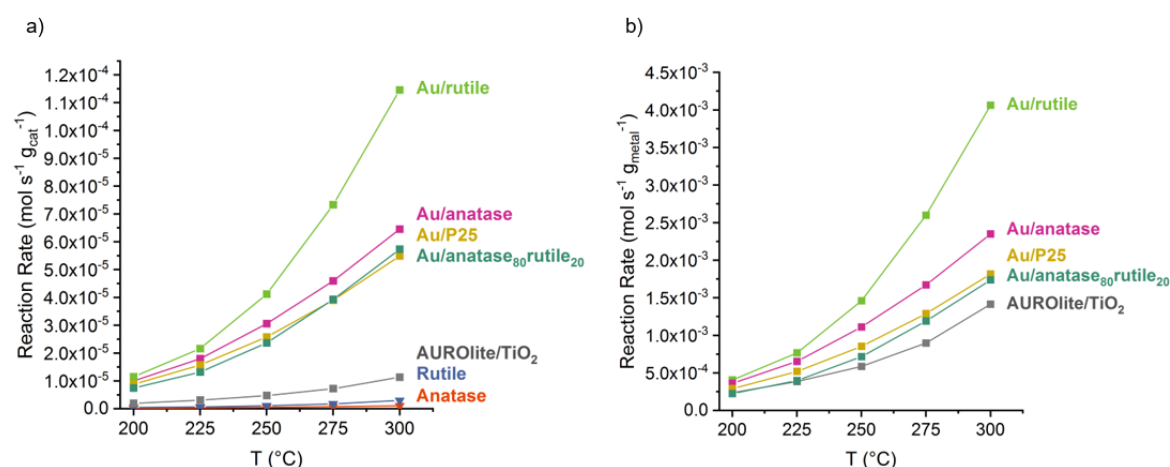


Figure 12. Comparison of Au/rutile (green), Au/anatase (purple), AUROLite/TiO₂ (grey), rutile (blue), anatase (orange), (a) reaction rate based on gram catalyst and (b) on gram metal (as determined by LA-ICP-MS, or for AUROLite/TiO₂ as provided by the manufacturer.). A total flow of approx. 51.2 mL, with 1.1 mL/min. EtOH and O₂, a 1:1 ratio of the educts (resulting in a partial pressure of 2.2 kPa) was used.

A glance on the selectivity reveals interesting differences between rutile and anatase. Whereas for Au/rutile (Figure 14 (a)), only ethyl acetate and, at 300°C, low amounts (0.05%) of acetic acid, are produced apart from acetaldehyde, for all other Au-catalysts much higher selectivity for acetic acid is observe: Up to 0.8% for Au/anatase (Figure 14 (b)), 0.6% for Au/P25 (Figure 14 (c)), 0.8% for Au/anatase₈₀rutile₂₀ (Figure 14 (f)) and 2.5% for AUROLite/TiO₂ (Figure 14 (g)).

The pure supports (at very low conversion level) produce relevant amounts of acetic acid (up to 4.6.% for rutile and 4.1% for anatase) as well as CO₂ (up to 3.8% for rutile and 7.8% for anatase).

The BET surface area of the Au/rutile catalyst was 28 m²/g and 33 m²/g for Au/anatase, thus showing that the BET surface area plays no relevant role in the different activity. For AUROLite/TiO₂ 20 m²/g were measured, which is also a comparable value.

Apart from TiO₂, also Al₂O₃ (as common “non-reducible” support) as well as ZnO were explored, Figure 13 ((a) for the reaction rate per gram catalyst and (b) per gram metal). Clearly, also on per metal basis, Au/rutile remains the most active catalyst. Interestingly, comparing the commercial AUROLite catalysts, both ZnO and Al₂O₃ are more active than TiO₂. Au/C remains the least active catalyst, however due to greatly different particle sizes, the result must be treated with caution. The selectivity of the latter two are presented in Figure 15. On alumina, relevant amounts of ethyl acetate, up to 5.1% at 300°C as well as minor amounts of up to 0.3% acetic acid are produced. On ZnO, however, not only higher activity is achieved, but also higher selectivity towards acetaldehyde, with only a maximum of 1.6% of ethyl acetate produced at 200°C which further decreases at higher temperatures to 1% at 300°C. No acetic acid or CO₂ are produced.

In contrast to all the other catalysts presented in this section, for Au/C the selectivity towards acetaldehyde is increasing with the temperature (from 97.9 to 99.2%, and the ethyl acetate selectivity decreasing accordingly). It can be assumed that the reason for this is the desorption of acetaldehyde from the Au surface, which prevents coupling of ethoxy species with acetaldehyde.

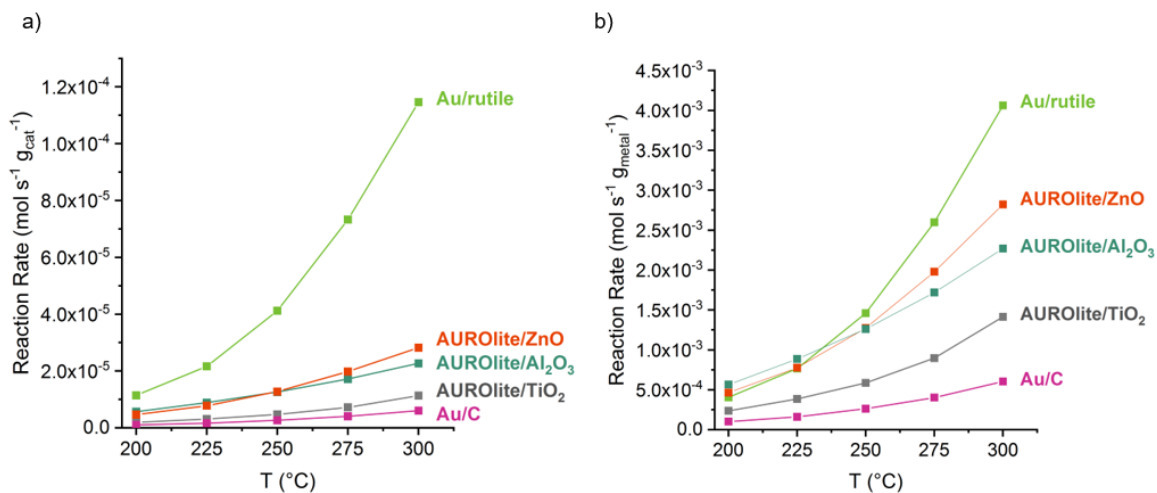


Figure 13. Comparison of Au/rutile (green, as reference for the most active Au/rutile based catalyst), AUROLite/ZnO (orange), AUROLite/Al₂O₃ (turquoise), AUROLite/TiO₂ (grey), Au/C (pink), (a) reaction rate based on gram catalyst and (b) on gram metal (as determined by LA-ICP-MS, or for the AUROLite samples as provided by the manufacturer.). A total flow of approx. 51.2 mL/min, with 1.1 mL/min. EtOH and O₂, a 1:1 ratio of the educts (resulting in a partial pressure of 2.2 kPa) was used.

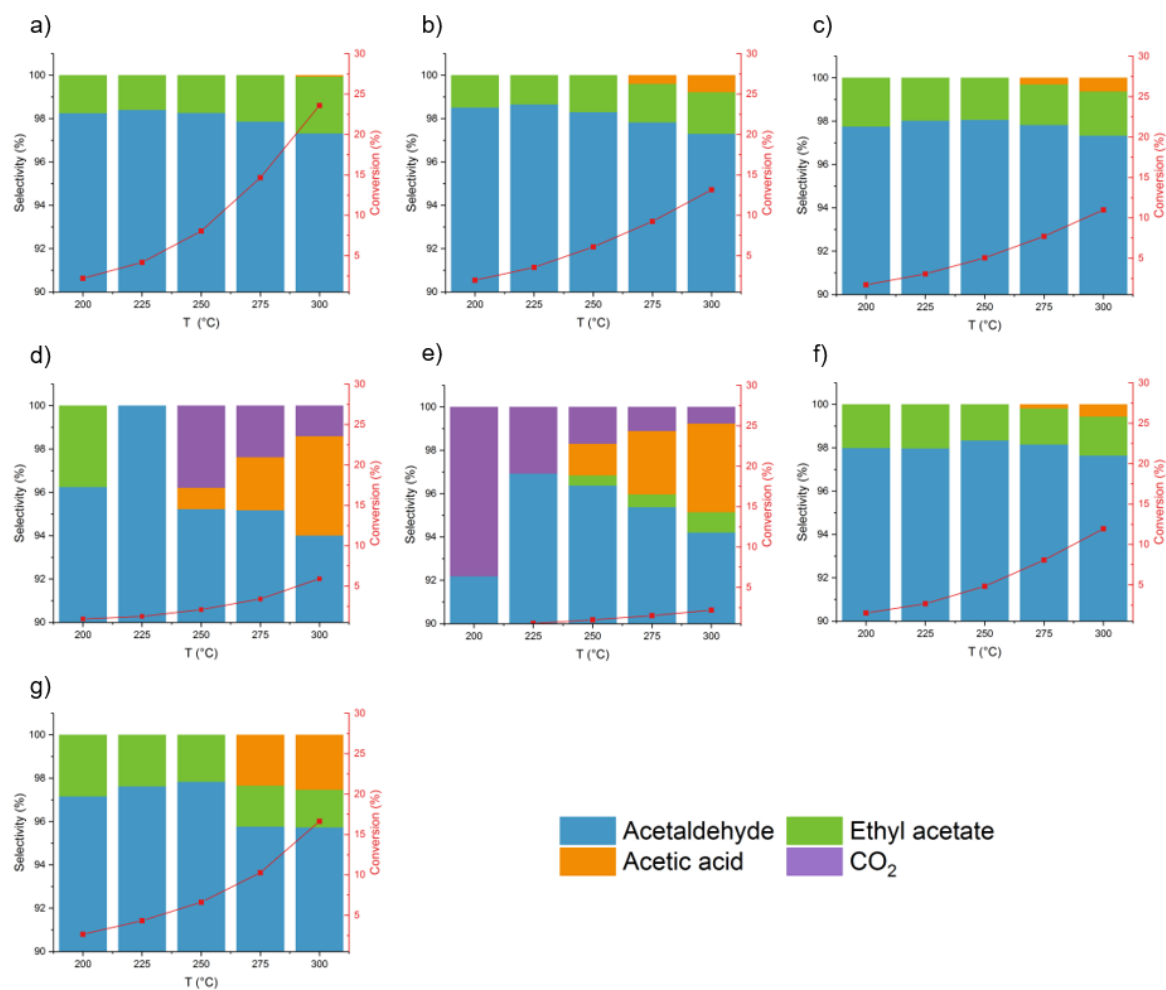


Figure 14. Selectivities and conversions for (a) Au/rutile, (b) Au/anatase, (c) Au/P25, (d) rutile and (e) anatase, (f) Au/anatase₈₀rutile₂₀ and (g) AUROLite/TiO₂. A total flow of approx. 51.2 mL/min, with 1.1 mL/min. EtOH and O₂, a 1:1 ratio of the educts (resulting in a partial pressure of 2.2 kPa) was used.

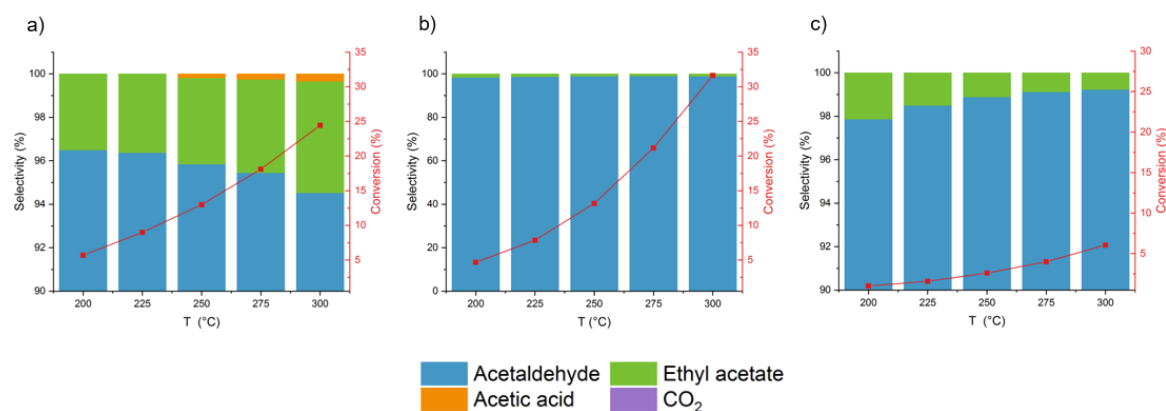


Figure 15. Selectivities and conversions for (a) AUROLite/Al₂O₃, (b) AUROLite/ZnO and (c) Au/C. A total flow of approx. 51.2 mL/min, with 1.1 mL/min. EtOH and O₂, a 1:1 ratio of the educts (resulting in a partial pressure of 2.2 kPa) was used.

Thus, due to these excellent properties of rutile as support, all further (bimetallic) samples are prepared on rutile only.

3.5. Computational Mechanistic Considerations^{IV}

3.5.1. Computational Methods

Energies and thermodynamic parameters were calculated using the VdW-DF2 functional^{133,134}, as implemented in the Vienna ab initio simulation package (VASP)^{135,136}. The VdW-DF2 functional allows accurate calculation of the binding energy and site preference of CH₃O and CH₃OH on Pt(111) and Cu(111)¹³⁷. The calculations were performed with spin polarization and a plane-wave basis set with a cutoff kinetic energy of 400 eV. The selection of Au(111) as a surface model was motivated by the structure-insensitivity of ethanol oxidation on Au as observed by Abad et al.⁶⁷ The Au(111) was modeled as a five-layer slab using a $p(4 \times 4)$ unit cell, the repeated cells are separated by a 15 Å vacuum layer. The optimized lattice constant, 4.33 Å, slightly exceeds the experimental value 4.07 Å¹³⁸. The Brillouin zone was sampled with a 3 x 3 x 1 Monkhorst-Pack grid. DFT is commonly known to be unable to describe gas phase oxygen accurately. The enthalpy and entropy of gas phase oxygen were therefore calculated from experimental data using FACTSAGE¹³⁹, by considering the oxidation of ethanol to acetaldehyde as the reference.

Kinetic coefficients for molecular adsorption were determined via collision theory, assuming a sticking coefficient of 1. Kinetic coefficients for surface reactions and for dissociative adsorption are calculated from transition state theory. Transition states were located with the climbing image nudged elastic band (cNEB)^{140,141} method and subsequently refined with the dimer¹⁴² method. The calculated kinetic coefficients were combined into a microkinetic model to simulate an ideal plug flow reactor. The mass balances for the gas phase species are described in Eq. (1).

^{IV} This chapter is based on the manuscript “Complex Kinetics for a Simple Reaction: Oxidative Dehydrogenation of Ethanol on Gold” by J. E. De Vrieze, A. Nagl, M. Latschka, S. Mostrou-Moser, J. Teržan, P. Djinović, F. Horak, A. Limbeck, A. Pintar, J. A. van Bokhoven, J. W. Thybaut, K. Föttinger, M. Saeys. The computational results were obtained by J. E. De Vrieze and a reprinted with permission to discuss the reaction mechanism on Au. The chapters on bimetallic catalysts build on the understanding of the monometallic Au catalysts shown in this chapter.

$$\frac{\partial C_i}{\partial t} + u_s \frac{\partial C_i}{\partial z} = \rho_{bed} C_t R_{w,i} \quad (1)$$

with C_i , the concentration of species i in mol m^{-3} , u_s the superficial velocity in m s^{-1} , ρ_{bed} the density of the catalyst bed in $\text{kg}_{\text{cat}} \text{m}^{-3}$, C_t the total site concentration in $\text{mol kg}_{\text{cat}}^{-1}$ and $R_{w,i}$ the net formation rate of species i in s^{-1} . A typical active site concentration of $1 \text{ mmol kg}_{\text{cat}}^{-1}$ was used.¹⁴³ The mass balances for the surface species are described in Eq. (2).

$$\frac{\partial \theta_i}{\partial t} = R_{w,i} \quad (2)$$

The transient equations were integrated until steady state, instead of the solving the steady-state equations themselves, to ensure smooth mathematical convergence. The set of transient equations was solved in an in-house FORTRAN code using the DASPK¹⁴⁴ solver. To discretize the axial coordinate of the reactor, a central differencing scheme was applied. Preliminary simulations, using the as-calculated kinetic model, showed surface coverage over 80% at lower temperatures ($<150^\circ\text{C}$). This is inconsistent with the model assumptions used in the DFT calculations, i.e., a surface coverage of 1/16 ML. Coverage effects have proven to strongly affect the kinetic parameters^{145,146} and therefore the predicted activity^{137,147}. We therefore applied the methodology, originally proposed by Jorgensen and Grönbeck¹⁴⁷, and extended the coverage correction we originally proposed for acetone hydrogenation on $\text{Cu}(111)$ ¹³⁷ to ethanol oxidation on $\text{Au}(111)$.

3.5.2. Ethanol Oxidation Pathways

Different oxidation pathways are available for the oxidation of ethanol to acetaldehyde on gold, the transition states of which are shown in annex section 9.8, Figure 115. With different species are available for oxidation, the hydrogen atom of the carbon and oxygen atom of ethanol can be transferred directly to the metal surface or to adsorbed atomic oxygen, surface hydroxyl species, molecular oxygen and surface hydroperoxyl species. Transfer of the hydrogen atom to surface oxygen, surface hydroxyl species, molecular oxygen and surface hydroperoxyl species will hereafter be referred to as proton transfer. Transfer of the hydrogen atom bound to the carbon atom in ethanol will be referred to as β -H elimination.

Oxidation of ethanol via direct transfer of hydrogen to the surface follows a similar profile as previously calculated with the PBE functional³⁴, Figure 16 a). An ethoxy intermediate is formed with a slightly lower barrier than the alkyl intermediate, 144 kJmol⁻¹ compared to 171 kJmol⁻¹. Both intermediates, however, are highly unstable compared to adsorbed ethanol, confirming that gold is inactive for ethanol dehydrogenation in the absence of oxygen. Hydrogen transfer from the alkyl species to the gold surface is a lower barrier than β -H elimination in the ethoxy intermediate.

Under aerobic conditions, surface oxygen atoms will be available via oxygen activation. As previously shown for methanol oxidation, these potentially have a significant role in activation of the alcohol²⁹. When atomic oxygen is available, Figure 16 b), the barrier for ethoxy formation decreases to 15 kJmol⁻¹ via proton transfer to surface oxygen atoms. The barrier for subsequent β -H elimination in the ethoxy intermediate remains practically identical when the hydrogen atom is transferred to the surface oxygen. The barrier for β -H elimination in ethanol, on the other hand drastically decreases, forming the alkyl intermediate with a barrier of 73 kJmol⁻¹. No transition state was found for proton transfer from the alkyl species to surface oxygen, all estimates obtained from cNEB calculations relaxed to the acetaldehyde during optimization with the dimer method. As such, the proton transfer of the alkyl intermediate to surface oxygen was assumed to be spontaneous. Since this reaction will later on be proven to be kinetically irrelevant, this has no implications on the model results.

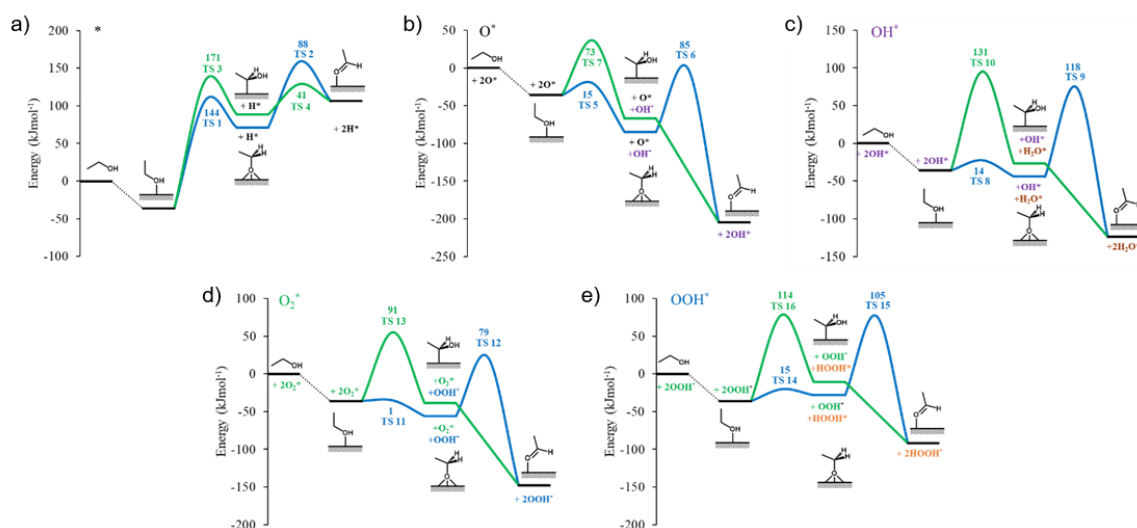


Figure 16. Electronic energy profiles for the oxidation of ethanol to acetaldehyde via the alkyl pathway (green lines) and alkoxy pathway (blue lines) using with the metal surface (a), surface oxygen (b), surface hydroxyl species (c), molecular oxygen (d) and hydroperoxide (e) as an oxidizing species. The corresponding transition states are shown in annex section 9.8, Figure 115.

Hydroxyl species, formed by hydrogen transfer from ethanol to surface oxygen, can also partake in the ethanol oxidation reaction, forming adsorbed water molecules¹⁴⁸, Figure 16 c). A very similar energy profile is obtained as for oxidation with surface oxygen, Figure 16 c). However, the barriers for β -H elimination are increased compared the surface oxygen reactions.

Zhang et al.³¹ proposed that, in addition to atomic oxygen and surface hydroxyl species, molecular oxygen and hydroperoxyl species can facilitate ethanol oxidation on silver doped Au(111) surfaces. In Figure 16 d) and Figure 16 e) it is shown that these pathways also open up on a pure Au(111) surface. Proton transfer from ethanol to molecular oxygen, forming the ethoxy intermediate, is practically inactivated, a barrier of 1 kJmol⁻¹. Similar to oxidation with atomic oxygen, the barrier for β -H elimination is almost unaffected, 79 kJmol⁻¹. Proton transfer from ethanol to the hydroperoxyl species is also facilitated, decreasing the barrier to 15 kJmol⁻¹. Subsequent β -H elimination to the hydroperoxyl species, however, is higher activated than direct transfer to the gold surface. Formation of the alkyl intermediate through β -H elimination with molecular oxygen (Figure 16 d)) and hydroperoxyl species (Figure 16 e)) is in line with the observations for ethanol oxidation with atomic oxygen (Figure 16 b)) and surface hydroxyl (Figure 16 c)) species, showing a slightly higher barrier than via direct hydrogen transfer to the surface. No transition state was found for proton transfer from the alkyl intermediate to molecular oxygen and

hydroperoxyl species, these steps are therefore assumed to be spontaneous. However, due to their kinetic irrelevance, proven in the kinetic modeling section, this has no significant on the simulation results.

To close the catalytic cycle and produce water, oxygen has to be activated, Figure 17. Oxygen can undergo either direct dissociation or hydrogenation to the hydroperoxyl species and subsequently to hydrogen peroxide (HOOH). Different hydrogenating species are available in the formation of these peroxides. First, hydrogen can be transferred from ethanol, surface ethoxy and ethyl species to molecular oxygen (Figure 16 d) and e)). Proton transfer from ethanol to molecular oxygen and surface hydroperoxyl species both have low activation barriers 1 and 15 kJmol⁻¹ respectively, while proton transfer from the alkyl species is spontaneous.

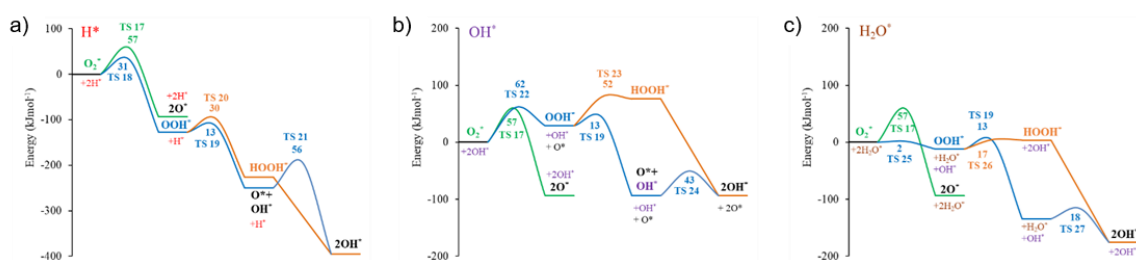


Figure 17. Electronic energy profiles for the activation of oxygen via direct dissociation (green), dissociation of surface hydroperoxide (blue) and dissociation of hydrogenperoxide (orange) using surface hydrogen (A), surface hydroxyl (B) and adsorbed water molecules (C) as a hydrogenating species. The transition states are shown in annex section 9.8, Figure 115.

Alternatively, molecular oxygen can be hydrogenated with surface hydrogen (Figure 17 a)). Direct hydrogenation of molecular oxygen has a significantly lower barrier than oxygen dissociation, 31 kJmol⁻¹ compared to 57 kJmol⁻¹. Subsequently, the hydroperoxyl species can again be hydrogenated with surface hydrogen, 30 kJmol⁻¹, which undergoes spontaneous dissociation into 2 hydroxyl species, or can dissociate directly, with a barrier of 19 kJmol⁻¹.

Similarly, molecular oxygen can be hydrogenated via proton transfer from surface hydroxyl species (Figure 17 b)) and adsorbed water molecules (Figure 17 b)). When a proton is transferred from a surface hydroxyl species to molecular oxygen, the hydrogenation steps

become slightly exothermic (Figure 17 b)). In addition, the hydrogenation steps are significantly higher activated than their corresponding dissociation steps. Proton transfer from adsorbed water molecules to molecular oxygen and hydroperoxyl species, on the other hand, are practically inactivated.

3.5.3. Simulation of Ethanol Oxidation with a Coverage Dependent First Principles Microkinetic Model

The relative importance of each of the proposed oxidation pathways is not only determined by the electronic energies, but also by coverage and entropy. As such, a microkinetic model is required to investigate the dominant reaction pathway(s) and identify the rate-controlling step(s). An overview of the adsorption coefficients for the different gas phase species used in this model is presented in Figure 9. All adsorption coefficients were determined via collision theory, assuming a sticking coefficient of 1.

Table 9. Adsorption rate and equilibrium coefficients at 500 K for the gas phase molecules in the model. The rate coefficients are calculated using collision theory and equilibrium coefficients from DFT. The rate coefficients for $H_2(g)$ dissociative adsorption are calculated from transition state theory.

Reaction	ΔH_r [kJmol ⁻¹]	ΔS_r [Jmol ⁻¹ K ⁻¹]	K_{eq} [-]	k_+ [s ⁻¹ Pa ⁻¹]	k_- [s ⁻¹]
$CH_3CH_2OH(g) + * \rightleftharpoons CH_3CH_2OH^*$	-30	-134	$1.5 \cdot 10^{-4}$	$1.3 \cdot 10^3$	$8.9 \cdot 10^{11}$
$CH_3CHO(g) + * \rightleftharpoons CH_3CHO^*$	-25	-133	$4.7 \cdot 10^{-5}$	$1.4 \cdot 10^3$	$2.9 \cdot 10^{12}$
$H_2(g) + 2 * \rightleftharpoons 2H^*$	36	-58	$1.7 \cdot 10^{-7}$	$3.5 \cdot 10^{-3}$	$2.1 \cdot 10^4$
$H_2O + * \rightleftharpoons H_2O^*$	-17	-103	$2.8 \cdot 10^{-4}$	$2.1 \cdot 10^3$	$7.8 \cdot 10^{11}$
$O_2(g) + * \rightleftharpoons O_2^*$	-6	-152	$5.9 \cdot 10^{-8}$	$1.6 \cdot 10^3$	$2.7 \cdot 10^{15}$

Because DFT is known to have difficulties with describing gas phase oxygen, its energy value was calculated using gas phase oxidation of ethanol to acetaldehyde as a reference. The resulting binding energy of oxygen is low, at about 6 kJ mol⁻¹ which is consistent with the low oxygen affinity of gold. The hydrogen binding energy is strongly positive, +36 kJmol⁻¹, indicating that atomic hydrogen is not stable on gold surfaces. An overview of the kinetic coefficients is shown in Table 10. Generally, kinetic coefficients were calculated using transition state theory. However, as shown in Figure 16, some reactions are not activated. The kinetic coefficients for non-activated reactions were calculated by fixing the rate coefficients of the exothermic step at 10¹³ s⁻¹, the corresponding forward/backward reaction step is subsequently calculated via thermodynamic consistency.

Table 10. Pre-exponential factors, activation energies and rate coefficients at 500 K for the surface reactions in the microkinetic model.

Reaction	A ⁺ (s ⁻¹)	E _a ⁺ (kJmol ⁻¹)	A ⁻ (s ⁻¹)	E _a ⁻ (kJmol ⁻¹)	k ₊ (s ⁻¹)	k ₋ (s ⁻¹)
Direct dehydrogenation						
$CH_3CH_2OH^* + * \rightleftharpoons CH_3CH_2O^* + H^*$	$7.9 \cdot 10^{10}$	141	$1.8 \cdot 10^{12}$	34	$1.5 \cdot 10^4$	$5.3 \cdot 10^8$
$CH_3CH_2OH^* + * \rightleftharpoons CH_3CHOH^* + H^*$	$5.7 \cdot 10^{11}$	170	$7.6 \cdot 10^{12}$	44	$1.0 \cdot 10^{-6}$	$1.8 \cdot 10^8$
$CH_3CH_2O^* + * \rightleftharpoons CH_3CHO^* + H^*$	$2.1 \cdot 10^{12}$	88	$1.0 \cdot 10^{10}$	45	$1.5 \cdot 10^3$	$1.8 \cdot 10^5$
$CH_3CHOH^* + * \rightleftharpoons CH_3CHO^* + H^*$	$5.8 \cdot 10^{13}$	41	$4.8 \cdot 10^{11}$	17	$3.1 \cdot 10^9$	$7.4 \cdot 10^9$
Proton transfer to surface oxygen atoms						
$CH_3CH_2OH^* + O^* \rightleftharpoons CH_3CH_2O^* + OH^*$	$7.1 \cdot 10^{10}$	11	$1.5 \cdot 10^{12}$	60	$5.5 \cdot 10^9$	$7.2 \cdot 10^5$
$CH_3CH_2OH^* + O^* + * \rightleftharpoons CH_3CHOH^* + OH^*$	$6.3 \cdot 10^{11}$	71	$7.6 \cdot 10^{12}$	102	$2.7 \cdot 10^4$	$1.8 \cdot 10^2$
$CH_3CH_2O^* + O^* \rightleftharpoons CH_3CHO^* + OH^*$	$2.7 \cdot 10^{12}$	84	$1.2 \cdot 10^{10}$	199	$4.3 \cdot 10^3$	$1.9 \cdot 10^{-11}$
$CH_3CHOH^* + O^* \rightleftharpoons CH_3CHO^* + OH^*$	$1.0 \cdot 10^{13}$	0	$7.9 \cdot 10^{10}$	133	$1.0 \cdot 10^{13}$	$9.2 \cdot 10^{-4}$
Proton transfer to surface hydroxyl species						
$CH_3CH_2OH^* + OH^* \rightleftharpoons CH_3CH_2O^* + H_2O^*$	$2.3 \cdot 10^{11}$	9	$2.3 \cdot 10^{10}$	14	$2.5 \cdot 10^{10}$	$3.1 \cdot 10^1$
$CH_3CH_2OH^* + OH^* + * \rightleftharpoons CH_3CHOH^* + H_2O^*$	$1.8 \cdot 10^{13}$	131	$1.1 \cdot 10^{12}$	117	$3.9 \cdot 10^{-1}$	$6.3 \cdot 10^{-1}$
$CH_3CH_2O^* + OH^* \rightleftharpoons CH_3CHO^* + H_2O^*$	$1.4 \cdot 10^{13}$	118	$3.1 \cdot 10^8$	187	$7.3 \cdot 10^0$	$8.1 \cdot 10^{-12}$
$CH_3CHOH^* + OH^* \rightleftharpoons CH_3CHO^* + H_2O^*$	$1.0 \cdot 10^{13}$	0	$3.9 \cdot 10^8$	88	$1.0 \cdot 10^{13}$	$2.3 \cdot 10^{-1}$
Proton transfer to molecular oxygen						
$CH_3CH_2OH^* + O_2^* \rightleftharpoons CH_3CH_2O^* + OOH^*$	$1.4 \cdot 10^{11}$	0.2	$4.3 \cdot 10^{10}$	13	$1.4 \cdot 10^{11}$	$3.1 \cdot 10^1$
$CH_3CH_2OH^* + O_2^* \rightleftharpoons CH_3CHOH^* + OOH^*$	$4.3 \cdot 10^{11}$	89	$3.3 \cdot 10^{11}$	90	$2.3 \cdot 10^2$	$1.5 \cdot 10^2$
$CH_3CH_2O^* + O_2^* \rightleftharpoons CH_3CHO^* + OOH^*$	$3.7 \cdot 10^{12}$	77	$1.1 \cdot 10^9$	162	$2.8 \cdot 10^4$	$1.2 \cdot 10^{-8}$
$CH_3CHOH^* + O_2^* \rightleftharpoons CH_3CHO^* + OOH^*$	$1.0 \cdot 10^{13}$	0	$4.9 \cdot 10^9$	103	$1.0 \cdot 10^{13}$	$8.5 \cdot 10^{-2}$
Proton transfer to hydroperoxide						
$CH_3CH_2OH^* + OOH^* \rightleftharpoons CH_3CH_2O^* + HOOH^*$	$8.2 \cdot 10^{11}$	9	$4.5 \cdot 10^{10}$	2	$9.2 \cdot 10^9$	$3.0 \cdot 10^{10}$
$CH_3CH_2OH^* + OOH^* \rightleftharpoons CH_3CHOH^* + HOOH^*$	$6.9 \cdot 10^{11}$	111	$2.2 \cdot 10^{11}$	85	$1.7 \cdot 10^0$	$2.9 \cdot 10^2$
$CH_3CH_2O^* + OOH^* \rightleftharpoons CH_3CHO^* + HOOH^*$	$1.8 \cdot 10^{12}$	103	$2.1 \cdot 10^8$	161	$3.1 \cdot 10^1$	$3.6 \cdot 10^{-9}$
$CH_3CHOH^* + OOH^* \rightleftharpoons CH_3CHO^* + HOOH^*$	$1.0 \cdot 10^{13}$	0	$2.1 \cdot 10^2$	64	$1.0 \cdot 10^{13}$	$4.0 \cdot 10^{-5}$
Oxygen activation						
$O_2^* + * \rightleftharpoons 2O^*$	$2.5 \cdot 10^{12}$	55	$5.9 \cdot 10^{12}$	149	$4.5 \cdot 10^6$	$1.5 \cdot 10^{-3}$
$O_2^* + H^* \rightleftharpoons OOH^* + *$	$1.3 \cdot 10^{13}$	29	$7.8 \cdot 10^{11}$	156	$1.2 \cdot 10^{10}$	$4.1 \cdot 10^{-5}$
$O_2^* + OH^* \rightleftharpoons OOH^* + O^*$	$1.0 \cdot 10^{12}$	58	$6.5 \cdot 10^{10}$	28	$7.9 \cdot 10^5$	$7.6 \cdot 10^7$
$O_2^* + H_2O^* \rightleftharpoons OOH^* + OH^*$	$2.4 \cdot 10^{10}$	0.1	$4.7 \cdot 10^{10}$	7	$2.4 \cdot 10^{10}$	$9.4 \cdot 10^9$

$OOH^* + H^* \rightleftharpoons HOOH^* + *$	$2.2 \cdot 10^{11}$	25	$5.1 \cdot 10^9$	124	$5.4 \cdot 10^8$	$5.2 \cdot 10^{-4}$
$OOH^* + OH^* \rightleftharpoons HOOH^* + O^*$	$3.8 \cdot 10^{14}$	57	$1.0 \cdot 10^{13}$	0	$3.9 \cdot 10^8$	$1.0 \cdot 10^{13}$
$OOH^* + H_2O^* \rightleftharpoons HOOH^* + OH^*$	$1.9 \cdot 10^{12}$	12	$1.0 \cdot 10^{13}$	0	$9.7 \cdot 10^{10}$	$1.0 \cdot 10^{13}$
$OOH^* + * \rightleftharpoons OH^* + O^*$	$6.8 \cdot 10^{12}$	19	$2.4 \cdot 10^{14}$	143	$7.4 \cdot 10^{10}$	$2.6 \cdot 10^{-1}$
$HOOH^* + * \rightleftharpoons 2OH^*$	$1.0 \cdot 10^{13}$	0	$1.4 \cdot 10^{16}$	182	$1.0 \cdot 10^{13}$	$1.4 \cdot 10^{-3}$
Oxygen hydrogenation						
$O^* + H^* \rightleftharpoons OH^* + *$	$4.2 \cdot 10^{12}$	55	$3.8 \cdot 10^{12}$	211	$8.4 \cdot 10^6$	$3.2 \cdot 10^{-10}$
$OH^* + H^* \rightleftharpoons H_2O^* + *$	$4.7 \cdot 10^{12}$	53	$2.1 \cdot 10^{10}$	165	$1.3 \cdot 10^7$	$1.2 \cdot 10^{-7}$
$O^* + H_2O^* \rightleftharpoons 2OH^*$	$1.1 \cdot 10^{10}$	10	$2.3 \cdot 10^{12}$	55	$9.9 \cdot 10^8$	$4.0 \cdot 10^6$

Due to enthalpy corrections, a negative activation energy was found for the proton transfer from hydrogen peroxide to surface hydroxyl species and oxygen atoms. Therefore, these reactions were also calculated using this strategy. Because of the way non-activated reactions were handled, the recombination of two hydroxyl groups into hydrogen peroxide has a high pre-exponential factor, 10^{16} s^{-1} . However, this step will later be shown to be kinetically irrelevant ($\text{DRC} < 0.01$) and, as a result, the absolute value of this pre-exponential factor has no effect on the model results.

Due to the high mobility of adsorbed water molecules and hydroperoxyl species, the entropic cost for proton transfer from these species is significantly higher than for direct hydrogenation. As a result, the pre-exponential factors for these steps are generally a few orders of magnitude lower than for direct hydrogenation, 10^8 to 10^{12} s^{-1} compared to 10^{10} to 10^{13} s^{-1} .

When the adsorption coefficients (Figure 9) and the kinetic coefficients are used to simulate the kinetics of ethanol oxidation, high ethoxy coverages are obtained at low temperature conditions, $150 \text{ }^\circ\text{C}$ and below, which is inconsistent with the “clean surface” assumption used in the DFT calculations. To remedy this, coverage effects must be considered. The coverage model, calculated for acetone hydrogenation on copper in our recent contribution¹³⁷, was therefore extended to ethanol oxidation on gold. Consistent with acetone model, only the coverage of atomic oxygen, surface hydroxyl species and surface alkoxide are significant, i.e. above 1%. In addition, the microkinetic model is only sensitive to the stability of atomic oxygen, surface hydroxyl and the alkoxy species. To extend this coverage correction model, several steps were required. The destabilization of oxygen, surface hydroxyl and ethoxy (alkoxy) due to the oxygen, hydroxyl and ethoxy coverage was estimated using *ab initio* calculations at different coverages, 1/9 ML to 4/9 ML for intra-species repulsion and 1/9 ML to 3/9 ML for inter-species repulsion (annex section

9.8, Figure 116 - Figure 124). The resulting destabilizations were subsequently fit to power law functions, as they have proven to show the best fit for these species¹³⁷, Figure 115 (annex section 9.8). The resulting destabilization functions are shown in Table 11. Coverage effects for the transition state were calculated via a typical Bronsted-Evans-Polanyi relationship with a transfer coefficient of 0.5.

Table 11. Intraspecies and interspecies repulsion correction functions to account for the effect of the dominant species, O, OH and ethoxy, on the sensitive species. The repulsion corrections are estimated in a coverage range of 1/16 to 1/3 ML.

Intraspecies repulsion (kJ mol ⁻¹)	
θ_{O} on O^*	$\delta G_{\text{O}}(\theta_{\text{O}}) = 443 \left(\theta_{\text{O}} - \frac{1}{16} \right)^{2.77}$
θ_{OH} on OH^*	$\delta G_{\text{OH}}(\theta_{\text{OH}}) = 173 \left(\theta_{\text{OH}} - \frac{1}{16} \right)^{2.40}$
θ_{ETH} on ETH^*	$\delta G_{\text{ETH}}(\theta_{\text{ETH}}) = 223 \left(\theta_{\text{ETH}} - \frac{1}{16} \right)^{1.83}$
Interspecies repulsion (kJ mol ⁻¹)	
θ_{O} on OH^*	$G_{\text{OH}}(\theta_{\text{O}}) = 360(\theta_{\text{O}})^{1.80}$
θ_{O} on ETH^*	$G_{\text{ETH}}(\theta_{\text{O}}) = 204(\theta_{\text{O}})^{1.18}$
θ_{OH} on O^*	$G_{\text{O}}(\theta_{\text{OH}}) = 481(\theta_{\text{OH}})^{1.91}$
θ_{OH} on ETH^*	$G_{\text{ETH}}(\theta_{\text{OH}}) = 171(\theta_{\text{OH}})^{1.78}$
θ_{ETH} on O^*	$G_{\text{O}}(\theta_{\text{ETH}}) = 165(\theta_{\text{ETH}})^{1.34}$
θ_{ETH} on OH^*	$G_{\text{OH}}(\theta_{\text{ETH}}) = 563(\theta_{\text{ETH}})^{2.37}$

By implementing these coverage-correction functions directly into the kinetic coefficients, the effect of coverage was accounted for during the simulations. Using this coverage dependent microkinetic model, a turnover frequency (TOF) of 1.9 s⁻¹ was found under standard conditions (200 °C, 15 kg_{cat}s mol_{EtOH}⁻¹, EtOH:O₂ and p_{tot} = 5.0 kPa), which is slightly higher than the experimentally measured TOF (Table 5). Under these conditions, the coverage is drastically reduced compared to the model without coverage corrections, Figure 19, and are within the range used to calculate the coverage corrections.

Using the coverage-dependent microkinetic model, the reaction orders of oxygen, Figure 18 a), and ethanol, Figure 18 b), were calculated between 100 °C and 300 °C and compared to the experimentally measured ones. In principle, an infinitesimally small variation of the partial pressure should be considered to calculate the reaction order. From an experimental perspective, however, a significant change in partial pressure is required to eliminate measurement errors. Therefore, we calculated the reaction orders using DFT at 1% variation and at the pressure variation used in the reaction order measurements to estimate

the effect of the pressure range and introduce error bars. As shown in Figure 18 a), the oxygen reaction order is rather sensitive to the pressure range between 100 °C and 200 °C while the ethanol reaction order remains practically unaffected. In general a good corresponding is observed between experiment and first principles microkinetics.

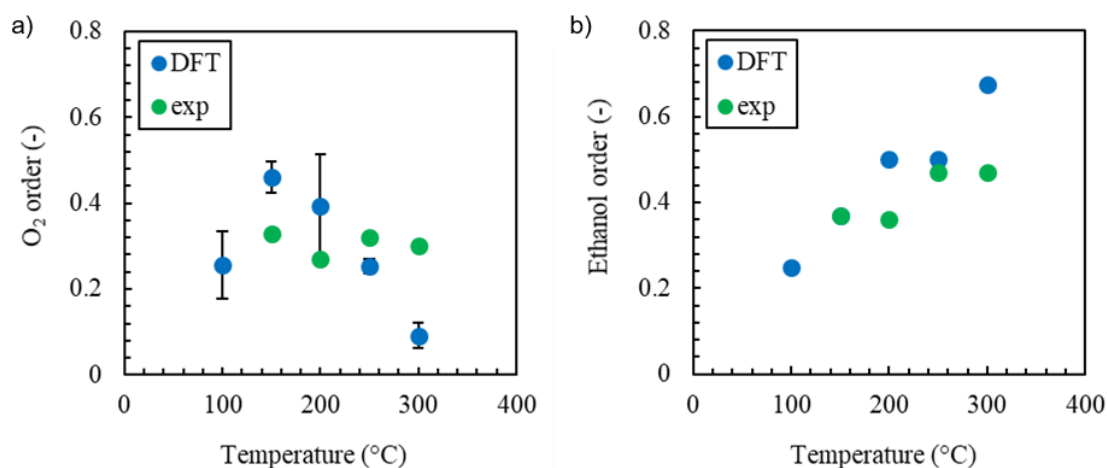


Figure 18. Comparison experimentally measured (green) and DFT calculated (blue) reaction orders of oxygen (A) and ethanol (B). The error bars indicate how reaction orders change when they are estimated with a 1% to a 50% partial pressure variation. Conditions: $15 \text{ kg}_{\text{cat}} \text{ s mol}_{\text{EtOH}}^{-1}$, $p_{\text{O}_2} = 2.5 \text{ kPa}$, $p_{\text{EtOH}} = 2.5 \text{ kPa}$.

The oxygen reaction order shows an almost constant value between 0.3 and 0.4 up to a temperature of 200 °C (Figure 18 a)). Above 200 °C, the DFT model predicts a decrease in oxygen reaction order as observed for Au/rutile (Table 5), rather than a constant reaction order as observed for Au/C. The ethanol reaction order generally increases with increasing temperature but is calculated to be almost constant between 200 °C and 250 °C (Figure 18 b)). Beyond 250 °C, the ethanol order increases further and again the order gets closer to the one for Au/rutile than the one for Au/C. To understand these trends, the surface coverages are investigated, and a reaction path analysis is performed.

Figure 19 shows the change in surface coverage as a function of temperature at the typical experimental conditions. As expected, the surface is relatively free at high temperatures and the ethoxy coverage decreases from 18% at 100°C to 0.2% at 300°C. Surprisingly, the oxygen coverage first shows a minimum at 200°C and the hydroxyl coverage gradually increases with temperature.

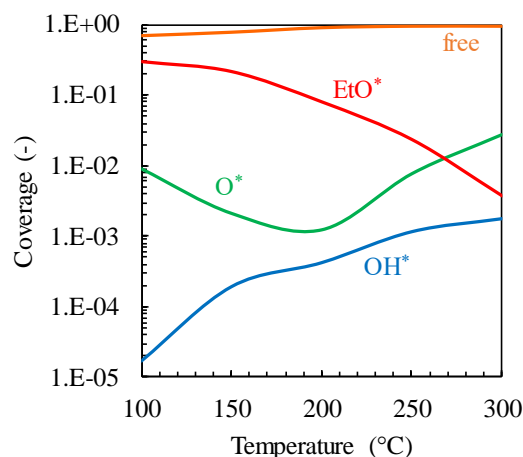


Figure 19. DFT calculated surface coverages of oxygen (green), hydroxyl species (blue), ethoxy (red) and empty sites (orange). Conditions: $15 \text{ kg}_{\text{cat}} \text{ s mol}_{\text{EtOH}}^{-1}$, $p_{\text{O}_2} = 2.5 \text{ kPa}$, $p_{\text{EtOH}} = 2.5 \text{ kPa}$.

A reaction path analysis was performed for the oxidation mechanism, a schematic representation is shown in Figure 20. All oxidation pathways proposed in literature were included and, rather than one being dominant, a mix of different pathways contribute to the oxidation activity at 200°C. Ethanol activation occurs via proton transfer mainly to surface hydroxyl species, 50%, but also a significant fraction to both atomic and molecular oxygen. The resulting ethoxy species subsequently transforms to acetaldehyde via β -H elimination.

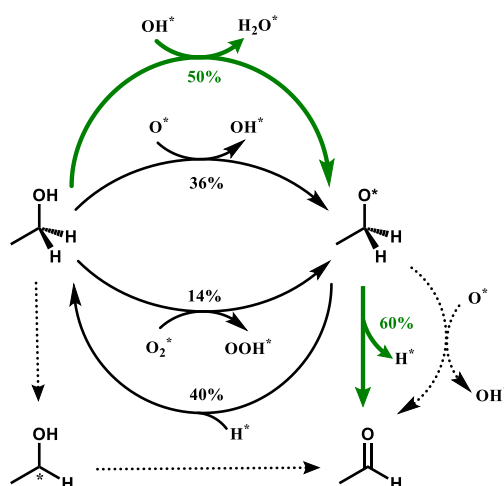


Figure 20. Reaction path analysis for the oxidation of ethanol to acetaldehyde. The numbers indicate the fraction of each component consumed in a particular reaction step. Dotted arrows indicate reaction steps with a fraction below 0.5%, while green arrows indicate reaction steps with a fraction equal to or above 50%. Conditions: $15 \text{ kg}_{\text{cat}} \text{ s mol}_{\text{EtOH}}^{-1}$, $p_{\text{tot}} = 5 \text{ kPa}$, $\text{EtOH}:\text{O}_2 = 1$, $T = 200 \text{ }^\circ\text{C}$.

However, a large amount (40%) of the ethoxy species go back to ethanol via direct hydrogenation of the oxygen atom. As such, the reaction generally follows the mechanism

as originally proposed by Xu et al.²⁸ but, rather than proton transfer only to oxygen, ethanol is activated by a mixture of different oxygen species. Proton transfer to the hydroperoxyl species, however, is not significant as the rate of proton transfer is significantly lower than the rate for hydroperoxyl dissociation (Table 10). The oxidation mechanism is strongly sensitive to the reaction temperature, as shown in Figure 125. The contribution of the proton transfer to molecular oxygen decreases with increasing temperature, from 24% at 100 °C to 1% at 250°C. This is caused by the difference in activation energy between direct dissociation and proton transfer, 55 and 0.2 kJmol⁻¹ respectively (Table 10). This also explains the evolution of oxygen coverage observed in Figure 19. At low temperatures, the effect on adsorption dominates, decreasing the coverage of molecular oxygen and, as a result, the coverage of atomic oxygen. At high temperatures, however, the oxygen dissociation dominates and more O₂ dissociates into atomic oxygen. The increase in hydroxyl coverage with temperature is a result of the increasing contribution of the proton transfer to atomic oxygen.

Similarly, a reaction path analysis is performed to identify the main pathway for oxygen activation, as presented in Figure 21. Two major pathways compete: direct dissociation and proton transfer from ethanol followed by hydroperoxyl dissociation. At 200 °C, most of the molecular oxygen undergoes proton transfer to the hydroperoxyl intermediate, 54%. A small of the molecular oxygen, 1%, is directly hydrogenated to hydroperoxyl. The remaining 45% undergoes direct dissociation. When the temperature increases, direct dissociation of oxygen becomes more dominant (Figure 126) because of the difference in activation energy as discussed previously. At 250 and 300 °C, direct dissociation is the dominant activation pathway with a contribution of 95% and 99% respectively. At low temperatures, however, the opposite is observed and oxygen activation via hydroperoxyl dissociation is dominant, 100% at 100 °C.

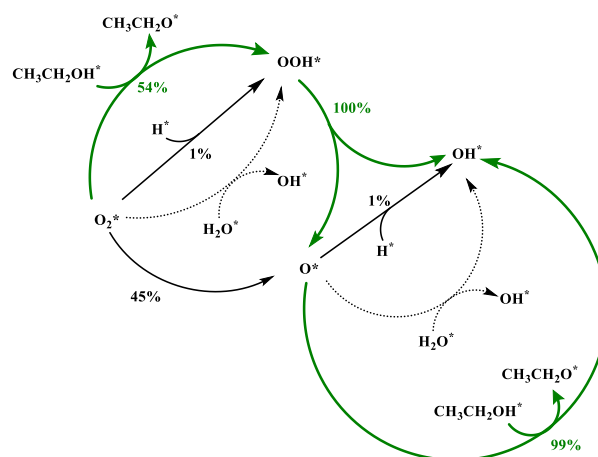


Figure 21. Reaction path analysis for the oxygen activation in ethanol oxidation to acetaldehyde. The numbers indicate the fraction of each component consumed in a particular reaction step. Dotted arrows indicate reaction steps with a fraction below 0.5%, while green arrows indicate reaction steps with a fraction equal to or above 50%. Conditions: $15 \text{ kg}_{\text{cat}} \text{ s mol}_{\text{EtOH}}^{-1}$, $p_{\text{tot}} = 0.05 \text{ bar}$, $\text{EtOH}:\text{O}_2 = 1$, $T = 200 \text{ }^\circ\text{C}$.

To fully understand the reaction orders calculated in Figure 18 and connect to the reaction mechanism, insight in the rate-limiting step(s) is required. In reaction networks with a large amount of reactions, the reaction rate is often determined by one reaction, i.e. the rate-limiting step(s). In addition, as the reaction mechanism changes with operating conditions, a change can in rate-limiting step(s) is possible. To systematically study the rate-limiting character of a reaction, Campbell et al.¹⁴⁹ defined the degree of rate control (DRC), Eq. (3), which is a normalized sensitivity factor of the overall reaction rate to the rate of an individual reaction step.

$$DRC_i = \frac{\partial \ln(R)}{\partial \ln(k_i)} \quad (3)$$

Using this definition for DRC, the evolution of the rate-limiting steps with temperature was evaluated, Figure 22. At low temperature (100 °C), the TOF is mainly determined by the β -H elimination in the ethoxy intermediate and direct activation of oxygen. The DRC for of the β -H elimination increases with increasing temperature in a similar fashion as the ethanol reaction order (Figure 18). Both reactions that determine oxygen activation, on the other hand, decrease with increasing temperature. The trend of the reaction order can thus be explained by a shift in rate-limiting step. At low temperature, the reaction rate is determined by both the activation of oxygen and oxidation of surface ethoxy species, resulting in an almost equal ethanol reaction order. When the temperature increases,

however, ethoxy oxidation becomes the single rate determining step and its DRC increases, decreasing the oxygen order and increasing the ethanol order.

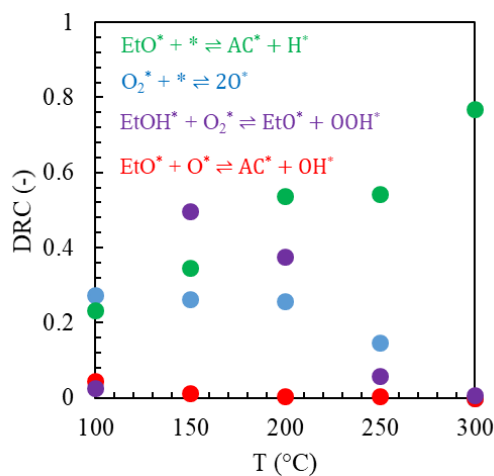


Figure 22. Degree of rate control for direct dehydrogenation of ethoxy species (green), direct dissociation of oxygen (blue), ethoxy dehydrogenation to oxygen (red) and proton transfer of ethanol to molecular oxygen (purple) at different temperatures. Conditions: $15 \text{ kg}_{\text{cat}} \text{ s mol}_{\text{EtOH}}^{-1}$, $p_{\text{tot}} = 0.05 \text{ bar}$, $\text{EtOH}:\text{O}_2 = 1$.

3.6. Conclusion

Carbon and rutile supported gold catalysts were investigated for ethanol oxidation. Both materials showed a very high selectivity to acetaldehyde (>95%) with ethyl acetate as the major side product (~ 3%). Au/C and Au/rutile also show a similar reaction rate at 200°C, with Au/rutile being more dependent on temperature. Even though they show a similar activity and selectivity under reaction conditions, a study of the reaction orders showed that the kinetics of Au/C and Au/rutile are significantly different. While the oxygen order remains almost constant at 0.3 with increasing temperatures on Au/C, it decreases to 0 at 300 °C on Au/rutile. The ethanol order increases on both materials but shows a stronger increase on Au/rutile. First principles microkinetics was applied to investigate the dominant reaction pathway and rationalize the change in reaction orders. Rather than one route being dominant, the reaction path analysis reveals that proton transfer of ethanol can go to atomic oxygen, surface hydroxyl species and molecular oxygen, the contribution of each step depending on the operating conditions. In addition, it was shown that the temperature dependence of the reaction orders is a result of a mix of rate-limiting steps. At low temperatures, both oxygen activation (both direct or via proton transfer to hydroperoxyl) and ethoxy oxidation are rate-limiting. When the temperature increases, the ethoxy β -H elimination becomes increasingly dominant resulting in an increase in the ethanol order. *Operando* DRIFTS measurements confirmed ethoxy species as predominantly present on

the surface. A dynamic behavior of the COO band was observed, correlating with conversion. However, DFT modeling confirmed the spectating character of that species.

Whereas Au/C turned out to be a viable model/reference system for the first principles microkinetics, its activity is the lowest of all the catalysts investigated (in fact, not only in this chapter, but in the whole thesis). The most obvious reason for this lies in the considerably larger gold particles on the carbon support, a mean size of 14.5 nm, as opposed to < 4 nm on all the other supports. It seems, the metal-support-interactions on oxide supports favor the formation of smaller nanoparticles exposing a higher number of active sites on the surface.

However, apart from this particle size effect, different supports have a profound effect on catalyst activity. The comparison of different commercial AUROLite catalysts showed an order in activity, Au/ZnO > Au/Al₂O₃ > Au/TiO₂. However, the mixture of anatase/rutile does not seem to have an as beneficial role as phase pure anatase or rutile. The latter, rutile, indeed exposes the highest activity and greatest effect. Thus Au/rutile has been chosen for the mechanistic studies and all further catalysts in this work are supported on rutile. With this result in mind, the new order of activity is Au/rutile > Au/ZnO > Au/anatase and Au/Al₂O₃, indicating a role of the reducibility of the support in the reaction.

Due to multiple factors playing a role, particle size, morphology of the support and even the possible role of Au at rutile/anatase interfaces as observed in photocatalysis²³ make an analysis of the exact reasons for the superior catalytic properties of rutile difficult. One possible explanation could lie in the involvement of surface oxygen at or close to Au perimeter sites (“Au-assisted Mars–van-Krevelen mechanism”)⁵¹ which could be favored on rutile. Also for photocatalysis, differences between rutile and anatase in the oxygen activation is discussed¹⁵⁰. The dual perimeter-concept predicts an active role of the support to provide active species for the Au/TiO₂ interface¹⁵¹, and indeed for different anatase crystal planes, different TOFs were observed for CO oxidation (Au/Ti-100 being the most active). Liu et al.¹⁵² report that Au/Ti-100 is able to of oxygen activation whereas Au/Ti-001 is found to be inert (or anatase). Also, the Au lattice is not deforming on rutile beyond minimal strain, suggesting minimum forces between Au and rutile, whereas for anatase, a strong epitaxial relationship was observed¹⁵¹. DFT calculation reveal differences in oxygen vacancies¹⁵³, with Morgan and Watson reporting more favorable vacancy formation for anatase¹⁵⁴. For the reducibility, however, anatase is predicted to be more difficult to reduce

than rutile¹⁵⁵. In the carbothermic reduction, on the other hand, rutile was found to reduce earlier, at a lower temperature of 830°C (anatase at 875°C)¹⁵⁶.

At this point, the reason for the higher activity of rutile remains unclear, however due to the experimental results, rutile is the preferred support.

4. Bimetallic Catalysts: Choice of the Promoter

Several different promoters have been investigated, Ag, Ru and Pt. 5 wt%. Au were combined with 1 wt.% promoter, except for Pt with 2 wt.%. The reason for this was the high atomic mass of Pt of 195.08, which is roughly twice as high as the respective atomic masses of Ag (107.87 g/mol) and Ru (101.07 g/mol). That way it was possible to keep the molar ratio of Au/promoter constant.

This first set of samples (batch 1), was prepared in small quantities to perform a kinetic screening, Figure 23, showing AuAg/rutile as the most performant catalyst, followed by Au/rutile and AuRu/rutile and Au/Pt. For other kinetic results showed in this thesis, a fresh set of samples was prepared, thus absolute values of the reaction rates are different (due to different particle size distributions, etc.). The AuRu/rutile marks a special case as, the very first screening (with undiluted samples) showed it to more active than the Au/rutile (data not shown). However, it seems, there is an ageing effect of the catalyst during storage. AuPt/rutile, on the other hand, demonstrates that the platinum indeed causes catalyst deactivation. Also, there are notable changes in the selectivity, as shown in Figure 24: Whereas for Au/rutile, relevant amounts of ethyl acetate and, at 300°C, 0.8% CO₂ were obtained, AuAg/rutile shows excellent selectivity for acetaldehyde (> 98%) with solely ethyl acetate as by-product. AuRu/rutile shows the highest amount of CO₂ produced (2.9% at 275°C and 5.0% at 300°C), but also, as the only catalyst, relevant amounts of acetic acid (1.7%). AuPt also produces ethyl acetate as by-product and no CO₂, however at very low conversion levels.

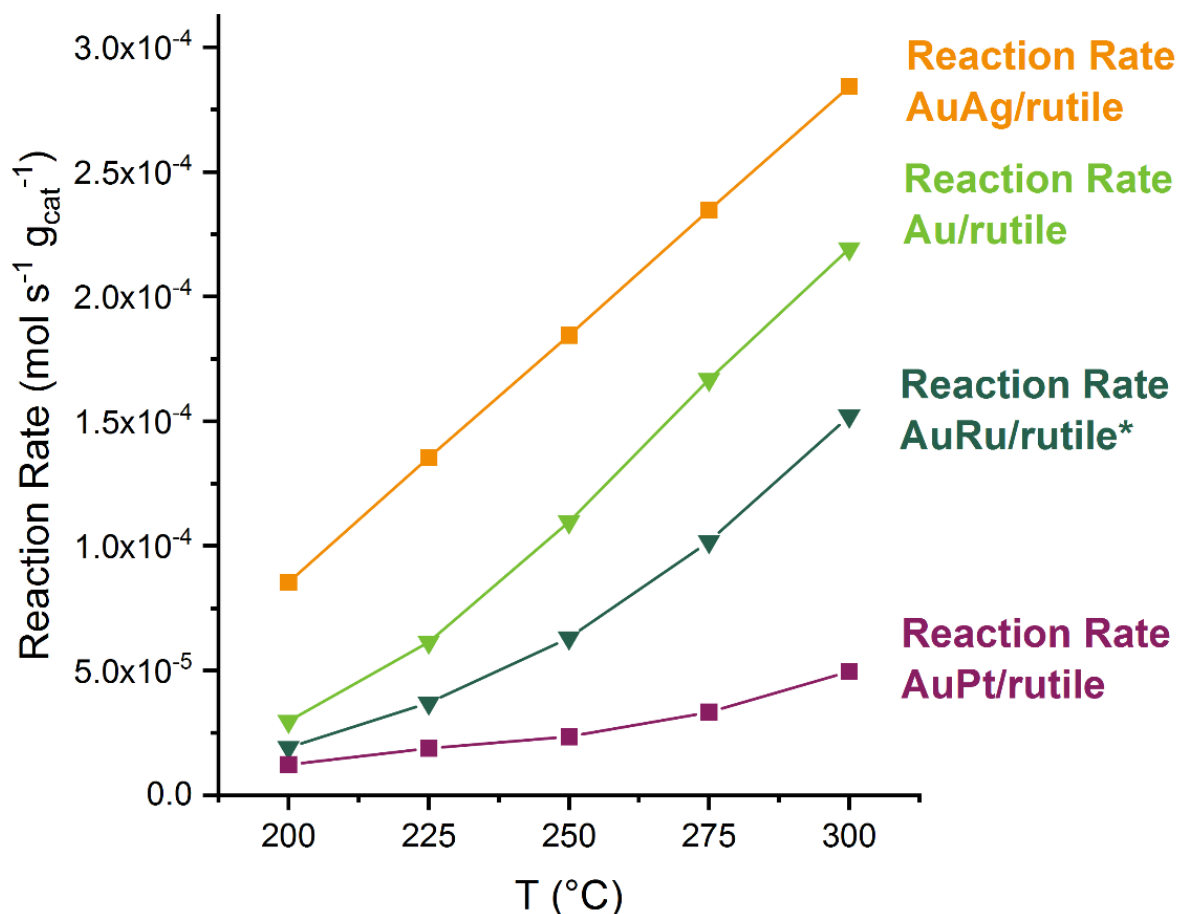


Figure 23. Kinetic measurements for AuAg/rutile (orange), Au/rutile (light green), AuRu/rutile (dark green) as well as AuPt/rutile (purple). Reaction rate was normalized to the catalyst amount (in gram). A total flow of approx. 51.2 mL/min, with 1.1 mL/min. EtOH and O₂, a 1:1 ratio of the educts (resulting in a partial pressure of 2.2 kPa) was used. AuRu/rutile is marked with a star to highlight its catalytical performance that is impacted by ageing effects. Initially, measured under non-optimum conditions without dilution, it showed 100% conversion, better than the Au/rutile (data not shown). The selectivity for these measurements is depicted in Figure 24.

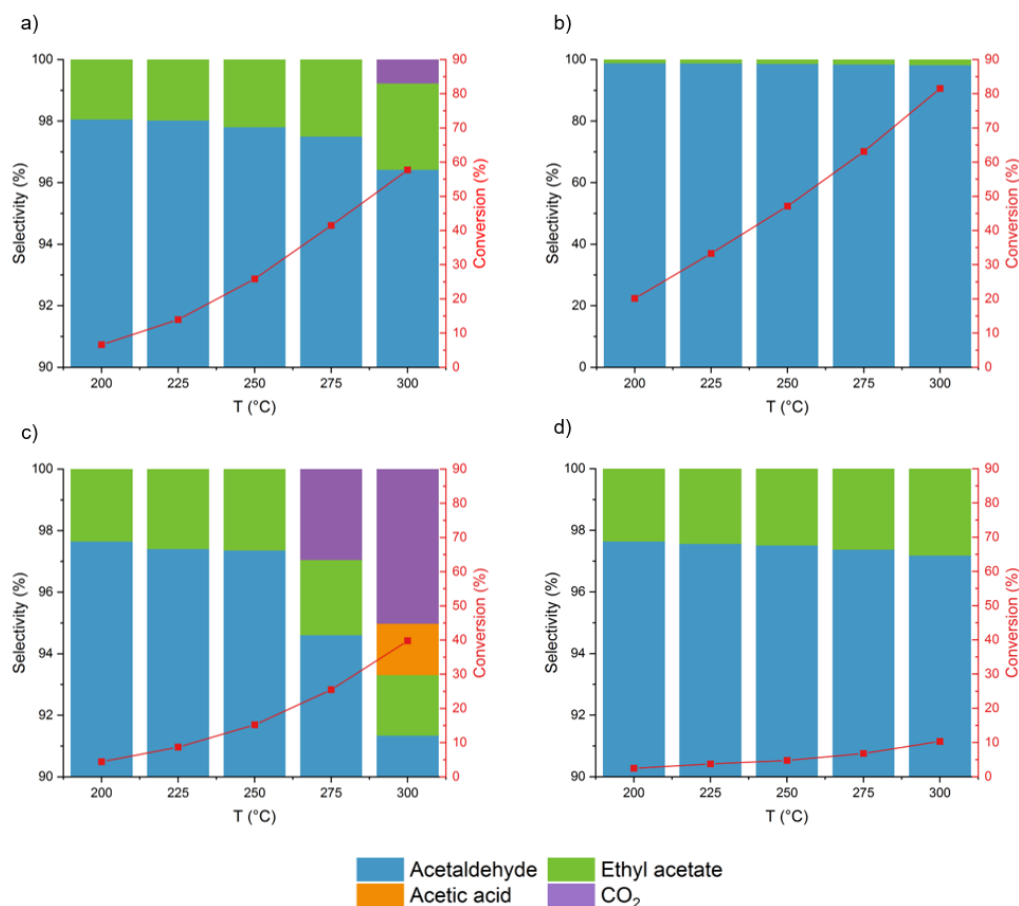


Figure 24. Selectivities for the measurements presented in Figure 23, (a) Au/rutile, (b) AuAg/rutile, (c) AuRu/rutile and (d) AuPt/rutile. Whereas for Au/rutile, relevant amounts of ethyl acetate and, at 300°C, 0.8% CO₂ were obtained, AuAg/rutile shows excellent selectivity for acetaldehyde (> 98%) with solely ethyl acetate as by-product. AuRu/rutile shows the highest amount of CO₂ produced (2.9% at 275°C and 5.0% at 300°C), but also, as the only catalyst, relevant amounts of acetic acid (1.7%). AuPt also produces ethyl acetate as by-product and no CO₂, however at very low conversion levels.

Furthermore, we tested a series of catalysts prepared by S. Mostrou-Moser at the ETH Zürich by flame spray pyrolysis (FSP): Au/TiO₂, AuAg/TiO₂, AuPt/TiO₂, AuPd/TiO₂ (particle sizes expected to be between 5 and 6 nm). The metal loading was 1.5 wt.%, with a 1:1 ratio of the two metals for the bimetallic samples. The TiO₂ support consisted mainly of anatase (anatase rutile ratio on average ca. 4.3:1, as determined by XRD at the ETH Zürich).

The results of the kinetic activity screening are depicted in Figure 25. In order to show the evolution of the conversion, the x-axis shows the reaction time (even though the measurement was performed starting at 100°C, due to the low conversion in this range, values are only shown for temperatures $\geq 200^\circ\text{C}$). Interestingly, none of the promoters exposes higher activity than the Au/TiO₂, and the activities are approximately by an order

of magnitude lower than for the DP/IWI-prepared samples, however a lower metal loading of 1.5 wt.% in total (Au/promoter = 1/1), in contrast to 5% Au + 1 wt%. promoter (and even 2 wt.% in case of Pt), must be considered. Furthermore, direct comparison, e.g. by normalizing the reaction rate to the metal loading, is difficult because of the varying Au/promoter ratio, which can have a profound effect on the catalytic activity. One of the huge advantages of FSP-prepared catalysts is the lack for need of post-processing (no need for calcination to remove residues from the synthesis and immediately formed nanoparticles, whereas for the DP-prepared catalysts pretreatment is an integral step to produce homogeneous nanoparticles), on the other hand, however, there is no control that the metal nanoparticles are on the surface of the support (which is guaranteed for the DP/IWI-prepared samples).

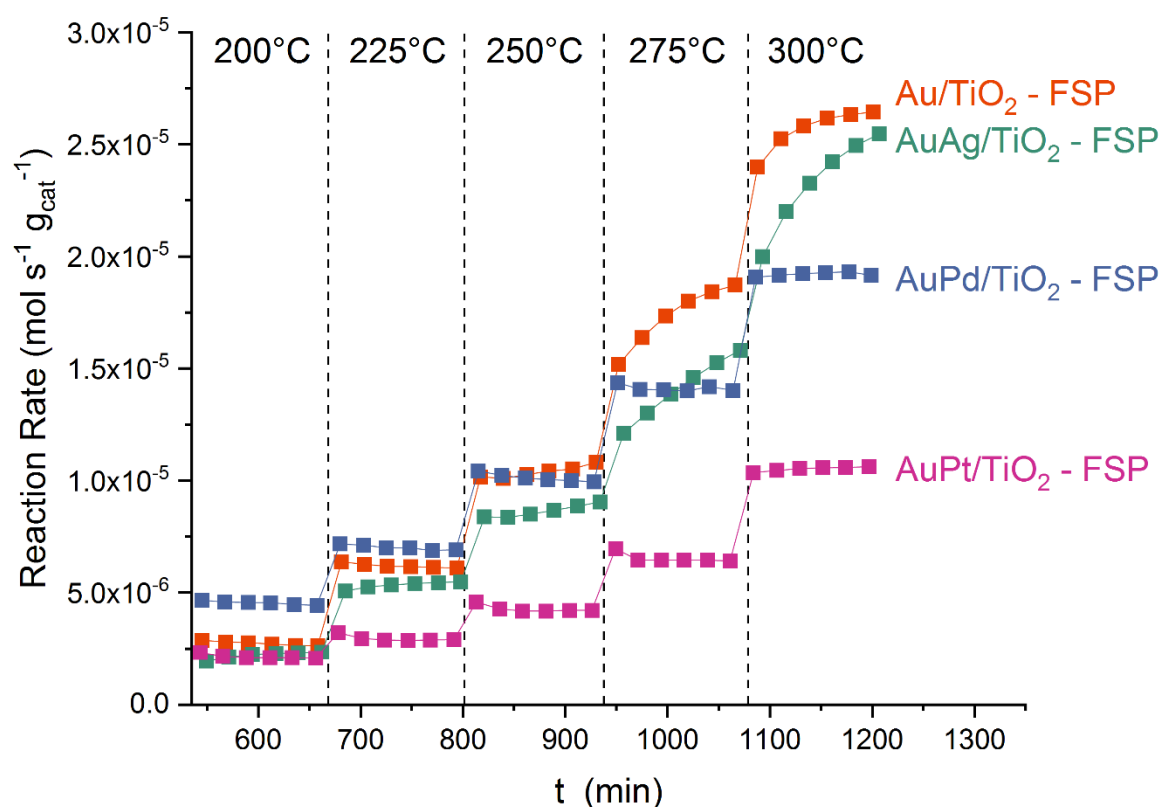


Figure 25. Comparison of FSP-prepared catalysts, Au/TiO₂ (orange), AuAg/TiO₂ (turquoise), AuPd/TiO₂ (blue) and AuPt/TiO₂. A total flow of approx. 51.2 mL/min, with 1.1 mL/min. EtOH and O₂, a 1:1 ratio of the educts (resulting in a partial pressure of 2.2 kPa) was used. Interestingly, for neither of the samples was a better activity than for the monometallic Au sample observed.

Whereas for all the samples the reaction time of approximately 2 hours 18 minutes (which equals six GC runs) for one condition was enough to reach steady-state conditions, this was

not the case for the AuAg/TiO₂ prepared by flame spray pyrolysis. Indeed, a similar trend was observed for one more catalyst, the AuAg/C, where then a longer time period (18 GC runs = 6.9 hours) was chosen. Unfortunately, for AuAg/TiO₂ this was not possible, due to lack of available sample. Evidently however, the catalyst is further increasing its activity, possibly the high temperatures favor migration of Au and Ag and the bimetallic particles are just forming under operando conditions at 300°C (to a lower extent, this is also observed for the Au/TiO₂ catalyst). Interestingly, this very same AuAg/TiO₂ didn't show any activity at all in the liquid phase. The influence of the liquid-phase and water will be discussed in chapter 6.

Figure 26 gives an overview of the selectivities of the catalysts. In all cases, acetaldehyde is the main product, however for Au/TiO₂ also up to 2.6% ethyl acetate, 2.9% acetic acid and the total oxidation product, CO₂, with 1.5% is produced at 300°C. Whereas AuAg/TiO₂ starts with nearly 100% selectivity for acetaldehyde, at 300°C produces about the same amount of ethyl acetate (2.5%), 4.9% acetic acid and no CO₂. AuPd/TiO₂ on the other hand, produces 8.7% CO₂ at 150°C, an amount that doubles to 15.2% at 300°C (and up to 9% ethyl acetate and 0.9% acetic acid). Thus, this catalyst has to be considered the worst of all the investigated ones. Among the FSP-prepared catalysts, the AuPt/TiO₂ produces most acid (up to 5.0% at 300°C), however also up to 2.6% ethyl acetate and 4.7% CO₂ were observed. Interestingly, as most by-products show a trend, here the acetic acid is mostly produced at 250°C and then decreases upon further temperature increase.

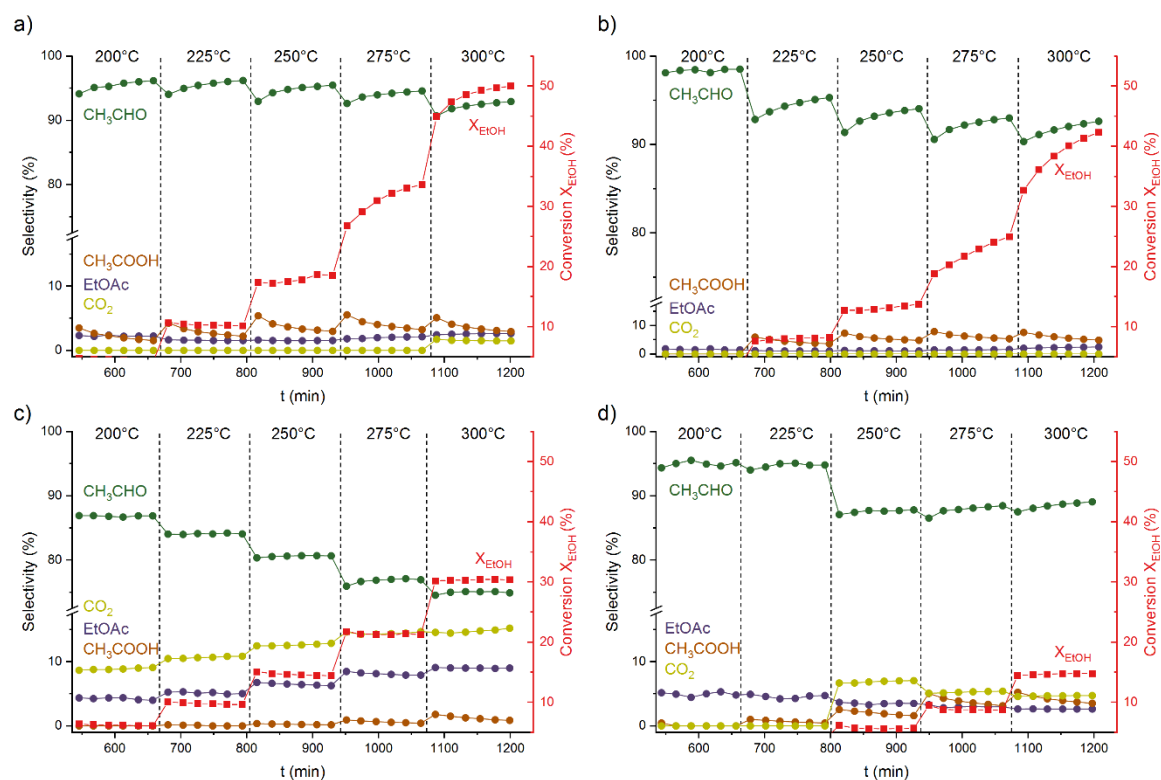


Figure 26. Selectivities and conversions for the samples prepared by flame spray pyrolysis, (a) Au/TiO_2 , (b) AuAg/TiO_2 , (c) AuPd/TiO_2 and (d) AuPt/TiO_2 . A total flow of approx. 51.2 mL, with 1.1 mL/min. EtOH and O_2 , a 1:1 ratio of the educts (resulting in a partial pressure of 2.2 kPa) was used. In all cases, acetaldehyde (CH_3CHO) is the main product, however ethyl acetate (EtOAc), acetic acid (CH_3COOH), and CO_2 are side-products observed.

Motivated by these results, further work focused on silver as promoter: It combines excellent activity, selectivity as well as stability. Ruthenium is the second very promising (provided, the ageing effect can be understood and controlled) catalyst, though no further investigation was undertaken.

5. Bimetallic Supported Gold-Silver Catalysts

5.1. Catalyst Characterization

Particle size distributions for the AuAg nanoparticles as well as their monometallic references were determined by STEM-HAADF, Figure 27 and Table 12. The micrographs show highly dispersed nanocrystalline nanoparticles. This was confirmed by XRD as shown in the annex, section 9.2. The TOFs were obtained by assuming a hemispherical shape of the particles and the mean particle sizes listed in Table 12.

Table 12. Mean particle sizes of the AuAg nanoparticles as well as their monometallic references.

Sample	Mean particle size (nm)	Particles considered
Au/rutile	3.3 ± 1.0 nm	292
AuAg/rutile	3.6 ± 1.2 nm	252
Ag/rutile	2.7 ± 0.4 nm	51
Au/C	14.5 ± 4.5 nm	60
AuAg/C	15.8 ± 5.1 nm	203

Au/rutile and AuAg/rutile have a very similar particle distribution with mean values of 3.3 ± 1.0 nm and 3.6 ± 1.2 nm, respectively. Sintering, e.g. due to the presence of AgCl (as residue from the synthesis)⁶⁵, is limited during the pretreatment process. The Ag/rutile sample does indeed have very small nanoparticles, 2.7 ± 0.4 nm. Au/C and AuAg/C have quite large particles of 14.5 ± 4.5 nm and 15.8 ± 5.1 nm, respectively.

The Au/rutile as well as the AuAg/rutile used for the *operando* studies (batch 4) at the synchrotron beamtimes (see section 5.3.2 and 5.3.3 for NAP-XPS, section 5.3.4 for XAS and section 6.3.2 for NAP-XPS and XAS measurements to determine the influence of water), have a similar size distribution of 2.8 ± 0.5 nm and 3.8 ± 0.8 nm, respectively (the size distributions as well as STEM-HAADF images are shown in the annex, section 9.6.2).

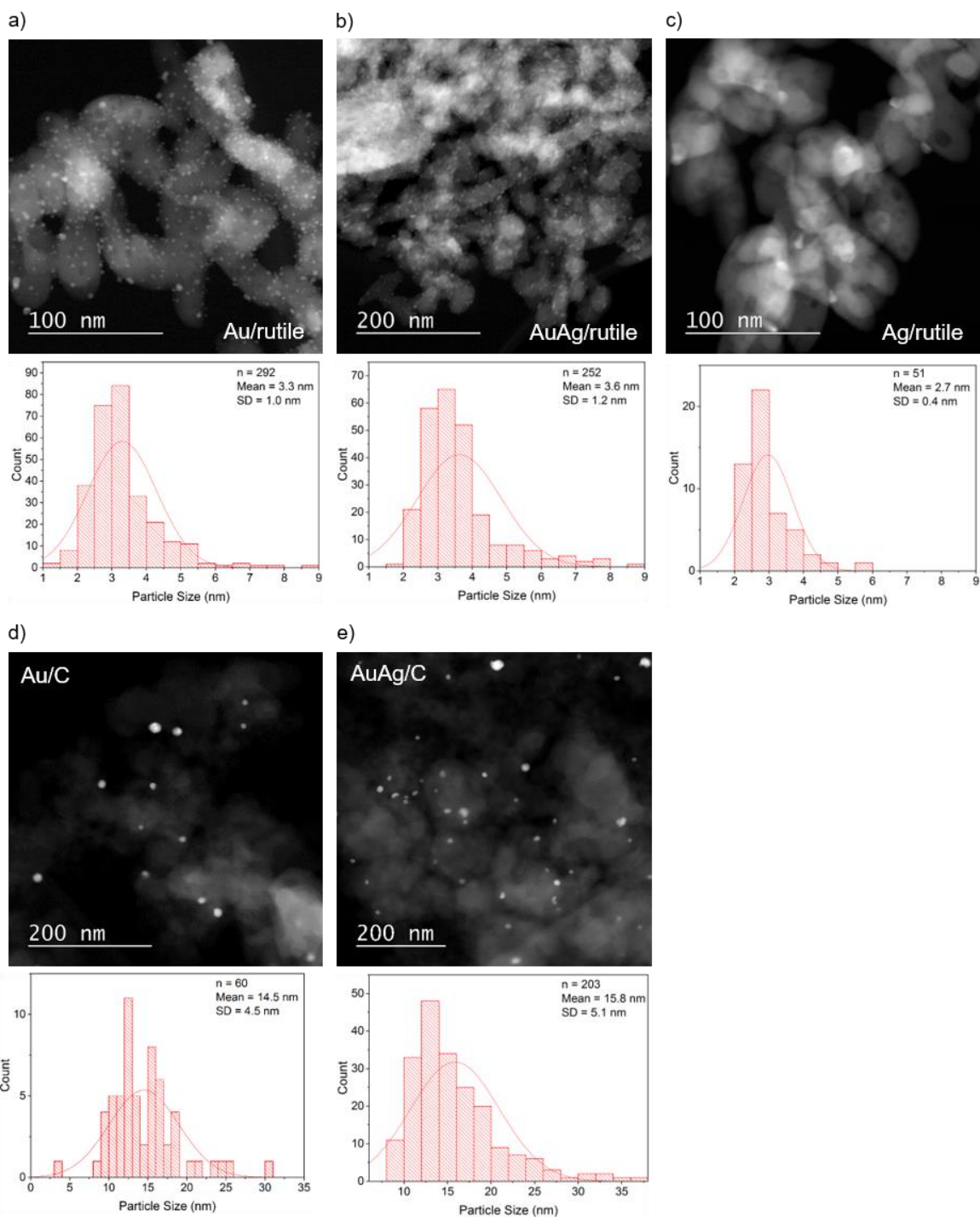


Figure 27. STEM-HAADF micrographs of a) Au/rutile, b) AuAg/rutile, c) Ag/rutile, d) Au/C and e) AuAg/C and their respective size distributions, which are also summarized in Table 12.

For both Au/rutile and AuAg/rutile, STEM-HAADF measurements were performed after the reaction to check for possible sintering. The respective size distributions (Figure 28) show a slight decrease in the mean particle size from 3.3 ± 1.0 nm after the pretreatment to 2.9 ± 0.9 nm after the reaction for Au/rutile. For AuAg/rutile, however, a sintering from

3.6 ± 1.2 nm to 4.3 ± 1.2 nm is observed resulting in a more size distribution closer to an ideal normal distribution. For both samples, a double-sided t-test was performed to confirm a significant difference between the respective measurements after pretreatment/after reaction. The same outcome could be observed for batch 4 of the Au/rutile and AuAg/rutile catalysts, showing a decrease of the mean particle size from 2.8 ± 0.5 nm to 2.6 ± 0.7 nm for Au/rutile and a sintering from 3.8 ± 0.8 nm to 4.7 ± 1.3 nm for AuAg/rutile (the size distributions as well as STEM-HAADF images are shown in the annex, section 9.6.2), thus confirming the trend observed.

The reason for the sintering was not further investigated, however, possibly the formation of Ag^+ is facilitated by chloride residues from the synthesis as reported in the work of Wang et al.⁶⁵, which could play a relevant role. Still, all the TOFs calculated in this thesis rely on the particle size distributions obtained after the pretreatment process.

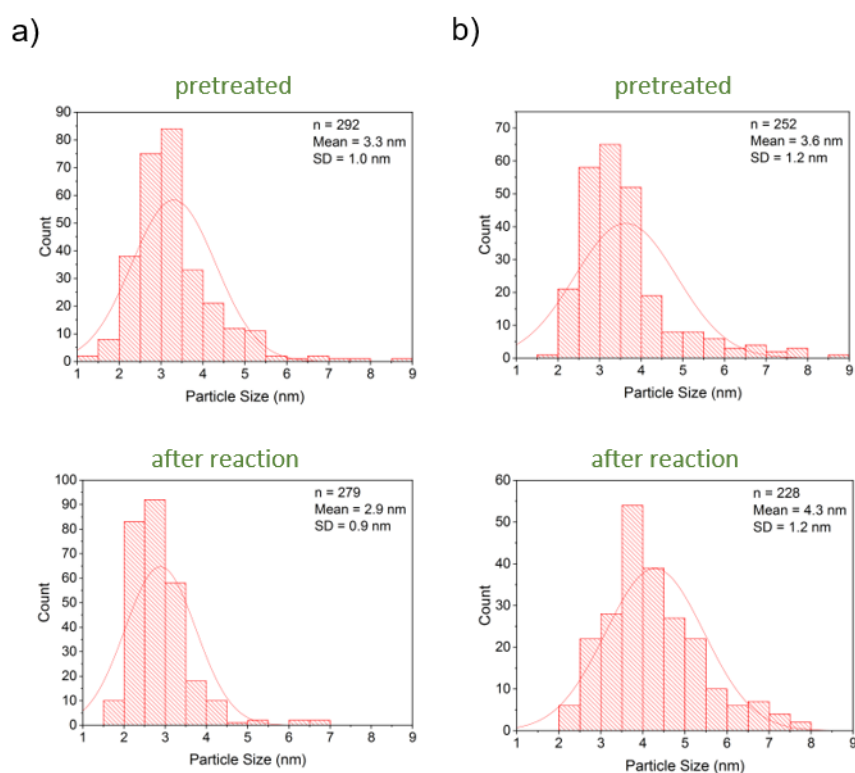


Figure 28 Size distributions after the pretreatment process and after the reaction, for (a) Au/rutile and (b) AuAg/rutile.

Due to the lower metal loading of 1 wt.% and the small nanoparticles as well as the considerably lower contrast, STEM-EDX/EELS was performed in order to verify the silver nanoparticle's identity, Figure 29. These STEM-EDX/EELS micrographs shown were imaged in cooperation with T. Schachinger, USTEM, TU Wien.

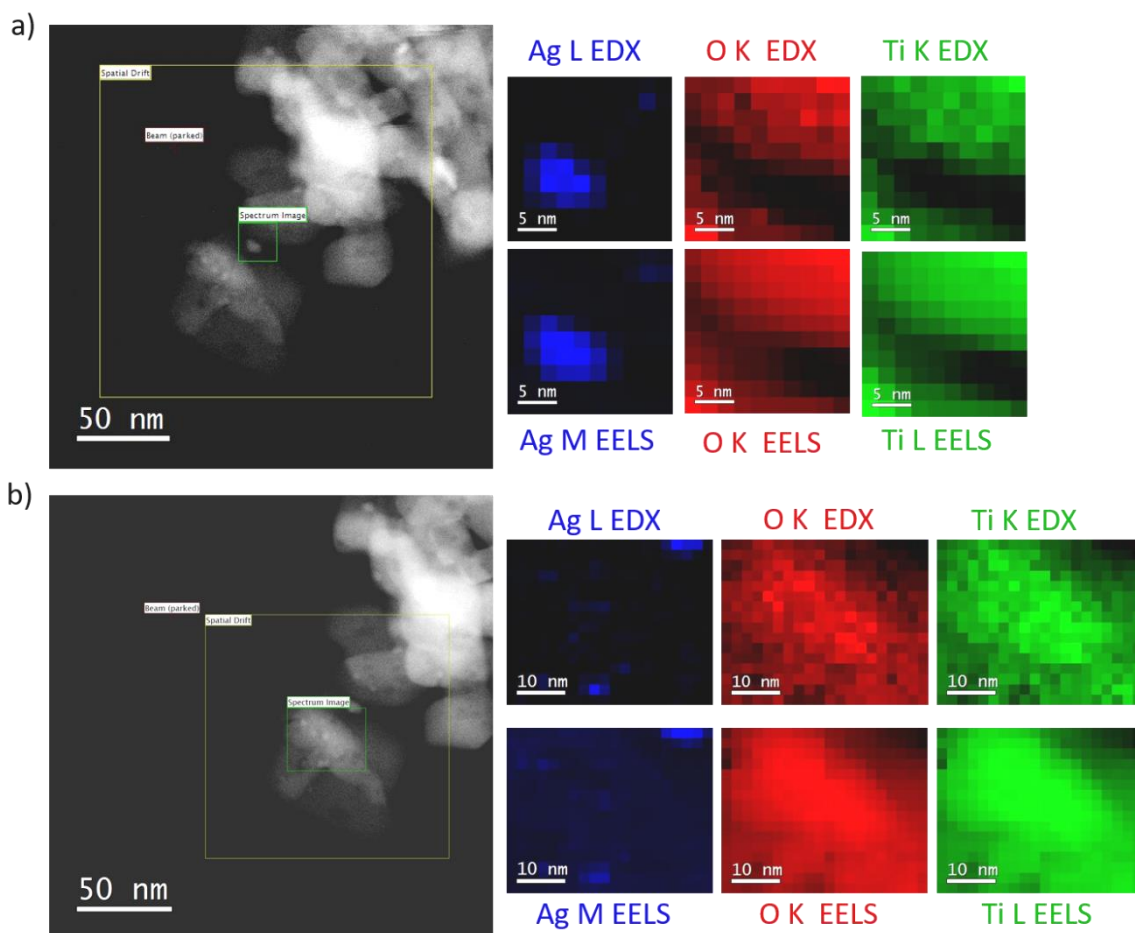


Figure 29. STEM-EDX/EELS of the Ag/rutile sample. Spots visible were confirmed to be Ag nanoparticles (with EELS, naturally, yielding higher spatial resolution. Measurements in cooperation with T. Schachinger, USTEM, TU Wien.

For the AuAg/rutile catalysts, their bimetallic character, alloying and possible segregation (though, under *ex-situ* conditions) were also imaged by STEM-EDX, Figure 30. Although the bimetallic character of the particles was confirmed, the limited spatial resolution as well as beam-damage prevented the proof or disproof of segregation.

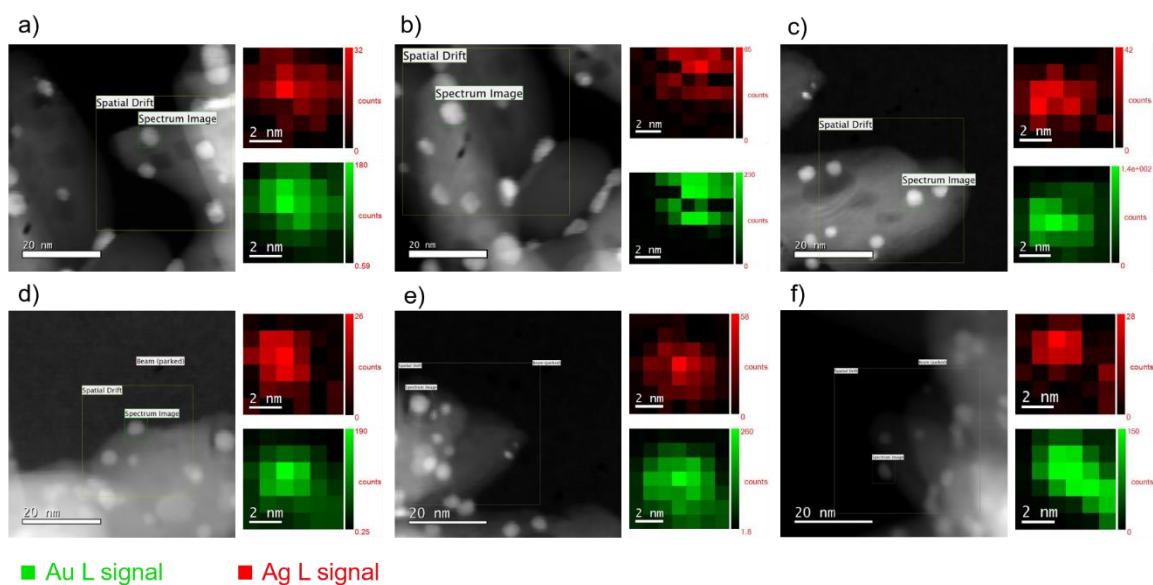


Figure 30. STEM-EDX measurements of three different nanoparticles (a-c) from the AuAg/rutile sample at USTEM, TU Wien. Although the bimetallic character of the particles was confirmed, spatial resolution was too low to either detect segregation or rule it out. Measurements in cooperation with T. Schachinger, USTEM, TU Wien.

Thus, using better instrumentation, measurements using a probe Cs-corrected Scanning Transmission Electron Microscope, in cooperation with G. Dražić and A. Pintar, Department for Environmental Sciences and Engineering, National Institute of Chemistry, Ljubljana, Slovenia, were done. Results, Figure 31, indicate wide areas with pure gold nanoparticles, as well as areas with small amounts of Ag within the Au particles. Most of the silver, however, is to be found in larger bimetallic particles of 3-5 nm size (see Table 13 for a standardless quantitative EDX analysis of six nanoparticles in that size range). No indication for Ag surface segregation could be found, although the situation could be different under *operando* conditions. HR-STEM imaging of the sample is depicted in Figure 34 (after the pretreatment of the sample) and Figure 35 (after reaction), whereas Figure 33 shows a detailed analysis of one of the larger particles (after pretreatment) with facets equivalent to (111) as well as (002). Figure 35 c) features an area with those larger bimetallic AuAg nanoparticles. Additional data supporting the claims of this chapter, line scans of the sample, are printed in the annex, section 9.6.

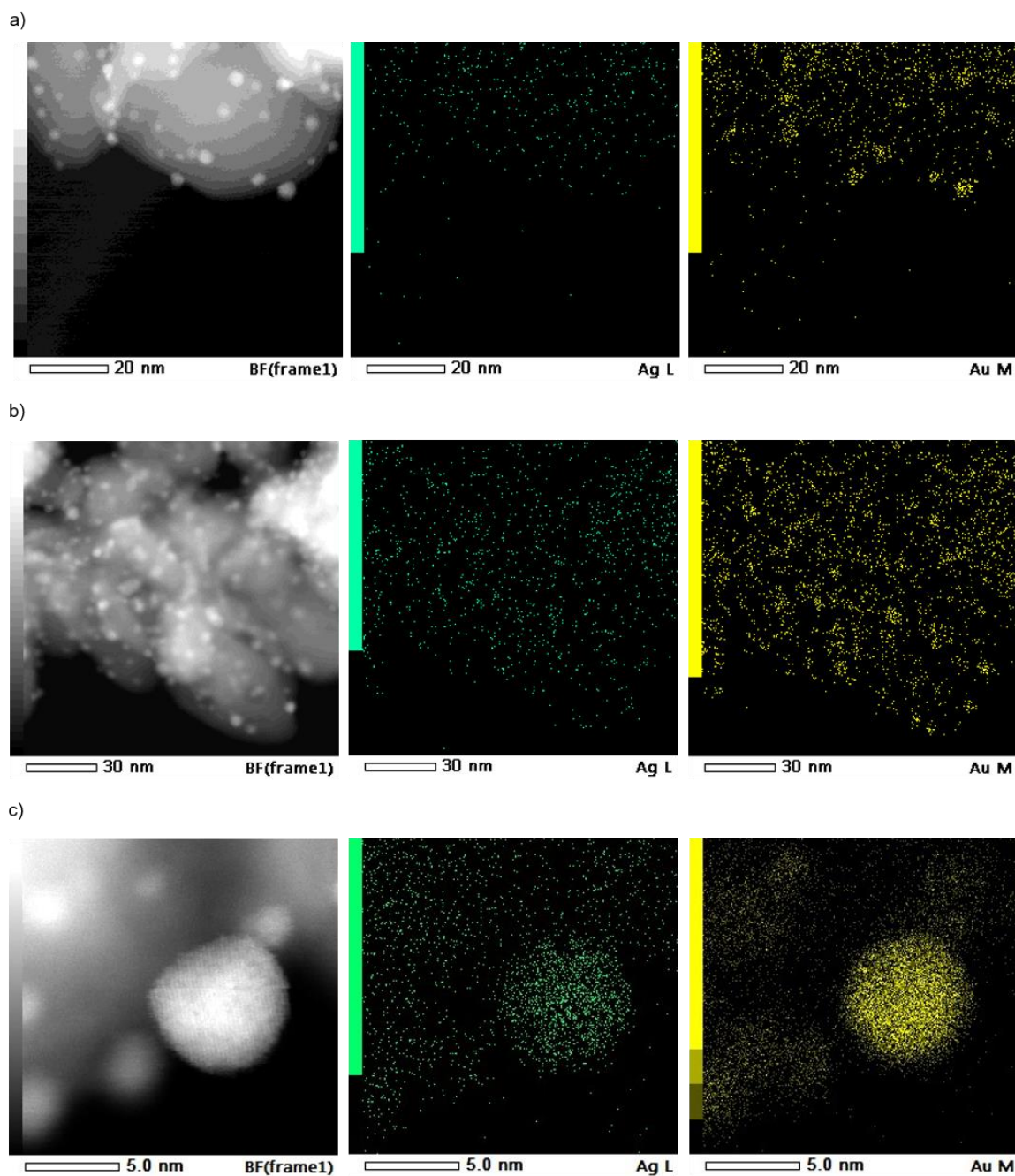


Figure 31. STEM-EDX imaging (at 200 kV) of three different areas, showing areas with pure gold nanoparticles (a), low amounts of Ag within the Au particles (b) and a larger particle of 4-5 nm. Most of Ag is located in 3 -5 nm-sized particles. Measurements in cooperation with G. Dražić and A. Pintar, Department for Environmental Sciences and Engineering, National Institute of Chemistry, Ljubljana, Slovenia. The corresponding EDX spectra for a) and b) are shown in Figure 32.

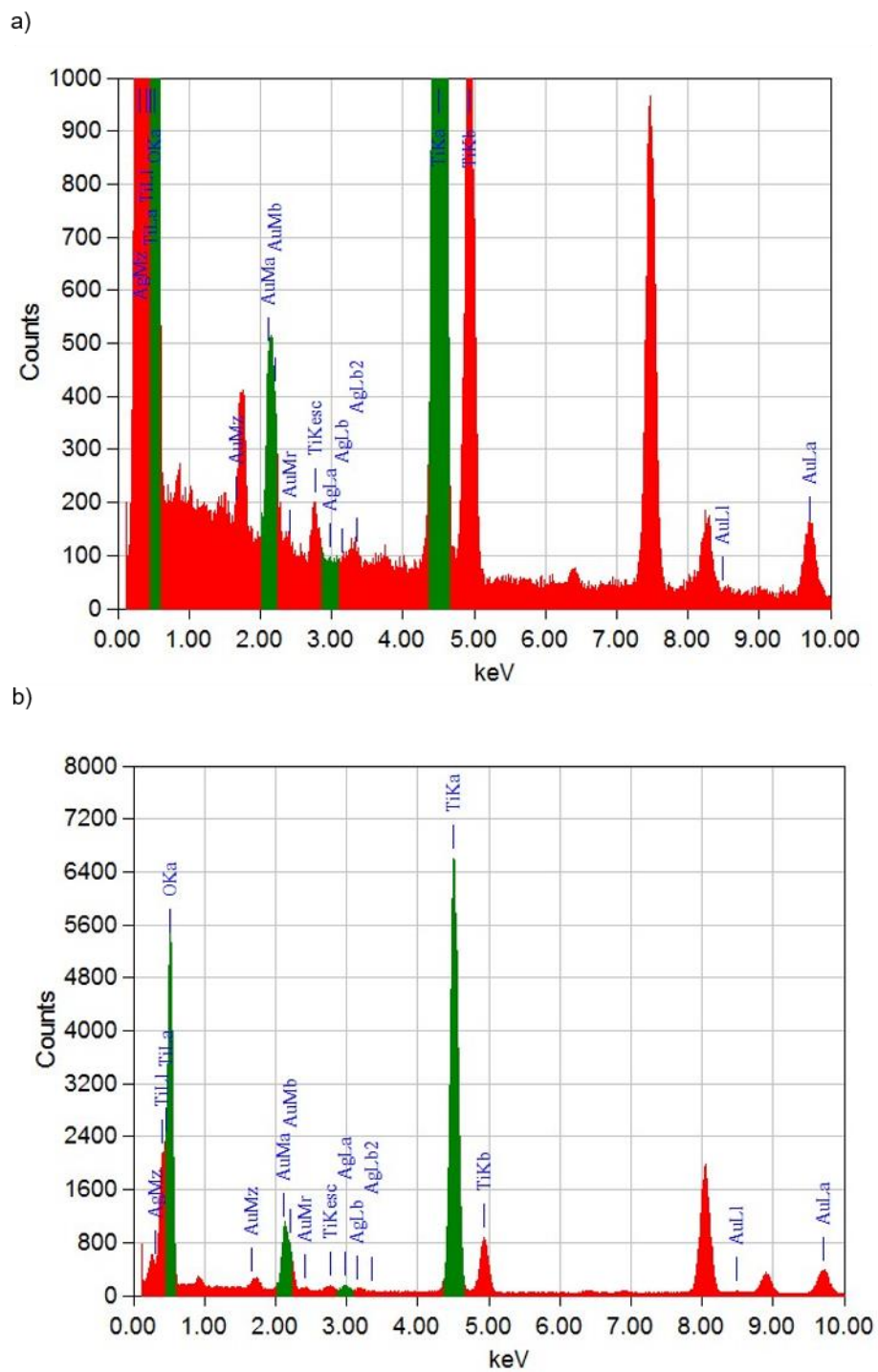


Figure 32. EDX spectra (taken at 200 kV) for the images presented in Figure 31 a) and b). For a), Ag is below the limit of detection (approx. 0.5 at.%) whereas in b) a small amount of Ag is present. Measurements in cooperation with G. Dražič and A. Pintar, Department for Environmental Sciences and Engineering, National Institute of Chemistry, Ljubljana, Slovenia.

Table 13 Standardless quantitative EDXS analysis of six different AuAg nanoparticles of 3-5 nm size, provided by G. Dražič. Due to the geometry and support effects, a relative error of at least 10% has to be assumed.

Element	(keV)	Counts	wt. %	Sigma	at. %
Ag L	2.984	25.57	15.2	24.41	24.7
Au M	2.12	137.19	84.8	13.9	75.4
Ag L	2.984	36.16	4.3	1.17	7.6
Au M	2.12	768.88	95.7	3.18	92.4
Ag L	2.984	61.18	19.8	15.15	31.0
Au M	2.12	244.73	80.2	11.08	69.0
Ag L	2.984	535.36	15.4	84.71	24.9
Au M	2.12	2899.61	84.6	212.45	75.1
Ag L	2.984	677.54	13.2	0.49	21.7
Au M	2.12	4389.3	86.8	1.23	78.3
Ag L	2.984	6.92	10.1	151.53	17.0
Au M	2.12	60.98	89.9	21.05	83.0

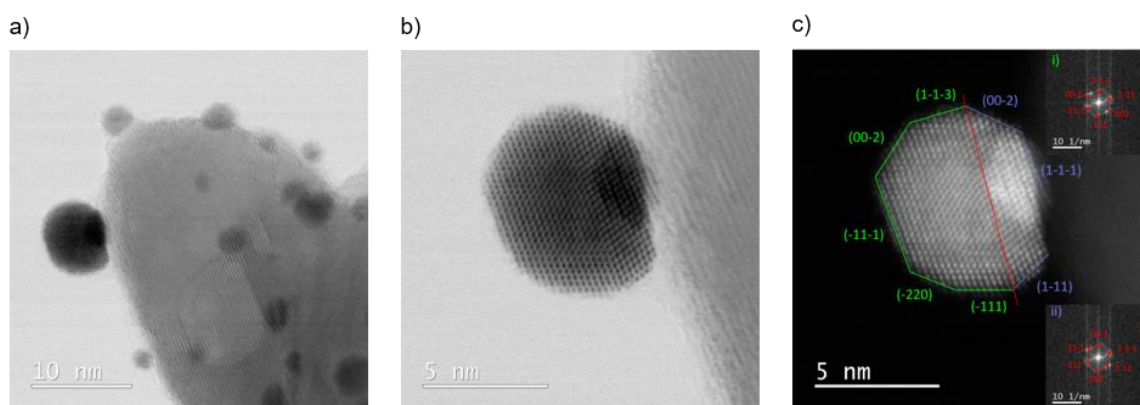


Figure 33. Brightfield STEM images, a) and b), of a larger particle from the AuAg/rutile sample, after pretreatment, taken at 200 kV. c) shows an analysis of the exposed facets, equivalent to (111) as well as (002). Measurements in cooperation with G. Dražič and A. Pintar, Department for Environmental Sciences and Engineering, National Institute of Chemistry, Ljubljana, Slovenia.

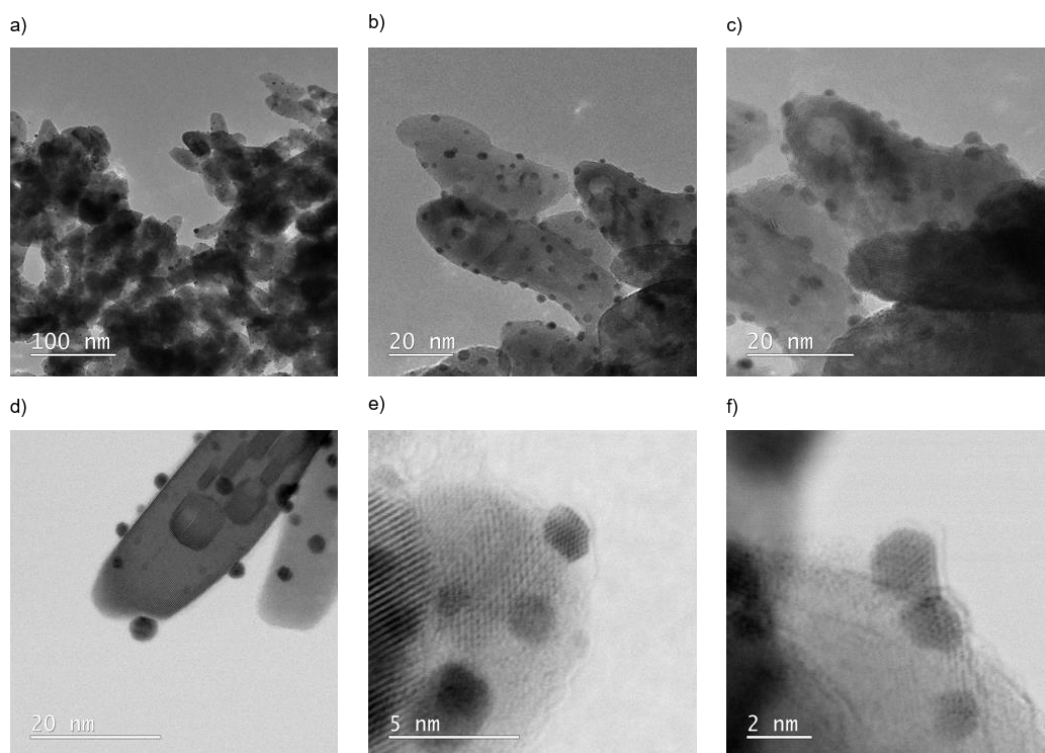


Figure 34. Brightfield STEM images from the AuAg/rutile sample, after pretreatment, taken at 80 kV. Measurements in cooperation with G. Dražič and A. Pintar, Department for Environmental Sciences and Engineering, National Institute of Chemistry, Ljubljana, Slovenia.

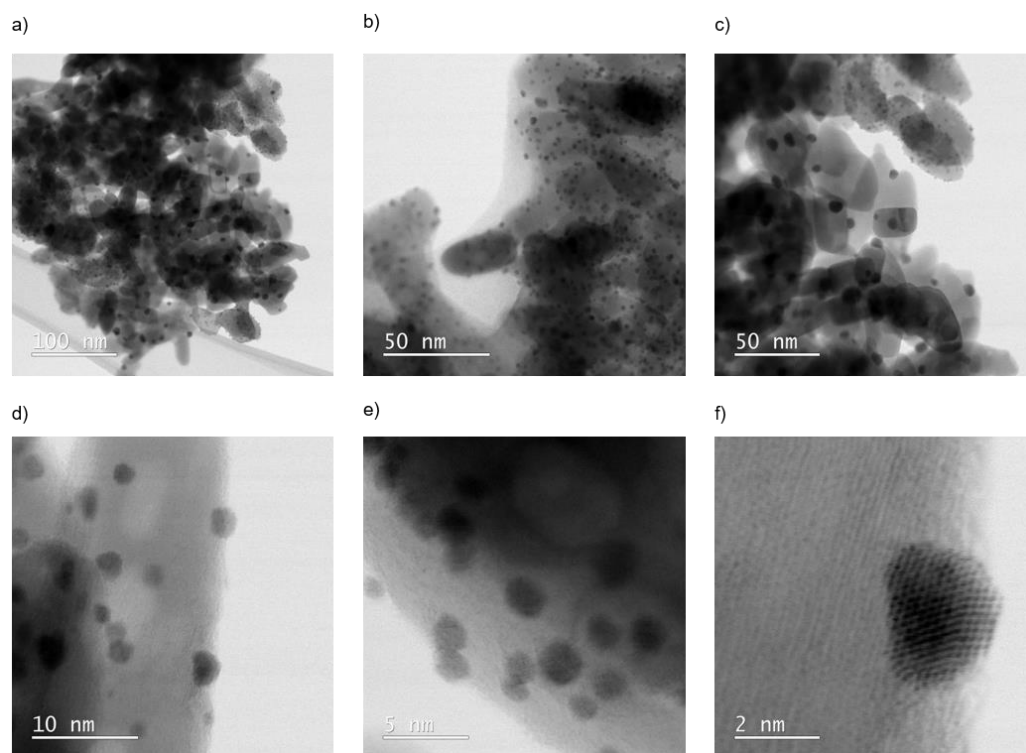


Figure 35. Brightfield STEM images from the AuAg/rutile sample, after reaction, taken at 80 kV. Measurements in cooperation with G. Dražič and A. Pintar, Department for Environmental Sciences and Engineering, National Institute of Chemistry, Ljubljana, Slovenia.

STEM-EDX was also performed for the AuAg/C sample to confirm the bimetallic character of the nanoparticles, Figure 36. Clearly, the nanoparticles are composed of Au and Ag, but separate Au/Ag, either single atoms or very small clusters, cannot be ruled out. Most likely the signals between the nanoparticles are noise or originate from scattered electrons.

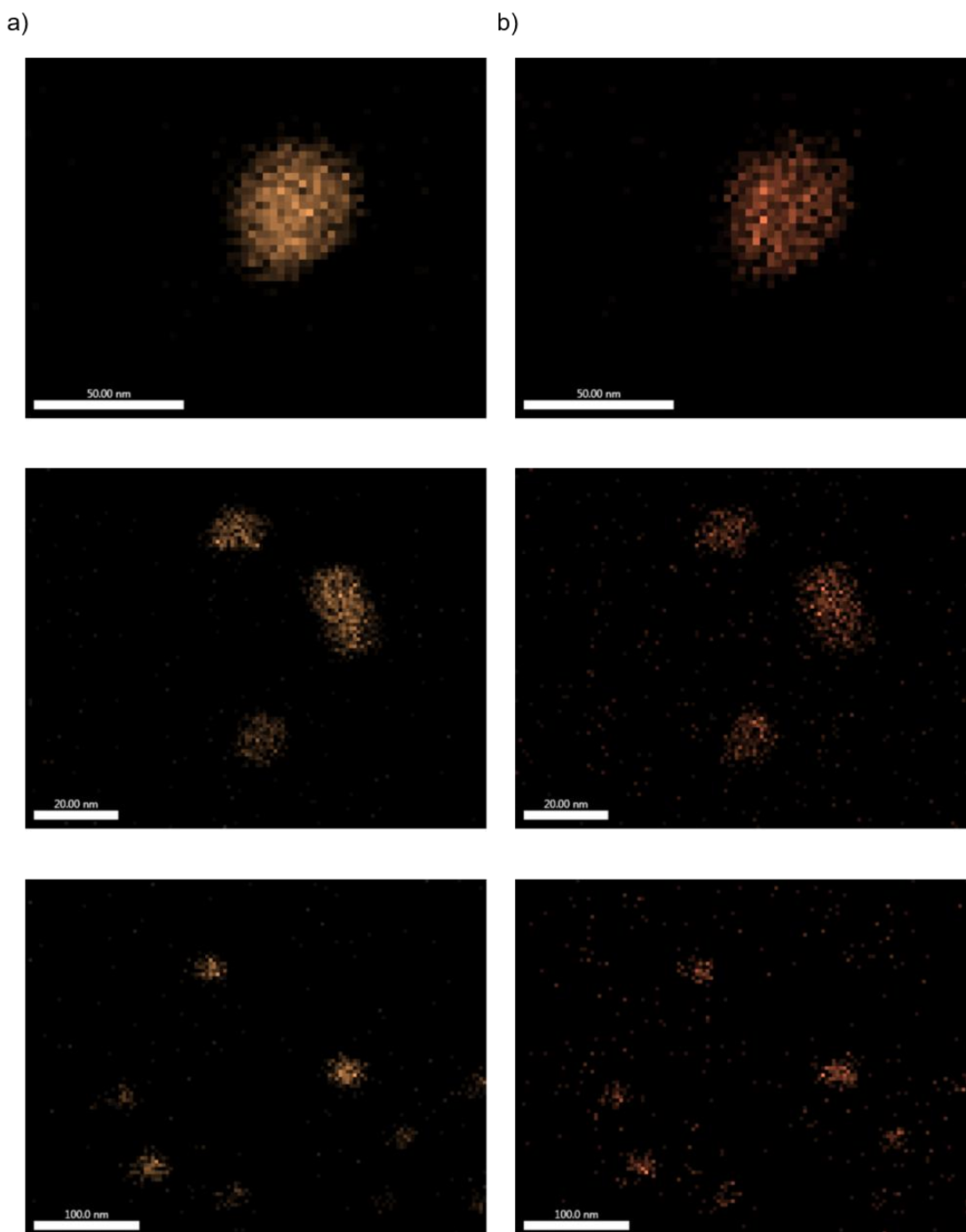


Figure 36. STEM-EDX measurements for the AuAg/C sample, (a) Au L-edge and (b) Ag L-edge. Due to the low signal intensity of Ag, switching to another lens was necessary, resulting in some spherical aberration. Clearly, the nanoparticles are of bimetallic nature. The signals between the larger nanoparticles most likely originate from scattered electrons, however some separate Au/Ag cannot be ruled out. Measurements in cooperation with K. Dobrezberger.

The samples were further characterized by TPD (experiment performed by J. Teržan in A. Pintar's group, Department for Environmental Sciences and Engineering, National Institute of Chemistry, Ljubljana, Slovenia), see Figure 37. Whereas the TPD of Au/rutile and rutile was discussed in detail in 3.3, the AuAg/rutile, Figure 37 b), and its differences from Au/rutile shall be discussed here. Whereas the peak pattern is very similar, all the peaks, Table 14 are shifted to higher temperatures for AuAg/rutile. The similarity of peaks points to the same adsorption/desorption pattern, but integration of the peak area above 250°C, shows 43% lower CO₂ production for AuAg/rutile and it is occurring at roughly 60°C higher temperatures.

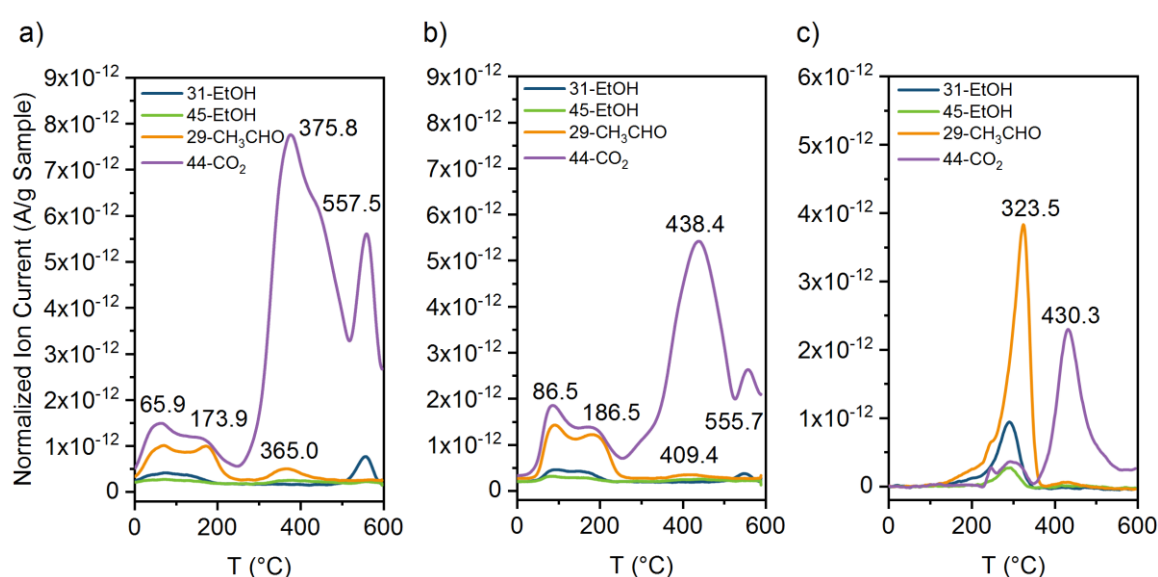


Figure 37. Ethanol TPD experiments for (a) Au/rutile, (b) AuAg/rutile and (c) rutile reference sample. *m/z* signals of 31 and 45 were used for the EtOH detection, whereas 29 was used for acetaldehyde (CH₃CHO) and 44 for CO₂. These TPD experiments were performed by J. Teržan in A. Pintar's group, Department for Environmental Sciences and Engineering, National Institute of Chemistry, Ljubljana, Slovenia.

Table 14. TPD peaks shown in Figure 37, a) Au/rutile and b) AuAg/rutile.

Compound	Au/rutile	AuAg/rutile
	T (°C) / E _{a,app} (kJmol ⁻¹)	T (°C) / E _{a,app} (kJmol ⁻¹)
Acetaldehyde/Ethanol	65.9 / 96	86.5 / 102
Acetaldehyde	137.9 / 128	186.5 / 131
Acetaldehyde	365.0 / 184	409.4 / 197
CO ₂	375.8 / 187	438.4 / 206
CO ₂	583.0 / 242	555.7 / 241

BET surface areas for the rutile-based catalysts are printed in Table 15.

Table 15 BET surface areas for the rutile-based catalysts.

Sample	BET surface area (m ² /g)
Rutile	103 (manufacturer: 105)
Au/rutile	28
AuAg/rutile	29
Au/rutile (batch 4, synchrotron)	39
AuAg/rutile (batch 4, synchrotron)	21

5.2. Kinetic Measurements and Mechanistic Considerations

Reaction rates as determined are depicted in Figure 38. Clearly, AuAg/rutile is the most active catalyst, clearly suggesting the synergistic effect between Au and Ag, followed by Au/rutile and Ag/rutile. Especially the latter is remarkable, as the metal loading is just 1 wt.%, in contrast to 5 wt.% for Au/rutile, and 5 wt.% Au with 1 wt.% Ag for AuAg/rutile. Au/C (1 wt.% Au) and AuAg/C (1 wt.% Au 0.2 wt.% Ag) are reference catalyst based on the commercial Au/C purchased from Strem Chemicals. Due to their large particles, (14.5 ± 4.5 nm for Au/C, 15.8 ± 5.1 nm for AuAg/C) the reaction rate is very low, however, also for the AuAg/C the promotional effect Ag is clearly observed.

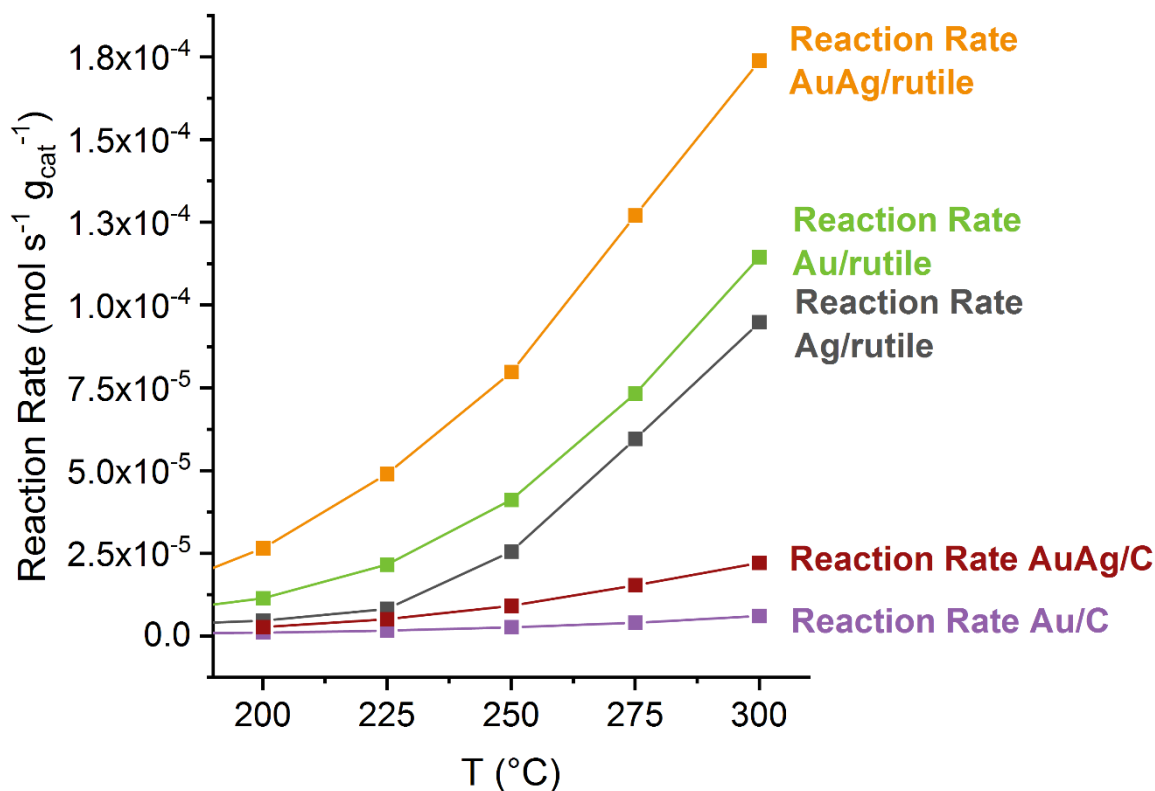


Figure 38. Kinetic measurements for AuAg/rutile (orange), Au/rutile (green), Ag/rutile (grey) as well as AuC/rutile (purple). Reaction rate was normalized to the catalyst amount (in gram). A total flow of approx. 51.2 mL, with 1.1 mL/min. EtOH and O₂, a 1:1 ratio of the educts (resulting in a partial pressure of 2.2 kPa) was used.

Turnover frequencies, calculated using the mean particle size and metal loading as determined previously, are shown in Figure 39 whereas the numerical values are listed in Table 5. Au/rutile and Au/C exhibit a very similar intrinsic activity at 200°C with a TOF of 0.18 s⁻¹. Interestingly, AuAg/C has a higher TOF of 3.42 s⁻¹ than AuAg/rutile 2.12 s⁻¹. Both curves have a similar slope and flatten at 275°C and 300°C, which indicates diffusion/transport limitation at the higher temperatures (conversion > 25%). Therefore, those temperatures were excluded from the calculation of activation energies. For Ag/rutile, the point the highest temperature was disregarded for the calculation of the apparent activation energy, 71.5 ± 7.3 kJmol⁻¹. The observed lower apparent activation for Au/C than for the Au/rutile is a trend that is also continued for the bimetallic samples (14.6 ± 8.5 in contrast to 23.0 ± 5.2 kJmol⁻¹). The TOFs for ethyl acetate are by an order of magnitude lower than for acetaldehyde, and acetic acid was only observed at higher temperatures (275°C and 300°C for AuAg/rutile, only 300°C for Au/rutile and Ag/rutile).

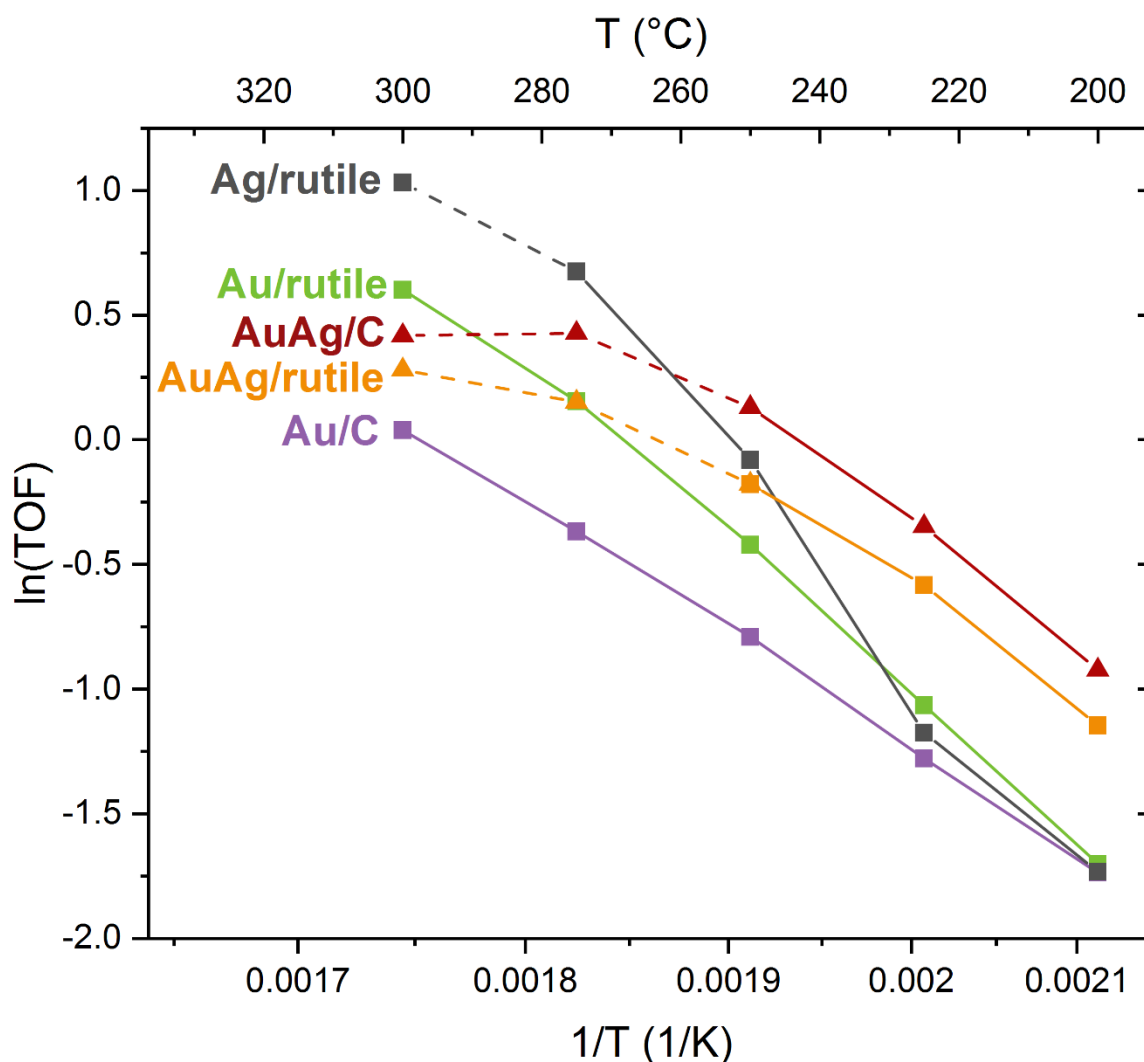


Figure 39. $\ln(\text{TOF})$ against $1/T$ are plotted for the EtOH TOF of AuAg/rutile (orange), Au/rutile (green), AuAg/C (dark red), Au/C (purple) and Ag/rutile (grey). TOFs are similar for both catalysts at low temperature and considerably larger for Au/rutile at higher temperature (numerical TOFs are listed in Table 16). Apparent activation energies calculated from this kinetic data are listed in Table 17 (for the bimetallic AuAg catalysts, the non-linear part of the dataset, marked with dashed lines, was excluded from the calculation). For the Ag/rutile sample, a considerably higher error must be assumed due to the S-shape of the curve which points to a distinctly different kinetic behavior of Ag.

Table 16 TOFs obtained for acetaldehyde, ethyl acetate and acetic acid production.

TOF Acetaldehyde [s^{-1}]					
	200°C	225°C	250°C	275°C	300°C
Au/rutile	0.18	0.35	0.66	1.17	1.83
Ag/rutile	0.17	0.30	0.96	2.24	3.53
AuAg/rutile	0.32	0.60	0.98	1.55	2.12
Au/C	0.18	0.28	0.45	0.69	1.04
AuAg/C	0.41	0.78	1.42	2.37	3.42
TOF Ethyl acetate [s^{-1}]					

	200°C	225°C	250°C	275°C	300°C
Au/rutile	3.1×10^{-3}	5.4×10^{-3}	1.1×10^{-2}	2.4×10^{-2}	4.7×10^{-2}
Ag/rutile	5.1×10^{-3}	6.3×10^{-3}	9.6×10^{-3}	2.2×10^{-2}	4.9×10^{-2}
AuAg/rutile	5.9×10^{-3}	9.5×10^{-3}	1.6×10^{-2}	2.7×10^{-2}	3.7×10^{-2}
Au/C	3.7×10^{-3}	4.1×10^{-3}	5.0×10^{-3}	6.0×10^{-3}	7.9×10^{-3}
AuAg/C	4.3×10^{-3}	5.4×10^{-3}	7.5×10^{-3}	1.1×10^{-2}	1.6×10^{-2}
TOF Acetic acid [s⁻¹]					
	200°C	225°C	250°C	275°C	300°C
Au/rutile					8.5×10^{-4}
Ag/rutile					1.6×10^{-2}
AuAg/rutile				1.2×10^{-3}	1.2×10^{-3}
Au/C					
AuAg/C					

Table 17 Apparent activation energies $E_{ac,app}$ of the investigated catalysts.

	$E_{ac,app}$ (kJmol ⁻¹)	Pearson R
AuAg/rutile	23.0 ± 5.2	0.9756
Au/rutile	52.6 ± 8.3	0.9996
Ag/rutile	71.5 ± 7.3	0.9897
AuAg/C	14.6 ± 8.5	0.8651
Au/C	40.2 ± 7.0	0.9995

Selectivities were > 97% for acetaldehyde for all catalysts, Figure 40, with ethyl acetate as the major side product. Only for AuAg/rutile (max. 0.07%), Au/rutile (max. 0.05%) and Ag/rutile (0.4%) was acetic acid observed at higher temperatures. AuAg/C was the only catalyst where relevant amounts of CO₂ formation was observed, interestingly decreasing with the temperature (from 0.3% at 200°C to 0.03% at 300°C). Possibly, this is because the acetaldehyde desorbs easier at higher temperatures and thus coverage is small enough to prevent total oxidation. No CH₄ resulting from acetaldehyde decomposition was observed.

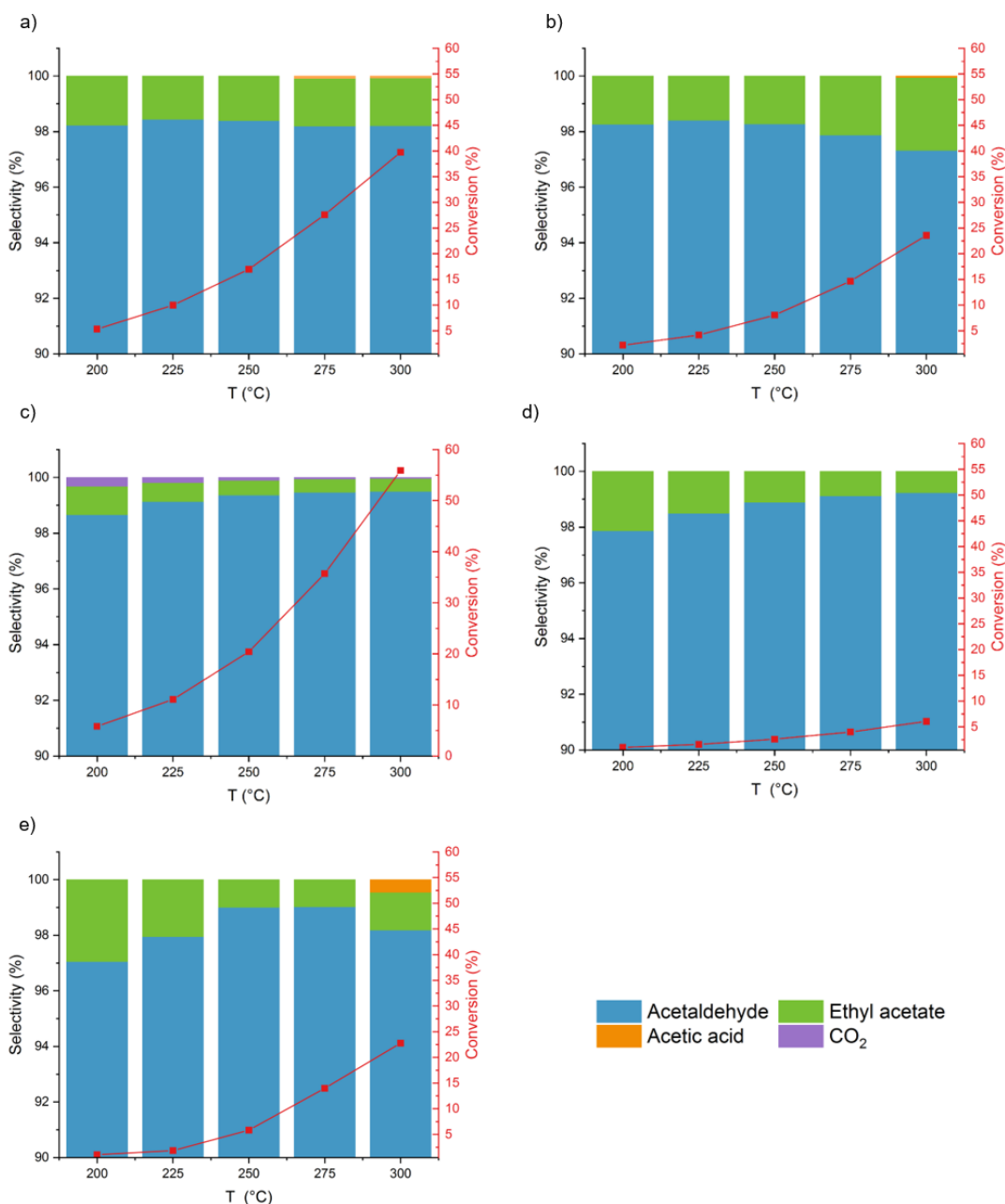


Figure 40. Selectivity of the studied catalysts, a) AuAg/rutile, b) Au/rutile, c) AuAg/C and d) Au/C and e) Ag/rutile. A total flow of 51.2 mL/min, with 1.1 mL/min EtOH and O₂, a 1:1 ratio of the educts (resulting in a partial pressure of 2.2 kPa) was used. Only for AuAg/C was CO₂ was observed, starting at 0.3% at 200°C decreasing to 0.03% at 300°C.

The high selectivity towards acetaldehyde is consistent with previous reports in literature^{36,60}. Upon temperature increase, the change of selectivity is different for every sample: For AuAg/rutile, the amount of ethyl acetate is around 2%, and at 275°C and 300°C some acetic acid is produced. For Au/rutile, the ethyl acetate amount is indeed slightly increasing from 1.7% to 2.6% and at 300°C some acetic acid is observed. Thus, the addition of Ag is not only improving activity, but also increases selectivity towards acetaldehyde

(starting from an already high level for Au/rutile). For both carbon-supported samples, Au/C and AuAg/C, selectivity is indeed increasing from around 98% to 99%. Ag/rutile shows the same trend, but at 300°C selectivity decreases again, and, from all the discussed samples in this chapter, the highest amount of acetic acid is observed. The decreasing temperature leads to decreasing ethyl acetate selectivity, which is a result of the ethyl acetate formation mechanism, coupling of an ethoxy species with acetaldehyde³³. With ethyl acetate formation being the result of a coupling of acetaldehyde with ethoxy species, again differences between rutile-based and carbon-based catalysts can be observed. For the latter, an expected decrease of ethyl acetate selectivity is observed with temperature increase, resulting from lower acetaldehyde coverage, which reduces the coupling probability. For rutile, again different kinetics for ethyl acetate are observed, however presence of silver greatly decreases the temperature dependence. Eventually, the reason for this could lie in the higher conversion, also at lower temperatures, leading to more acetaldehyde coverage also at lower temperatures and thereby decreasing the difference between higher and lower temperatures.

As discussed in chapter 3 for the monometallic Au samples, there is a coupling of ethoxy species with acetaldehyde³³. Increased temperature reduces the acetaldehyde coverage and thus also the coupling probability (the same mechanism is expected for the reduced CO₂ formation). The exceptional trend observed for rutile-supported catalysts, indicating a different kinetics for the ethyl acetate formation on Au/rutile, is not observed for AuAg, where the ethyl-acetate formation remains constant.

For all the catalysts discussed, reaction order measurements were undertaken. Variation of O₂ as well as ethanol partial pressures, Figure 42, resulted in the reaction orders calculated by linear regression. An overview of the numerical values is given in Table 18 and graphically shown in Figure 41.

Table 18. Reaction orders obtained for Au/rutile, AuAg/rutile, Ag/rutile, Au/C and AuAg/C.

	Au/rutile		AuAg/rutile		Ag/rutile		Au/C		AuAg/C	
	EtOH Order	O ₂ Order	EtOH Order	O ₂ Order	EtOH Order	O ₂ Order	EtOH Order	O ₂ Order	EtOH Order	O ₂ Order
150°C	0.42 ± 0.02	0.18 ± 0.02	0.45 ± 0.02	0.07 ± 0.01	0.40 ± 0.01	-0.03 ± 0.07	0.37 ± 0.02	0.33 ± 0.01	0.33 ± 0.01	0.15 ± 0.04
200°C	0.48 ± 0.02	0.20 ± 0.02	0.48 ± 0.01	0.11 ± 0.01	0.43 ± 0.03	-0.12 ± 0.05	0.36 ± 0.01	0.27 ± 0.03	0.56 ± 0.03	0.13 ± 0.09
250°C	0.75 ± 0.05	0.12 ± 0.02	0.53 ± 0.03	0.21 ± 0.04	0.57 ± 0.06	0.04 ± 0.09	0.47 ± 0.02	0.32 ± 0.02	0.51 ± 0.02	0.34 ± 0.04
300°C	0.89 ± 0.02	0.03 ± 0.06	0.52 ± 0.01	0.29 ± 0.03	0.68 ± 0.05	-0.03 ± 0.03	0.47 ± 0.00	0.30 ± 0.03	0.55 ± 0.03	0.28 ± 0.09

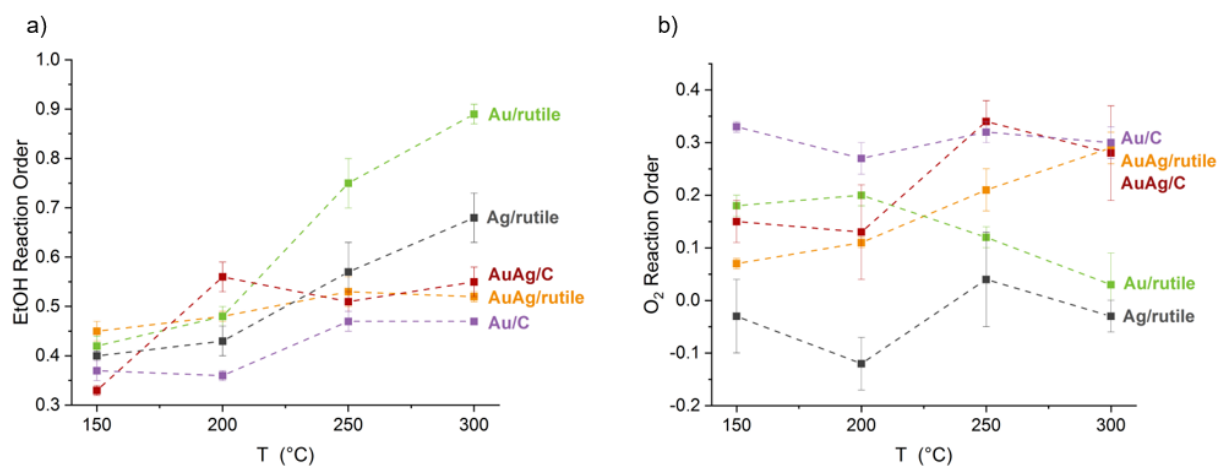


Figure 41. Graphical overview of the reaction orders, a) EtOH and b) O₂, listed in Table 18, AuAg/rutile (orange), Au/rutile (green), AuAg/C (dark red), Au/C (purple) and Ag/rutile (grey).

For all the temperatures, a good fit is observed between the logarithm of the partial pressure and the logarithm of the reaction rate for both Au/rutile and Au/C. Firstly, the ethanol reaction order shall be discussed: For all rutile supported samples, it starts around 0.4 (0.42 for Au/rutile, 0.45 for AuAg/rutile and 0.40 for Ag/rutile) and then increase with the temperature. However, whereas for Au/rutile a doubling to 0.89 is observed, the temperature dependence of the reaction order is much lower for AuAg/rutile (0.52 and 0.68 for Ag/rutile at 300°C). For Au/C and AuAg/C the EtOH reaction orders start at 0.37 and 0.33 and go up to 0.47 and 0.55, respectively. Therefore, it seems, in the AuAg/rutile

systems the silver greatly reduces the reaction order at the higher temperatures. Silver alone, on Ag/rutile, also shows a lower EtOH order, but with 0.68 it is still relevantly higher than in the AuAg sample.

For the O₂ reaction order, on the other hand, we observe a change from 0.18 at 150°C to 0.03, basically zero, for Au/rutile. The oxygen activation is not the rate-limiting step in the reaction. Adding silver to the catalyst means a start at 0.07 and an increase to 0.29. Therefore, silver does seem to have an effect on the oxygen activation. Importantly, when looking at Au/C and AuAg/C, a very different picture presents itself. As already established in chapter 3, carbon can be assumed to be inert and thus the carbon-based catalysts present a good model system to study the “pure” gold and bimetallic gold particles. Clearly, a role of the rutile support must be assumed, as for Au/C, the oxygen reaction order remains fairly constant at approximately 0.3 whereas it changes quite substantially for Au/rutile (see detailed discussion of this in chapter 3). Widmann and Behm assume oxygen species on the Au/TiO₂ catalysts, determined by temporal analysis of products (TAP) reactor, for the CO oxidation, to be proportional to the interface between Au and the TiO₂ support and relevant for the reaction⁵¹.

When comparing the two carbon-supported samples, Au/C und AuAg/C, the oxygen order remains constant on Au/C, while on AuAg it starts at a lower order, 0.18 at 150°C and then increases to approximately to the level of Au/C (0.30), 0.28. This is an entirely different behavior than what is observed for the rutile-based catalysts, where the AuAg also starts lower than its Au counterpart, but the oxygen reaction order is significantly higher at increased temperatures, 0.29, as opposed to 0.03 for the Au.

This confirms that the silver plays a very different role on the rutile-supported catalysts than on the carbon, which explains the different behavior. Of course, this has profound effect on the kinetics.

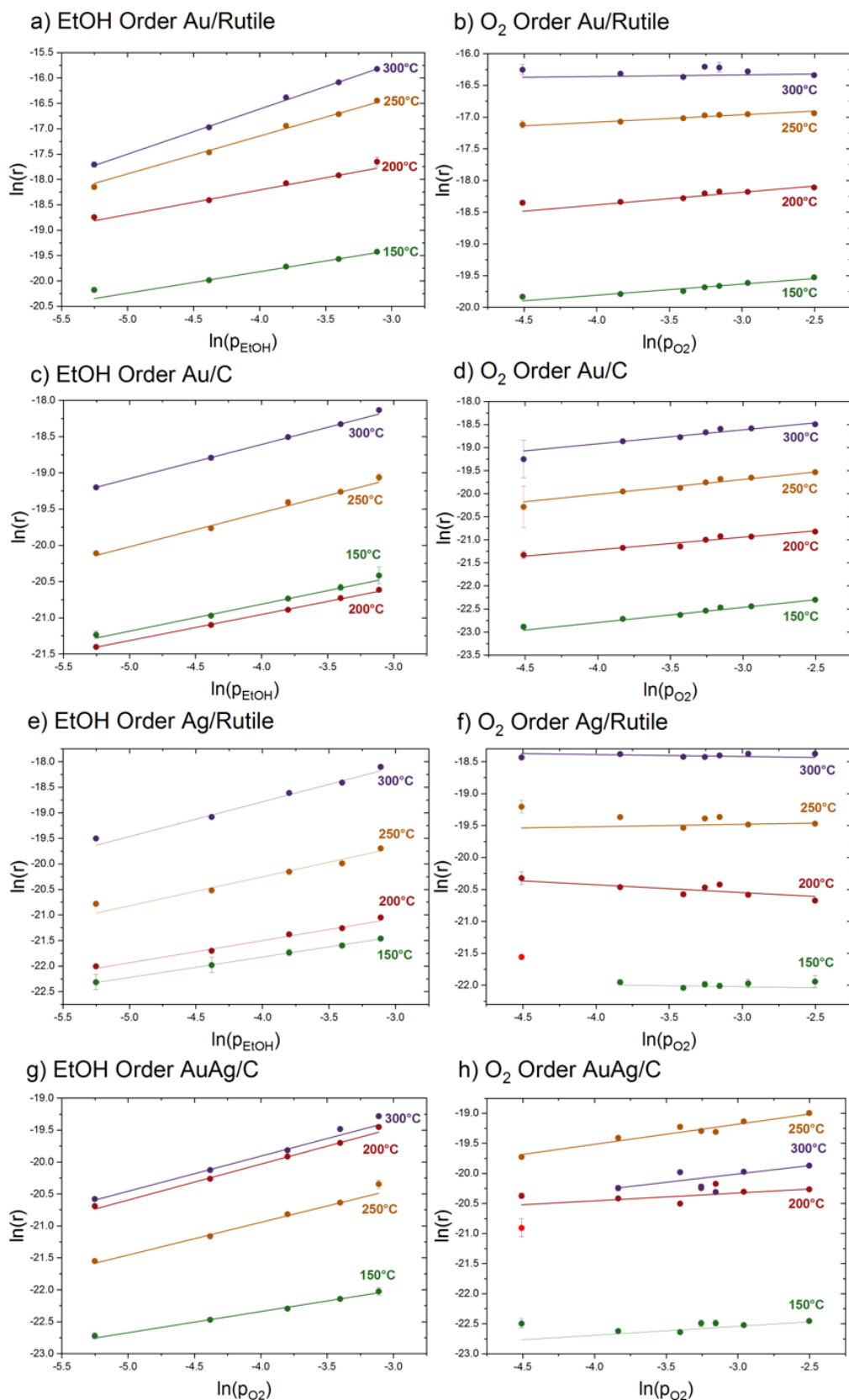


Figure 42. $\ln(r)$ vs. $\ln(p)$ plots used to calculate the reaction orders of EtOH (a) and O₂ (b) for Au/rutile, for AuAg/rutile (c,d), Ag/rutile (e,f) and AuAg/C (g,h), respectively. Outliers marked in red, in (f) and (h) were excluded from the calculations. The values of the respective reaction orders are listed in Table 18.

5.3. Operando Studies

5.3.1. DRIFTS

The existing *operando* DRIFTS measurements performed on the monometallic Au samples, section 3.3, is complemented by measurements on the bimetallic AuAg system. Steady-state measurements under *operando* conditions at 150°C and 250°C (EtOH/O₂ ratio = 1/1, 2 kPa = 1.1 mL/min, ~ 50 mL total flow), Figure 43, show that in principle the same bands are seen for AuAg/rutile, Au/rutile, but also Ag/rutile.

Again, Figure 43 a), the broad band at 3417 cm⁻¹ corresponds to the ν(OH) of adsorbed EtOH¹²⁴ which can be also adsorbed in multilayers¹²⁴ and can interact with remaining hydroxyl groups (3690, 3660 and 3629 cm⁻¹) of rutile^{125,126} (and form ethoxy species¹²⁶). This can be seen in the contour plot, Figure 51, where the whole measurement series is depicted. It is much more pronounced for rutile and Ag/rutile which have a higher BET surface area as in the synthesis no washing step was involved. The same holds true for the C-H bands at 2976 cm⁻¹, 2935 cm⁻¹ and 2873 cm⁻¹ which were assigned to ν_a(CH₃), ν_s(CH₃), ν_a(CH₂) and ν_s(CH₂)^{124-126,128-131} of ethanol, ethoxy and, possibly, also acetaldehyde¹²⁷.

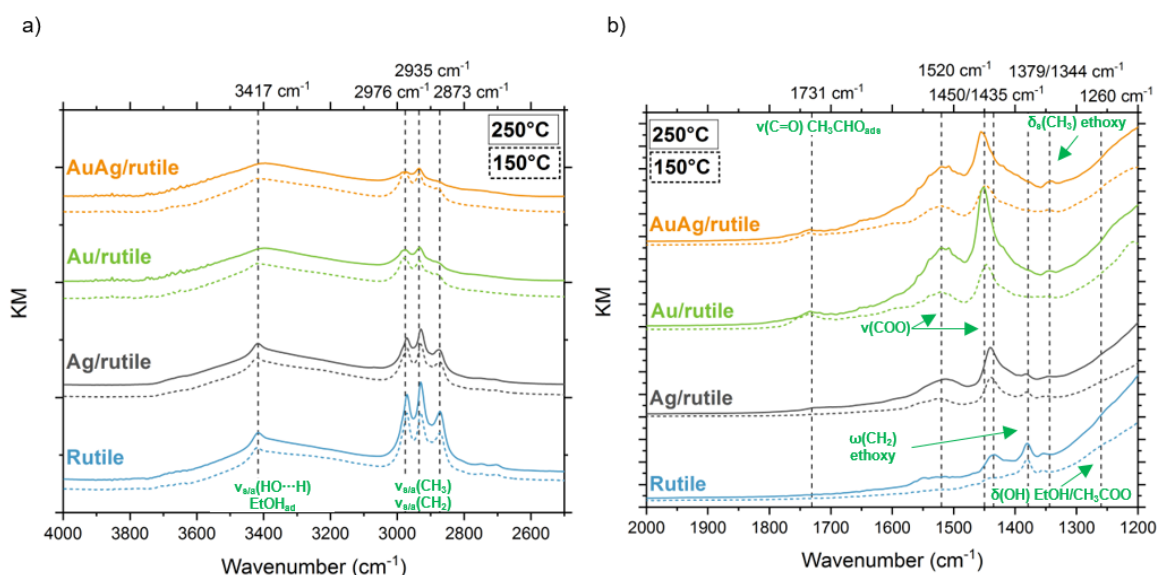


Figure 43. Comparison of DRIFTS spectra under *operando* conditions (EtOH/O₂ partial pressures 2 kPa = 1.1 mL/min, ~ 50 mL total flow) between (a) 4000-2500 cm⁻¹ and (b) 2500-1100 cm⁻¹. (a) shows the range of ν(OH) and ν(CH), which is dominated by ethanol and ethoxy species, whereas in (b) mainly COO and ethoxy species are visible.

The (partial) exchange of hydroxyl groups^{126,127} for ethoxy groups on the surface can be well understood looking at the difference spectra presented in Figure 44 a). Here, the last

spectrum after pretreatment and before flowing the reaction feed consisting of EtOH (and later O₂) was subtracted (for all difference spectra shown in this chapter, that spectrum was translated in the y-axis for optimum visibility). The 3678, 3657, 3722 cm⁻¹ bands are negative, and then depending on the conditions, the band at 3417 cm⁻¹, EtOH_{ad} varied with the reaction conditions. For rutile and Ag/rutile, we see a substantial amount adsorbed, whereas for Au/rutile and AuAg/rutile the much higher conversion leads to less EtOH adsorbed (and more acetaldehyde desorbed). The ν(CH) in the region between 4000 and 2500 cm⁻¹ is lower at 250°C than at 150°C, correlating with the conversion. This is not the case for the rutile reference.

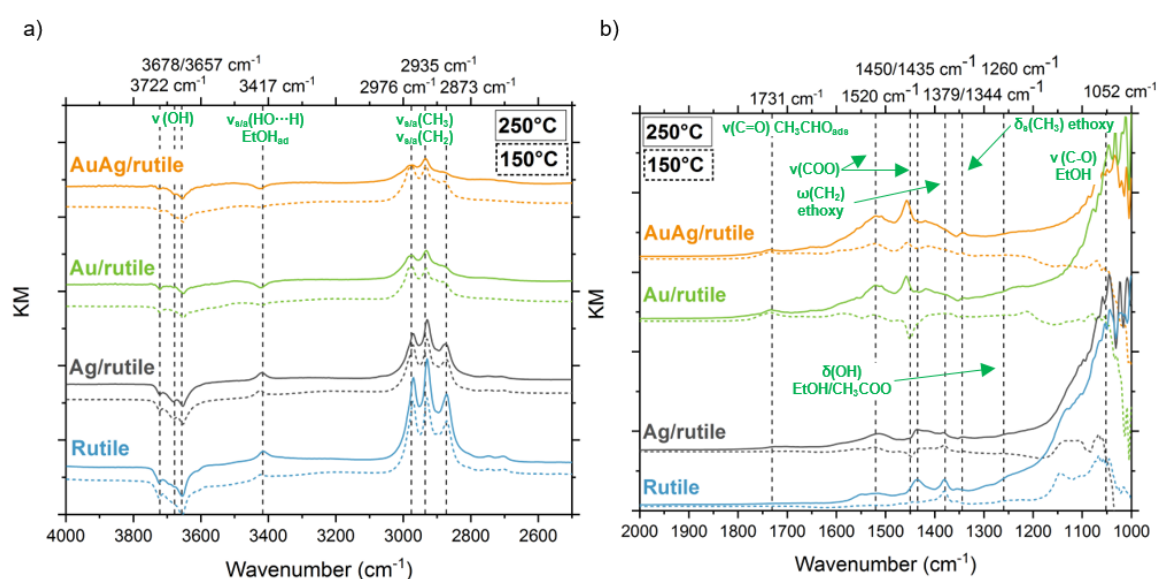


Figure 44. Comparison of DRIFTS difference-spectra under operando conditions (EtOH/O₂ partial pressures 2 kPa = 1.1 mL/min, ~ 50 mL total flow) between (a) 4000-2500 cm⁻¹ and (b) 2500-1100 cm⁻¹. The last spectrum after pretreatment/before EtOH introduction was subtracted. (a) shows the adsorbed EtOH as well as ν_{s/a} of CH₂ and CH₃ of EtOH/ethoxy and negative peaks due to the partial substitution of OH-species on the titania by adsorbed EtOH, whereas in (b) mainly COO and ethoxy species are observed. At 1052 cm⁻¹; the ν(C-O) of EtOH is visible at 250°C (at 150°C, the peak is negative). Due to the high and noisier background (lower transmittance of the CaF₂ window), however (see Figure 45) the signal/noise ratio in this region is considerably lower.

In the region of 1900-1200 cm⁻¹, Figure 44, the band at 1731 cm⁻¹ is assigned to the ν(CO) of adsorbed acetaldehyde¹²⁹ (and possibly also in the gas-phase¹²⁶). It is more prominent in AuAg/rutile and Au/rutile where conversion is significantly higher.

For the rutile, as discussed in chapter 3.3, the broad 1435 cm⁻¹ signal can be attributed to adsorbed acetate^{124,131} (1438 cm⁻¹ and 1443 cm⁻¹ in literature^{124,131}), ν_{ip}(C-O) of η²-acetaldehyde¹³⁰ or η²-acetyl¹³⁰ (1432 cm⁻¹ in literature) and δ_{as}(CH₃) of acetaldehyde/ethoxy^{126,127} (1444 cm⁻¹ in literature^{126,127}). The 1379 cm⁻¹ band is assigned

to $\delta_s(\text{CH}_3)$ of ethoxy species^{126,129} whereas 1344 cm^{-1} can be attributed to $\omega(\text{CH}_3)/\delta(\text{CH}_3)$ of ethoxy, acetyl and η -acetaldehyde¹³⁰ (1344 cm^{-1} is the maximum on Au/rutile as well as AuAg/rutile, on pure rutile the band is shifted to a slightly higher wavenumber of 1354 cm^{-1}) or adsorbed acetate¹²⁴ (1340 cm^{-1}). The situation between Au/rutile, as discussed in chapter 3.3, and AuAg/rutile is very similar: Entirely the same bands are visible for both samples, see Table 8 in section 3.3.

However, more information can be gained by taking the difference spectra, Figure 44 b), into account. At 1052 cm^{-1} the stretching vibration of C-O of adsorbed EtOH^{124,132} could be observed. Furthermore the species at 1520 cm^{-1} and 1450 cm^{-1} , both of which can be attributed to $\nu(\text{COO})$ ^{126,128,129,131}, are distinctly different at AuAg/rutile and Au/rutile at 150°C . For the latter, negative peaks are visible due to the disappearance of COO from organic residues from the synthesis, as discussed in chapter 3.3 and shown by Tan et al.¹²⁹. On AuAg/rutile, there is a clear positive peak, either because of the higher conversion on the sample, or because there was less COO from the synthesis remaining on the surface.

Interestingly, the Ag/rutile sample shows nearly identical bands. Due to the missing washing step and the low metal loading of 1 wt.% Ag, it resembles the rutile reference very much, however the COO region is much more pronounced. Also, the band at 1450 cm^{-1} is missing, suggesting different COO species on the Ag/rutile surface. The dynamic behavior, of the COO species, as discussed in section 3.3, can be also observed for all the other samples. Again, based on the results of the first principle kinetic modelling, a spectating role of the COO is assumed.

The different reaction conditions, (1) after pretreatment/before introduction of EtOH (pretreatment conditions: conditions (20% O_2 , heating from RT to 400°C with a holding time of 30 min), (2) EtOH, (3) EtOH/ O_2 , (4) O_2 are compared in Figure 46 as well as Figure 47 showing difference spectra (conditions (2) to (4) where measured under both 150°C and 250°C). Naturally, bands associated with ethanol or acetaldehyde are only appearing after switching to condition (2). Between (2) and (3) only minor differences can be observed, e.g. a higher peak at 1731 cm^{-1} , adsorbed acetaldehyde, in (3) due to higher conversion. Switching to oxygen, condition (4) decreases the amount of adsorbed species again, leading to a smaller COO peak (which, it seems, reacts slower to changes in the conversion) and (almost complete) removal of 2976 cm^{-1} , 2935 cm^{-1} and 2873 cm^{-1} which were assigned to $\nu_a(\text{CH}_3)$, $\nu_s(\text{CH}_3)$, $\nu_a(\text{CH}_2)$.

The evolution of the bands under reaction conditions over time are depicted in Figure 50 as waterfall plots (for the difference spectra) and in Figure 51 as contour plots for all spectra, including the pretreatment process. Changes in the intensity of the C-H bands as well as the COO bands can be seen in those plots. Also the exchange of hydroxyl groups on the support with adsorbed ethoxy species upon switching to reaction conditions is observable in the contour plots.

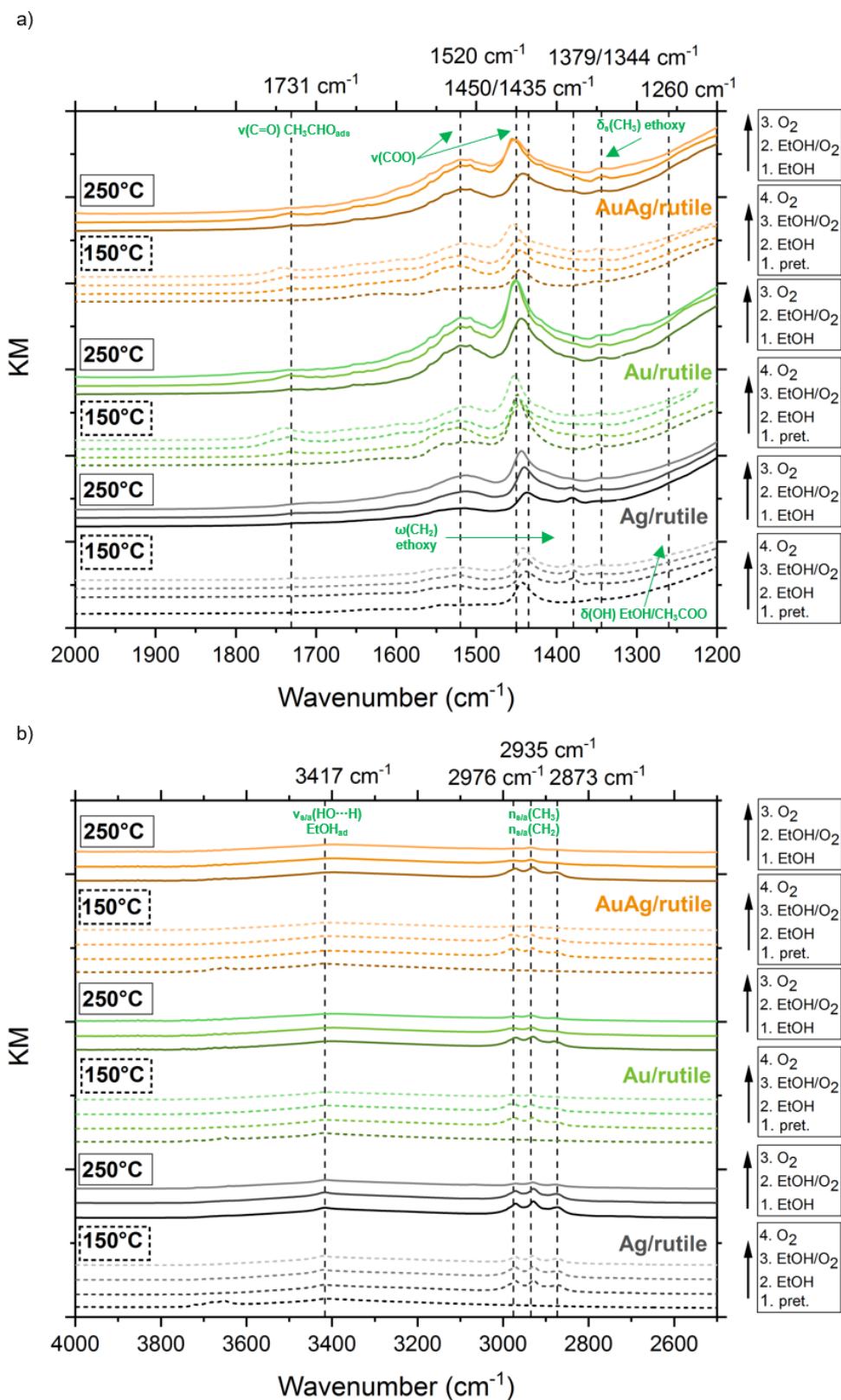


Figure 46. Overview of the DRIFTS spectra of AuAg/rutile, Au/rutile and Ag/rutile under different conditions. At 150°C: (1) after pretreatment/before introduction of EtOH, (2) EtOH, (3) EtOH/O₂, (4) O₂. At 250°C: (1) EtOH, (2) EtOH/O₂, (3) O₂, (4) O₂ and/or EtOH partial pressures were kept at 2 kPa = 1.1 mL/min at a total flow of approx. 50mL/min.

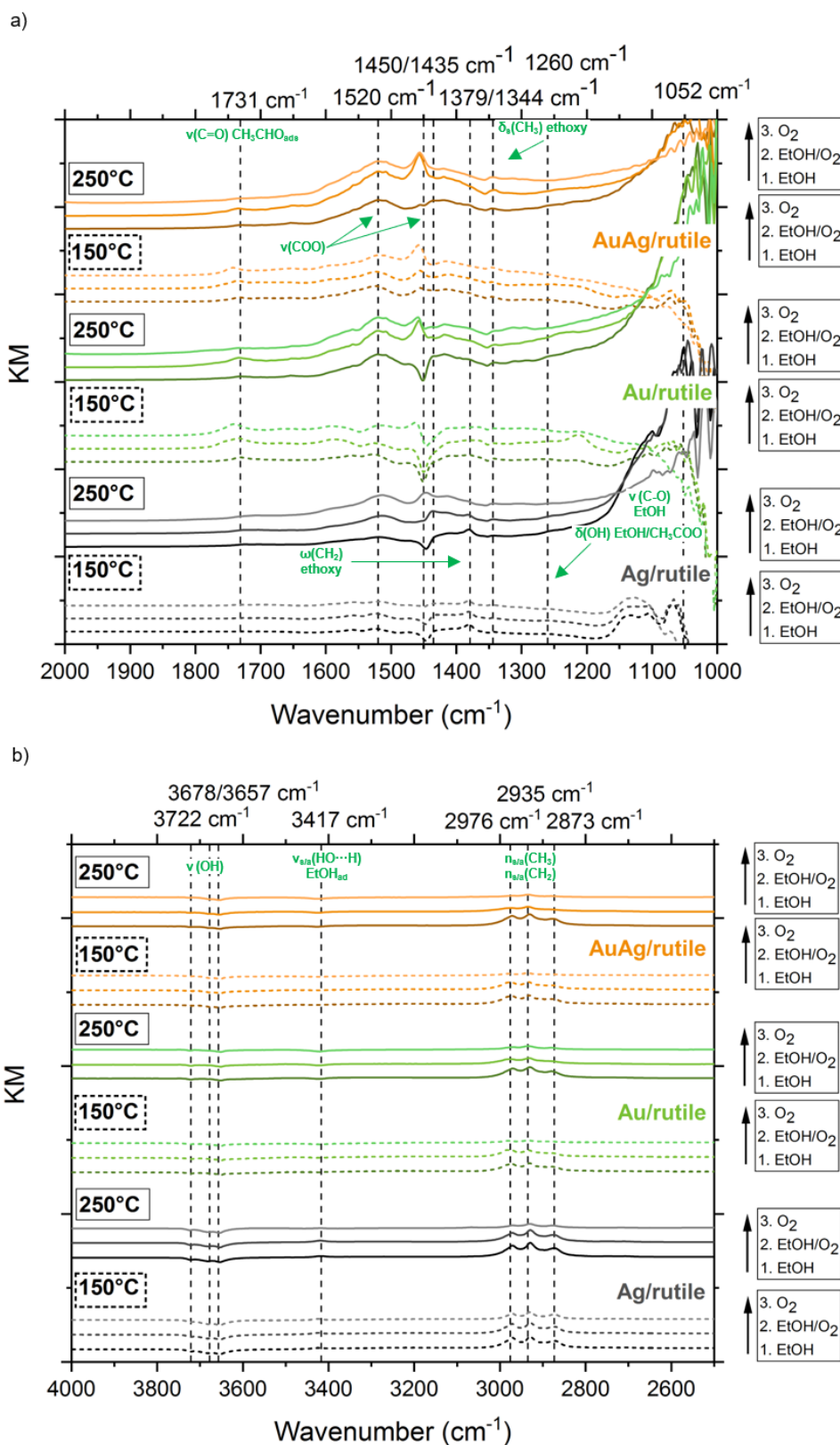


Figure 47. Overview of the DRIFTS difference-spectra of AuAg/rutile, Au/rutile and Ag/rutile under different conditions. At 150°C: (1) EtOH, (2) EtOH/O₂, (3) O₂. At 250°C: (1) EtOH, (2) EtOH/O₂, (3) O₂. O₂ and/or EtOH partial pressures were kept at 2 kPa = 1.1 mL/min at a total flow of approx. 50 mL/min. The last spectrum after pretreatment/before EtOH introduction was subtracted.

Reference measurements on rutile, Figure 48, show the same bands that were also observed for Au/rutile and AuAg/rutile. However, whereas the $\nu_{s/a}$ of CH_2 and CH_3 are very prominent due to low conversion of $< 4\%$ (partly also owing to the high surface area of $105 \text{ m}^2/\text{g}$ as opposed to approx. $40 \text{ m}^2/\text{g}$ for the metal-loaded catalysts), the COO bands as well as the $\nu(\text{C}=\text{O})$ band at 1731 cm^{-1} associated with CH_3CHO are considerably smaller. Thus, a larger proportion of the ethoxy species on the metal-containing catalysts is likely to be located on the support, however the increase of COO bands can be clearly attributed to the influence of the metal nanoparticles (adsorbates on metal, spillover from the metals to TiO_2 , re-adsorption of the products).

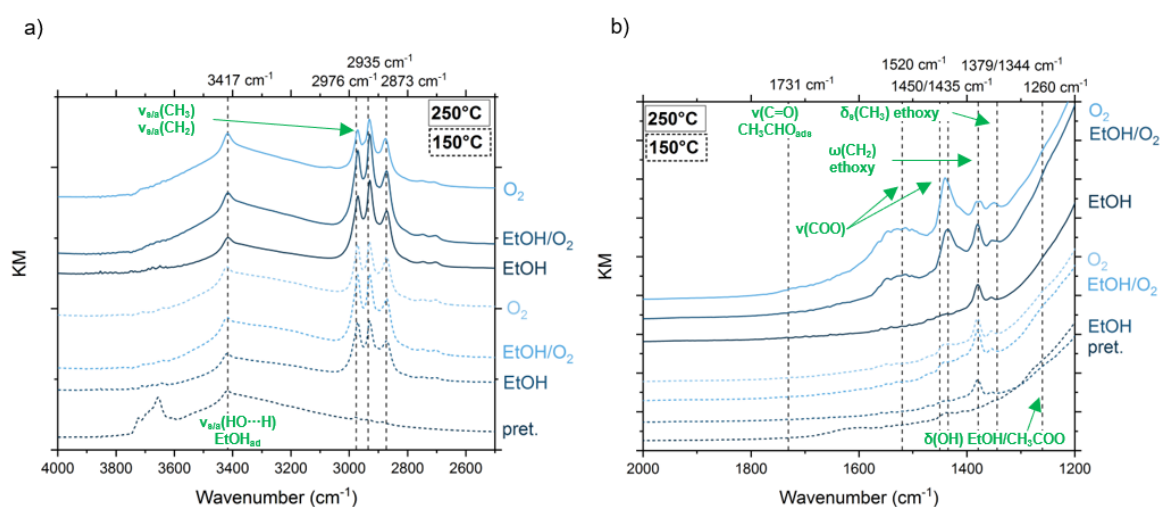


Figure 48. Overview of the DRIFTS spectra of rutile under different conditions. At 150°C : (1) after pretreatment/before introduction of EtOH. (2) EtOH, (3) EtOH/ O_2 . At 250°C : (1) EtOH, (2) EtOH/ O_2 . O_2 and/or EtOH partial pressures were kept at $2 \text{ kPa} = 1.1 \text{ mL/min}$ at a total flow of approx. 50 mL/min . All the features observed for Au/rutile, AuAg/rutile as well as Ag/rutile are also observed for the pure rutile. However, whereas the $\nu_{s/a}$ of CH_2 and CH_3 are very prominent due to low conversion of $< 4\%$ (partly also owing to the high surface area of $105 \text{ m}^2/\text{g}$ as opposed to approx. $40 \text{ m}^2/\text{g}$ for the metal-loaded catalysts), the COO bands as well as the $\nu(\text{C}=\text{O})$ band at 1731 cm^{-1} associated with CH_3CHO are considerably smaller. Thus, a larger proportion of the ethoxy species on the catalysts is likely to be located on the support, however the increase of COO bands can be clearly attributed to the metal nanoparticles.

For the Au/C and AuAg/C samples, Figure 49, owing to the low signal intensity (very dark carbon-based powder and very low metal loadings of 1 wt.% Au and, for the AuAg/C sample, 0.2 wt.% Ag) only ethoxy species, $\delta(\text{CH}_3)$ 1379 cm^{-1} , as well as the $\omega(\text{CH})$ bands at 2976 cm^{-1} , 2935 cm^{-1} and 2873 cm^{-1} are visible. Two small peaks at approx. 1257 and 1226 cm^{-1} are attributed to $\delta(\text{OH})$, possibly ethanol^{60,128,131,132} or acetaldehyde¹²⁷. For both samples, apart from the appearance of bands after introducing the reaction feed, no changes in time could be observed.

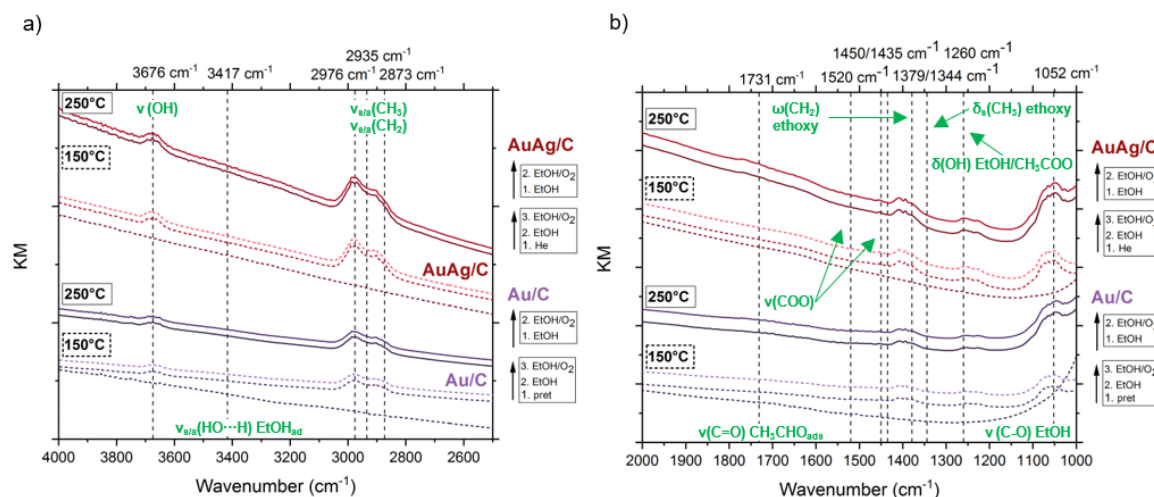


Figure 49. Overview of the DRIFTS spectra of Au/C and AuAg/C under different conditions. At 150°C: (1) after pretreatment/before introduction of EtOH. (2) EtOH, (3) EtOH/O₂. At 250°C: (1) EtOH, (2) EtOH/O₂. O₂ and/or EtOH partial pressures were kept at 2 kPa = 1.1 mL/min at a total flow of approx. 50 mL/min. Due to the low signal intensity (very dark carbon-based powder and very low metal loadings of 1 wt.% Au and, for the AuAg/C sample, 0.2 wt.% Ag) only ethoxy species are visible. The COO-bands are marked to highlight their absence for these measurements.

In conclusion, ethoxy species were observed on all catalysts. On the carbon-based samples, they originate mostly from the metal nanoparticles (as the TPD of the carbon shows no essential interaction with EtOH at these temperatures), while on the rutile-based samples, a large fraction of ethoxy species is present on the rutile surface.

In fact, essentially all features that are observed for Au/rutile and AuAg/rutile can also be observed on the rutile reference sample, those attributed to acetaldehyde in (considerably) lower intensity. There is a dynamic behavior of COO species, first originating from organic residues on the sample, later from acetate species on the catalysts surface. Though it correlates with the conversion, it is assumed to be a spectator.

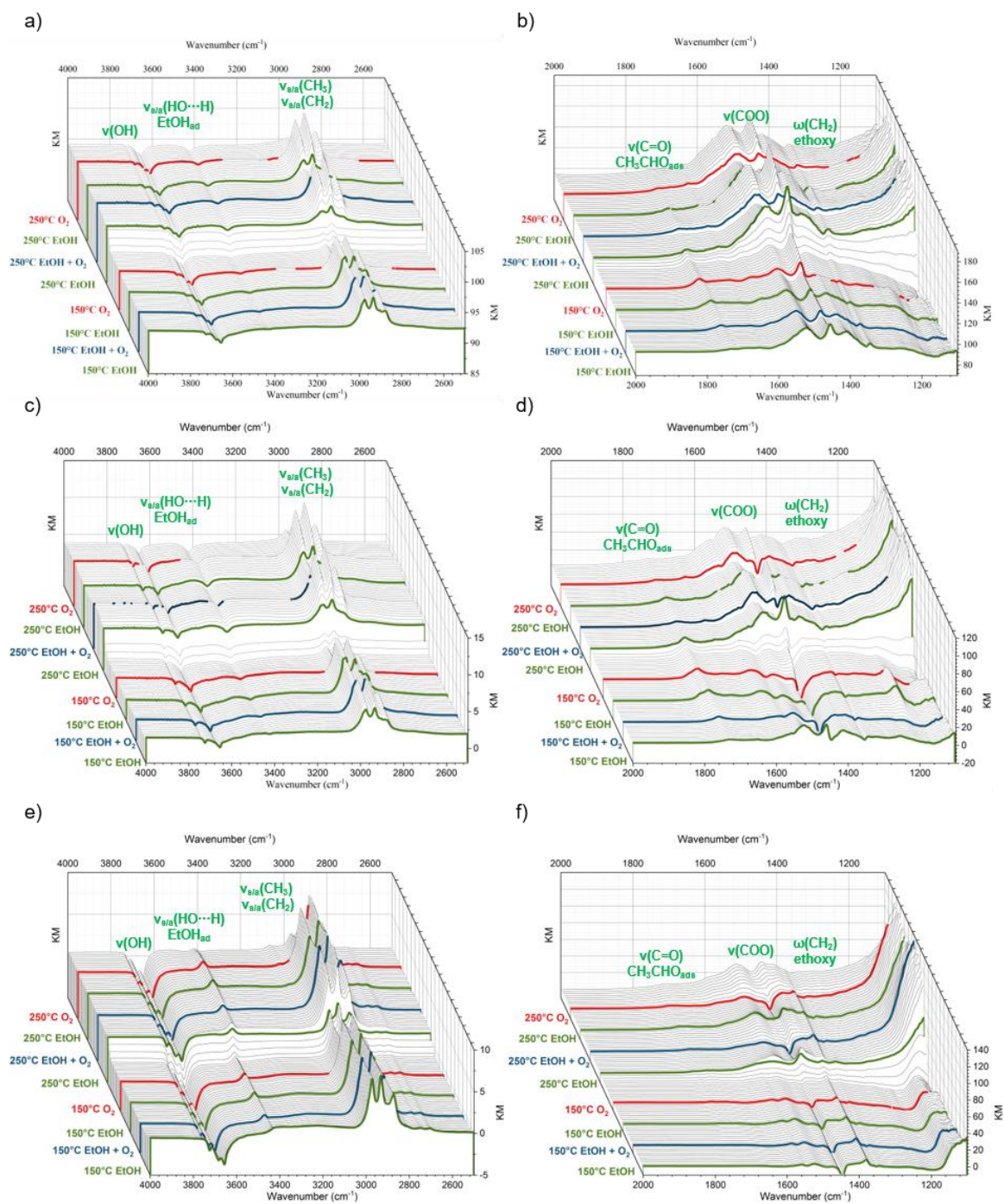


Figure 50. Waterfall plots for the time-resolved operando DRIFTS measurements, regions between 4000-2500 cm^{-1} and 2500-1100 cm^{-1} . Difference spectra, obtained by subtracting the spectrum after pretreatment (prior to the start of the reaction), are shown. (a,b) correspond to Au/rutile, (c,d) to AuAg/rutile and (e,f) to Ag/rutile. Measurements were undertaken under the conditions (I) EtOH, (II) EtOH + O₂, (III) EtOH, (IV) O₂ at a total flow of ~ 50 mL/min (O₂ and/or EtOH partial pressures: 2 kPa = 1.1 mL/min) at both 150°C and 250°C.

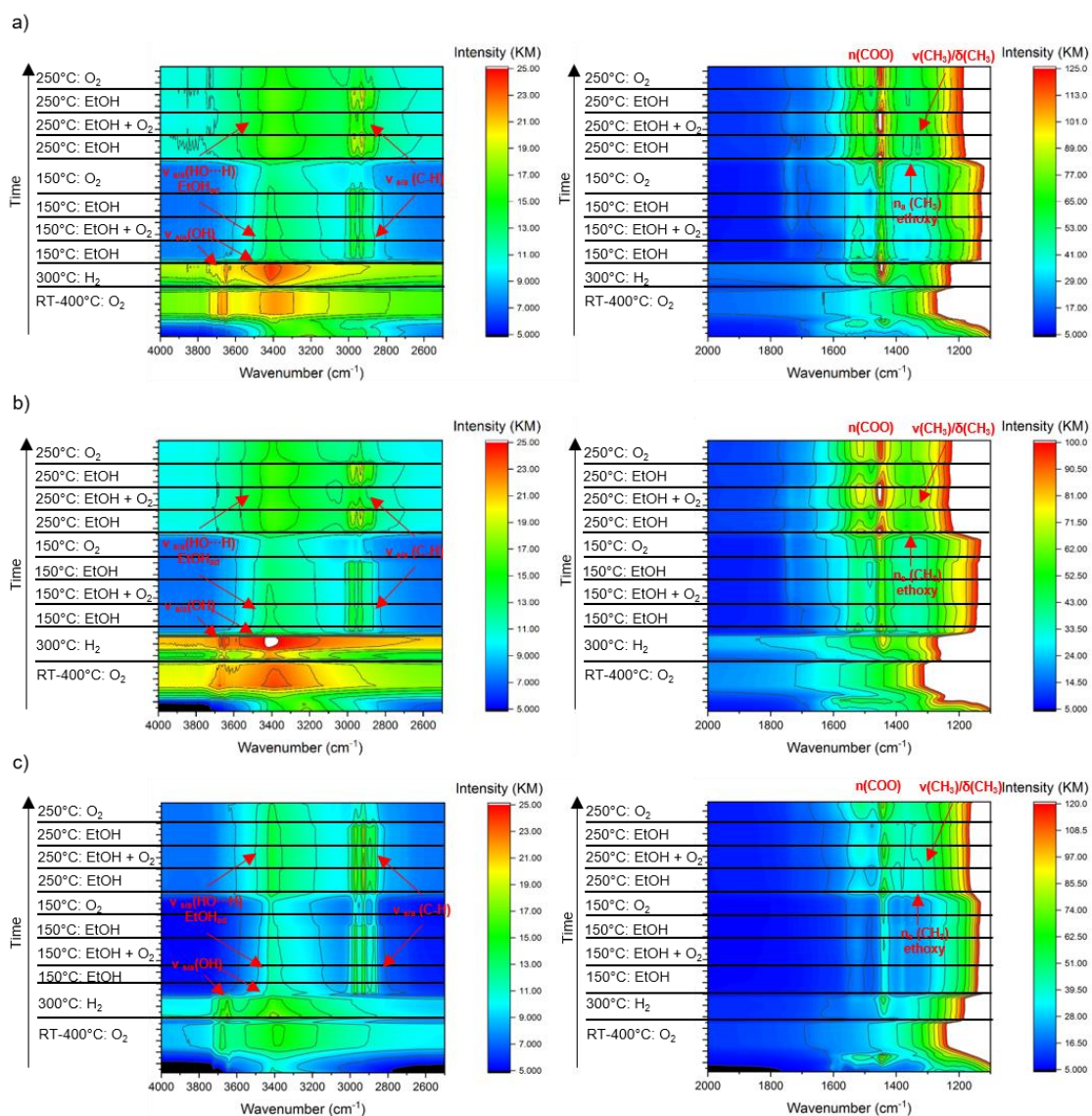


Figure 51. Contour plots for the time-resolved operando DRIFTS measurements, regions between 4000–2500 cm^{-1} and 2500–1100 cm^{-1} . The evolution of spectra, including the pretreatment (20% O_2 from RT to 400°C for 30 minutes, followed by 30 minutes of 5% H_2 at 300°C) under the conditions (I) EtOH, (II) EtOH + O_2 , (III) EtOH, (IV) O_2 at a total flow of ~ 50 mL/min (O_2 and/or EtOH partial pressures: 2 kPa = 1.1 mL/min) at both 150°C and 250°C.

5.3.2. NAP-XPS at ISS/BESSY II

The Au 4f region does not show a difference between Au/rutile and AuAg/rutile, Figure 52. The binding energy was found to be 84.4 eV for Au 4f_{7/2} and 88.1 eV for Au 4f_{5/2} (FWHM 1.0 eV for both). Whereas for other reactions, e.g. oxidation with ozone¹⁵⁷ or CO oxidation¹⁵⁸, oxidized Au/Au^{δ+} or atomically dispersed Au^{159,160} was reported, no such species were found in this experiment. While for Au/rutile, involvement of Au^{δ+} would have been indication for an oxygen activation mechanism, in the bimetallic system the oxidation of Ag may be expected. For Au/rutile this finding, however, is in alignment with

the computational results from De Vrieze et al., described in section 3.5, that suggest that metallic gold is able to activate oxygen.

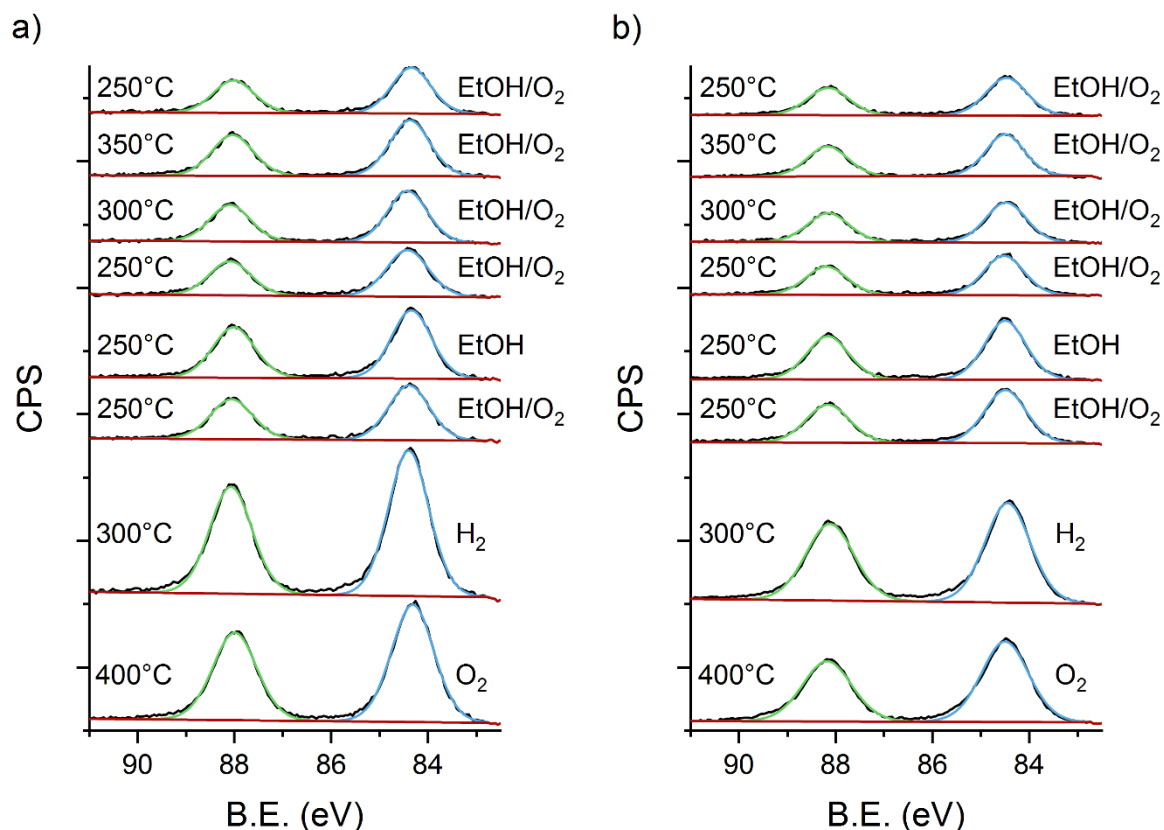


Figure 52. Au 4f detail scans for various conditions, pretreatment under oxidative and reductive conditions as well as reaction with EtOH/O₂ = 1/1 (at different reaction temperatures: 250-350°C) and EtOH only (at 250°C), (a) Au/rutile sample and (b) AuAg/rutile sample. For either sample, no Au^{δ+} could be detected. The spectra were taken at an E_{kin} of 310 eV at a total pressure of 0.5 mbar (except under H₂ atmosphere, where only 0.33 mbar could be reached).

The Ag 3d detail scans and MNN Auger peaks are shown in Figure 53. The Ag 3d_{5/2} maximum was found at a binding energy of 368.3 eV with a FWHM of 0.8 eV and the Ag 3d_{3/2} was at 305.7 eV with a FWHM of 0.8 eV, respectively (under EtOH/O₂ atmosphere, the first condition where signal intensity was high enough to also measure the MNN Auger peaks). The Auger peaks were not integrated due to the low intensity with maxima at a kinetic energy of 351.7 and 359.7 eV.

Due to the low signal intensity, it was not possible to reliably determine an oxidation state for Ag (during pretreatment, the count rate even was too low to obtain the Auger peaks). The reason for this low intensity was the counterintuitive *depletion* of Ag (in contrast to an expected surface oxidation/segregation of Ag), as proven by measurement with two different kinetic energies, 310 eV and 700 eV, Figure 54. The respective values of the

Au/Ag atomic ratios at these two different kinetic energies are listed in Table 19. For Ag/rutile, the same observation, migration of Ag away from the surface, was observed (nominal values: 2.7 for Au/Ag and 0.37 for Ag/Au). However, as there was no Ag detectable anymore after pretreatment, the measurement was stopped (data not shown in this thesis). This Ag depletion phenomenon is discussed in detail in section 5.3.1, as it was investigated in detail at the ALBA CIRCE beamline with more than just two different information depths. Also, it was possible to measure Ag/rutile under *operando* conditions.

Table 19 Atomic ratios, Au/Ag and Ag/Au, during pretreatment and reaction. The nominal value are nominal value: for 2.7 for Au/Ag and 0.37 for Ag/Au.

	E_{kin} (eV)	Au/Ag	Ag/Au
Pretreatment - O₂ (400°C)	310	10.8	0.09
Pretreatment - O₂ (400°C)	700	6.9	0.14
Pretreatment - H₂ (400°C)	310	36.3	0.03
Pretreatment - H₂ (400°C)	700	10.8	0.09
EtOH/O₂ = 1/1 (250°C)	310	30.0	0.03
EtOH/O₂ = 1/1 (250°C)	700	9.0	0.11
EtOH (250°C)	310	18.6	0.05
EtOH (250°C)	700	7.5	0.13
EtOH/O₂ = 1/1 (350°C)	310	18.4	0.05
EtOH/O₂ = 1/1 (350°C)	700	9.1	0.11
EtOH/O₂ = 1/1 250C (2)	310	12.6	0.08
EtOH/O₂ = 1/1 250C (2)	700	6.6	0.15

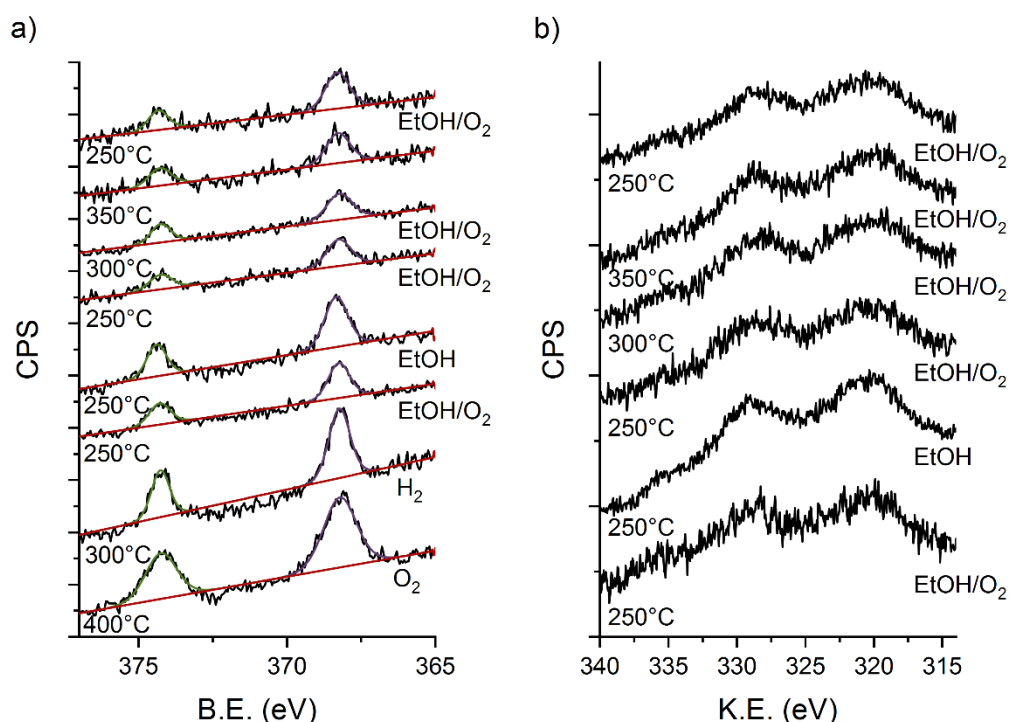


Figure 53. (a) Ag 3d detail scans for the AuAg/rutile sample under different conditions, pretreatment under oxidative and reductive pretreatment conditions as well as reaction with EtOH/O₂ = 1/1 (at different reaction temperatures: 250-350°C) and EtOH only (at 250°C). (b) depicts the respective Ag MNN Auger peaks (during pretreatment, signal intensity was too low to obtain detail scans). The spectra were taken at an E_{kin} of 310 eV.

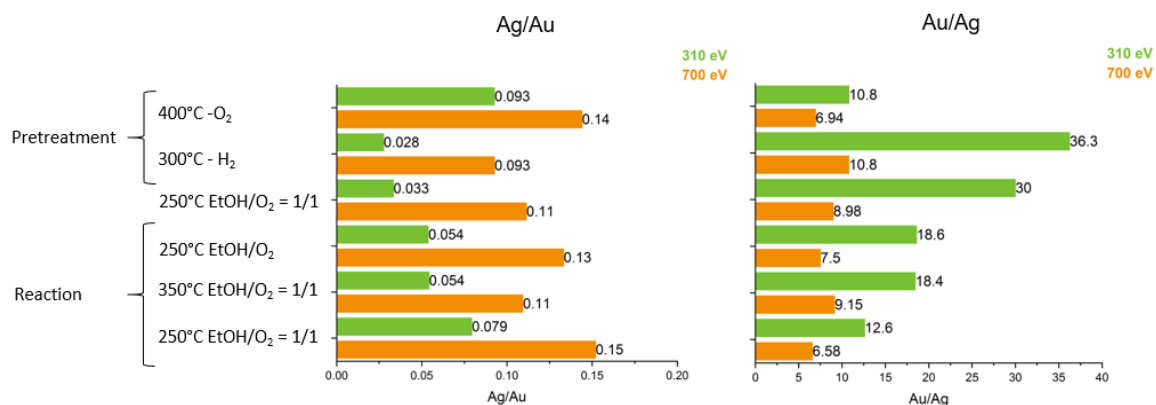


Figure 54. Depth profiling obtained by taking the Au 4f/Ag 3d peak areas and the cross-sections as published in¹²³ for the respective energies ($E_{kin} = 310/700$ eV) into account. In contrast to an expected segregation of Ag on the surface, the contrary, migration of Ag from the surface is taking place.

The Ti 2p detail scans, on the other hand, show a shift of the Ti 2p_{3/2}, Figure 55 (the dashed line marks the peak maximum under the reducing conditions of the pretreatment). At reducing conditions, the Ti 2p_{1/2} is located at a binding energy of 464.8 eV (FWHM: 2.2 eV) and the Ti 2p_{3/2} at 459.1 eV (FWHM: 1.4 eV) whereas under EtOH atmosphere (the

most extreme shift) the peaks are shifted by 0.4 eV to higher binding energies (Ti 2p_{1/2} 465.2 eV with FWHM of 2.2 eV, Ti 2p_{3/2} 459.5 eV with a FWHM 1.3 eV).

This behavior is observed for both samples, AuAg/rutile and Au/rutile. Such an effect has been shown in literature^{161,162} as a shift in the fermi level under hydrogen atmosphere, and it can also be observed under EtOH atmosphere, which significantly changes the conditions for the rutile surface. However, proof of Ti³⁺ species was inconclusive, only for the Au/Ag was a small shoulder in the Ti 2p_{3/2} peak under EtOH-only conditions observed (marked with a star in Figure 55).

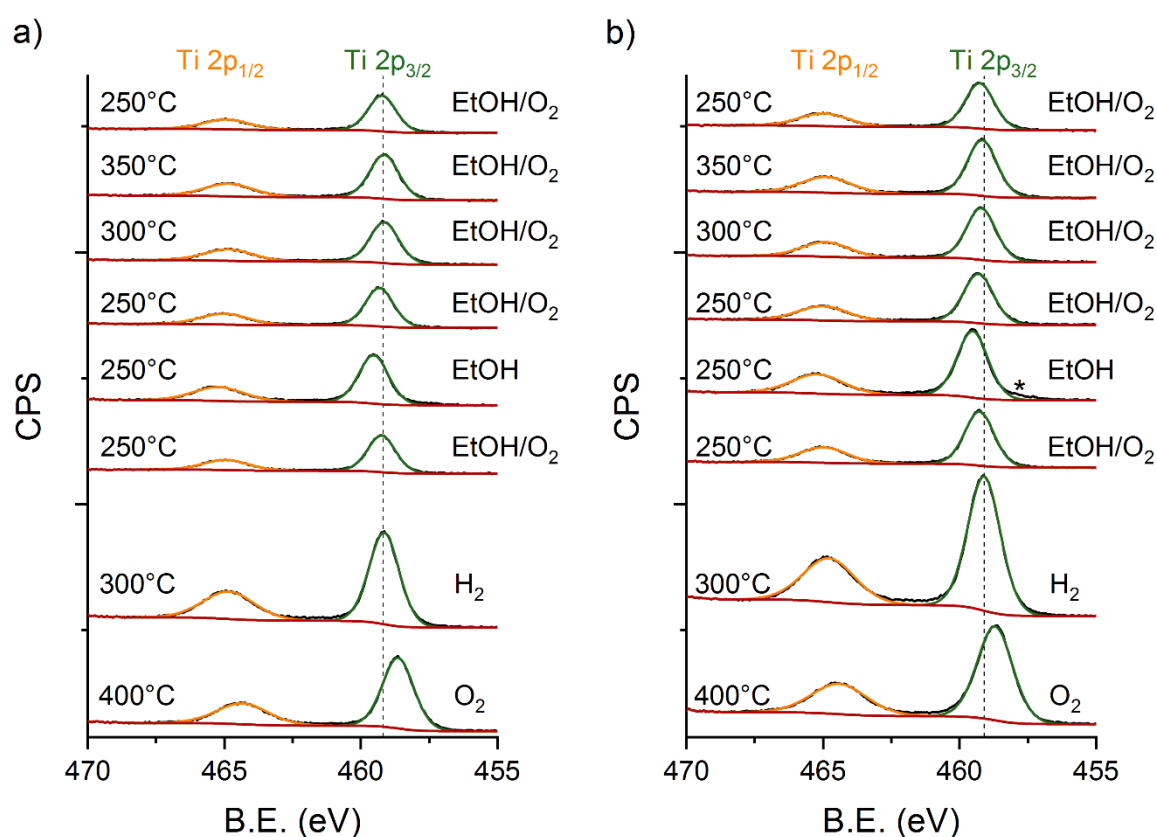


Figure 55. Ti 2p details scans of Au/rutile (a) and AuAg/rutile (b). The dashed line marks the peak maximum of the Ti 2p_{1/2} to mark the shifts that take place after switching from oxygen to hydrogen in the pretreatment. Also, under EtOH atmosphere, without oxygen, a further shift towards a higher binding energy is observed. Proof of Ti³⁺ species was inconclusive, only for the Au/Ag was a small shoulder in the Ti 2p_{3/2} peak under EtOH-only conditions observed (marked with a star). The spectra were taken at an E_{kin} of 310 eV.

This shift in the fermi level can also be observed for the O 1s spectra as shown in Figure 56. The insufficient fit results from a second peak located at the left shoulder of the O 1s peak corresponding to surface oxygen species such as OH-groups, ethoxy, H₂O, ethanol, acetate, etc. In this section, the focus was on the peak shift of the O 1s, whereas the respective species were fitted for the data in section 5.3.3 (ALBA). Like for Ti 2p, also here

a shift in binding energy from 530.5 eV (FWHM: 1.7 eV) under reductive conditions to 531.1 eV (FWHM: 1.8 eV), + 0.6 eV was observed.

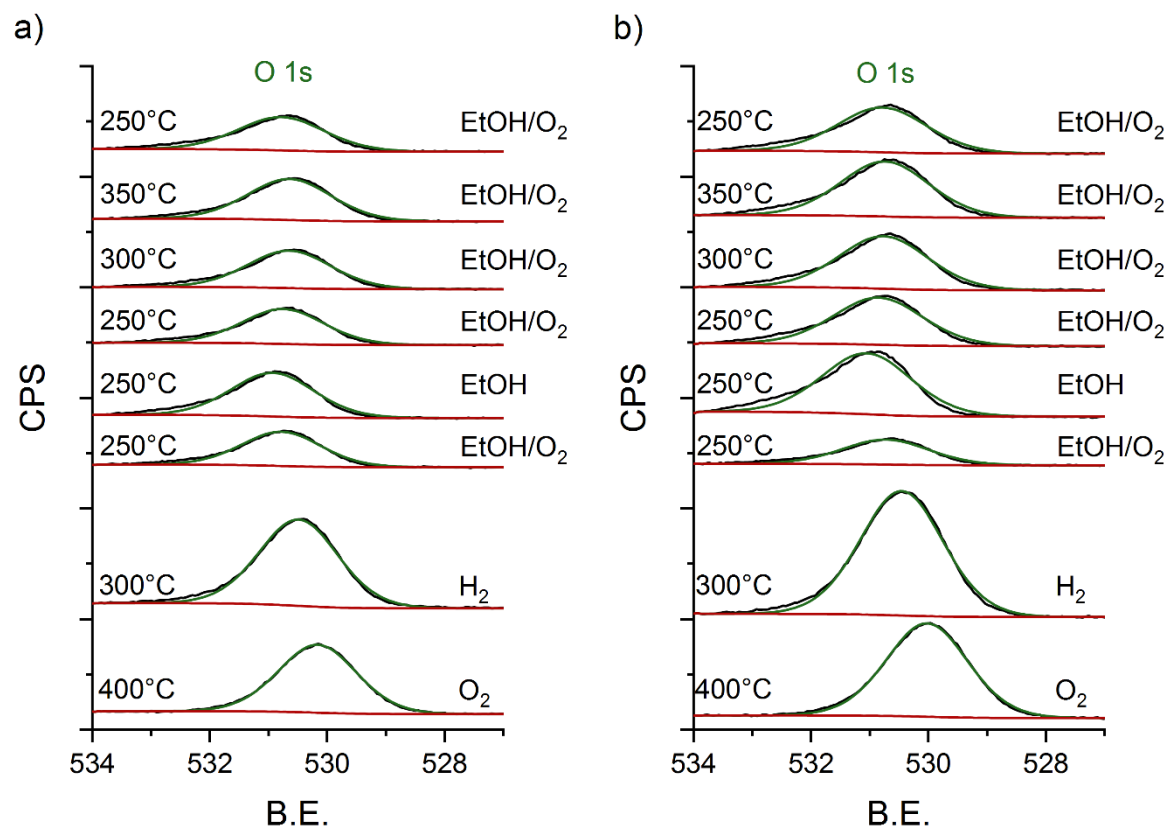


Figure 56. O1s spectra for (a) Au/rutile and (b) AuAg/rutile, under different conditions, pretreatment under oxidative and reductive pretreatment conditions as well as reaction with EtOH/O₂ =1/1 (at different reaction temperatures: 250-350°C) and EtOH only (at 250°C). Spectra were taken at a kinetic energy of 310 eV.

MS data is shown in the annex, section 9.7.1, illustrating quantitatively the behavior observed within the plug-flow reactor of the kinetic setup of the lab: Conversion increases with the introduction of oxygen and is significantly decreased under dehydrogenation conditions with EtOH only as feed. This low conversion accounts for the high dead volume within the XPS cell, the low pressure of 0.5 mbar and a pellet that does not favor gas-flow as a powder catalyst bed in the kinetic setup in the lab does.

The respective C1s spectra are depicted in the annex, section 9.7.1. As the measured pellets were prepared by dilution with graphite, no further evaluation of the C1s took place. Further results of this beamtime are printed in chapter 6, where the influence of water on the reaction is discussed.

5.3.3. NAP-XPS at CIRCE/ALBA

Near ambient-pressure XPS, NAP-XPS, was performed for AuAg/rutile as well as Ag/rutile as the corresponding reference sample. Prior to pretreatment, at room temperature and under UHV, conditions, due to charging no usable spectra could be obtained. However, starting with the pretreatment, under oxidative conditions (5 mL/min O₂ at a pressure of 0.5 mbar) and heating, conductivity significantly improved.

Detail spectra of the respective elements from the AuAg/rutile sample at an E_{kin} of 310 eV are depicted under different conditions, Ag 3d (Figure 57), Ag MNN Auger (Figure 58), Au 4f (Figure 59). Under EtOH atmosphere (where the Ag 3d peaks are highest), Ag 3d_{5/2} peak is found at a binding energy of 312.0 eV (FWHM: 0.7 eV) whereas the Ag 3d_{3/2} is located at 306.0 eV (FWHM: 0.6 eV). The Auger peaks are located at kinetic energies of 345.1, 354.4 and 362.4 eV.

Corresponding spectra for the Ag/rutile reference sample are listed in the annex, section 9.7.2.

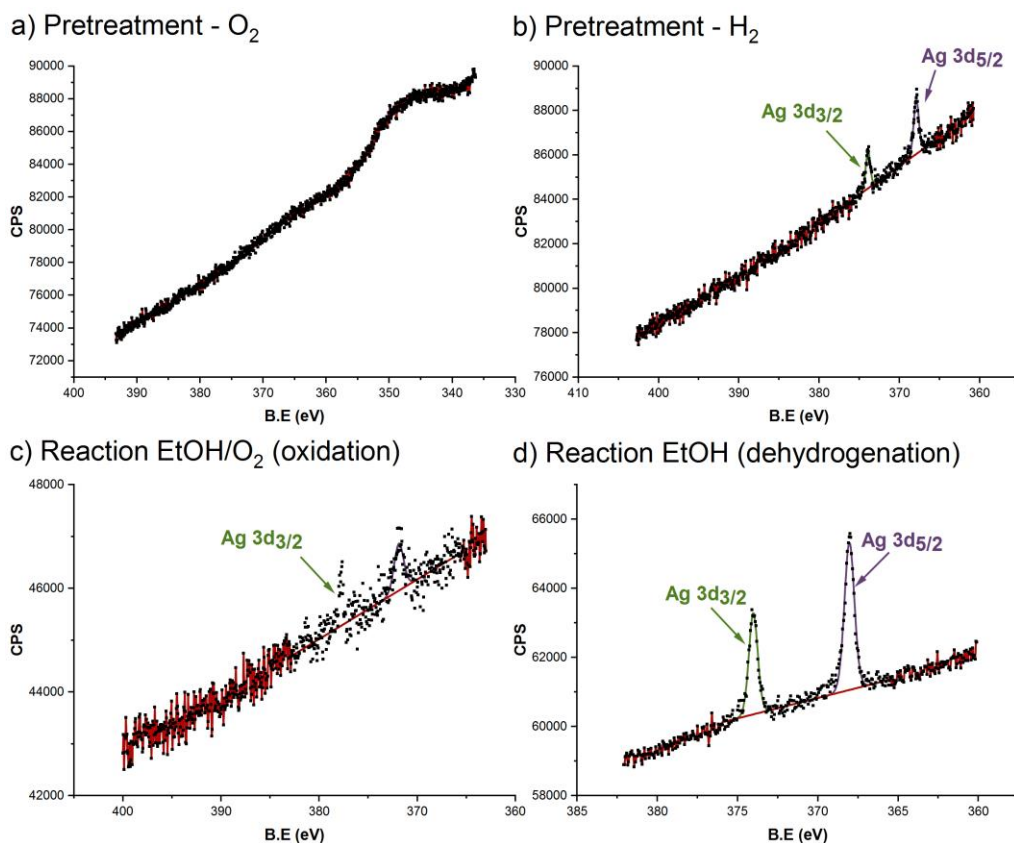


Figure 57. Ag 3d detail scans for the AuAg/rutile sample obtained under different conditions, (a) pretreatment under O_2 ($400^\circ C$), (b) pretreatment under H_2 ($300^\circ C$), (c) oxidation with a ratio of $EtOH/O_2 = 1/1$ ($250^\circ C$), (d) dehydrogenation conditions, $EtOH$ only ($250^\circ C$). During the pretreatment, under oxidative conditions, there is charging. After the pretreatment, however, depletion of Ag from the surface is observed (c, d), to a higher degree under oxidative conditions and to a lower degree during dehydrogenation. The respective Ag Auger peaks for (b-d) are depicted in Figure 58.

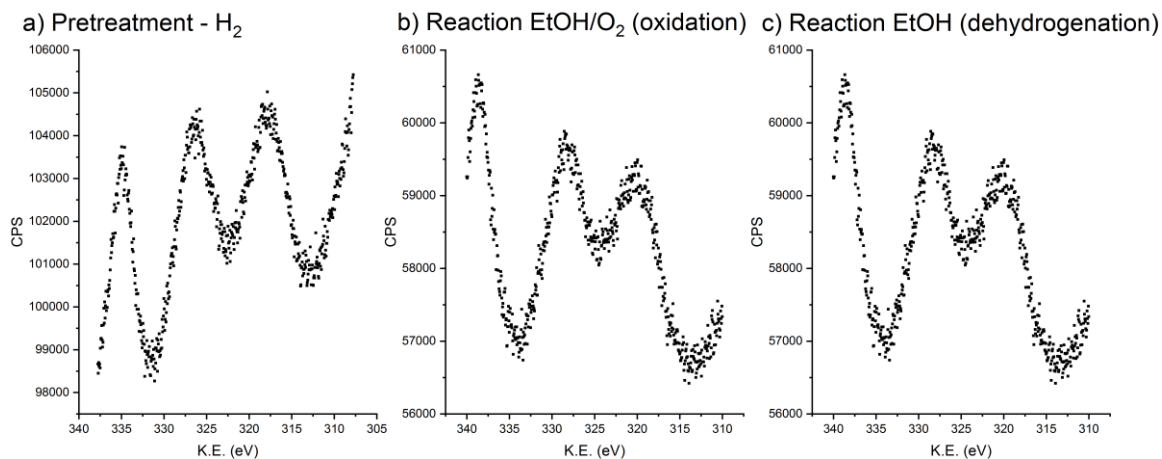


Figure 58. Ag MNN Auger signals for the AuAg/rutile sample obtained under (a) pretreatment under H_2 ($300^\circ C$), (b) oxidation with a ratio of $EtOH/O_2 = 1/1$ ($250^\circ C$), (c) dehydrogenation conditions, $EtOH$ only ($250^\circ C$).

In this beamtime, again no $\text{Au}^{\delta+}$ species could be detected, see Figure 59. The Au 4f_{5/2} is situated at a binding energy of 311.1 eV (FWHM: 0.8 eV), and the Au 4f_{7/2} at 307.4 eV (FWHM: 0.8 eV), respectively.

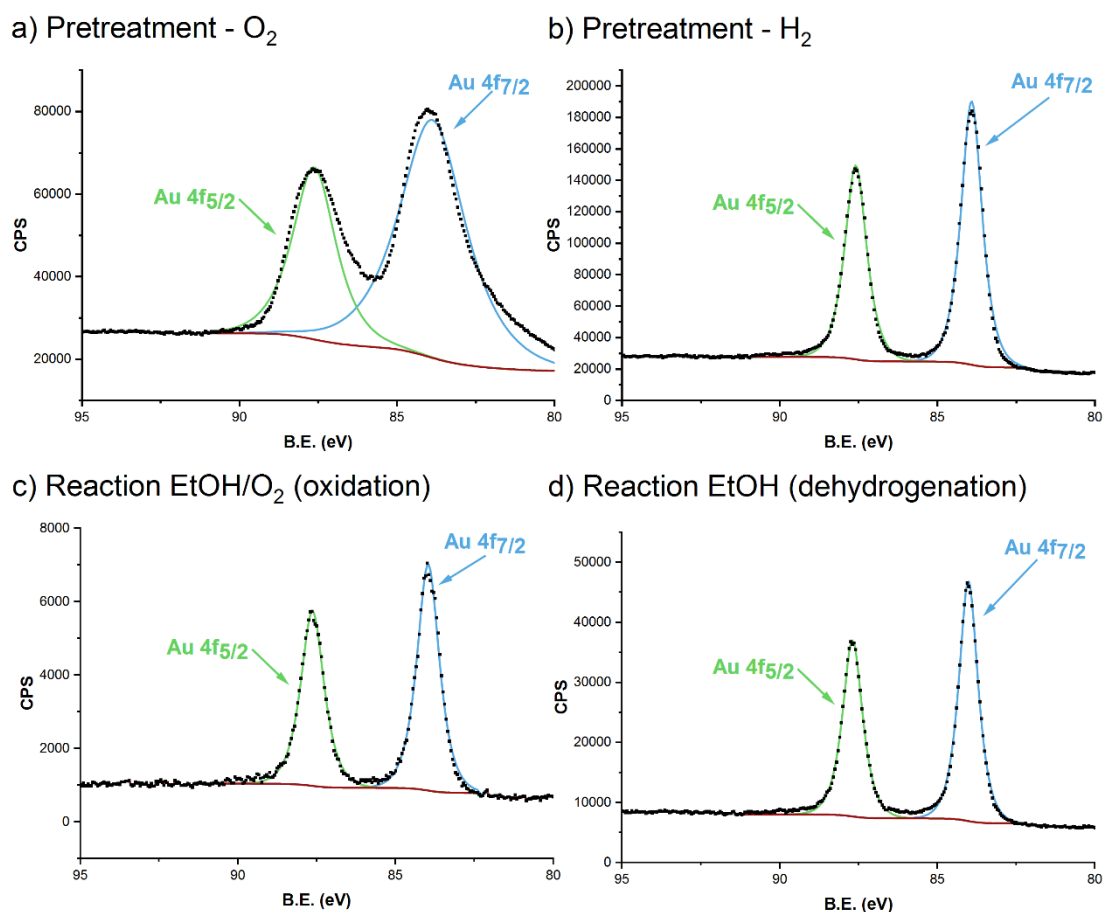


Figure 59. Au 4f detail scans obtained under different conditions, (a) pretreatment under O₂ (400°C), (b) pretreatment under H₂ (300°C), (c) oxidation with a ratio of EtOH/O₂ = 1/1 (250°C), (d) dehydrogenation conditions, EtOH only (250°C). During the pretreatment, under oxidative conditions, charging is observed. No $\text{Au}^{\delta+}$ could be detected.

Due to higher conversion under oxidative dehydrogenation conditions (with O₂ present), the C 1s detail scans, Figure 61, show a clear difference between oxidation conditions (EtOH/O₂ = 1/1) and dehydrogenation conditions (EtOH only). Taking into account the results from the DRIFTS measurements, C-O species can be attributed to ethoxy/ethanol, whereas O=C=O is likely to be originating from acetate species. As no graphite was used for the pellet, no C 1s signal is to be found prior to ethanol introduction. The identified peaks correspond to a binding energy of 305.8, 307.4, 308.8 and 309.7 eV.

However, taking into account the MS data, a relatively low conversion must be assumed: The signal of acetaldehyde ($m/z = 29$, calculated taking the fragmentation of EtOH, which

also shares the fragment into account) is very low, noisy and there's no noticeable difference between AuAg/rutile, Figure 60 a), and Ag/rutile, Figure 60 b). However, qualitatively, higher ethanol conversion can be observed with O₂ present than without (oxidation vs. dehydrogenation conditions). This low conversion accounts for the high dead volume within the XPS cell (approx. 40 L), the low pressure of 0.5 mbar and a pellet that does not favor gas-flow as a powder catalyst bed in the kinetic setup in the lab does.

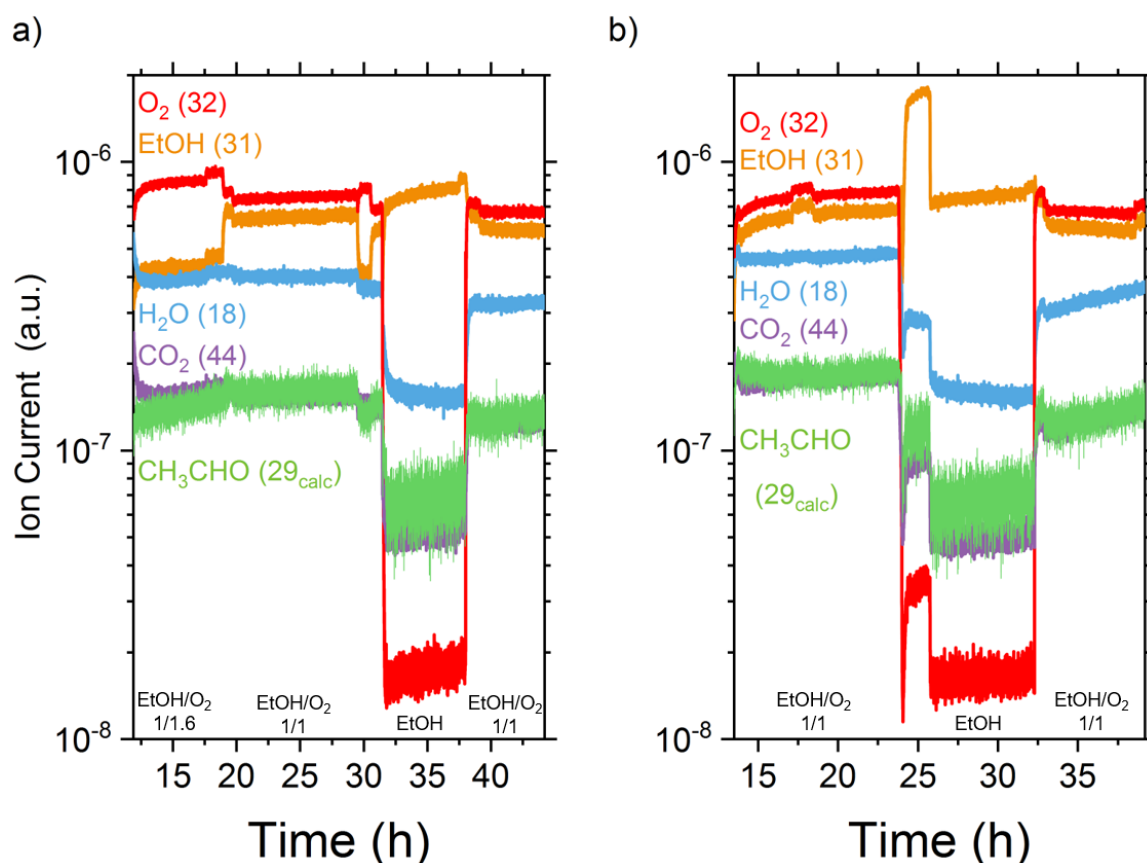


Figure 60. MS data for (a) AuAg/rutile and (b) Ag/rutile. As $m/z = 29$ is not only the most intense peak for acetaldehyde, but also typical for EtOH, the signal of acetaldehyde was calculated using the known fragmentation as published by NIST. For both samples, the signal of acetaldehyde was low and noisy, indicating very low conversion. As the m/z of 44 is also present in acetaldehyde, CO₂ formation is unlikely.

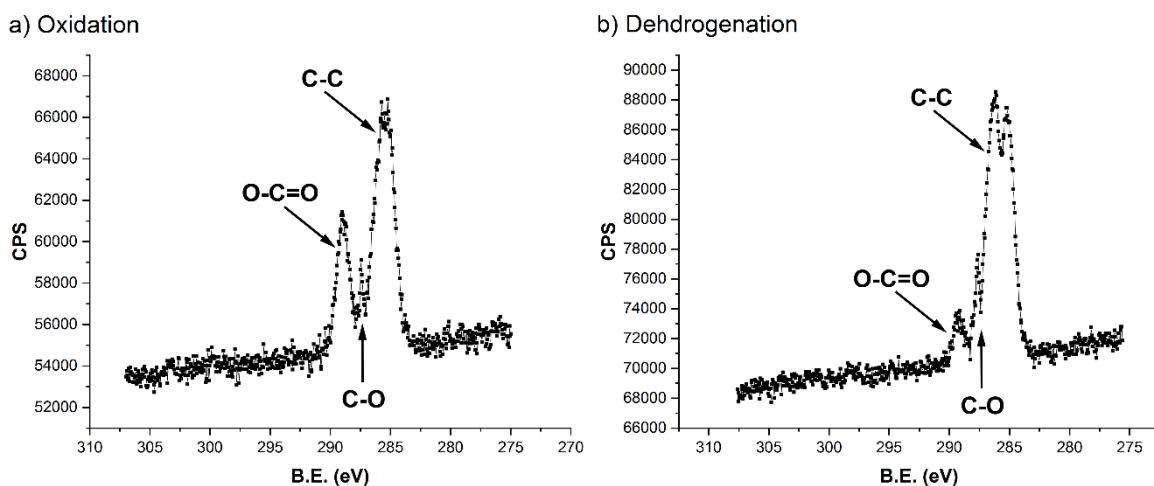


Figure 61. *C1s* detail scans of AuAg/rutile under different conditions, (a) oxidation ($\text{EtOH}/\text{O}_2 = 1/1$) and (b) dehydrogenation (EtOH only). Clearly, due to higher conversion under oxidation conditions, the O-C=O peak is larger than at dehydrogenation conditions. Spectra were taken at 250°C . The identified peaks correspond to a binding energy of 305.8, 307.4, 308.8 and 309.7 eV.

For the Ti 2p detail scans (B.E. of Ti^{4+} 311.2 eV and 312.6 eV for Ti^{3+} with a FWHM of 1.0 eV for both), on the other hand, the Ti^{3+} is less pronounced at oxidation conditions (3.67 %), Figure 62 a), than at dehydrogenation conditions (5.36 %), Figure 62 b). While a more reduced titania surface is not surprising, the it cannot yet Ti^{3+} be seen as proof for a Mars-van-Krevelen mechanism. However, kinetic measurements that show a trend towards (slightly) lower O_2 reaction order for the rutile supported catalysts (as opposed to the carbon-supported ones), a role of the support in the oxygen activation can be assumed.

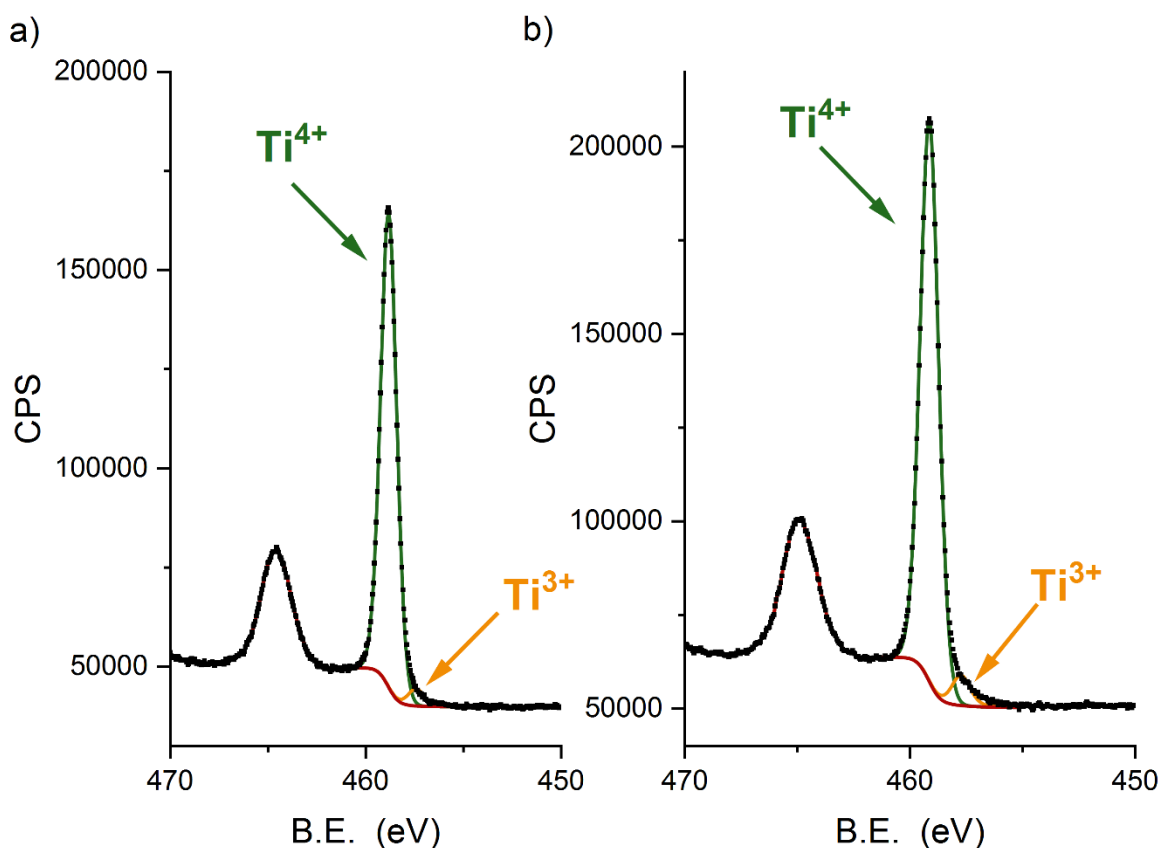


Figure 62. Ti 2p detail scans of the AuAg/rutile catalyst at (a) oxidation conditions ($\text{EtOH}/\text{O}_2 = 1/1$) and (b) dehydrogenation conditions (EtOH only). The fraction of Ti^{3+} is 3.67 % for (a) and 5.36 % for (b). Spectra taken at 250°C .

The corresponding O 1s spectra are depicted in Figure 63. Whereas during the oxidation step of the pretreatment, charging is still predominant, the oxidation peak is significantly higher during reaction conditions. Under reducing conditions the binding energy of the O 1s main peak is 309.7 eV (FWHM: 1.2 eV) and the O_{surf} peak, corresponding to oxygen surface species, OH, H_2O , ethoxy, acetate, etc., is located at 308.1 eV (FWHM: 1.2 eV). The shift of 0.4 towards higher binding energies as discussed in section 5.3.2 (BESSY) is also observed here, but not further discussed.

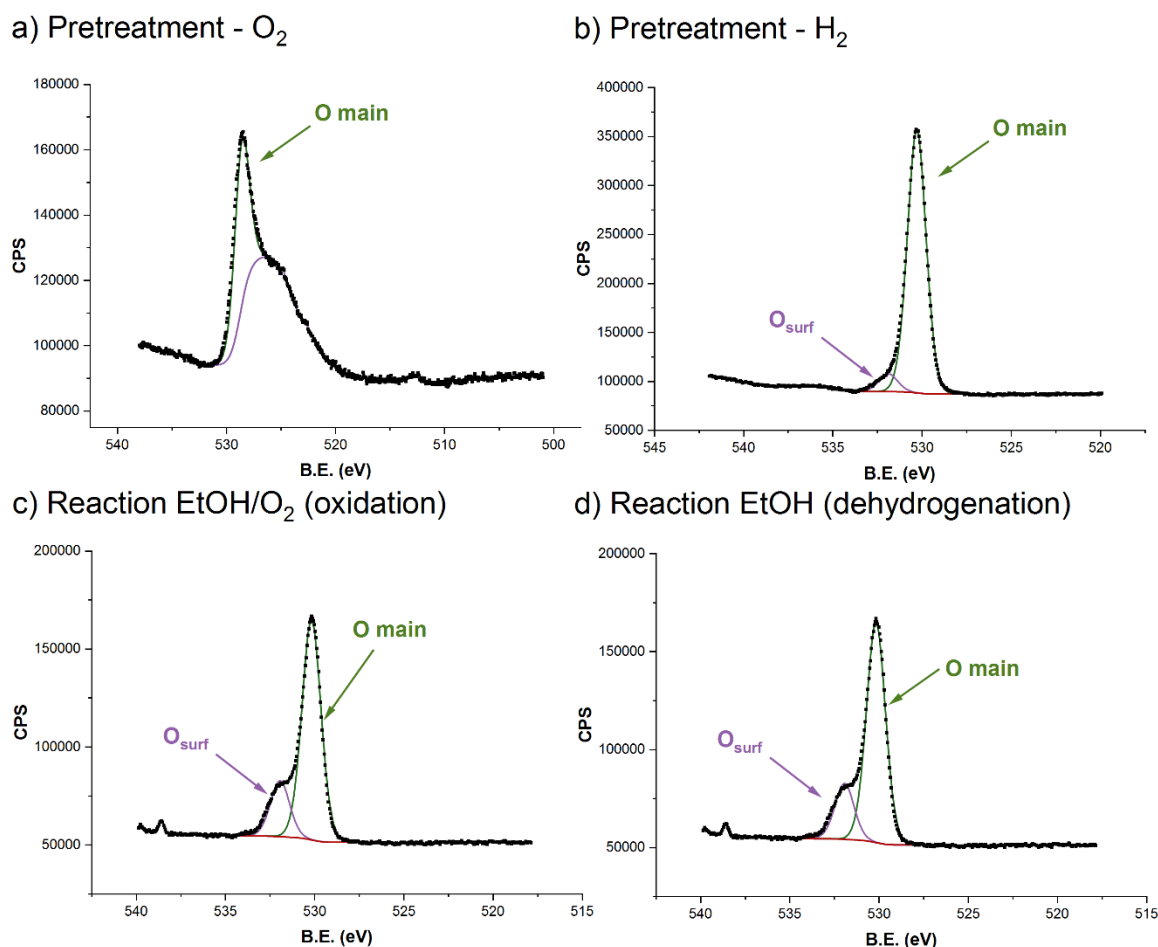


Figure 63. O 1s detail spectra of the AuAg/rutile spectra, (a) under oxidative conditions during pretreatment (400°C), (b) reducing conditions during pretreatment (300°C) as well as (c) oxidation conditions (250°C, EtOH/O₂ = 1/1) and (d) dehydrogenation conditions (250°C, EtOH only). During pretreatment, under oxygen atmosphere, charging is still predominant. O_{surf} marks surface species such as OH, H₂O, ethoxy etc.

The depth profiling using different kinetic energies (100, 310 and 670 eV) in order to determine the distribution of the Ag in the surface-near region and analyze the surface composition and oxidation state of the Ag, yielded a surprising massive *depletion* of Ag on the catalyst surface (Table 20, Figure 64). Quantification using the survey scans, measured at an excitation energy of 1100 eV, Figure 65, confirmed this.

During pretreatment under oxidative conditions, the Ag disappears almost completely from the surface (which is why no details scans were measured at an E_{kin} of 100 eV), only to reappear under reductive conditions at 300°C under H₂ flow. However, both the Au/Ag ratio of 484.7 under oxidative conditions and 238.9 under reductive conditions (compared at a kinetic energy of 310 eV) are far away from the nominal value of 2.7 for Au/Ag and 0.37 for Ag/Au. Also under reaction conditions, the gold is enriched on the surface and the

Ag/Au ratio is, at all measured kinetic energies, approximately an order of magnitude lower than expected from the nominal value.

However, the evolution of the Ag/Au ratio as well as the relative Ag peak area (determined from the survey spectra) indicates a dynamic behavior of the Ag: Switching from the EtOH/O₂-feed to EtOH-only, leads to a higher Ag concentration on the surface, and it further increases when switching to EtOH/O₂ again, suggesting that Ag is not permanently removed from the surface. This reversibility was also confirmed by the reappearance of Ag under reducing conditions. However this affects only a small fraction of the silver, while most of the silver remains migrated away from the surface after the pretreatment.

Table 20. a) Au/Ag ratios as well as b) Ag/Au ratios determined for different E_{kin} values using cross-sections published in¹²³. The enormous deviation from the nominal values ($Au/Ag = 2.7$, $Ag/Au = 0.37$) suggests massive depletion of Ag from the surface. Values are ordered by E_{kin} and not in order of measurement.

	E_{kin}	Au/Ag	Ag/Au
Pretreatment - O ₂ (400°C)	310	90.7	0.0110
Pretreatment - O ₂ (400°C)	310	484.7	0.0020
Pretreatment - H ₂ (300°C)	100	348.6	0.0029
Pretreatment - H ₂ (300°C)	310	238.9	0.0042
Pretreatment - H ₂ (300°C)	670	57.6	0.0174
EtOH/O ₂ = 1/1.6 (250°C)	100	98.2	0.0102
EtOH/O ₂ = 1/1.6 (250°C)	310	55.7	0.0180
EtOH/O ₂ = 1/1.6 (250°C)	670	13.4	0.0747
EtOH/O ₂ = 1/1 (250°C)	100	124.9	0.0080
EtOH/O ₂ = 1/1 (250°C)	310	16.0	0.0627
EtOH (250°C)	100	26.0	0.0385
EtOH (250°C)	310	24.6	0.0406
EtOH (250°C)	670	30.7	0.0326
EtOH/O ₂ = 1/1 (250°C)	100	47.3	0.0211
EtOH/O ₂ = 1/1 (250°C)	310	9.2	0.1089
EtOH/O ₂ = 1/1 (250°C)	670	8.7	0.1155

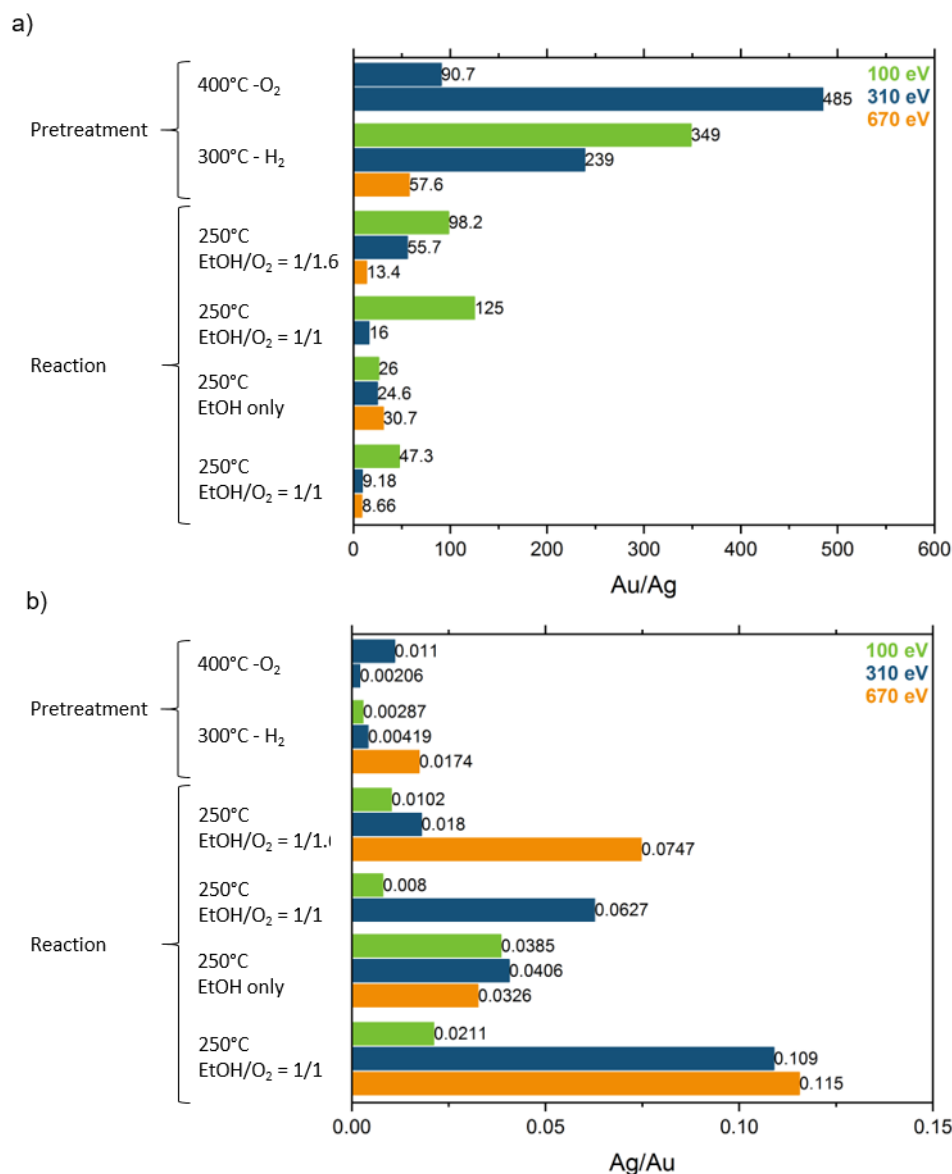


Figure 64. a) Au/Ag ratios as well as b) Ag/Au ratios determined for different E_{kin} values using cross-sections published in¹²³. The enormous deviation from the nominal values ($Au/Ag = 2.7$, $Ag/Au = 0.37$) suggests massive depletion of Ag from the surface. After pretreatment, the Ag is almost completely gone, whereas under reaction conditions some more Ag is available (under EtOH atmosphere more than under oxidation conditions with the EtOH/O₂ ratio of 1/1). This suggests a dynamic behavior of Ag, with different Ag surface concentrations depending on the atmosphere. Values are ordered by E_{kin} and not in order of measurement. Measurements were performed under steady-state conditions.

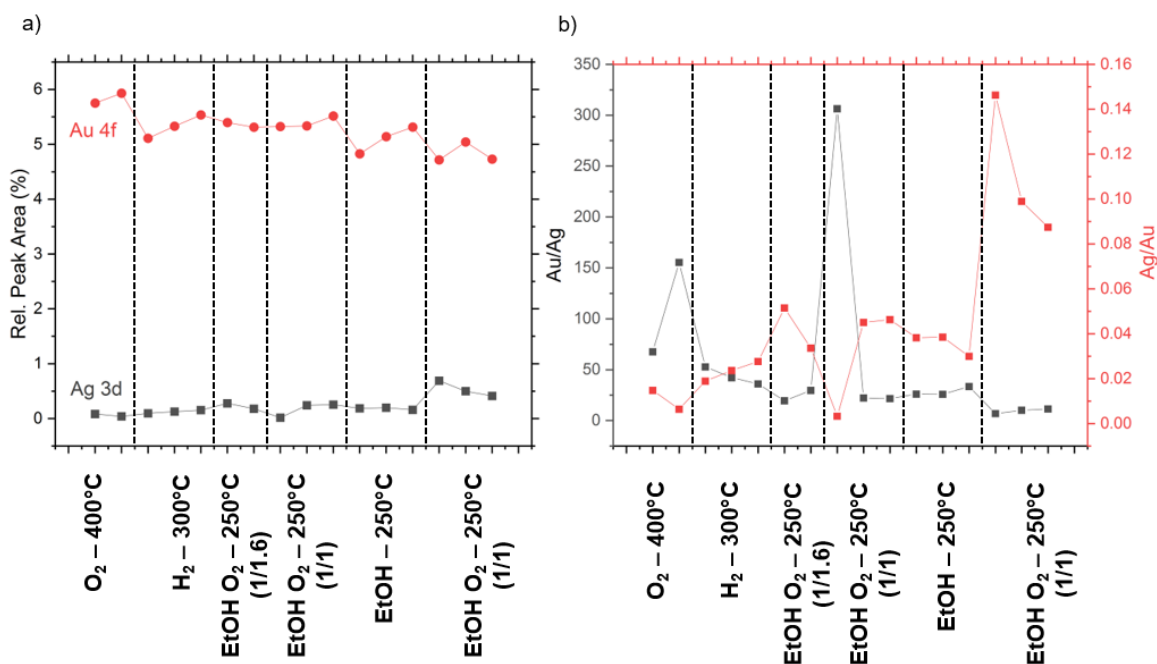


Figure 65. Evolution of the (a) relative peak area of the Au 4f peak and the Ag 3d peak as well as the (b) Au/Ag and Ag/Au ratio, as obtained from the survey scans (excitation energy of 1100 eV).

Reference measurements^V at the Ag/rutile sample confirm the depletion of Ag from the surface, Figure 66/Table 21 for the relative Ag 3d peak area obtained from survey scans ($E_{\text{exc}} = 1100 \text{ eV}$) and Figure 67 for the Ag 3d peaks at different information depths ($E_{\text{kin}}=100 \text{ eV}$, 310 eV and 670 eV) and under reaction conditions. Due to the absence of Au in the sample, graphite was added to both as internal standard. Thus, charging was also reduced so that survey spectra could be taken at UHV prior to the pretreatment (where the Ag is still present as AgNO₃ from the incipient wetness impregnation) and during the heatup period, Figure 66. The initially high Ag relative peak area of nearly 5% is quickly reduced to even zero under every condition.

Also, the Ag 3d details scans at different penetrations depths reveal the massive surface depletion of Ag. Both under oxidation conditions (EtOH/O₂ = 1/1, Figure 67 a)) and dehydrogenation conditions (EtOH only, Figure 67 b)), at the most surface sensitive measurement parameters ($E_{\text{kin}} = 100 \text{ eV}$), no Ag can be detected. The deeper the information depths reaches, $E_{\text{kin}} = 310 \text{ eV}$ and 670 eV), the more Ag can be detected.

Thus, with the Ag/rutile the migration of Ag away from the surface could be confirmed, and moreover, the possibility of a core-shell effect where Ag moves into the core of the

^V The corresponding detail spectra for the Ag/rutile spectra are shown in the annex, section 9.7.2.

AuAg particles could be eliminated as reason for the Ag surface depletion in the AuAg sample.

Table 21. Relative peak intensities of Ag 3d for the Ag/rutile reference sample.

	Rel. Peak Ag 3d Peak Area (%)
UHV	4.820
O ₂ Heatup period	4.550
O ₂ (400°C)	0.767
O ₂ (400°C)	< LOD
O ₂ (400°C)	0.233
H ₂ (300°C)	< LOD
H ₂ (300°C)	0.078
EtOH/O ₂ = 1/1 (250°C)	0.030
EtOH/O ₂ = 1/1 (250°C)	0.069
EtOH (250°C)	0.069
EtOH (250°C)	0.125
EtOH (250°C)	< LOD
EtOH/O ₂ = 1/1 (250°C)	0.048
EtOH/O ₂ = 1/1 (250°C)	< LOD

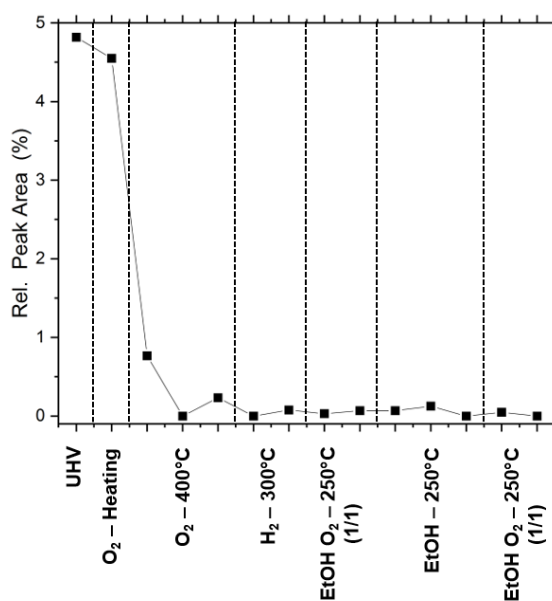


Figure 66. Graphical representation of the relative Ag 3d peak area (%) for the Ag/rutile sample. The mixture with graphite as internal standard allowed taking spectra at UHV conditions and during the heating up period. Clearly, a massive depletion of Ag from the surface during the pretreatment process is taking place.

a) EtOH/O₂ = 1/1

b) EtOH

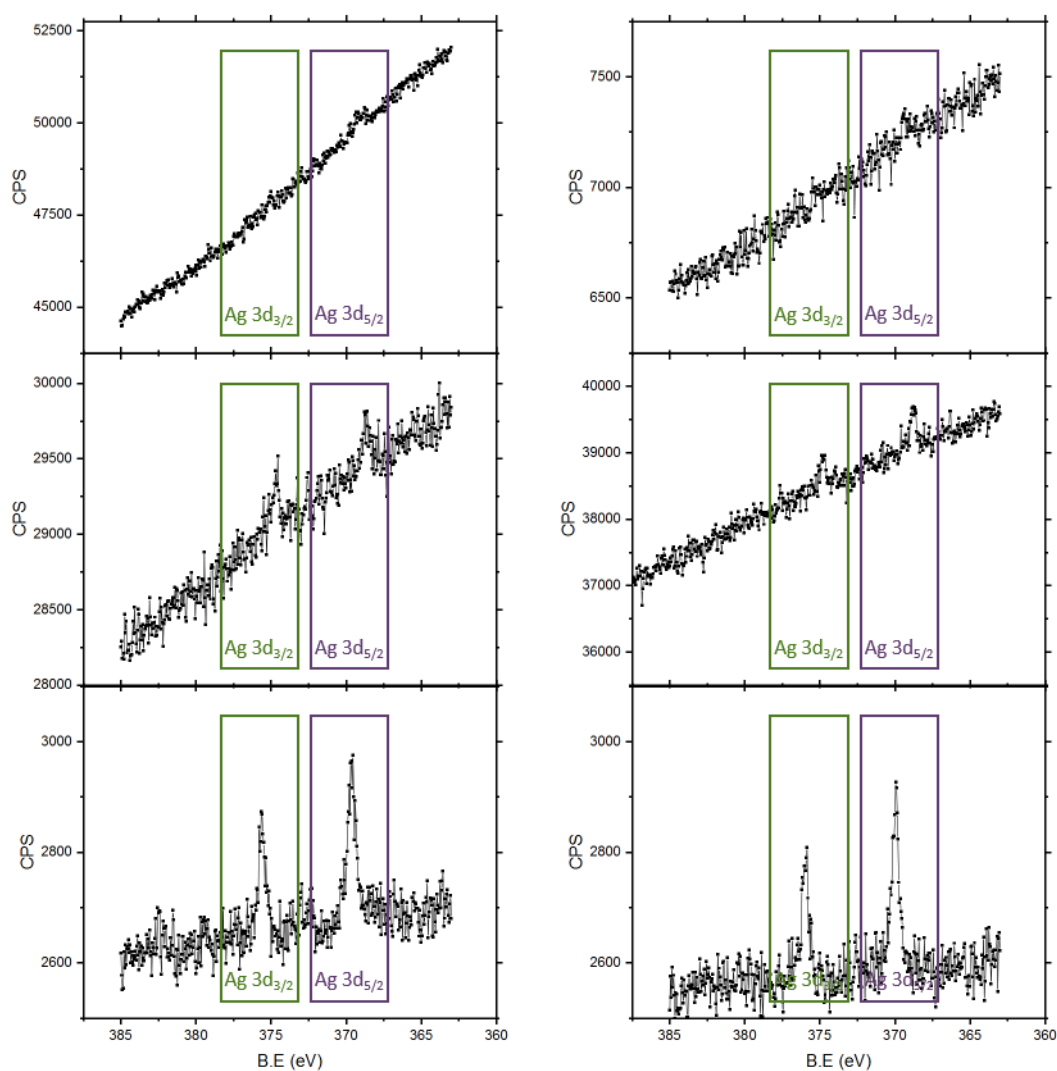


Figure 67. Comparison of Ag 3d detail scans for the Ag/rutile sample under (a) oxidation conditions with EtOH/O₂ = 1/1 as well as under (b) EtOH atmosphere, dehydrogenation conditions, only.

This surprising result of the Ag depletion from the surface during pretreatment and reaction conditions disproves silver segregation effects postulated in literature^{90,98,100}. The promotional effect of the silver in the AuAg catalysts as well as in the Ag reference (which, indeed an active and selective catalyst for the selective EtOH oxidation itself) is thus even more mysterious: The promotional effect must either originate from the astonishingly small amount of Ag remaining on the surface (<1 mol% Ag) or from the effect of Ag on the Au or rutile structure, but far away from the surface detected by XPS.

Regarding the oxidation state, for both AuAg/rutile as well as Ag/rutile, the kinetic energy of the Ag MNN Auger peaks was plotted against the binding energy of the Ag 3d in a Wagner plot (for all E_{kin} measured), Figure 68. There is no indication for any oxidation of

silver, and the silver has to assumed to be in metallic state on the surface. However, the points cluster also relatively far away from the Ag literature reference: The reason for this could lie in the often very small signal intensity (due to the silver depletion), which certainly leads to a higher relative error. Also, the nanoparticulate silver measured shows other K.E./B.E. ratios/characteristics than the silver literature reference¹⁶³.

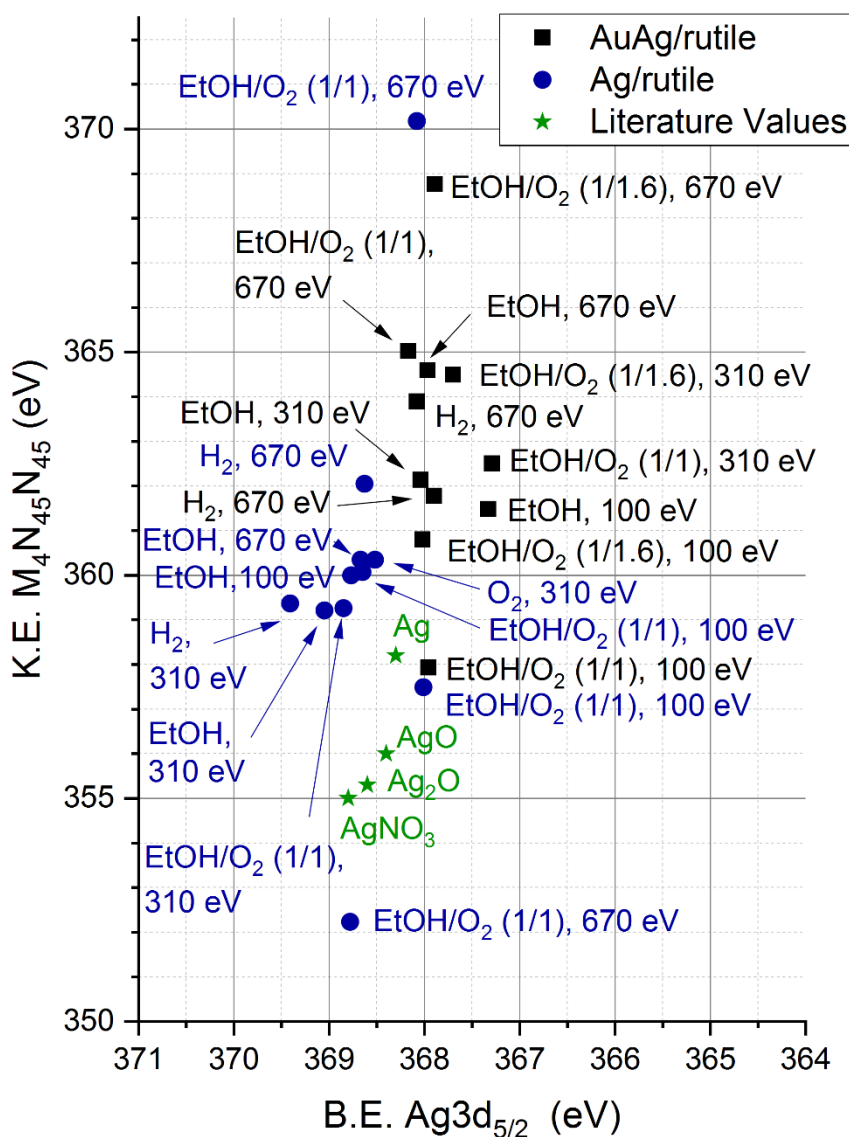


Figure 68. Wagner plot for AuAg/rutile (black) and Ag/rutile (blue) as well as the literature values of metallic Ag, AgO, Ag₂O and AgNO₃¹⁶³.

Auger-Parameters as defined by Gaarenstroom and Winograd¹⁶⁴, that is the addition of the kinetic energy of the Auger transition and binding energy of the core level. The respective values are printed in Table 22, for AuAg/rutile, and Table 23

Table 22. Auger parameters for the AuAg/rutile sample under different conditions.

	Ag3d _{5/2}	M ₄ N ₄₅ N ₄₅	Auger- Parameter
H ₂ , 300°C (E _{kin} = 310 eV)	367.90	361.78	729.68
H ₂ , 300°C (E _{kin} = 670 eV)	368.08	363.90	731.98
EtOH/O ₂ = 1/1.6, 250°C (E _{kin} = 310 eV)	367.70	364.50	732.20
EtOH/O ₂ = 1/1.6, 250°C (E _{kin} = 670 eV)	367.89	368.77	736.66
EtOH/O ₂ = 1/1.6, 250°C (E _{kin} = 100 eV)	368.02	360.81	728.83
EtOH/O ₂ = 1/1.6, 250°C (E _{kin} = 310 eV)	372.74	357.65	730.39
EtOH/O ₂ = 1/1, 250°C (E _{kin} = 310 eV)	371.87	359.71	731.58
EtOH/O ₂ = 1/1, 250°C (E _{kin} = 100 eV)	368.08	361.18	729.26
EtOH/O ₂ = 1/1, 250°C (E _{kin} = 100 eV)	367.96	357.93	725.89
EtOH/O ₂ = 1/1, 250°C (E _{kin} = 310 eV)	372.75	357.61	730.36
EtOH/O ₂ = 1/1, 250°C (E _{kin} = 310 eV)	372.75	357.61	730.36
EtOH, 250°C (E _{kin} = 310 eV)	368.04	362.14	730.18
EtOH, 250°C (E _{kin} = 670 eV)	367.97	364.60	732.57
EtOH, 250°C (E _{kin} = 100 eV)	367.33	361.49	728.82
EtOH/O ₂ = 1/1, 250°C (E _{kin} = 310 eV)	367.29	362.51	729.80
EtOH/O ₂ = 1/1, 250°C (E _{kin} = 670 eV)	368.17	365.03	733.20
EtOH/O ₂ = 1/1, 250°C (E _{kin} = 100 eV)	367.44	359.67	727.11

Table 23. Auger parameter for the Ag/rutile sample. Under different conditions.

	Ag3d _{3/2}	M ₄ N ₄₅ N ₄₅	Auger- Parameter
O ₂ , 400°C (E _{kin} = 310 eV)	374.43	360.35	734.78
H ₂ , 300°C (E _{kin} = 310 eV)	375.15	359.37	734.52
H ₂ , 300°C (E _{kin} = 670 eV)	374.68	362.05	736.73
H ₂ , 300°C (E _{kin} = 100 eV)	380.21	359.03	739.24
EtOH/O ₂ = 1/1, 250°C (E _{kin} = 670 eV)	374.08	370.18	744.26
EtOH/O ₂ = 1/1, 250°C (E _{kin} = 100 eV)	380.21	357.49	737.70
EtOH, 250°C (E _{kin} = 310 eV)	374.77	359.21	733.98
EtOH, 250°C (E _{kin} = 670 eV)	374.67	360.35	735.02

EtOH, 250°C ($E_{\text{kin}} = 100 \text{ eV}$)	363.21	360.00	723.21
EtOH/O₂ = 1/1, 250°C ($E_{\text{kin}} = 310 \text{ eV}$)	374.84	359.26	734.10
EtOH/O₂ = 1/1, 250°C ($E_{\text{kin}} = 670 \text{ eV}$)	374.75	352.23	726.98
EtOH/O₂ = 1/1, 250°C ($E_{\text{kin}} = 100 \text{ eV}$)	380.21	360.07	740.28

Also here, comparison with literature¹⁶³ shows that there is no match with the Auger parameter of Ag (726.0 - 726.40 eV), AgO (724.20, 724.80, 723.50 eV), Ag₂O (724.30, 724.50 eV) or AgNO₃ (723.80 eV).

5.3.4. Operando XAS

Au LIII spectra (measured at the ALBA BL22 - CLÆSS beamline) of the measured samples, Au/rutile and AuAg/rutile, are shown in Figure 69. Apart from the first spectrum, taken at room temperature prior to pretreatment, the spectra at the different conditions, after oxidation (20% O₂ at 400°C), after reduction (5% H₂ at 300°C) as well as reaction conditions (EtOH/O₂ = 1/1 at 250°C and 300°C) are identical. A linear combination fit (LCF), using Au foil, Au₂O₃ powder and AuCl₄ powder as references, see Figure 70, shows limited suitability of these bulk references for the nanocrystalline sample. Especially before pretreatment, probably due to the amorphous character of Au with possible residues of AuCl₄, the residual plot reveals the quite different nature of the species present under these conditions.

Under oxidative conditions, Figure 70 b), reductive conditions, Figure 70 c), reaction conditions at 250°C and 300°C conditions, Figure 70 d) and e), the fit shows reasonable agreement with the measurement, suggesting reduced Au, apart from smaller differences near the edge, especially the feature at 11946 eV is much less pronounced in the experiment. This underlines the limited suitability of the bulk references for this nanoparticulate system with particles sizes around 3 nm. However, in good agreement with the NAP-XPS results, a completely reduced gold can be assumed. In Figure 72, an LCF was performed using the Au/rutile sample itself after the reduction as references. Clearly, nearly perfect fits show that under both EtOH/O₂ flow as well as EtOH flow the sample does not differ from the Au/rutile sample after reduction, all features can be explained. Thus, after pretreatment and under reaction conditions, the gold remains reduced at all

times. For AuAg/rutile the same LCFs have been performed, Figure 71 for the LCFs with Au foil, Au₂O₃ and AuCl₄ as reference, and Figure 73 where the Au/rutile sample (!) was used at reference. The same results were obtained, proving also Au in the reduced state in the AuAg sample under all investigated conditions and no different behavior of the Au in Au/rutile and AuAg/rutile.

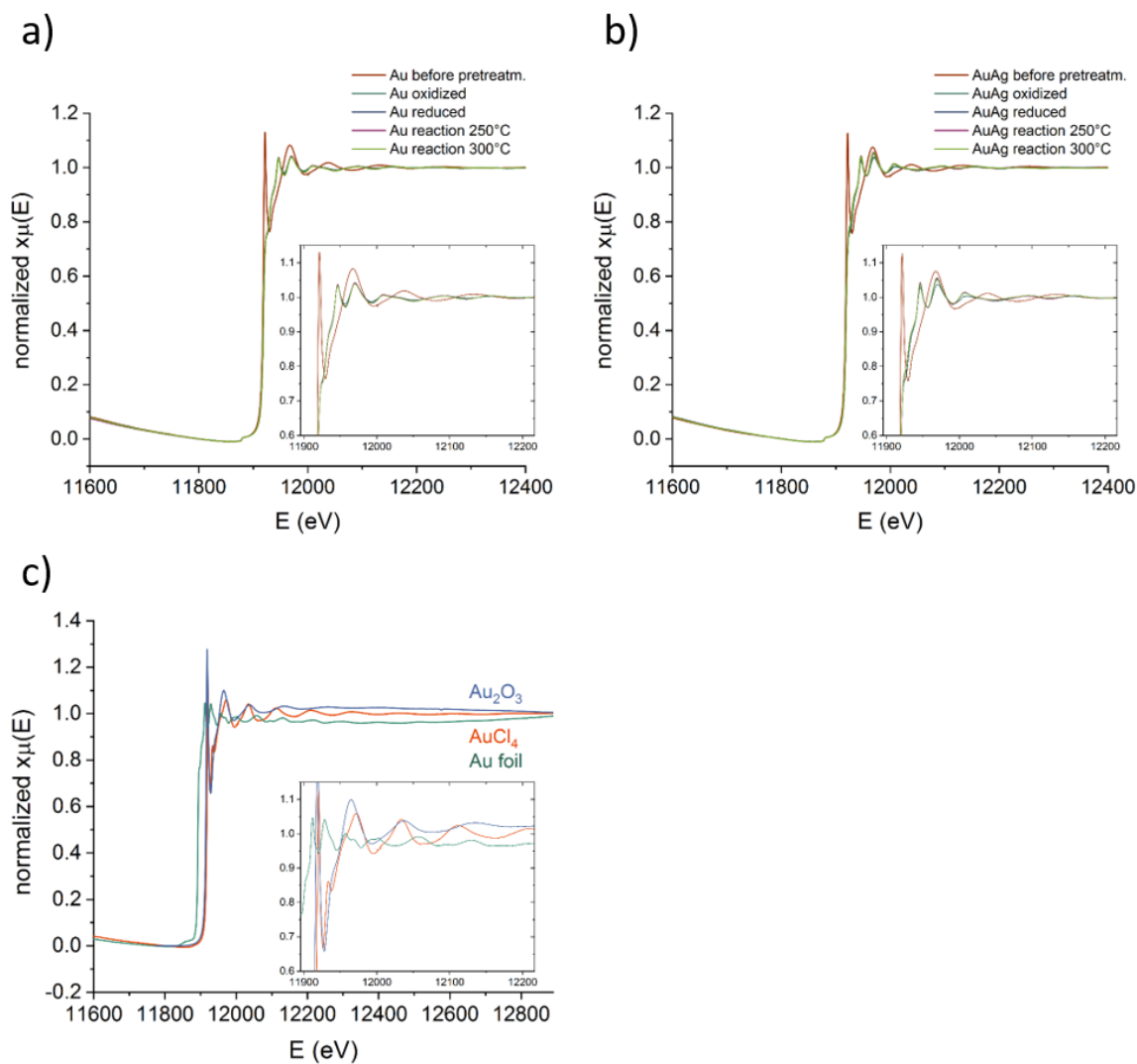


Figure 69. Au LIII spectra under operando conditions (before pretreatment, after oxidation, after reduction, during reaction with EtOH/O₂ at 250°C and 300°C for (a) Au/rutile, (b) AuAg/rutile. (c) shows the ex-situ references Au₂O₃, AuCl₄ and Au foil.

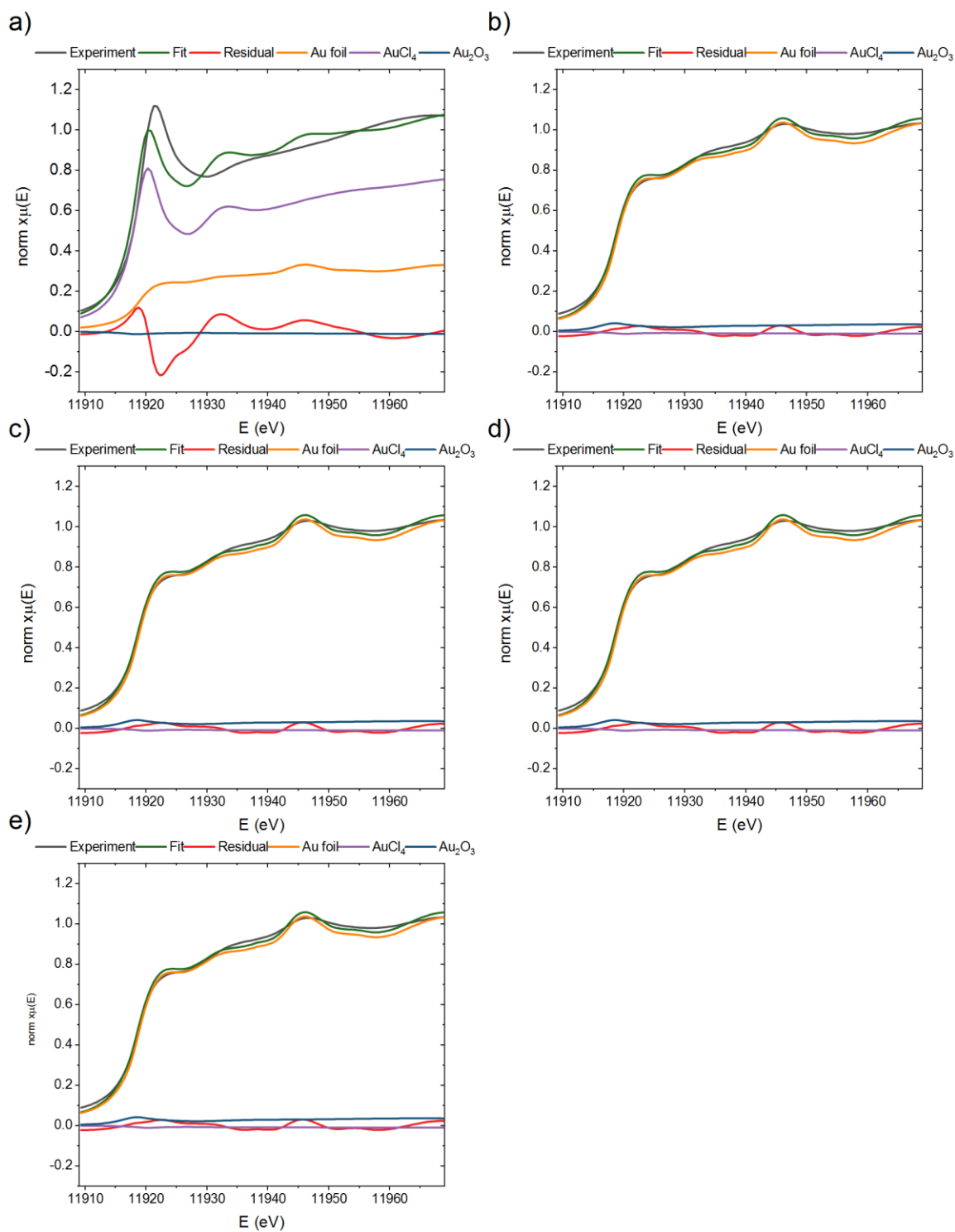


Figure 70. Linear combination fits (LCFs) for the Au/rutile sample of the XANES area (-10 to + 50 eV from the tabulated Au LIII edge) using Au foil, AuCl₄ and Au₂O₃ as references. Whereas before pretreatment, a), the reference prove as not suitable to capture all features, reasonable fits could be obtained for b) after oxidation, c) after reduction and d), e), during reaction with EtOH/O₂ at 250°C and 300°C.

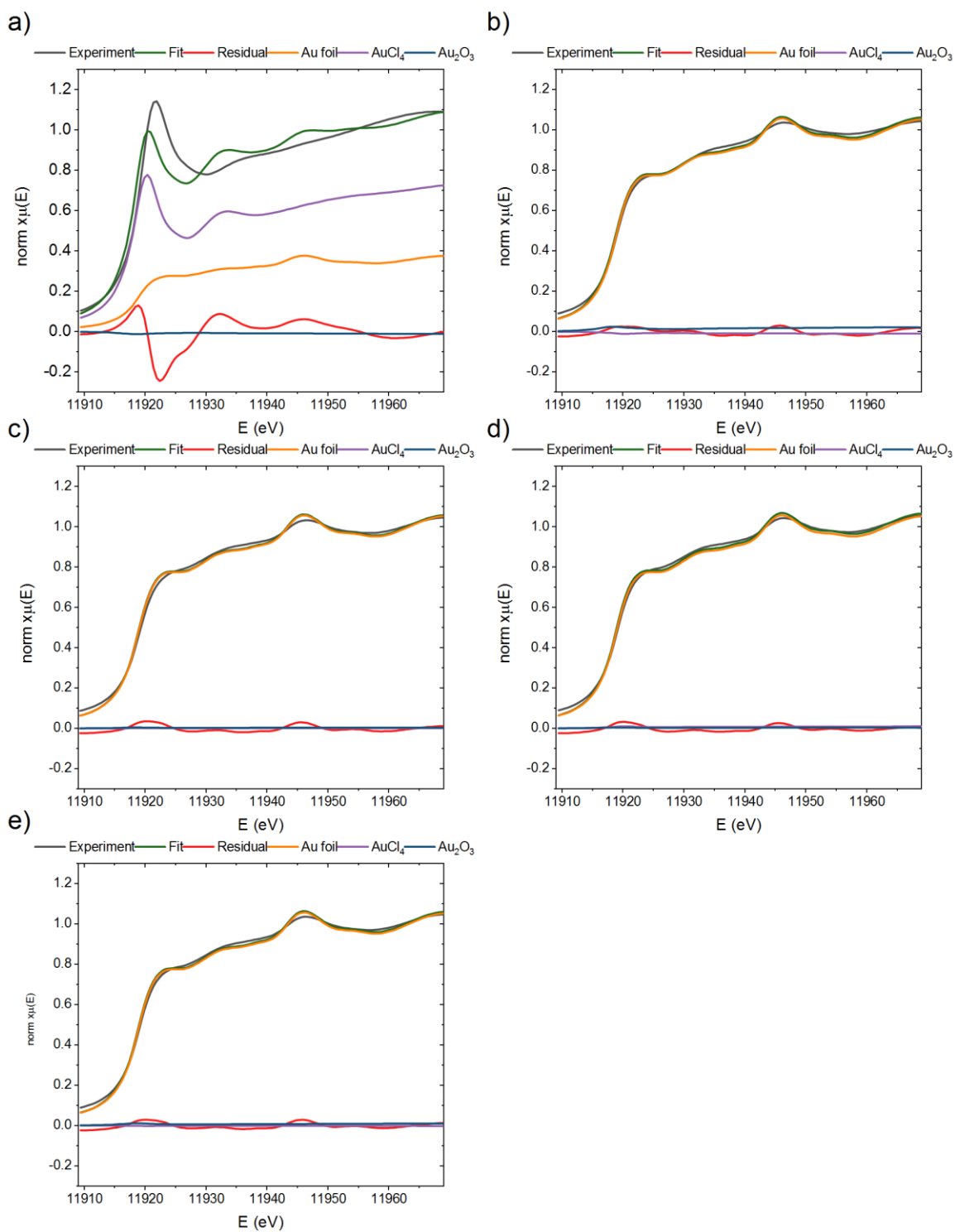


Figure 71. Linear combination fits (LCFs) for the AuAg/rutile sample of the XANES area (-10 to + 50 eV from the tabulated Au LIII edge) using Au foil, AuCl_4 and Au_2O_3 as references. Whereas before pretreatment, a), the reference prove as not suitable to capture all features, reasonable fits could be obtained for b) after oxidation, c) after reduction and d), e), during reaction with EtOH/O_2 at 250°C and 300°C .

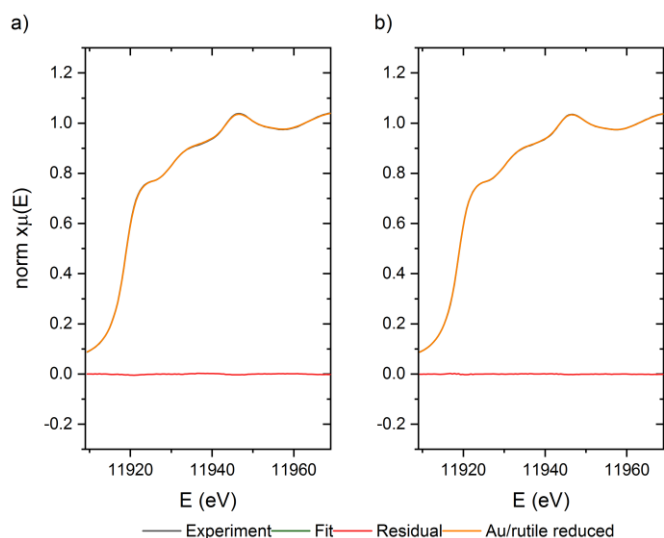


Figure 72. Linear combination fits (LCFs) for the Au/rutile sample of the XANES area (-10 to + 50 eV from the tabulated Au LIII edge) using the sample itself in the reduced state as reference. a) shows reaction with EtOH/O₂ at 250°C and b) at 300°C.

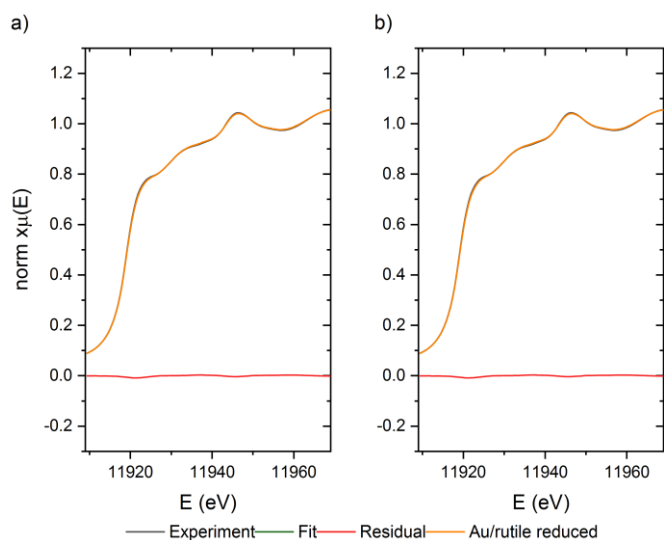


Figure 73. Linear combination fits (LCFs) for the AuAg/rutile sample of the XANES area (-10 to + 50 eV from the tabulated Au LIII edge) using the Au/rutile sample in the reduced state as reference. a) shows reaction with EtOH/O₂ at 250°C and b) at 300°C.

The Ag K-edge was measured at the Diamond Light Source, B18 beamline. The respective spectra for the Ag/rutile, AuAg/rutile sample and the ex-situ references, Ag₂O and Ag foil are shown in Figure 74. For both samples, the spectra obtained at 400°C under 20% O₂ are significantly different from both the reduced state (300°C, 5% H₂) and reaction conditions (both EtOH/O₂ and EtOH only). The larger whiteline of the oxidized samples, in particular of Ag/rutile, suggests a significant fraction of the Ag to be present in an oxidized state, however, the characteristic double peak observed in Ag₂O and AgO¹⁶⁵ is absent and the

spectrum resembles rather that of AgNO_3^{165} , the precursor used for synthesis (unfortunately, however no reference was available for the LCF). Upon reduction the XANES region changes more towards the metallic state. When comparing the spectra of Ag/rutile, Figure 74a), and AuAg/rutile, Figure 74b), the spectrum of Ag/rutile after reduction and during reaction shows more clearly the characteristic features of metallic Ag up to higher energies above the edge, while those oscillation features vanish faster with increasing energy on AuAg/rutile. This suggests that the coordination environment of the monometallic Ag/rutile resembles more that of the bulk metal foil than of AuAg/rutile, which might be explained by a lower crystallinity, smaller nanoparticles or the potential contribution of Au in the bimetallic particles.

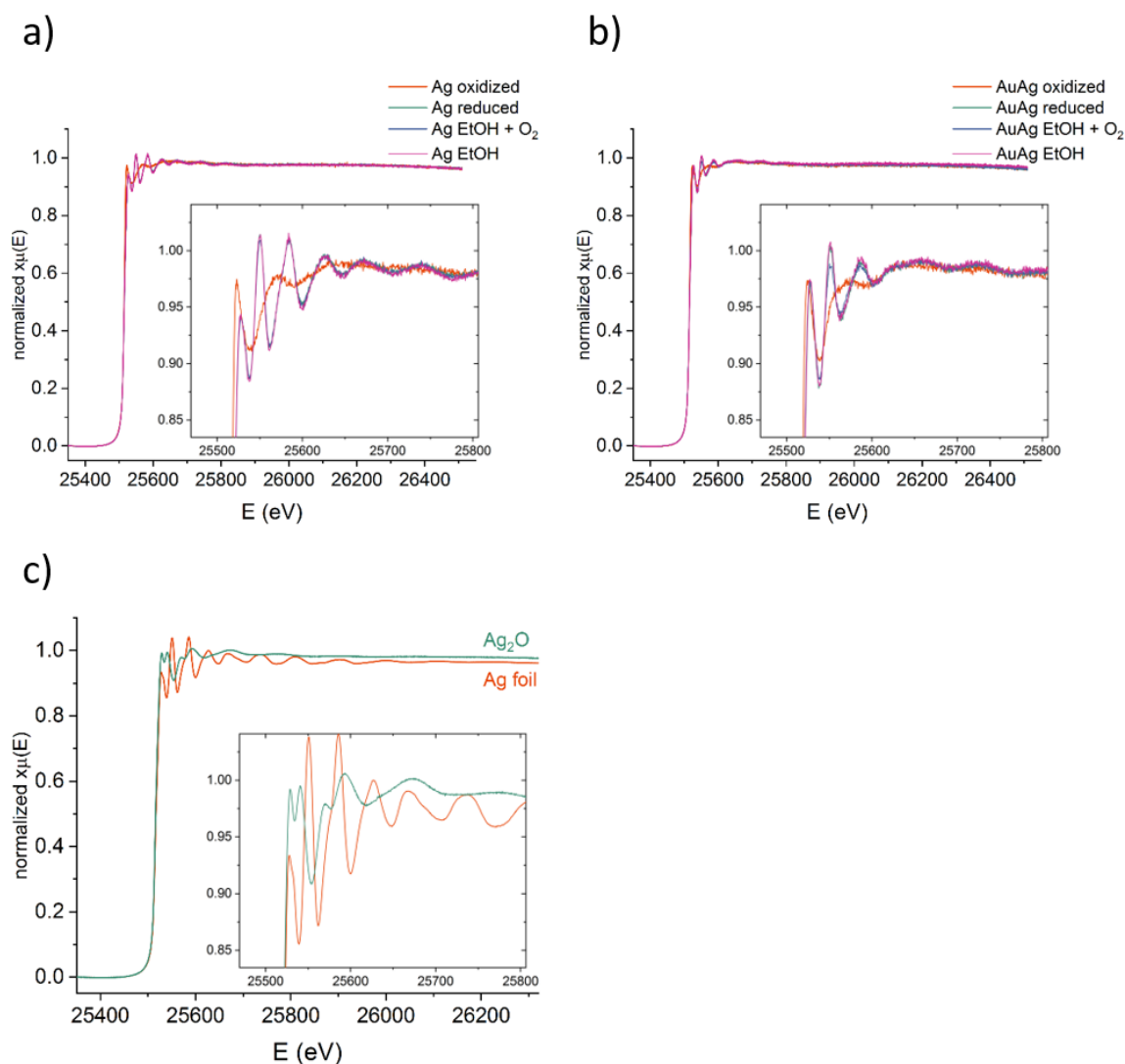


Figure 74. Ag K-edge spectra for a) Ag/rutile, b) AuAg/rutile, both in-situ during the pretreatment process and under operando conditions with EtOH/O₂ and EtOH only. c) shows the ex-situ references Ag₂O and the Ag foil.

Linear combination fits (LCFs) were undertaken for both samples, Ag/rutile (Figure 75) and AuAg/rutile (Figure 76) using Ag₂O and the Ag foil as reference. After the oxidation at 400°C under 20% O₂, the fit indicates non-suitable standards, leaving the exact nature of the Ag/rutile after the oxidation state undefined. After the reduction step (5% H₂ at 300°C, Figure 75 b), during the reaction with EtOH/O₂ at 250°C, Figure 75 c), during the reaction with EtOH only, Figure 75 d), a reasonable good agreement with the fit is achieved. Quantitative values are given in Table 24, showing that even after the reduction step on the AuAg/rutile sample roughly 65% of the Ag is reduced, which decreases to 54% at reaction conditions with EtOH/O₂ but later increases again to > 66% under EtOH. For Ag/rutile, the amount of reduced Ag remains constant at approximately 65%. Therefore, the reducing step of the pretreatment is not generating 100% reduced Ag and a significant proportion of oxidized Ag remains. A reasonable fit is achieved with the Ag₂O bulk reference, however not all contributions to the XANES can be captured, either due to the nanocrystalline character of the particles or because there are unknown Ag species present. The latter can be hypothesized due to the unusual results from the NAP-XPS (Wagner plot and Auger parameters).

Importantly, however, the disagreement of experiment and fit after the oxidation of the pretreatment step shows that Ag₂O is not at all a suitable reference for that condition and that other Ag species are present. Whereas during the pretreatment, after the oxidation step, AgNO₃ could be still present, this explanation does not hold for the reaction conditions anymore (as there was a reduction step in between, where the LCF was in good agreement with the experiment with Ag₂O and the Ag foil as references), where Ag/rutile after oxidation was successfully used as reference for the LCF.

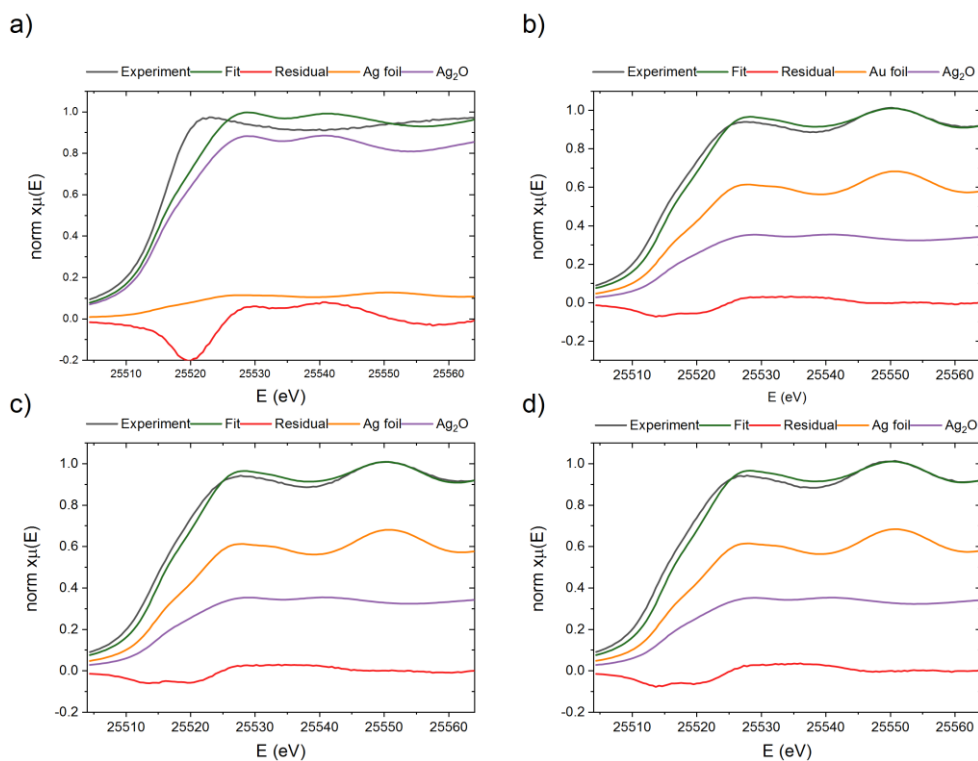


Figure 75. Linear combination fits (LCFs) for Ag/rutile after oxidation (20% O₂ at 400°C), a), after reduction (5% H₂ at 300°C) and during reaction at 250°C with EtOH/O₂, c), and EtOH only, d). Ag foil and Ag₂O were used as references.

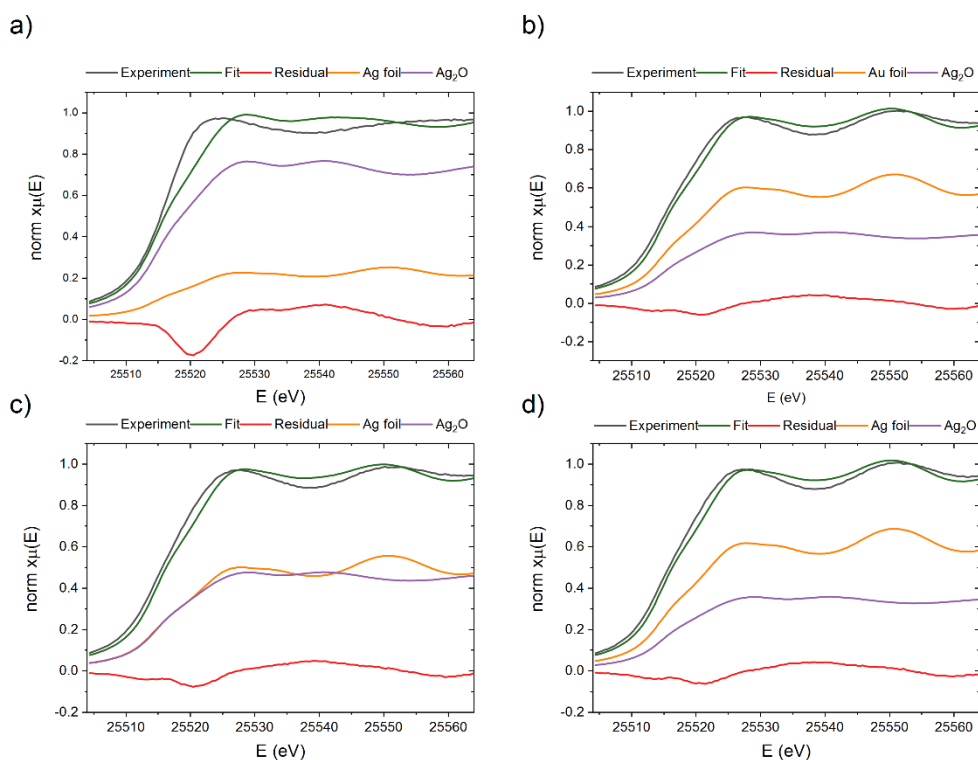


Figure 76. Linear combination fits (LCFs) for AuAg/rutile after oxidation (20% O₂ at 400°C), a), after reduction (5% H₂ at 300°C) and during reaction at 250°C with EtOH/O₂, c), and EtOH only, d). Ag foil and Ag₂O were used as references.

Thus, to gain further understanding of the system, for both samples, Ag/rutile and AuAg/rutile, LCFs were carried out by using the Ag/rutile after oxidation and Ag/rutile after reduction as references, see Figure 77 for Ag/rutile and Figure 78 for AuAg/rutile. This approach yields considerably better agreement with experimental data.

For the Ag/rutile sample, under oxidative dehydrogenation conditions with EtOH/O₂, the experiment is fully fitted with the Ag/rutile reference after reduction, see Figure 77 a). Under dehydrogenation conditions, Figure 77 b), 2% of the spectrum can be characterized by Ag/oxidized sample. This must not be confused with the proportion of oxidized silver as also after reduction, a significant amount of Ag remains oxidized. However, while under state-steady conditions the XANES spectrum under EtOH/O₂ flow is equivalent to the one after the reduction step, a contribution from the XANES spectrum under oxidative conditions can be observed under EtOH conditions.

For AuAg/rutile, already under EtOH/O₂ flow a significant contribution, 21%, from the Ag/rutile spectrum under oxidative conditions could be observed which then decreases to 8% under EtOH flow (without oxygen). Therefore, an opposite trend is observed for the two samples. It becomes also clear from the residual plots that certainly not all features of the Ag in the AuAg/rutile can be captured by the Ag/rutile reference, but some currently unknown contributions remain.

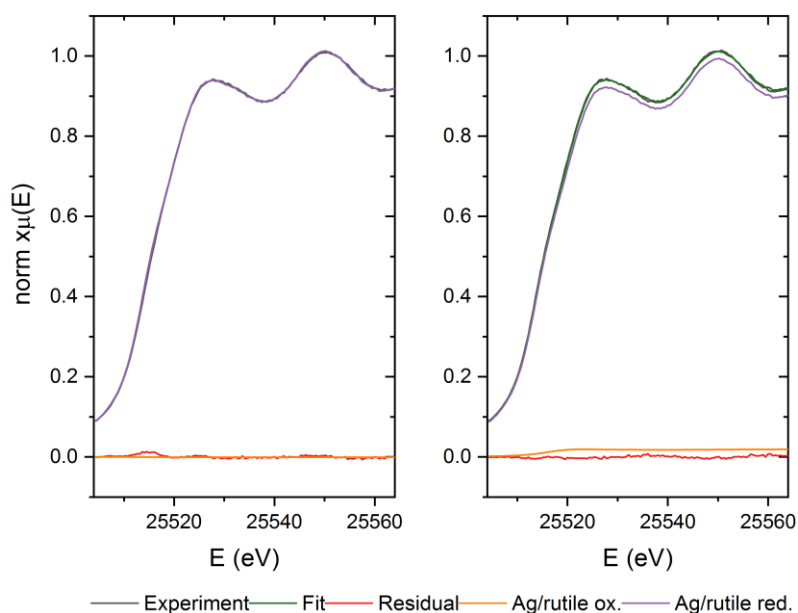


Figure 77. Linear combination fits (LCFs) for Ag/rutile during reaction with EtOH/O₂, a), and EtOH only, b). Ag/rutile after oxidation and Ag/rutile after reduction were used as standard.

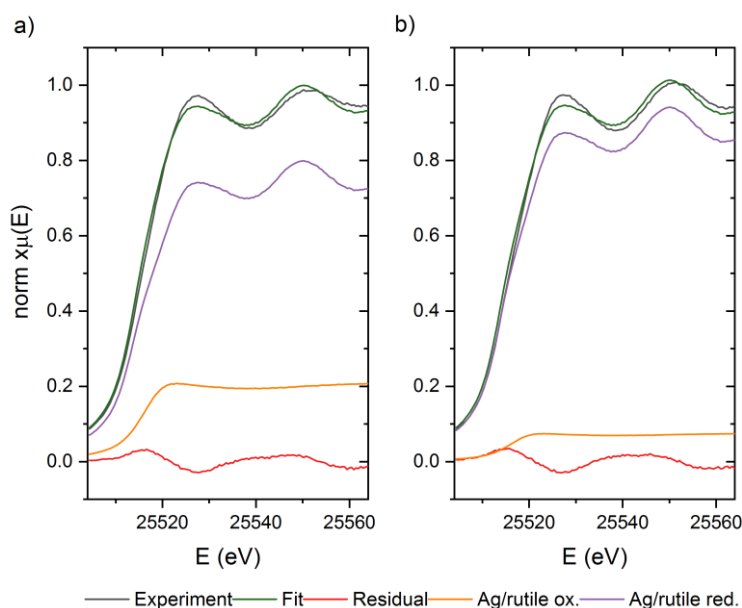


Figure 78. Linear combination fits (LCFs) for AuAg/rutile during reaction with EtOH/O₂, a), and EtOH only, b). Ag/rutile after oxidation and Ag/rutile after reduction were used as standard.

Table 24. Quantitative of the linear combination fittings (LCFs) with the Ag foil and Ag₂O as references for AuAg/rutile and Ag/rutile. The state after the oxidation is not well defined through the references, thus values are indicative only.

	AuAg/rutile		Ag/rutile	
	Ag foil weight	Ag ₂ O weight	Ag foil weight	Ag ₂ O weight
After oxidation (400°C)*	0.24 ± 0.09	0.77 ± 0.08	0.12 ± 0.10	0.89 ± 0.10
After reduction (300°C)	0.65 ± 0.04	0.37 ± 0.04	0.66 ± 0.04	0.36 ± 0.04
EtOH/O₂ (250°C)	0.54 ± 0.0	0.48 ± 0.05	0.66 ± 0.04	0.36 ± 0.04
EtOH (250°C)	0.66 ± 0.04	0.36 ± 0.04	0.66 ± 0.05	0.36 ± 0.05

Concluding, the measurements at the Au LIII-edge confirm the assumption of no Au^{δ+} in either of the catalysts based on NAP-XPS results. For the Ag K-edge, a significant difference between Ag and AuAg could be found: Using the Ag/rutile after oxidation and reduction as reference for the LCF, for Ag/rutile an increase of the contribution of the spectrum of the oxidized sample could be observed, whereas the opposite, a decrease is observed for AuAg/rutile.

In both cases significant amounts of oxidized silver were found under reaction conditions, complementing the NAP-XPS results. Whereas the vast majority of silver atoms remains reduced, a significant amount seems to undergo oxidation.

5.4. Conclusion

Addition of Ag to the Au-catalysts increases activity and selectivity towards acetaldehyde, > 97% (from an already high level for the Au/rutile sample). Also, regarding catalyst activity, silver has a higher relative effect on the reaction rate on the carbon support than on rutile, although on a much lower conversion level.

For ethanol reaction orders on AuAg systems, the silver greatly reduces the reaction order at higher temperatures. Silver alone, on Ag/rutile, also shows a lower EtOH order, but it is still relevantly higher than in the AuAg sample. The O₂ reaction order, however, reveals a very different behavior for carbon-based catalysts and rutile-based catalysts: AuAg/rutile starts at nearly zero at 150°C and then increases to 0.29, a quite opposite trend to Au/rutile is observed (there, a decrease from 0.18 to nearly zero is seen). This illustrates how Ag is influencing the oxygen activation, where the reaction rate is indeed depending on the oxygen partial pressure. Also, on AuAg/C, an effect of silver is observed, where the reaction order is also increasing from 0.15 at 150°C to 0.3 at 300°C. On Au/C, the final oxygen reaction order at 300°C is also 0.3, however there is no temperature dependency.

The initial hypothesis, that the AuAg system is consisting of bimetallic AuAg particles, could not be confirmed. In fact, *operando* measurements show a massive depletion of Ag from the surface on the rutile-based catalysts, presumably due to migration of silver into the TiO₂ bulk. While the Ag surface concentration varies with the reaction conditions (EtOH in contrast to EtOH/O₂) the vast majority of the Ag remains unavailable for the surface. Clearly, there is a promotional effect as well as influence on the reaction orders, meaning that, even though most of the silver is away from the surface, it does have an influence on catalysis.

The difference to AuAg/C lies not only in the absence of an oxide support: STEM-EDX reveals the presence of bimetallic AuAg particles, and assuming the Ag cannot migrate into the carbon support, the promotional effect there is expected to originate from the AuAg alloy.

Both in the NAP-XPS and XAS, no $\text{Au}^{\delta+}$ could be found, strengthening experimental evidence for the computational result that Au^0 itself is able to activate the molecular oxygen. The finding of Ti^{3+} under dehydrogenation conditions could point to oxygen activation on the Au/ TiO_2 interface, explaining improved catalytic effect in the presence of rutile (as opposed to Au/C), as suggested in literature for the CO oxidation (“Au-assisted Mars–van-Krevelen mechanism”)⁵¹. The silver does play a role in this process, however, the experimental proof is very hard to obtain due to the surprisingly low surface concentration of Ag. Although there is no indication of oxidized silver, the Wagner plot and the Auger parameters point to a silver species different from “traditional” Ag_2O or metallic silver. In XAS, on the other hand, the XANES shows the presence of oxidized silver species. Also here, the difference between fit and experiment suggests that it must be different from Ag_2O .

Even though the exact role of silver remains unclear, the often suggested^{90,98,100} segregation of silver on the surface of the AuAg nanoparticle must be rejected when a TiO_2 support is used. In fact, an astonishing enrichment of Au is observed on the catalyst surface due to this migration of Ag. Future experiments must prove if this surface depletion of silver is limited to a rutile supported catalyst or if it can also be observed on other oxide supports and on carbon.

DRIFTS experiments revealed no additional species than already observed for Au/rutile, supporting the hypothesis that the Au/rutile and AuAg/rutile in fact share a similar reaction mechanism involving the same intermediates (under steady-state conditions). The promotional effect of silver could indeed play a role in the oxygen activation, a process difficult to observe in DRIFTS.

6. The Influence of Water and Comparison with the Liquid Phase Reaction

6.1. Catalyst Characterization

STEM-HAADF measurements were performed after the reaction with water to test for water-induced sintering effects, Figure 79. Interestingly, the trend shown without water in the feed, smaller particles for Au/rutile (3.3 ± 1.0 nm to 2.9 ± 0.9 nm) and sintering for AuAg/rutile (3.6 ± 1.2 nm to 4.3 ± 1.2 nm) is in fact reversed upon water introduction. For Au/rutile, a sintering to 3.7 ± 0.9 nm is observed (while exhibiting higher activity, see section 6.3) whereas smaller particles for AuAg/rutile were observed (2.6 nm \pm 0.7 nm).

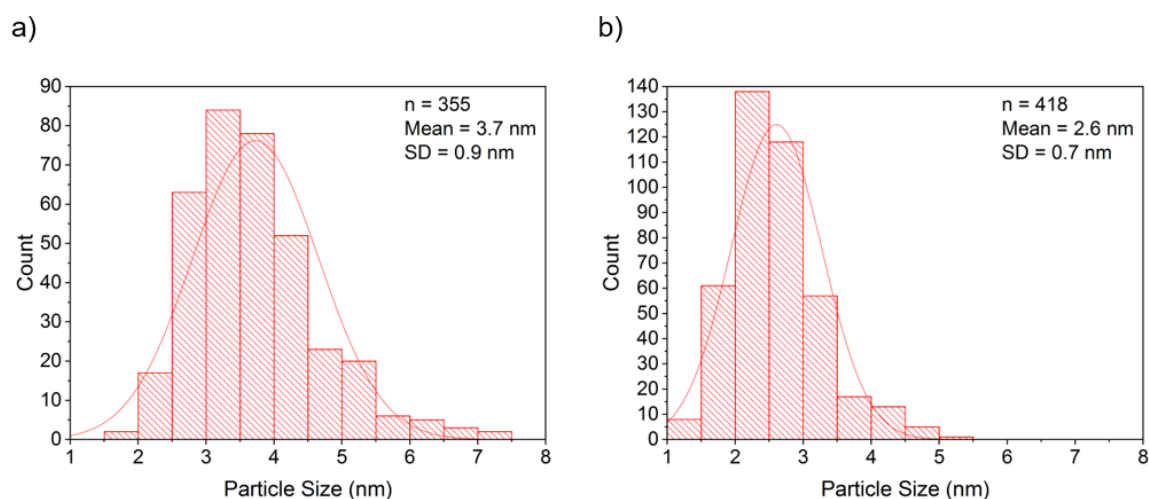


Figure 79. Size distributions obtained by STEM-HAADF for (a) Au/rutile and (b) AuAg/rutile. Interestingly, the trend shown in chapter 5.1, smaller particles for Au/rutile (3.3 ± 1.0 nm to 2.9 ± 0.9 nm) and sintering for AuAg/rutile (3.6 ± 1.2 nm to 4.3 ± 1.2 nm) is in fact reversed upon water introduction. For Au/rutile, a sintering to 3.7 ± 0.9 nm is observed (while exhibiting higher activity, see section 6.3) whereas smaller particles for AuAg/rutile were observed (2.6 nm \pm 0.7 nm).

6.2. Liquid Phase Results (ETH Zurich)

The Au/rutile sample as well as the bimetallic catalysts presented in section 4 (AuAg/rutile, AuRu/rutile and AuPt/rutile) were measured in aqueous phase by S. Mostrou-Moser at the ETH Zürich. The results are reprinted with permission.

Figure 80 shows the results, which are in stark contrast to the gas-phase behavior of the catalysts. The main product is acetic acid with ethyl acetate as the major side product (alongside with acetaldehyde and CO_2). The high selectivity towards CO_2 can be explained with the high conversion obtained in the batch reactor, $> 60\%$ for AuAg/rutile and $> 90\%$

for the other samples. Regarding the conversion, the catalysts can be ordered as follows: AuPt > Au > AuRu > AuAg. However, the monometallic Au/rutile can be regarded as the best catalyst due to the lower CO₂ selectivity. Surprisingly, the AuAg/rutile, favored in the gas-phase reaction, is the least active one in the liquid phase (gas phase: AuAg > Au > AuRu > AuPt). For the AuAg/TiO₂ sample prepared by flame spray pyrolysis, even no activity was detected in the liquid phase, whereas it works in gas-phase (though worse than the Au/TiO₂ prepared by FSP). Notably, also in the liquid-phase, AuAg/rutile shows the highest selectivity to acetaldehyde, the main product in the gas-phase, however at lower conversion. Only for AuRu was there any acetic acid in relevant amounts observed in the gas-phase. In aqueous phase, for all catalysts investigated, the main product (> 40%) is acetic acid. Beside CO₂; which is hardly produced in gas-phase, ethyl-acetate (the most important side product in gas-phase) is the main side product.

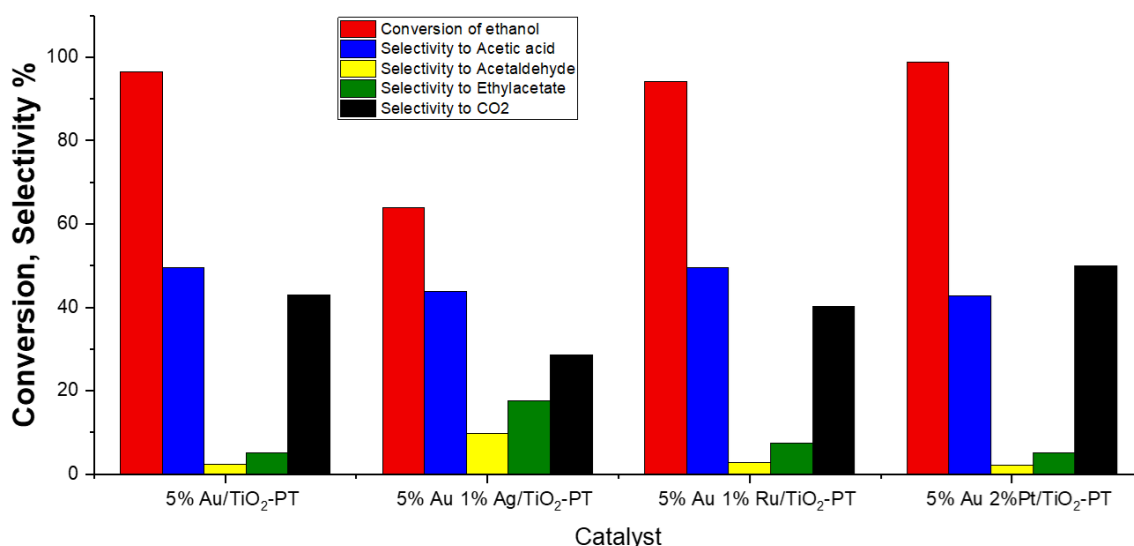


Figure 80. Kinetic results of the reaction in the liquid phase. The reaction was performed at the following conditions in a batch reactor: $p = 15 \text{ bar O}_2$, 10mL of 5 vol.% EtOH/H₂O (liq), 50 mg catalyst, $T=150^\circ\text{C}$, reaction time =4 h. The catalysts were pretreated at the TU Wien and then shipped to the ETH Zürich, and thus have been exposed to the ambient prior to reaction. These experiments were performed by S. Mostrou-Moser, ETH Zürich and the results are reprinted with permission.

Thus, to determine if the observed results must be attributed to the different phase (of course, also different reaction conditions, temperature and pressure can make a difference) or the presence of water, also the gas-phase reaction was investigated with water addition to the feed as described in the next chapter.

6.3. Influence of Water in the Gas-Phase Reaction

6.3.1. Kinetic Results

As described in the experimental section, after a measurement without water, at partial pressures of 1.1 kPa EtOH/O₂, two different water partial pressures were investigated: 1.1 kPa EtOH/O₂ with 0.6 kPa H₂O and 1.1 kPa EtOH/O₂ with 2.0 kPa H₂O. To check the reversibility of the effect, e.g. due to water-facilitated sintering, also a final measurement without water was conducted. To indicate the purging time to flush the water out of the kinetic setup, which, for experimental reasons, varied for each sample, the x-axis shows an interruption after 400 minutes. Hence, the “net reaction” time, not taking account the purging of the system, is plotted in Figure 81. The temperature was kept constant at 250°C.

The results, Figure 81, show a clear positive catalytic effect for water for the Au/rutile sample. Indeed, more water, at a higher partial pressure of 2.0 kPa, is beneficial for acetaldehyde formation. Taking into account that H₂O is also a product, thus this result is counter-intuitive from the thermodynamic standpoint. For Au/C, however, water did not have a beneficial effect on acetaldehyde formation, however due to the low conversion, as also depicted in Figure 82, the relative error must assumed to be higher. Ag/rutile, is also showing a different behavior than the Au/rutile sample: A decrease of acetaldehyde formation is observed. The bimetallic AuAg/rutile system shows different reaction rates depending on the water partial pressure: Under condition (II), 0.6 kPa water, a low decrease of activity was observed, whereas under condition (III), 2.0 kPa H₂O, an increase is observed. The small changes for the Au/Ag, however, must be put into relation to the change of the EtOH feed different between the conditions, which are +3.5 % EtOH from (I) to (II) and + 2% from (I) to (III). Quantitatively, the changes in acetaldehyde formation relative to the starting conditions, (I) without water, are summarized in Table 25. However, the activity is increasing and does not decrease to value at the start of the reaction as observed for the other catalysts, when switching back to condition (I).

Table 25. Average changes, in percent, in the CH₃CHO formation rate relative to the first measurement condition, without H₂O in the feed.

Condition	AuAg/rutile	Au/rutile	Ag/rutile	Au/C
(II) 0.6 kPa H₂O	-4.0	37.9	-18.2	-2.8
(III) 2.0 kPa H₂O	3.4	63.7	-23.9	-55.1
(I) no H₂O	4.5	10.3	-4.4	-6.2

Thus, looking at the conversion, Figure 82, complements the picture as the (slight) variation of the feed is considered. Quantitative changes of the conversion, relative to condition (I), without water are printed in Figure 31. Indeed, whereas AuAg/rutile is rather indifferent to water, the beneficial effect of water is clearly visible for Au/rutile, and for Ag/rutile a decrease of conversion, from approx. 20% to 16% can be observed, which is not so evident when looking at the CH₃CHO formation rate, Figure 81.

Table 26. Average changes, in percent, in the conversion relative to the first measurement condition, without H₂O in the feed.

Condition	AuAg/rutile	Au/rutile	Ag/rutile	Au/C
(II)	4.7	51.4	5.9	-25.6
(III)	2.1	62.0	-12.6	-59.2
(I)	2.9	8.4	5.9	-14.0

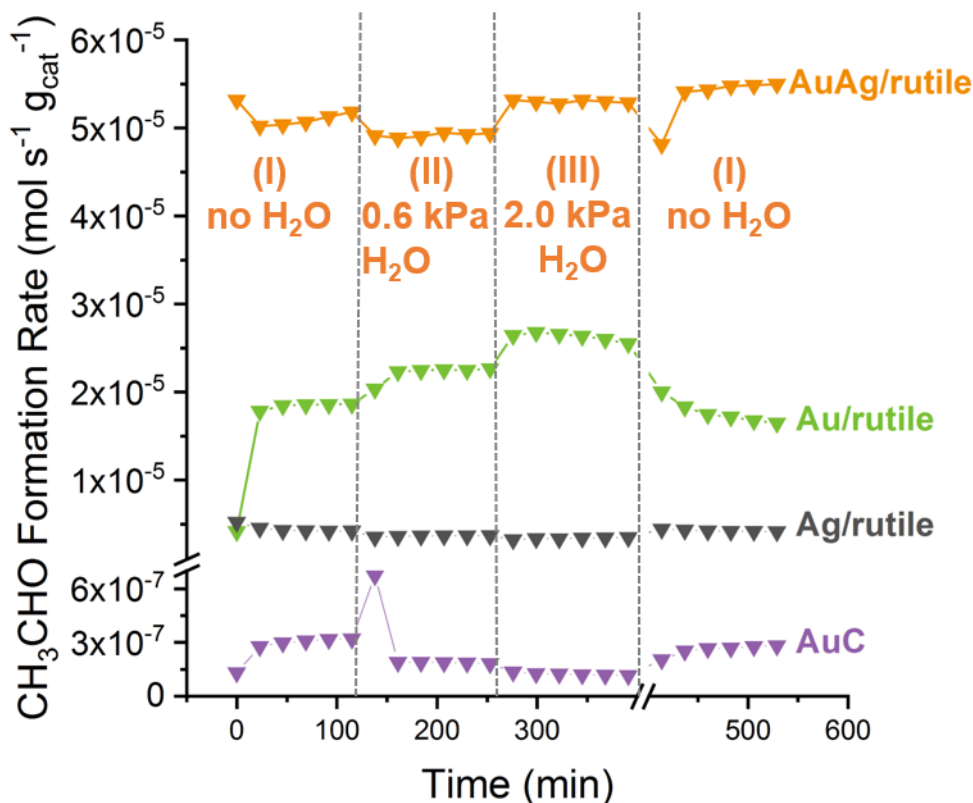


Figure 81. CH₃CHO formation rates for the measurements investigating the influence of water, AuAg/rutile (orange), Au/rutile (green), Ag/rutile (grey) as well as AuC/rutile (purple). The reaction was performed isothermally at 250°C under three different conditions: (I) 1.1 kPa EtOH/O₂ (no water), (II) 1.1 kPa EtOH/O₂ and 0.6 kPa H₂O and (III) 1.1 kPa EtOH/O₂ and 2.0 kPa H₂O. To see the reversibility of the water introduction effect, the measurement was concluded with applying conditions (I), without water, again.

The addition of water does not change the product distribution significantly with acetaldehyde being the main product, Figure 82. No shift towards acetic acid, the main product in liquid phase was observed, probably because the easy desorption of acetaldehyde is not at all hindered by water. For both AuAg/rutile and Au/rutile, the selectivity is de facto unchanged upon water addition. In condition (III), at a water partial pressure of 2.0 kPa, for Ag/rutile, small amounts of CO₂ formation, up to 1.0% is observed. At the beginning of the reaction, without water, up to 3% acetic acid are formed, which is then reduced to approx. 1.5% and stays at that level even when the water is removed from the feed. Au/C, on the other hand has relevant CO₂ formation, up to 7%, at the end of condition (II), which then remains after switching off water, but is slowly reducing in time to below 3%.

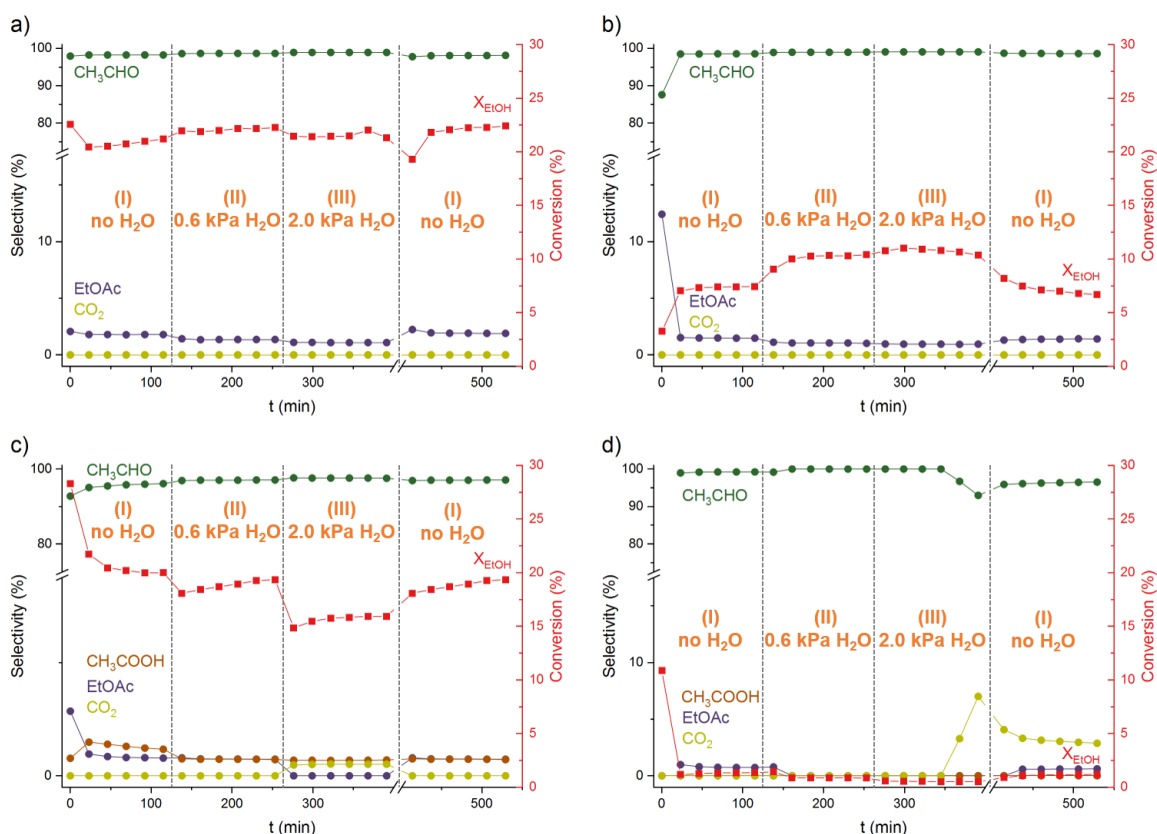


Figure 82. Selectivities for (a) AuAg/rutile, (b) Au/rutile, (c) Ag/rutile and (d) Au/C. The reaction was performed isothermally at 250°C under three different conditions: (I) 1.1 kPa EtOH/O₂ (no water), (II) 1.1 kPa EtOH/O₂ and 0.6 kPa H₂O and (III) 1.1 kPa EtOH/O₂ and 2.0 kPa H₂O. To see the reversibility of the water introduction effect, the measurement was concluded with applying conditions (I), without water, again.

Fujitani et al.⁶¹ report that, as observed by XPS measurements, water stabilizes oxidized Au species, Au(OH)₃ and Au₂O₃, during CO oxidation. However, unlike others for the CO oxidation¹⁵⁸, in this work no Au^{δ+} species could be detected. Moreover, a direct involvement of water in the O₂ activation (via the formation of hydroperoxy species)⁶¹ is proposed. In connection with the TiO₂ support, hydroxyl species play an important role in the oxygen adsorption⁶¹. As reported in a review of Diebold¹⁶⁶, in UHV, a high sticking coefficient of H₂O alongside a tendency to dissociate at vacancies is known for TiO₂. Water is known to interact with titania surfaces and surface hydroxyls can easily affect adsorption and reaction processes¹⁶⁶.

The amount of oxygen species on the Au/TiO₂ catalysts, determined by temporal analysis of products (TAP) for the CO oxidation (without water), was found to be proportional to the interface between Au and the TiO₂ support (the authors also postulate a mechanism, involving surface lattice oxygen at or close to Au perimeter sites, “Au-assisted Mars–van-

Krevelen mechanism”)⁵¹. Direct proof of this mechanism by NAP-XPS, sections 5.3.2 and 5.3.3, could not be achieved.

Thus, the indifference of the AuAg/rutile catalyst to water could lie in the oxygen activation. If oxygen availability, not necessarily O₂, but an activated form as required for the oxidation reaction, is not the limiting step anymore due to the promoting effect of Ag, naturally, water-enhanced oxygen activation would not result in a higher rate anymore. However, interestingly, on Ag there is a clear negative effect of the water in the feed.

Notably, the effect of water seems to be reversible: For Au/rutile, the promotional effect of H₂O disappears, and activity decreases to the point before water introduction. Also for Ag/rutile a “recovery” to higher conversion can be observed. For AuAg/rutile, as the conversion and CH₃CHO formation was changed on a smaller level only, this reversibility is not so clear and would probably take a longer time to reach steady-state conditions. Also for Au/C, the CO₂ formation is decreasing again after ceasing the water feed, but longer measurements would be necessary to prove the full reversibility. Thus reversibility is strongly in line with the kinetic role of water proposed based on computational results.

At this point, a small excursion into computational results obtained by J. E. de Vrieze shall be given. These results are reprinted with permission.

While at lower temperatures, below 250°C, a small increase of the TOF is observed, this is not true for higher temperatures, Figure 83. This is well in accordance with the kinetic data presented above where the Au/C does not show increased conversion (in fact, on a low conversion level due to the average large particle size of 14.5 nm, even a small decrease of activity is observed). This results in a water reaction order of approximately 0.1 for low temperatures and 0 above 250°C. The reaction order of O₂ for Au shows in fact a similar trend, although at higher values, which lead to the hypothesis that H₂O plays a role in the oxygen activation.

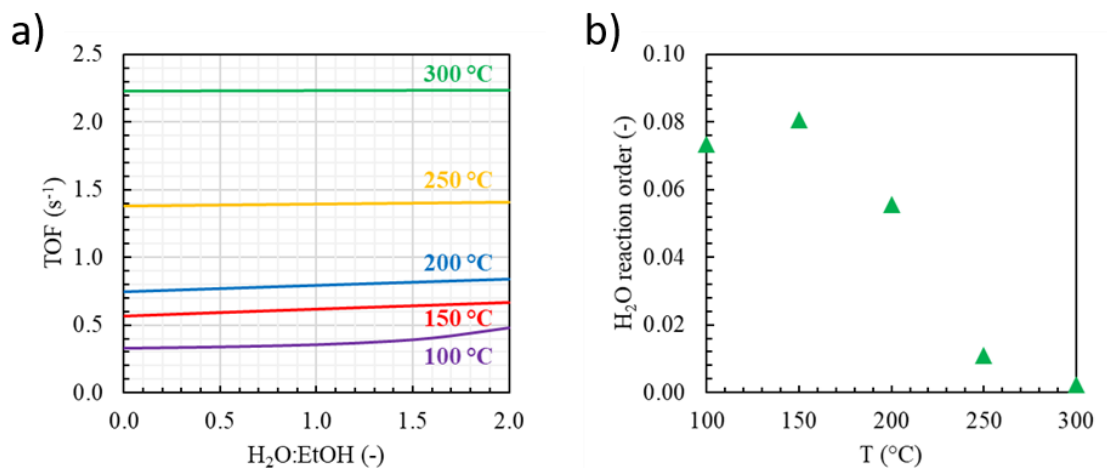


Figure 83. a) The effect of the temperature on the turnover frequency for different water-to-ethanol ratios and b) water reaction order for different reaction temperatures. Conditions: $X_{EtOH} = 10\%$, $EtOH:O_2 = 1:1$, $p_{EtOH} = 2.5$ kPa.

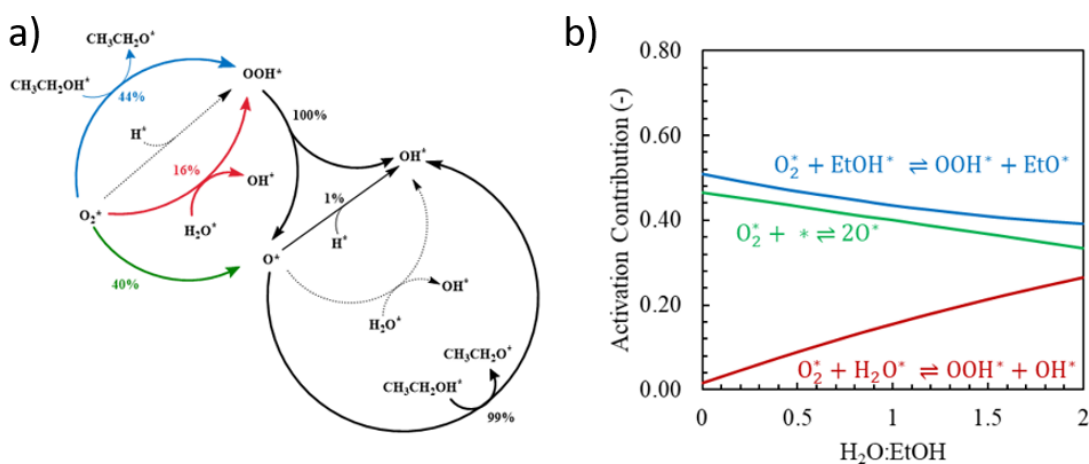


Figure 84. a) Reaction pathway for oxygen activation at a $H_2O:EtOH$ 1:1 molar ratio. The numbers indicate the fraction of each component consumed in the respective reaction step. Dotted arrows indicate reaction steps with a fraction below 0.5%. B. Activation pathway contribution for the significant oxygen activation pathway as a function of the water-to-ethanol molar ratio. Conditions: $T = 200$ °C, $X_{EtOH} = 10\%$, $EtOH:O_2 = 1:1$, $p_{EtOH} = 2.5$ kPa.

When $H_2O:EtOH = 1$, a significant fraction of O_2 is hydrogenated to OOH^* via proton transfer from water, something that didn't occur significantly in the absence of water (previous work). As such, water opens an alternative, low activated pathway for O_2 activation.

However, these calculations take the Au(111) surface into account, but disregard the support which seems to play a tremendous role in the interplay with water. This tremendous role of water was also studied by Grabow for CO oxidation⁴³.

Comparing to liquid-phase, the very different results could not be reproduced in the gas-phase, suggesting an entirely different reaction mechanism for each phase. AuAg/rutile still is very active with water, and even though water is beneficial for the Au/rutile sample, it cannot keep up with the AuAg/rutile reaction rate. Likewise, water introduction did not shift the selectivity towards acetic acid; acetaldehyde is still the main product produced with high yields.

6.3.2. Operando Spectroscopy

Operando DRIFTS measurements, Figure 85, were performed for the Au/rutile as well as the AuAg/rutile sample. In fact, for both samples, the spectra with/without water are nearly identical. Only the C-H bands as well as the $\nu(\text{C}=\text{O})$ band of $\text{CH}_3\text{CHO}_{\text{ads}}$ are slightly more pronounced for Au/rutile for the reaction conditions with water, indicating higher conversion as shown in section 6.3.1. The band attributed to COO (see section 3.3/5.3.1) at 1450 cm^{-1} is shifted to higher wavenumbers with water (1454 cm^{-1}) as well as for the Au/rutile sample (under both conditions), possibly due to the co-adsorption of water. Interestingly, this difference cannot be observed in the spectra presented in section 5.3.1, indicating some variability in the COO region from measurement to measurement.

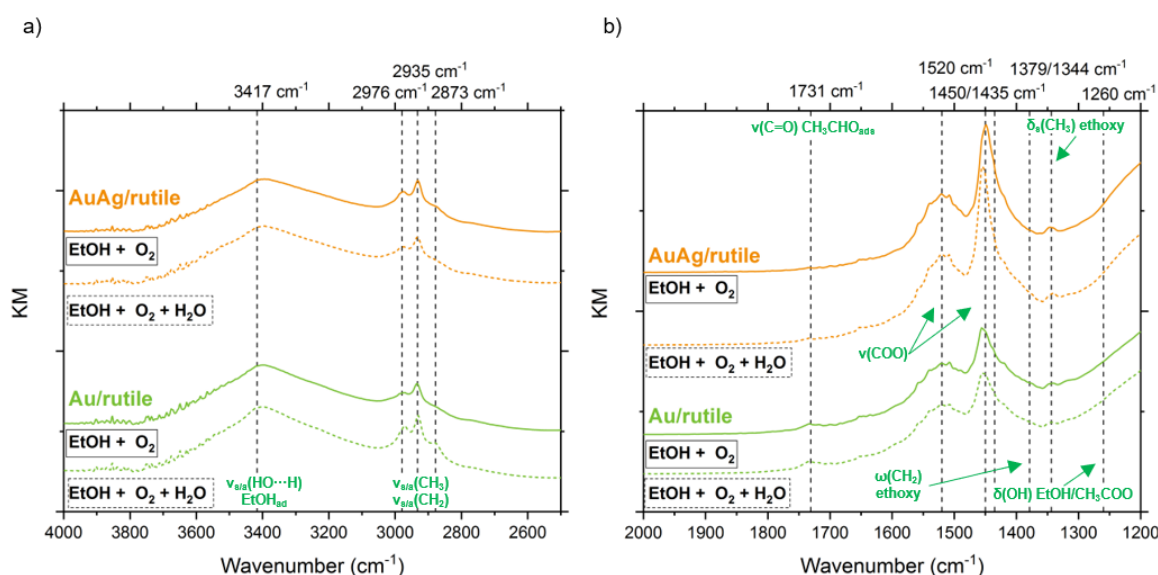


Figure 85. DRIFTS spectra for AuAg/rutile (orange) and Au/rutile (green). The solid lines indicate measurements without water, only EtOH/O₂ (1.1 kPa EtOH/O₂ He at a total flow of 49.6 mL/min) whereas the dashed lines mark the measurements EtOH/O₂/H₂O (1.1 kPa EtOH/O₂ and 2.0 kPa H₂O at a total flow of 50.6 mL/min). The displayed spectra are nearly identical, only the C-H bands as well as the $\nu(\text{C}=\text{O})$ band of $\text{CH}_3\text{CHO}_{\text{ads}}$ are slightly more pronounced for Au/rutile for the reaction conditions with water, indicating higher conversion as shown in section 6.3.1.

These nearly identical spectra showing the same species on the catalyst surface corroborates the hypothesis that the H₂O is supporting the oxygen activation and that the promotional effect of water is indeed a kinetic effect.

However, to probe for electronic changes upon water introduction, as part of the NAP-XPS beamtime at the ISISS beamline, BESSY II, also the influence of water addition to the feed was investigated. The Ag 3d detail/MNN Auger spectra are shown in Figure 86, whereas the Au 4f, Ti 2p and O 1s detail scans are depicted in Figure 87. The respective C1s spectra are shown in the annex, section 9.7.1.

The Ag 3d_{5/2} maximum was found at a binding energy of 368.3 eV with a FWHM of 0.8 eV and the Ag 3d_{3/2} was at 305.7 eV with a FWHM of 0.8 eV, respectively. Further binding energies relevant in this section: 84.4 eV for Au 4f_{7/2} and 88.1 eV for Au 4f_{5/2} (FWHM = 1.0 for both), for Ti 2p_{1/2} 464.8 eV (FWHM: 2.2 eV) and for Ti 2p_{3/2} 459.1 eV (FWHM: 1.4 eV), for O 1s 530.5 eV (FWHM: 1.7 eV). Also here, for the O 1s, the fitting of oxygen surface species (OH, H₂O, ethoxy, acetate, etc.) was not performed.

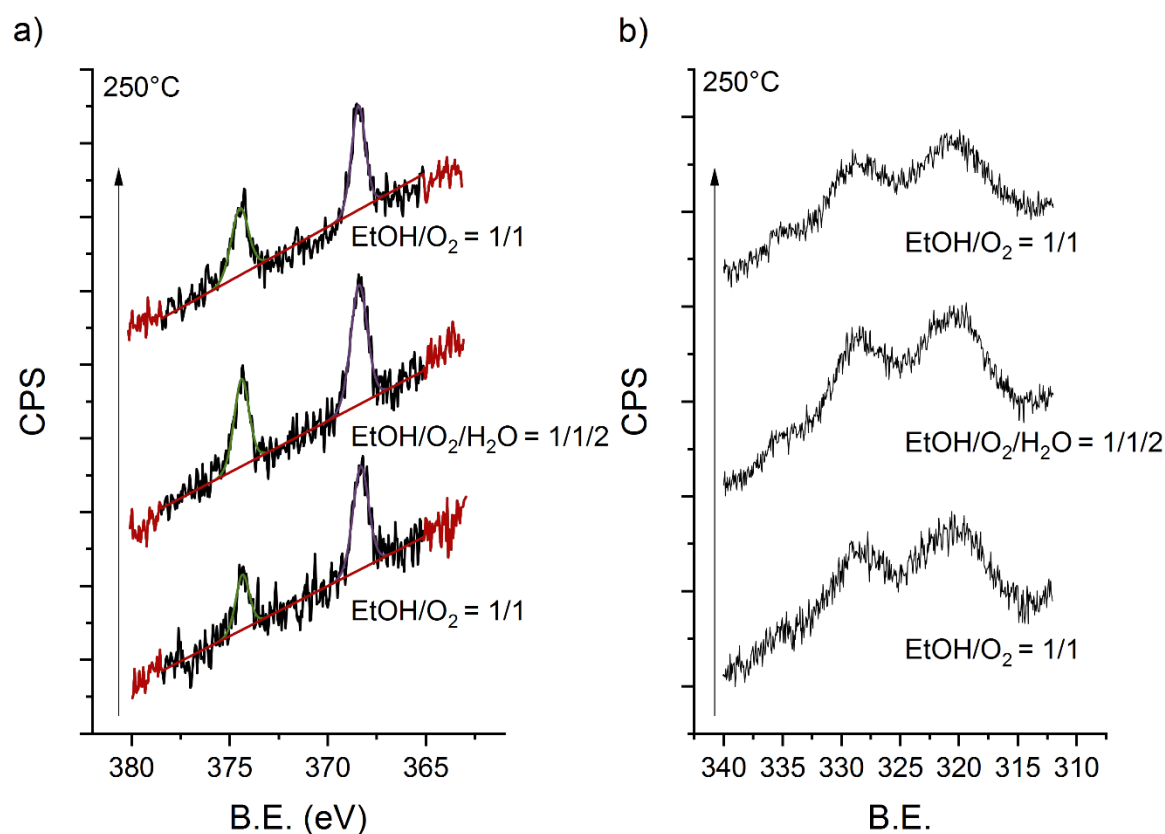


Figure 86. (a) Ag 3d peak of the AuAg/rutile sample as well as the (b) respective MNN Auger peaks. The spectra at the bottom were taken prior to water introduction whereas the top was taken after ending the water feed. EtOH/O₂ ratios were 1/1 with 2.5 mL/min flow of each, and for the measurement of the water-containing feed, additional 5 mL/min were added. Clearly, no difference of water is observed with the presence/absence of water. Spectra were taken at a kinetic energy of 310 eV.

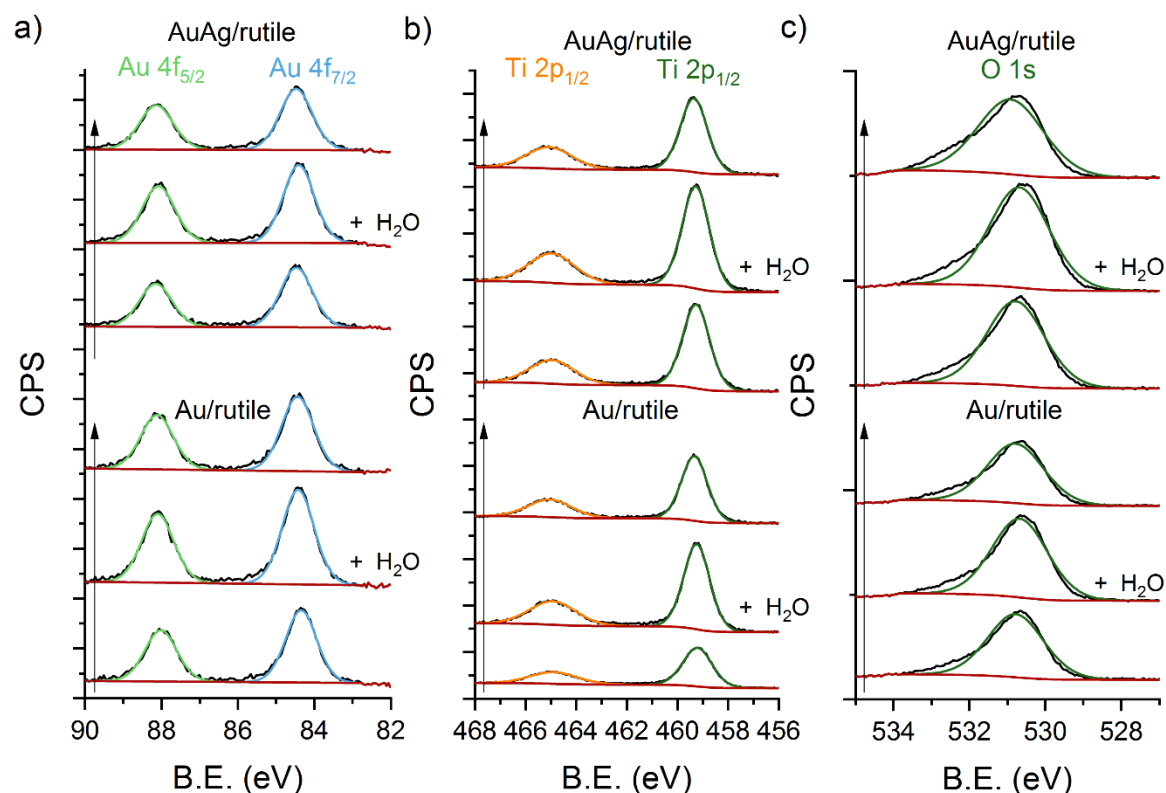


Figure 87. Detail spectra for Au/rutile (bottom) and AuAg/rutile (top) prior to H₂O introduction, during the reaction with EtOH/O₂/H₂O and after removing the H₂O from feed again, (a) Au 4f, (b) Ti 2p_{1/2} and (c) O 1s. The feed consisted of 2.5 mL/min EtOH and O₂ (each, resulting in a ratio of 1/1) and, for the measurement of the water influence, 5 mL/min were added (resulting in an EtOH/O₂/H₂O of 1/1/2), always at total pressure of 0.5 mbar and a temperature of 250°C. The spectra were taken at a kinetic energy of 310 eV.

For neither catalyst nor reaction condition, was any change to the electronic structure induced by water observed in the NAP-XPS. Peaks in Figure 86 (Ag 3d) and Figure 87 (Au 4f, Ti 2p and O 1s) are slightly higher under H₂O-containing atmosphere, possible only due to different scattering of photoelectrons at gas molecules.

A different situation presents itself for the Ag K-edge XAS measurements performed at the Diamond Light Source, B18 beamline. Figure 88 shows an enlarged view of the post-edge part of the XANES spectrum, a) for Ag/rutile and b) for AuAg/rutile. Whereas there is hardly any difference is observed for Ag/rutile, with and without the presence of water, the spectra differ significantly for AuAg/rutile.

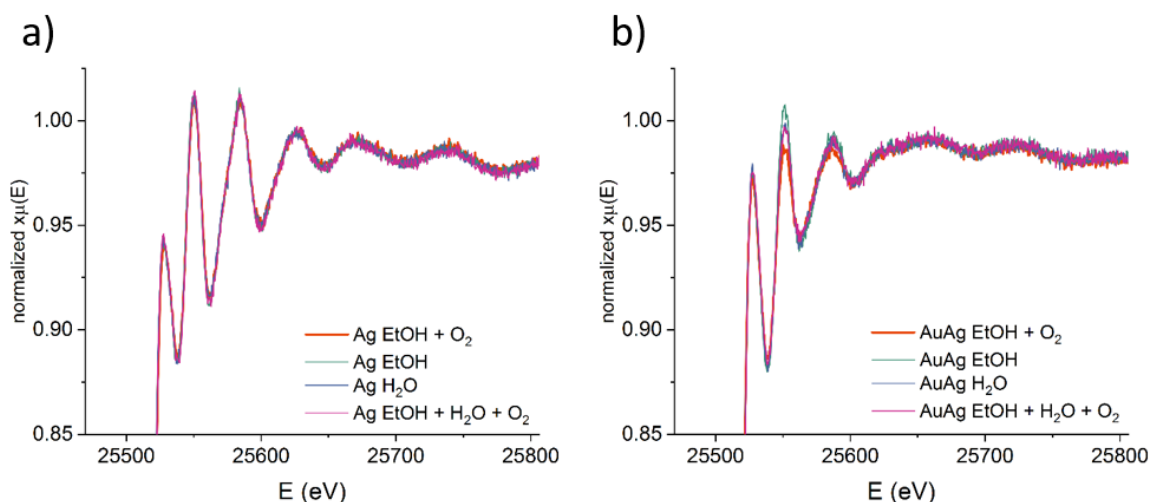


Figure 88. Enlargement of the post-edge part of the XANES for a) Ag/rutile and b) AuAg/rutile under different operando conditions: EtOH + O₂, EtOH only, H₂O only, EtOH + H₂O + O₂. Whereas there is hardly any difference is observed for Ag/rutile, the spectra differ significantly for AuAg/rutile.

Linear combination fits (LCFs) using Ag foil and Ag₂O as references were undertaken for both Ag/rutile and AuAg/rutile, Figure 89 and Figure 90, respectively. Table 27 shows the corresponding numerical results. For the AuAg/rutile, the weight of the Ag foil reference is the lowest with 54% under EtOH/O₂ flow, whereas under EtOH, H₂O and EtOH/H₂O/O₂ it increases to > 60% with the highest value in the most reducing atmosphere ethanol only. For the Ag/rutile sample, only very small variations were found and all values were within the error range of the fits, suggesting the fraction of reduced Ag remains more or less constant at around 66%. The slightly larger Ag₂O contribution was found for an atmosphere of water only.

Table 27. Quantitative of the linear combination fittings (LCFs) with the Ag foil and Ag₂O as references for AuAg/rutile and Ag/rutile under operando conditions.

	AuAg/rutile		Ag/rutile	
	Ag foil weight	Ag ₂ O weight	Ag foil weight	Ag ₂ O weight
EtOH/O ₂ (250°C)	0.54 ± 0.0	0.48 ± 0.05	0.66 ± 0.04	0.36 ± 0.04
EtOH (250°C)	0.66 ± 0.04	0.36 ± 0.04	0.66 ± 0.05	0.36 ± 0.05
H ₂ O (250°C)	0.61 ± 0.04	0.41 ± 0.04	0.64 ± 0.05	0.37 ± 0.04
EtOH/H ₂ O/O ₂ (250°C)	0.61 ± 0.04	0.41 ± 0.04	0.69 ± 0.04	0.32 ± 0.04

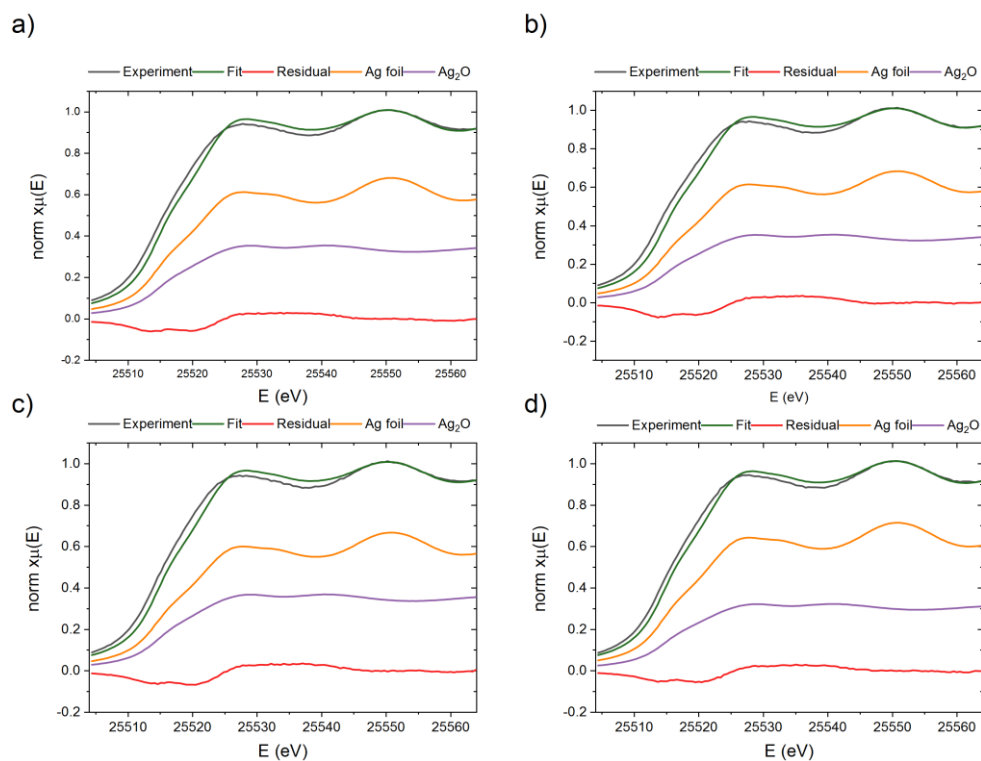


Figure 89. Linear combination fits (LCFs) for Ag/rutile exposed to a) 1.1 mL/min EtOH/ O_2 , b) 1.1 mL/min EtOH, c) H_2O and d) 1.1 mL/min EtOH/ H_2O and 0.25 mL/min O_2 . Ag foil and Ag_2O were used as references.

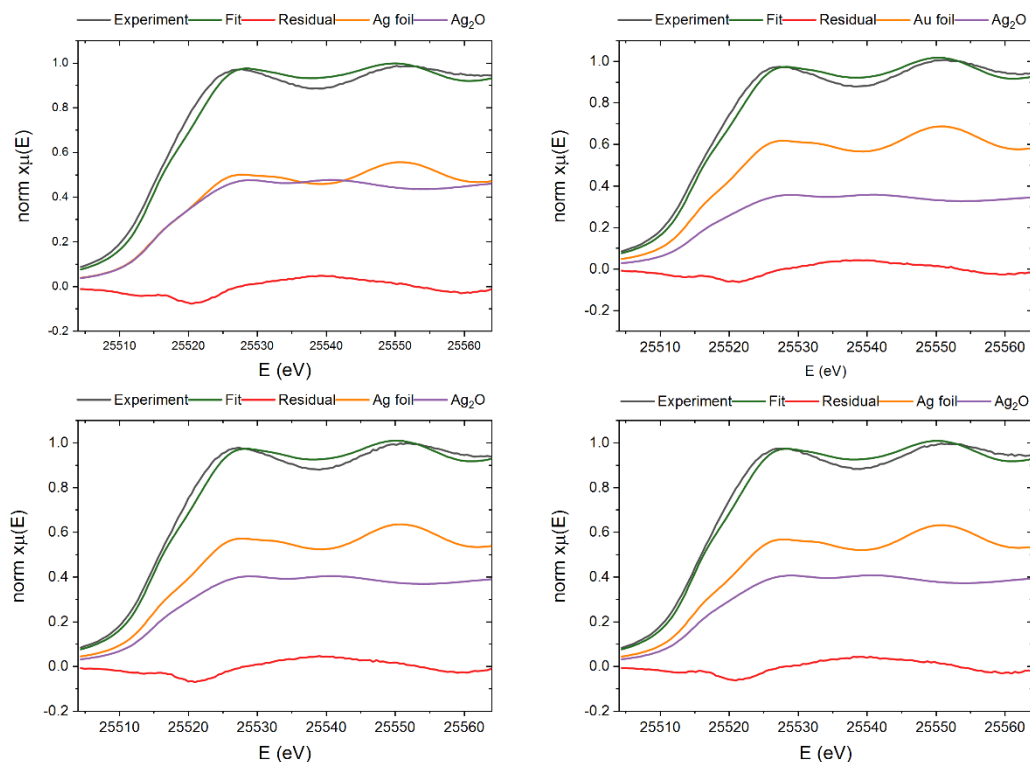


Figure 90. Linear combination fits (LCFs) for AuAg/rutile exposed to a) 1.1 mL/min EtOH/ O_2 , b) 1.1 mL/min EtOH, c) H_2O and d) 1.1 mL/min EtOH/ H_2O and 0.25 mL/min O_2 . Ag foil and Ag_2O were used as references.

However, using Ag/rutile after oxidation and after reduction, as the more suitable reference, yields a clearer overview of the results, see Figure 91 for Ag/rutile and Figure 92 for AuAg/rutile. Table 28 lists the numerical results of the fits showing that AuAg/rutile spectra can be fitted with significantly larger weight of the Ag/rutile after oxidation, 21% under EtOH/O₂ flow which decreases to 8% for EtOH only and then increases to 13% and 11% under H₂O flow and EtOH/H₂O/O₂ flow, respectively. For Ag/rutile, the XANES spectrum can be nearly solely described with the Ag/rutile after reduction.

However again, it has to be kept in mind that Ag/rutile after the reduction does not at all equal 100% reduced silver, but is still fitted with 36% weight for the Ag₂O reference. These fits serve merely to help in identifying potential changes under different reaction atmospheres.

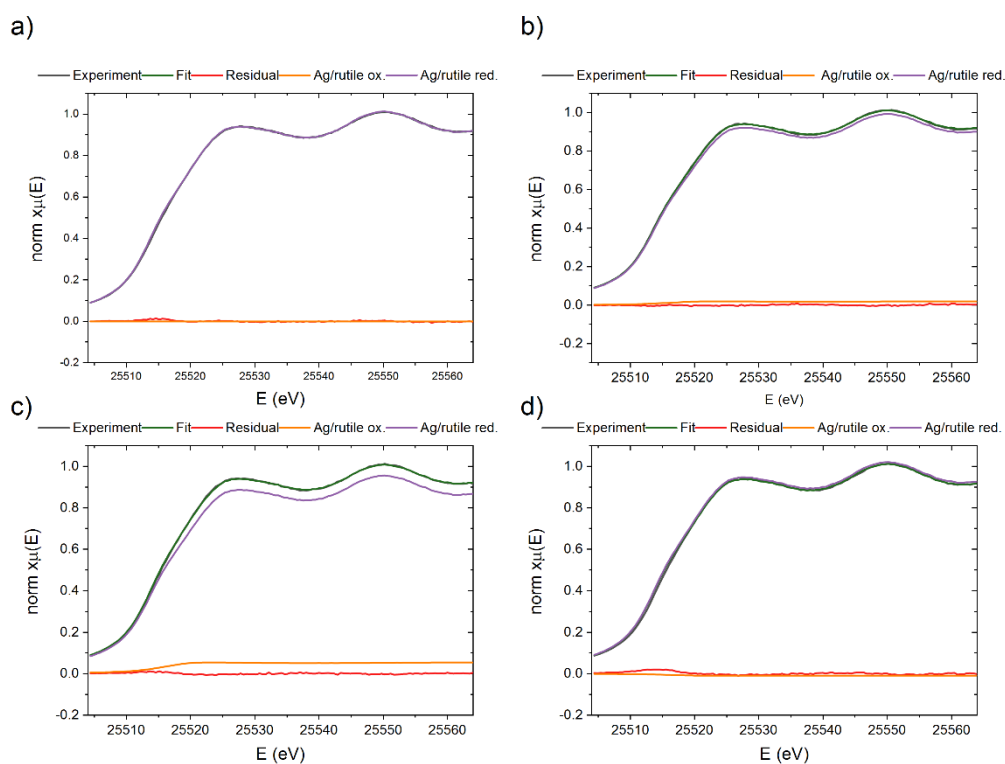


Figure 91. Linear combination fits (LCFs) for Ag/rutile exposed to a) 1.1 mL/min EtOH/O₂, b) 1.1 mL/min EtOH, c) H₂O and d) 1.1 mL/min EtOH/H₂O and 0.25 mL/min O₂. Ag/rutile after oxidation and after reduction were used as references.

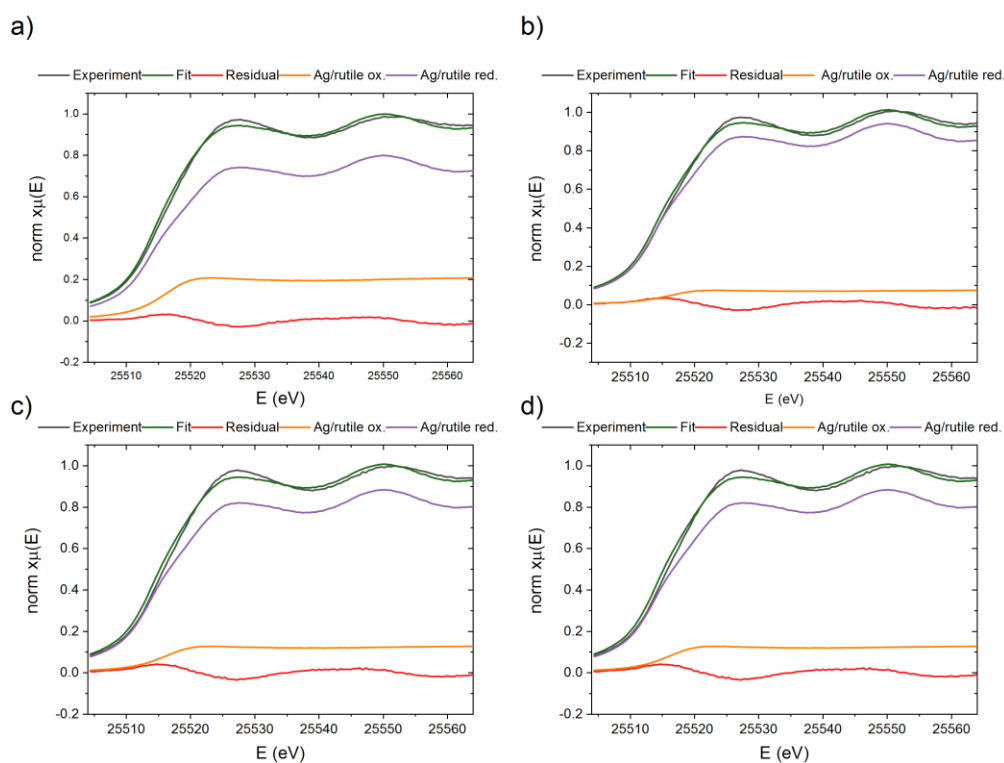


Figure 92. Linear combination fits (LCFs) for AuAg/rutile exposed to a) 1.1 mL/min EtOH/O₂, b) 1.1 mL/min EtOH, c) H₂O and d) 1.1 mL/min EtOH/H₂O and 0.25 mL/min O₂. Ag/rutile after oxidation and after reduction were used as references.

Table 28. Quantitative of the linear combination fittings (LCFs) with the Ag/rutile after oxidation and after reduction as references for AuAg/rutile and Ag/rutile under operando conditions.

	AuAg/rutile		Ag/rutile	
	Ag/rutile red. weight	Ag/rutile ox. weight	Ag/rutile red. weight	Ag/rutile ox. weight
EtOH/O₂ (250°C)	0.79 ± 0.02	0.21 ± 0.02	1.00 ± 0.02	0.00 ± 0.01
EtOH (250°C)	0.93 ± 0.03	0.08 ± 0.03	0.98 ± 0.03	0.02 ± 0.00
H₂O (250°C)	0.87 ± 0.03	0.13 ± 0.03	0.94 ± 0.03	0.06 ± 0.01
EtOH/H₂O/O₂ (250°C)	0.90 ± 0.03	0.11 ± 0.03	1.01 ± 0.03	-0.01 ± 0.01

Thus, whereas the Ag in the Ag/rutile sample remains relatively unchanged during the different reaction conditions, the amount reduced silver is increasing for AuAg/rutile when switching from EtOH/O₂ to EtOH, H₂O or EtOH/H₂O/O₂. Possibly this gives an

explanation why reaction rate is rather not much affected from H₂O for Ag/rutile while the AuAg/rutile is reacts rather sensitively to water.

6.4. Conclusion

Water imposes various effects on the investigated catalysts. For the Au/rutile catalyst, a clear promotional effect is observed, more water leads to higher activity. As reported in literature⁶¹ and supported by calculations from J.E. de Vrieze, the water promotes the oxygen activation, thus leading to higher reaction rates. For Ag/rutile on the other hand the effect of water is relatively small, even a (small) decline in activity is observed. Therefore, for AuAg/rutile, a combination of the two effects is expected, and a slight decline for low water partial pressures of 0.6 kPa is seen whereas at 2.0 kPa the activity increases again. Interestingly, for Au/C, this promotional effect could not be observed, showing that rutile is an essential element in the promotional effect of water.

Several methods have been employed to test for water-induced changes to the catalyst and/or to the reaction mechanism. STEM-HAADF showed a surprising sintering due to water for Au/rutile, which does not reduce the catalytic activity. In fact, the promotional effect of water is not only overcompensating for the sintering: Also ending the H₂O feed results in nearly the same reaction rate as observed before water introduction (eventually a slight decrease could be suspected). For AuAg/rutile, water seems to lead to smaller particles, which is exactly the opposite trend that is observed for Au/rutile and AuAg/rutile without water. However, also here, no particle size effect could be observed.

In the NAP-XPS experiment, no electronical changes imposed by water could be observed and the adsorbed species, as measured by DRIFTS, don't show a different pattern with water. In XAS measurements of the Ag K-edge, however for AuAg/rutile an increased proportion of reduced Ag was observed under reaction conditions involving water whereas the Ag/rutile remained unaffected by water addition. However, the most likely kinetic nature of the water effect seems to be reversible and not corresponding to any changes in the catalyst structure.

The comparison with the liquid phase resulted in the striking revelation that catalysts showing high activity in the liquid-phase don't do so in the gas-phase and vice versa. Catalysts can be ordered by activity in the liquid-phase as follows: AuPt > Au > AuRu >

AuAg (with Au being the more interesting catalyst as it shows higher selectivity). Surprisingly, the AuAg/rutile, favored in the gas-phase reaction, is the least active one in the liquid phase (gas phase: AuAg > Au > AuRu > AuPt). In fact, for the liquid-phase both solvation⁵⁷ and the gold-water interface³⁰ play a role in the proposed reaction mechanism, both of which are absent in the gas-phase. Thus, the observed differences between liquid-phase and gas-phase can indeed be attributed to different reaction mechanisms due to different phases and cannot be explained by the sole presence of water in the reaction feed.

7. General Conclusions

In this thesis, modified supported Au catalysts were explored for the selective ethanol oxidation, a both economically and ecologically interesting reaction to establish green chemistry and substitute fossil feedstock.

Starting with a thorough understanding of the monometallic gold system, high selectivities of > 97% towards acetaldehyde were observed with no significant total oxidation of ethanol to CO₂. From the different supports investigated in this work (ZnO, Al₂O₃ and TiO₂), the TiO₂ in the rutile modification was proved to be the best catalyst support yielding high reaction rates, acetaldehyde selectivity and stability. Whereas use of anatase showed reasonable activity, though below rutile, mixtures of anatase and rutile (commercially as AUROLite/TiO₂ or prepared on P25 or an artificial mixture of 80% anatase and 20% rutile) showed considerably lower product formation.

A carbon-supported commercial catalyst, Au/C, was used as model system for Au nanoparticles on an inert support. This provided a quantitative measure of the rutile support's influence on the reaction as well as a reference system to validate computational DFT results obtained by J. E. de Vrieze in M. Saeys' group, Ghent University, Belgium.

Experimental and computational results were in good agreement for the Au/C catalyst. Rather than one route being dominant, the reaction path analysis showed that proton transfer of ethanol can go to atomic oxygen, surface hydroxyl species and molecular oxygen, the contribution of each step depending on the operating conditions. In addition, it was shown that the temperature dependence of the reaction orders is a result of a mix of rate-limiting steps. At low temperatures, both oxygen activation (both direct or via proton transfer to hydroperoxyl) and ethoxy oxidation are rate-limiting. When the temperature increases, the ethoxy β -H elimination becomes increasingly dominant resulting in an increase in the ethanol order. The different reaction order for EtOH and O₂ for the Au/rutile sample can be attributed to rutile: It shows a higher EtOH order and an oxygen order that is decreasing with the temperature, indicating better availability of oxygen at higher temperatures, possible due to higher mobility of oxygen vacancies or a higher degree of Ti³⁺ species.

Bimetallic catalysts were prepared on the basis of phase-pure rutile and various promoting metals were tested: Ag, Ru, Pt. flame spray pyrolysis-prepared from M. Mostrou-Moser from the van Bokhoven group with Ag, Pd and Pt was also evaluated.

Silver was identified to be the most suitable promoter for the gas-phase oxidation, increasing the reaction rate as well as improving selectivity (on an already high level). Ag had a profound influence by decreasing the reaction orders for EtOH and O₂. The latter suggests involvement in the oxygen activation. STEM-EDX revealed bimetallic AuAg particles on both carbon and rutile after the pretreatment. However, under *operando* conditions, NAP-XPS reveals a drastic depletion of Ag from the rutile surface, surprisingly rather eliminating the possibility of Ag₂O formation on the nanoparticle surface. For the AuAg/C, an alloying and no Ag depletion from the surface is hypothesized, explaining the different kinetic results.

Thus, the majority of the silver in Au/rutile is catalytically active being far away from the gold, supposedly within the rutile, facilitating oxygen activation there (and also involving EtOH, as the effect on the EtOH reaction rate is not negligible). For both Au/rutile and AuAg/rutile, DRIFTS revealed ethoxy species as the dominant intermediate on the surface as well as COO bands that are increasing/decreasing with conversion, however, computational results show that these acetate species assume a spectating role only. Depending on the conversion, also acetaldehyde could be detected on the surface.

Finally, the influence of water was investigated, first by comparing the gas-phase reaction to the liquid-phase reaction, the latter performed by M. Mostrou-Moser in the van Bokhoven group, ETH Zürich. A reversed trend of active catalysts was found, with the catalyst activity ordered as follows in the liquid-phase: AuPt > Au > AuRu > AuAg (with Au being the more interesting catalyst as it shows higher selectivity). Surprisingly, the AuAg/rutile, favored in the gas-phase reaction, is the least active one in the liquid phase (gas phase: AuAg > Au > AuRu > AuPt). Gas-phase experiments with water in the feed revealed that water has an activating effect on Au/rutile and all in all just minor effects on Ag/rutile. For the bimetallic AuAg, a slight decrease of activity was found at 0.6 kPa water and an increase at a water partial pressure of 2.0 kPa, showing a mixed, rather complex effect on Au and Ag. Interestingly, the promotional effect was depending on the presence of rutile and could not be observed for Au/C. Thus, it could be proved that the results of the liquid-phase could not be reproduced in the gas-phase by water introduction, showing

that the different behavior must be attributed to the liquid-phase and a different reaction mechanism must be assumed. Also, for the gas-phase, NAP-XPS involving a water-containing feed did not show any water-induced electronical changes and DRIFTS did not reveal any different species on the catalyst surface. In XAS measurements of the Ag K-edge, however for AuAg/rutile an increased proportion of reduced Ag was observed under reaction conditions involving water whereas the Ag/rutile remained unaffected by water addition. However, the kinetic nature of the water effect seems to be reversible and not corresponding to any changes in the catalyst structure, leading to the conclusion that the effect is a merely kinetic one (especially for Au/rutile, where no silver is involved).

This is supported by the fact that the effect of water is reversible for the investigated catalysts. Interestingly, a water-induced sintering effect could be observed for Au/rutile and a decrease of the mean particle size for AuAg/rutile. Both effects seem to have limited effect on the catalytic activity. Also, for the reaction without water, the observed trend is reversed, showing smaller particles for Au/rutile and (minor) sintering for AuAg/rutile.

Even though this thesis deals with bimetallic Au catalysts, a few words about the Ag/catalysts shall be spent: With its low metal loading of 1 wt.% on rutile and substantially lower cost, Ag/rutile is a remarkably interesting catalyst for the ethanol oxidation (as well as other alcohols¹⁶⁷). Furthermore, it also shows the very same Ag depletion effect while still being catalytically active.

In conclusion, the AuAg catalyst supported on rutile is a very promising system for ethanol oxidation. In this thesis, together with the project partners, we disproved the common believe that Ag atoms dispersed in the Au surface are responsible for the increased catalyst performance. However, the research results also raise a lot of new questions: where the silver goes to and how it promotes ethanol oxidation, while migrating into the support. Knowledge of this promotional mechanism is vital for catalyst optimization, something specifically important when working with expensive materials like gold. Based on the work I performed throughout my thesis, I propose the following future work to move closer in solving the AuAg puzzle:

In-depth evaluation of the EXAFS data obtained at ALBA and the Diamond Light Source will shed more light on the oxidation state of the silver and its chemical surrounding. *In-situ* (S)TEM can give more information on the silver's mysterious whereabouts (currently underway). Furthermore, comparing the behavior on differently supported AuAg catalysts

(e.g. ZnO, Al₂O₃) and performing (NAP-)XPS will reveal if this depletion effect can be found in other systems too.

Information on reaction intermediates can be obtained by DRIFTS under dynamic conditions using the Concentration Modulation Approach (CMA) with Phase Sensitive Detection (PSD) analysis^{168,169}, an approach that was successfully employed in our group for the Pd₂Ga/Ga₂O₃ system¹⁷⁰. That way, very small changes under non-steady-state conditions can be made visible, giving insight into the mechanistic differences between the AuAg/rutile and the Au/rutile system.

8. References

- (1) Hagen, J. *Industrial Catalysis - A Practical Approach*, Third Comp.; Wiley-VCH Verlag GmbH & Co. KGaA: Weinheim, 2015.
- (2) Dodds, D. R.; Gross, R. A. *Science* **2007**, *318* (5854), 1250–1251.
- (3) Vennestrøm, P. N. R.; Osmundsen, C. M.; Christensen, C. H.; Taarning, E. *Angew. Chemie - Int. Ed.* **2011**, *50* (45), 10502–10509.
- (4) Taarning, E.; Egeblad, K.; Christensen, C. H.; Rass-Hansen, J.; Marsden, C. C. *ChemSusChem* **2008**, *1* (4), 283–289.
- (5) International Energy Agency. Market Report Series: Renewables 2018 <https://www.iea.org/renewables2018/transport/> (accessed Mar 27, 2019).
- (6) Sarkar, N.; Ghosh, S. K.; Bannerjee, S.; Aikat, K. *Renew. Energy* **2012**, *37* (1), 19–27.
- (7) Aditiya, H. B.; Mahlia, T. M. I.; Chong, W. T.; Nur, H.; Sebayang, A. H. *Renew. Sustain. Energy Rev.* **2016**, *66*, 631–653.
- (8) Stephen, J. D.; Mabee, W. E.; Saddler, J. N. *Biofuels, Bioprod. Biorefining* **2012**, *6* (2), 159–176.
- (9) Zabed, H.; Sahu, J. N.; Suely, A.; Boyce, A. N.; Faruq, G. *Renew. Sustain. Energy Rev.* **2017**, *71* (January), 475–501.
- (10) Söderberg, C.; Eckerberg, K. *For. Policy Econ.* **2013**, *33* (2013), 112–119.
- (11) Rarbach, M.; Sötl, Y. *Chim. Int. J. Chem.* **2013**, *67* (10), 732–734.
- (12) Clariant. Groundbreaking for Clariant’s Sunliquid® Cellulosic Ethanol Plant in Romania <https://www.clariant.com/en/Corporate/News/2018/09/Groundbreaking-for-Clariantrsquos-sunliquidreg-cellulosic-ethanol-plant-in-Romanianbsp> (accessed Mar 27, 2019).
- (13) Eckert, M.; Fleischmann, G.; Jira, R.; Bolt, H. M.; Golka, K. *Ullmann’s Encyclopedia of Industrial Chemistry*. December 15, 2006.
- (14) Reinhard, J. *Angew. Chemie Int. Ed.* **2009**, *48* (48), 9034–9037.
- (15) Le Berre, C.; Serp, P.; Kalck, P.; Torrence, G. P. *Ullmann’s Encyclopedia of*

Industrial Chemistry. March 26, 2014.

- (16) Pina, C. Della; Falletta, E.; Rossi, M. *Chem. Soc. Rev.* **2012**, *41* (1), 350–369.
- (17) Tembe, S. M.; Patrick, G.; Scurrall, M. S. *Gold Bull.* **2009**, *42* (4), 321–327.
- (18) Thompson, D. T. *Platin. Met. Rev.* **2004**, *48* (4), 169–172.
- (19) Corma, A.; Garcia, H. *Chem. Soc. Rev.* **2008**, *37* (9), 2096–2126.
- (20) Haruta, M.; Kobayashi, T.; Sano, H.; Yamada, N. *Chem. Lett.* **1987**, *16* (2), 405–408.
- (21) Haruta, M.; Yamada, N.; Kobayashi, T.; Iijima, S. *J. Catal.* **1989**, *115* (2), 301–309.
- (22) Murdoch, M.; Waterhouse, G. I. N.; Nadeem, M. A.; Metson, J. B.; Keane, M. A.; Howe, R. F.; Llorca, J.; Idriss, H. *Nat. Chem.* **2011**, *3* (6), 489–492.
- (23) Tsukamoto, D.; Shiraishi, Y.; Sugano, Y.; Ichikawa, S.; Tanaka, S.; Hirai, T. *J. Am. Chem. Soc.* **2012**, *134* (14), 6309–6315.
- (24) Prati, L.; Rossi, M. *J. Catal.* **1998**, *176* (2), 552–560.
- (25) Christensen, C. H.; Jørgensen, B.; Rass-Hansen, J.; Egeblad, K.; Madsen, R.; Klitgaard, S. K.; Hansen, S. M.; Hansen, M. R.; Andersen, H. C.; Riisager, A. *Angew. Chemie* **2006**, *118* (28), 4764–4767.
- (26) Wittstock, A.; Zielasek, V.; Biener, J.; Friend, C. M.; Bäumer, M. *Science* (80-.). **2010**, *327* (5963), 319–322.
- (27) Xu, B.; Madix, R. J.; Friend, C. M. *J. Am. Chem. Soc.* **2010**, *132* (46), 16571–16580.
- (28) Xu, B.; Liu, X.; Haubrich, J.; Madix, R. J.; Friend, C. M. *Angew. Chemie Int. Ed.* **2009**, *48* (23), 4206–4209.
- (29) Xu, B.; Haubrich, J.; Baker, T. A.; Kaxiras, E.; Friend, C. M. *J. Phys. Chem. C* **2011**, *115* (9), 3703–3708.
- (30) Zope, B. N.; Hibbitts, D. D.; Neurock, M.; Davis, R. J. *Science* (80-.). **2010**, *533* (OCTOBER), 74–79.
- (31) Zhong, W.; Liang, J.; Hu, W.; Cao, X.; Jia, C.; Jiang, J. *Phys. Chem. Chem. Phys.* **2016**, *18* (15), 9969–9978.

- (32) Kosuda, K. M.; Wittstock, A.; Friend, C. M.; Bäumer, M. *Angew. Chemie Int. Ed.* **2012**, *51* (7), 1698–1701.
- (33) Liu, X.; Xu, B.; Haubrich, J.; Madix, R. J.; Friend, C. M. *J. Am. Chem. Soc.* **2009**, *131* (16), 5757–5759.
- (34) Guan, Y.; Hensen, E. J. M. *Appl. Catal. A Gen.* **2009**, *361* (1–2), 49–56.
- (35) Boronat, M.; Corma, A.; Illas, F.; Radilla, J.; Ródenas, T.; Sabater, M. J. *J. Catal.* **2011**, *278* (1), 50–58.
- (36) Gong, J.; Mullins, C. B. *J. Am. Chem. Soc.* **2008**, *130* (49), 16458–16459.
- (37) Dong, W.; Reichenberger, S.; Chu, S.; Weide, P.; Ruland, H.; Barcikowski, S.; Wagener, P.; Muhler, M. *J. Catal.* **2015**, *330*, 497–506.
- (38) Shang, C.; Liu, Z.-P. *J. Am. Chem. Soc.* **2011**, *133* (25), 9938–9947.
- (39) Liu, Z.-P.; Gong, X.-Q.; Kohanoff, J.; Sanchez, C.; Hu, P. *Phys. Rev. Lett.* **2003**, *91* (26), 266102.
- (40) Liu, Z.-P.; Hu, P.; Alavi, A. *J. Am. Chem. Soc.* **2002**, *124* (49), 14770–14779.
- (41) Wittstock, A.; Neumann, B.; Schaefer, A.; Dumbuya, K.; Kübel, C.; Biener, M. M.; Zielasek, V.; Steinrück, H.-P.; Gottfried, J. M.; Biener, J. *J. Phys. Chem. C* **2009**, *113* (14), 5593–5600.
- (42) Abad, A.; Concepción, P.; Corma, A.; García, H. *Angew. Chemie - Int. Ed.* **2005**, *44* (26), 4066–4069.
- (43) Saavedra, J.; Doan, H. A. H. A.; Pursell, C. J.; Grabow, L. C.; Chandler, B. D. *Science* (80-.). **2014**, *345* (6204), 1599–1602.
- (44) Camellone, M. F.; Zhao, J.; Jin, L.; Wang, Y.; Muhler, M.; Marx, D. *Angew. Chemie - Int. Ed.* **2013**, *52*, 5780–5784.
- (45) Mullen, G. M.; Evans, E. J.; Sabzevari, I.; Long, B. E.; Alhazmi, K.; Chandler, B. D.; Mullins, C. B. *ACS Catal.* **2017**, *7* (2), 1216–1226.
- (46) Shekhar, M.; Wang, J.; Lee, W.-S.; Williams, W. D.; Kim, S. M.; Stach, E. A.; Miller, J. T.; Delgass, W. N.; Ribeiro, F. H. *J. Am. Chem. Soc.* **2012**, *134* (10), 4700–4708.

- (47) Ide, M. S.; Davis, R. J. *Acc. Chem. Res.* **2014**, *47* (3), 825–833.
- (48) Gao, Y.; Zeng, X. C. *ACS Catal.* **2012**, *2* (12), 2614–2621.
- (49) Van Bokhoven, J. a.; Louis, C.; Miller, J. T.; Tromp, M.; Safonova, O. V.; Glatzel, P. *Angew. Chemie - Int. Ed.* **2006**, *45* (28), 4651–4654.
- (50) Comotti, M.; Li, W. C.; Spliethoff, B.; Schüth, F. *J. Am. Chem. Soc.* **2006**, *128* (3), 917–924.
- (51) Widmann, D.; Behm, R. J. *Angew. Chemie - Int. Ed.* **2011**, *50* (43), 10241–10245.
- (52) Widmann, D.; Behm, R. J. *Acc. Chem. Res.* **2014**, *47* (3), 740–749.
- (53) Prati, L.; Martra, G. *Gold Bull.* **1999**, *32* (3), 96–101.
- (54) Heeskens, D.; Aghaei, P.; Kaluza, S.; Strunk, J.; Muhler, M. *Phys. Status Solidi* **2013**, *250* (6), 1107–1118.
- (55) Christensen, C. H.; Jørgensen, B.; Rass-Hansen, J.; Egeblad, K.; Madsen, R.; Klitgaard, S. K.; Hansen, S. M.; Hansen, M. R.; Andersen, H. C.; Riisager, A.; Rass- Hansen, J.; Egeblad, K.; Madsen, R.; Klitgaard, S. K.; Hansen, S. M.; Hansen, M. R.; Andersen, H. C.; Riisager, A. *Angew. Chemie - Int. Ed.* **2006**, *45* (28), 4648–4651.
- (56) Mostrou, S.; Sipócz, T.; Nagl, A.; Földi, B.; Darvas, F.; Föttinger, K.; Van Bokhoven, J. A. *React. Chem. Eng.* **2018**, *accepted* (1), 1–38.
- (57) Muñoz-Santiburcio, D.; Farnesi Camellone, M.; Marx, D. *Angew. Chemie - Int. Ed.* **2018**, *57* (13), 3327–3331.
- (58) Singh, A.; Rangaiah, G. P. *Ind. Eng. Chem. Res.* **2017**, *56* (18), 5147–5163.
- (59) Sobolev, V. I.; Koltunov, K. Y.; Simakova, O. A.; Leino, A. R.; Murzin, D. Y. *Appl. Catal. A Gen.* **2012**, *433–434*, 88–95.
- (60) Holz, M. C.; Tölle, K.; Muhler, M. *Catal. Sci. Technol.* **2014**, *4* (10), 3495–3504.
- (61) Fujitani, T.; Nakamura, I.; Haruta, M. *Catal. Letters* **2014**, *144* (9), 1475–1486.
- (62) Villa, A.; Wang, D.; Su, D. S.; Prati, L. *Catal. Sci. Technol.* **2015**, *5* (1), 55–68.
- (63) Carrettin, S.; McMorn, P.; Johnston, P.; Griffin, K.; Kiely, C. J.; Hutchings, G. J.

- Phys. Chem. Chem. Phys.* **2003**, *5* (6), 1329–1336.
- (64) Porta, F.; Prati, L. *J. Catal.* **2004**, *224* (2), 397–403.
- (65) Wang, A.; Liu, X. Y.; Mou, C. Y.; Zhang, T. *J. Catal.* **2013**, *308*, 258–271.
- (66) Jiang, P.; Porsgaard, S.; Borondics, F.; Kober, M.; Caballero, A.; Bluhm, H.; Besenbacher, F.; Salmero, M. *J. Am. Chem. Soc.* **2010**, *132* (9), 2858–2859.
- (67) Abad, A.; Corma, A.; García, H. *Chem. - A Eur. J.* **2008**, *14* (1), 212–222.
- (68) Chen, M. S.; Goodman, D. W. *Science (80-.)*. **2004**, *306* (October), 252–255.
- (69) Remediakis, I. N.; Lopez, N.; Nørskov, J. K. *Angew. Chemie - Int. Ed.* **2005**, *44* (12), 1824–1826.
- (70) Weiher, N.; Beesley, A. M.; Tsapatsaris, N.; Delannoy, L.; Louis, C.; Van Bokhoven, J. A.; Schroeder, S. L. M. *J. Am. Chem. Soc.* **2007**, *129* (8), 2240–2241.
- (71) Dimitratos, N.; Lopez-Sanchez, J. A.; Hutchings, G. J. *Chem. Sci.* **2012**, *3* (1), 20–44.
- (72) Davis, S. E.; Ide, M. S.; Davis, R. J. *Green Chem.* **2013**, *15* (1), 17–45.
- (73) Fiorenza, R.; Crisafulli, C.; Scirè, S.; Scirè, S. *Int. J. Hydrogen Energy* **2016**, *41* (42), 19390–19398.
- (74) Liu, J. H.; Wang, A. Q.; Chi, Y. S.; Lin, H. P.; Mou, C. Y. *J. Phys. Chem. B* **2005**, *109* (1), 40–43.
- (75) Fiorenza, R.; Crisafulli, C.; Condorelli, G. G.; Lupo, F.; Scirè, S. *Catal. Letters* **2015**, *145* (9), 1691–1702.
- (76) Sandoval, A.; Aguilar, A.; Louis, C.; Traverse, A.; Zanella, R. *J. Catal.* **2011**, *281* (1), 40–49.
- (77) Wang, A. Q.; Liu, J. H.; Lin, S. D.; Lin, T. S.; Mou, C. Y. *J. Catal.* **2005**, *233* (1), 186–197.
- (78) Povia, M.; Casu, A.; George, C.; Genovese, A.; Montanari, T.; Prato, M.; Manna, L. *Nano Lett.* **2013**, *13* (2), 752–757.
- (79) Xu, J.; White, T.; Li, P.; He, C.; Yu, J.; Yuan, W.; Han, Y. *J. Am. Chem. Soc.* **2010**,

- 10398–10406.
- (80) Sun, J.; Han, Y.; Fu, H.; Qu, X.; Xu, Z.; Zheng, S. *Chem. Eng. J.* **2017**, *313*, 1–9.
- (81) Holgado, J. P.; Ternero, F.; Gonzalez-Delacruz, V. M.; Caballero, A. *ACS Catal.* **2013**, *3* (9), 2169–2180.
- (82) Enache, D. I.; Edwards, J. K.; Landon, P.; Solsona-espriu, B.; Carley, A. F.; Herzing, A. A.; Watanabe, M.; Kiely, C. J.; Knight, D. W.; Hutchings, G. J. *Science* **2006**, *311* (5759), 362–365.
- (83) Marx, S.; Baiker, A. *J. Phys. Chem. C* **2009**, *113* (15), 6191–6201.
- (84) Guan, Y.; Hensen, E. J. M. *J. Catal.* **2013**, *305*, 135–145.
- (85) Aguirre, A.; Barrios, C. E.; Aguilar-Tapia, A.; Zanella, R.; Baltanás, M. A.; Collins, S. E. *Top. Catal.* **2016**, *59* (2–4), 347–356.
- (86) Han, C. W.; Majumdar, P.; Marinero, E. E.; Aguilar-Tapia, A.; Zanella, R.; Greeley, J.; Ortalan, V. *Nano Lett.* **2015**, *15* (12), 8141–8147.
- (87) Kotolevich, Y.; Kolobova, E.; Pestryakov, A.; Ortega, J. E. C.; Bogdanchikova, N.; Corberán, V. C.; Khramov, E.; Zubavichus, Y.; Pakrieva, R. Z. and E. *Current Organic Synthesis*. 2017, pp 323–331.
- (88) Chang, F. W.; Lai, S. C.; Roselin, L. S. *J. Mol. Catal. A Chem.* **2008**, *282* (1–2), 129–135.
- (89) Calzada, L. A.; Collins, S. E.; Han, C. W.; Ortalan, V.; Zanella, R. *Appl. Catal. B Environ.* **2017**, *207*, 79–92.
- (90) Zheng, J.; Qu, J.; Lin, H.; Zhang, Q.; Yuan, X.; Yang, Y.; Yuan, Y. **2016**, 1–10.
- (91) Benkó, T.; Beck, A.; Frey, K.; Srankó, D. F.; Geszti, O.; Sáfrán, G.; Maróti, B.; Schay, Z. *Appl. Catal. A Gen.* **2014**, *479*, 103–111.
- (92) Venugopal, A.; Aluha, J.; Mogano, D.; Scurrell, M. S. *Appl. Catal. A Gen.* **2003**, *245* (1), 149–158.
- (93) Blume, R.; Hävecker, M.; Zafeiratos, S.; Teschner, D.; Vass, E.; Schnörch, P.; Knop-Gericke, A.; Schlögl, R.; Lizzit, S.; Dudin, P.; Barinov, A.; Kiskinova, M. *Phys Chem Chem Phys* **2007**, *9* (27), 3648–3657.

- (94) Yamaguchi, K.; Mizuno, N. *Angew. Chemie - Int. Ed.* **2002**, *41* (23), 4538–4542.
- (95) Schwank, J. *Gold Bull.* **1985**, *18* (1), 2–10.
- (96) Bao, X.; Muhler, M.; Schedel-Niedrig, T.; Schlögl, R. *Phys. Rev. B* **1996**, *54* (3), 2249–2262.
- (97) Schmid, M.; Reicho, A.; Stierle, A.; Costina, I.; Klikovits, J.; Kostelnik, P.; Dubay, O.; Kresse, G.; Gustafson, J.; Lundgren, E.; Andersen, J. N.; Dosch, H.; Varga, P. *Phys. Rev. Lett.* **2006**, *96* (14), 146102.
- (98) Guisbiers, G.; Mendoza-Cruz, R.; Bazán-Díaz, L.; Velázquez-Salazar, J. J.; Mendoza-Perez, R.; Robledo-Torres, J. A.; Rodriguez-Lopez, J.-L.; Montejano-Carrizales, J. M.; Whetten, R. L.; José-Yacamán, M. *ACS Nano* **2016**, *10* (1), 188–198.
- (99) Zheng, N.; Stucky, G. D. *J. Am. Chem. Soc.* **2006**, *128* (44), 14278–14280.
- (100) Wang, A. Q.; Chang, C. M.; Mou, C. Y. *J. Phys. Chem. B* **2005**, *109* (40), 18860–18867.
- (101) Zanella, R.; Giorgio, S.; Henry, C. R.; Louis, C. *J. Phys. Chem. B* **2002**, *106* (31), 7634–7642.
- (102) Zanella, R.; Basiuk, E. V.; Santiago, P.; Basiuk, V. A.; Mireles, E.; Puente-Lee, I.; Saniger, J. M. *J. Phys. Chem. B* **2005**, *109* (34), 16290–16295.
- (103) Zanella, R.; Delannoy, L.; Louis, C. *Appl. Catal. A Gen.* **2005**, *291* (1–2), 62–72.
- (104) Zanella, R.; Louis, C. *Catal. Today* **2005**, *107–108*, 768–777.
- (105) Serna, P.; Concepción, P.; Corma, A. *J. Catal.* **2009**, *265* (1), 19–25.
- (106) Makosch, M.; Kartusch, C.; Sá, J.; Duarte, R. B.; van Bokhoven, J. a.; Kvashnina, K.; Glatzel, P.; Fernandes, D. L. a.; Nachtegaal, M.; Kleymentov, E.; Szlachetko, J.; Neuhold, B.; Hungerbühler, K. *Phys. Chem. Chem. Phys.* **2012**, *14* (7), 2164.
- (107) Hugon, A.; Delannoy, L.; Louis, C. *Gold Bull.* **2008**, *41* (2), 127–138.
- (108) Louis, C. *Catalysts* **2016**, *6* (8), 110.
- (109) Sasirekha, N.; Sangeetha, P.; Chen, Y. W. *J. Phys. Chem. C* **2014**, *118* (28), 15226–15233.

- (110) Zheng, J.; Qu, J.; Lin, H.; Zhang, Q.; Yuan, X.; Yang, Y.; Yuan, Y. *ACS Catal.* **2016**, *6* (10), 6662–6669.
- (111) Miao, T.; Song, Y.; Bi, C.; Xia, H.; Wang, D.; Tao, X. *J. Phys. Chem. C* **2015**, *119* (32), 18434–18443.
- (112) Haldar, K. K.; Kundu, S.; Patra, A. *ACS Appl. Mater. Interfaces* **2014**, *6* (24), 21946–21953.
- (113) Monga, A.; Pal, B. *New J. Chem.* **2015**, *39*, 304–313.
- (114) Shell, C.; Au, A.; Nanoparticles, C.; Guo, S.; Zhang, X.; Zhu, W.; He, K.; Su, D.; Mendoza-garcia, A.; Ho, S. F.; Lu, G.; Sun, S. *J. Am. Chem. Soc.* **2014**, 15026–15033.
- (115) Zanella, R.; Delannoy, L.; Louis, C. *Appl. Catal. A Gen.* **2005**, *291* (1–2), 62–72.
- (116) Simonelli, L.; Marini, C.; Olszewski, W.; Ávila Pérez, M.; Ramanan, N.; Guilera, G.; Cuartero, V.; Klementiev, K. *Cogent Phys.* **2016**, *3* (1), 1–10.
- (117) Dent, A. J.; Cibirin, G.; Ramos, S.; Smith, A. D.; Scott, S. M.; Varandas, L.; Pearson, M. R.; Krumpa, N. A.; Jones, C. P.; Robbins, P. E. *J. Phys. Conf. Ser.* **2009**, *190* (November).
- (118) Prestipino, C. PrestoPronto <http://soonready.github.io/PrestoPronto/> (accessed Apr 30, 2019).
- (119) Velasco-Vélez, J. J.; Pfeifer, V.; Hävecker, M.; Wang, R.; Centeno, A.; Zurutuza, A.; Algara-Siller, G.; Stotz, E.; Skorupska, K.; Teschner, D.; Kube, P.; Braeuninger-Weimer, P.; Hofmann, S.; Schlögl, R.; Knop-Gericke, A. *Rev. Sci. Instrum.* **2016**, *87* (5).
- (120) Bluhm, H.; Hävecker, M.; Knop-Gericke, A.; Kleimenov, E.; Schlögl, R.; Teschner, D.; Bukhtiyarov, V. I.; Ogletree, D. F.; Salmeron, M. *J. Phys. Chem. B* **2004**, *108* (38), 14340–14347.
- (121) Pérez-Dieste, V.; Aballe, L.; Ferrer, S.; Nicolàs, J.; Escudero, C.; Milán, A.; Pellegrin, E. *J. Phys. Conf. Ser.* **2013**, *425* (PART 7), 2–6.
- (122) Ogletree, D. F.; Bluhm, H.; Lebedev, G.; Fadley, C. S.; Hussain, Z.; Salmeron, M. *Rev. Sci. Instrum.* **2002**, *73* (11), 3872–3877.

- (123) Yeh, J. J.; Lindau, I. *At. Data Nucl. Data Tables* **1985**, 32 (1), 1–155.
- (124) Yu, Z.; Chuang, S. S. C. *J. Catal.* **2007**, 246 (1), 118–126.
- (125) Rismanchian, A.; Chen, Y. W.; Chuang, S. S. C. *Catal. Today* **2016**, 264, 16–22.
- (126) Gonzalez-Yañez, E. O.; Fuentes, G. A.; Hernández-Terán, M. E.; Fierro-Gonzalez, J. C. *Appl. Catal. A Gen.* **2013**, 464–465, 374–383.
- (127) Henych, J.; Štengl, V.; Mattsson, A.; Österlund, L. *Photochem. Photobiol.* **2015**, 91 (1), 48–58.
- (128) Coronado, J. M.; Kataoka, S.; Tejedor-Tejedor, I.; Anderson, M. A. *J. Catal.* **2003**, 219 (1), 219–230.
- (129) Tan, T. H.; Scott, J.; Ng, Y. H.; Taylor, R. A.; Aguey-Zinsou, K. F.; Amal, R. *ACS Catal.* **2016**, 6 (12), 8021–8029.
- (130) Gomes, J. F.; Bergamaski, K.; Pinto, M. F. S.; Miranda, P. B. *J. Catal.* **2013**, 302, 67–82.
- (131) Wu, W.-C.; Chuang, C.-C.; Lin, J.-L. *J. Phys. Chem. B* **2000**, 104 (36), 8719–8724.
- (132) Araña, J.; Doña-Rodríguez, J. M.; González-Díaz, O.; Tello Rendón, E.; Herrera Melián, J. A.; Colón, G.; Navío, J. A.; Pérez Peña, J. *J. Mol. Catal. A Chem.* **2004**, 215 (1–2), 153–160.
- (133) Lee, K.; Murray, É. D.; Kong, L.; Lundqvist, B. I.; Langreth, D. C. *Phys. Rev. B* **2010**, 82 (8), 81101.
- (134) Klimeš, J.; Bowler, D. R.; Michaelides, A. *Phys. Rev. B* **2011**, 83 (19), 195131.
- (135) Kresse, G.; Hafner, J. *Phys. Rev. B* **1993**, 47 (1), 558–561.
- (136) Kresse, G.; Hafner, J. *Phys. Rev. B* **1993**, 48 (17), 13115–13118.
- (137) De Vrieze, J. E.; Thybaut, J. W.; Saeys, M. *ACS Catal.* **2018**, 8 (8), 7539–7548.
- (138) Wyckoff, R. W. G. *Am. Mineral. Cryst. Struct. Database* **1963**.
- (139) Bale, C. W.; Chartrand, P.; Degterov, S. A.; Eriksson, G.; Hack, K.; Mahfoud, R. Ben; Melançon, J.; Pelton, A. D.; Petersen, S. *Calphad* **2002**, 26 (2), 189–228.
- (140) Henkelman, G.; Uberuaga, B. P.; Jónsson, H. *J. Chem. Phys.* **2000**, 113 (22), 9901–

- 9904.
- (141) Henkelman, G.; Jónsson, H. *J. Chem. Phys.* **2000**, *113* (22), 9978–9985.
- (142) Henkelman, G.; Jónsson, H. *J. Chem. Phys.* **1999**, *111* (15), 7010–7022.
- (143) Rajkhowa, T.; Marin, G. B.; Thybaut, J. W. *Appl. Catal. B Environ.* **2017**, *205*, 469–480.
- (144) Brown, P. N.; Hindmarsh, A. C.; Petzold, L. R. *SIAM J. Sci. Comput.* **1994**, *15* (6), 1467–1488.
- (145) Dobrin, S. *Phys. Chem. Chem. Phys.* **2012**, *14* (35), 12122–12129.
- (146) Zhuo, M.; Borgna, A.; Saeys, M. *J. Catal.* **2013**, *297*, 217–226.
- (147) Jørgensen, M.; Grönbeck, H. *J. Phys. Chem. C* **2017**, *121* (13), 7199–7207.
- (148) Zope, B. N.; Hibbitts, D. D.; Neurock, M.; Davis, R. J. *Science (80-.)*. **2010**, *330* (6000), 74–78.
- (149) Campbell, C. T. *Top. Catal.* **1994**, *1* (3–4), 353–366.
- (150) Buchalska, M.; Kobielski, M.; Matuszek, A.; Pacia, M.; Wojtyła, S.; Macyk, W. *ACS Catal.* **2015**, *5* (12), 7424–7431.
- (151) Panayotov, D. A.; Morris, J. R. *Surf. Sci. Rep.* **2016**, *71* (1), 77–271.
- (152) Liu, L.; Gu, X.; Cao, Y.; Yao, X.; Zhang, L.; Tang, C.; Gao, F.; Dong, L. *ACS Catal.* **2013**, *3* (12), 2768–2775.
- (153) Mattioli, G.; Filippone, F.; Alippi, P.; Amore Bonapasta, A. *Phys. Rev. B* **2008**, *78* (24), 241201.
- (154) Morgan, B. J.; Watson, G. W. *J. Phys. Chem. C* **2010**, *114*, 2321–2328.
- (155) Bouzoubaa, A.; Markovits, A.; Calatayud, M.; Minot, C. *Surf. Sci.* **2005**, *583* (1), 107–117.
- (156) Setoudeh, N.; Saidi, A.; Welham, N. J. *J. Alloys Compd.* **2005**, *390* (1–2), 138–143.
- (157) Klyushin, A. Y.; Rocha, T. C. R.; Hävecker, M.; Knop-Gericke, A.; Schlögl, R. *Phys. Chem. Chem. Phys.* **2014**, *16* (17), 7881–7886.
- (158) Klyushin, A. Y.; Greiner, M. T.; Huang, X.; Lunkenbein, T.; Li, X.; Timpe, O.;

- Friedrich, M.; Hävecker, M.; Knop-Gericke, A.; Schlögl, R. *ACS Catal.* **2016**, *6* (5), 3372–3380.
- (159) Lee, S.; Fan, C.; Wu, T.; Anderson, S. L. *Surf. Sci.* **2005**, *578* (1–3), 5–19.
- (160) Tóth, M.; Kiss, J.; Oszkó, A.; Pótári, G.; László, B.; Erdohelyi, A. *Top. Catal.* **2012**, *55* (11–13), 747–756.
- (161) Fukutani, K.; Wilde, M.; Ogura, S. *Chem. Rec.* **2017**, *17* (2), 233–249.
- (162) Fukada, K.; Matsumoto, M.; Takeyasu, K.; Ogura, S.; Fukutani, K. *J. Phys. Soc. Japan* **2015**, *84* (6), 064716.
- (163) Naumkin, A. V.; Kraut-Vass, A.; Gaarenstroom, S. W.; Powell, C. J. National Institute of Standards and Technology 2012.
- (164) Gaarenstroom, S. W.; Winograd, N. *J. Chem. Phys.* **1977**, *67* (8), 3500–3506.
- (165) Yin, C.; Tyo, E.; Kuchta, K.; von Issendorff, B.; Vajda, S. *J. Chem. Phys.* **2014**, *140* (17), 174201.
- (166) Diebold, U. *Surf. Sci. Rep.* **2003**, *48* (x), 53–229.
- (167) Salaev, M. A.; Sobolev, V. I.; Vodyankin, A. A.; Ten, S.; Torbina, V. V.; Vodyankina, O. V.; Mamontov, G. V. *Catalysts* **2018**, *8* (10), 447.
- (168) Baurecht, D.; Fringeli, U. P. *Rev. Sci. Instrum.* **2001**, *72* (10), 3782–3792.
- (169) Urakawa, A.; Bürgi, T.; Baiker, A. *Chem. Eng. Sci.* **2008**, *63* (20), 4902–4909.
- (170) Haghofer, A.; Ferri, D.; Föttinger, K.; Rupprechter, G. *ACS Catal.* **2012**, *2* (11), 2305–2315.

9. Appendix

9.1. Catalyst Synthesis

Table 29. Weights used for the synthesis of the monometallic Au samples.

	Amount prepared (g)	Au (mg)	Au(III)chloride (weighted sample)
Batch 1			
Au/rutile (5 wt.%)	5.0	250	499.86 mg (508.0 mg)
Batch 2			
Au/rutile (5 wt.%)	10.0	500	999.72 mg (1.01 g)
Batch 3			
Au/rutile (5 wt.%)	4.0	200	399.89 mg (401.9 mg)
Au/anatase (5 wt.%)	1.0	50	99.97 mg (102.6 mg)
Au/P25	1.0	50	99.97 mg (99.9 mg)
Au/anatase₈₀rutile₂₀	1 (0.82 rutile, 0.18 anatase)	50	99.99 mg (101.3 mg)
Batch 4			
Au/rutile (5 wt.%)	10	500	999.72 mg (1.00 g)

Table 30. Weights used for the synthesis of the bimetallic samples.

	Amount prepared [g]	Promotor [mg]	Metal salt [mg] (weighted sample)
Batch 1			
AuRu/rutile	1 (on 1.0191 Au/rutile)	10	20.52 (24.80) (Ru(III)chloride hydrate)
AuPt/rutile	1 (on 1.0062 g Au/rutile)	20	34.54 (36.6) (Platinum(IV)chloride)

AuAg/rutile	1 (on 1.0037 g Au/rutile)	10	15.75 (15.70) (AgNO ₃)
Batch 2			
AuRu/rutile	3 (on 3.0010 g Au/rutile)	30	61.57 (61.60) (Ru(III)chloride hydrate)
AuAg/rutile	5 (on 5.0018 g Au/rutile)	50	78.74 (78.70) (AgNO ₃)
Batch 3			
AuAg/rutile	1 (on 1.0050 g Au/rutile)	10	15.75 (15.80) (AgNO ₃)
Batch 4			
AuAg/rutile	5 (5.0013 g Au/rutile)	50	78.74 (78.60) (AgNO ₃)

9.2. XRD Analysis of Catalysts

XRD is shown for the Au/rutile catalyst in Figure 93, in pristine state after the synthesis as well as after the pretreatment step. Only in the diffractogram of the pretreated catalyst there is a small (and broad) gold peak (marked with an orange star), which indicates the formation of highly dispersed and nanocrystalline particles are formed during the synthesis. All the other peaks as well as all the peaks in the diffractogram of the pristine sample can be attributed to rutile (01-072-4817). Au/C, AuAg/rutile and Au/rutile are compared in Figure 94. The large peak attributed to Au in the diffractogram of Au/C is explained by the large mean particle size of 14.5 nm. Figure 95 shows a comparison of the different TiO₂-based catalysts, supported on rutile, anatase (00-021-1272), P25 and a mixture of 80% rutile and 20% anatase. The results of the Rietveld refinement are listed in Table 31.

Table 31. Results of the Rietveld refinement for the TiO₂-based catalysts. Only anatase and rutile are listed in the table, as the obtained values for Au are not correct due to the nanocrystalline character of Ag.

	Anatase (wt.%)	Rutile (wt.%)
AUROLite/TiO₂	82.2	17.7
Au/anatase₃₀rutile₂₀	78.3	19.1
Au/P25	87.0	13.0
Au/anatase	99.7	0.0
Au/rutile	0.0	99.9

The detailed parameters for the measurement were as follows: PANalytical X'Pert (PANalytical) PRO powder diffractometer in Bragg-Brentano geometry.

X-ray tube: Cu LFF; wavelength: CuK α : $\lambda_1 = 1.5406 \text{ \AA}$, $\lambda_2 = 1.5444 \text{ \AA}$; voltage: 40 kV at 40 mA; power: 1600 W (max. power 2200 W); Ni-K β -Filter, Θ/Θ goniometer: PW3050/60; goniometer radius 200 mm; fixed divergence slit 0.5°; fixed anti scatter slit 2°; detector: X'Celerator; scanning length 2.546°, fixed anti scatter slit 5.5°; max. diffraction angle 2 Θ , 5-90°, step size 0.0200535°, time per step 70.485 s.

The Rietveld refinements were performed using Highscore Plus (PANalytical). The respective fittings are shown in Figure 96 till Figure 102. For simplicity, only diffractograms of the Batch 3 as well as catalysts with different TiO₂ modifications are shown. These diffractograms are representative for the other samples discussed in this thesis.

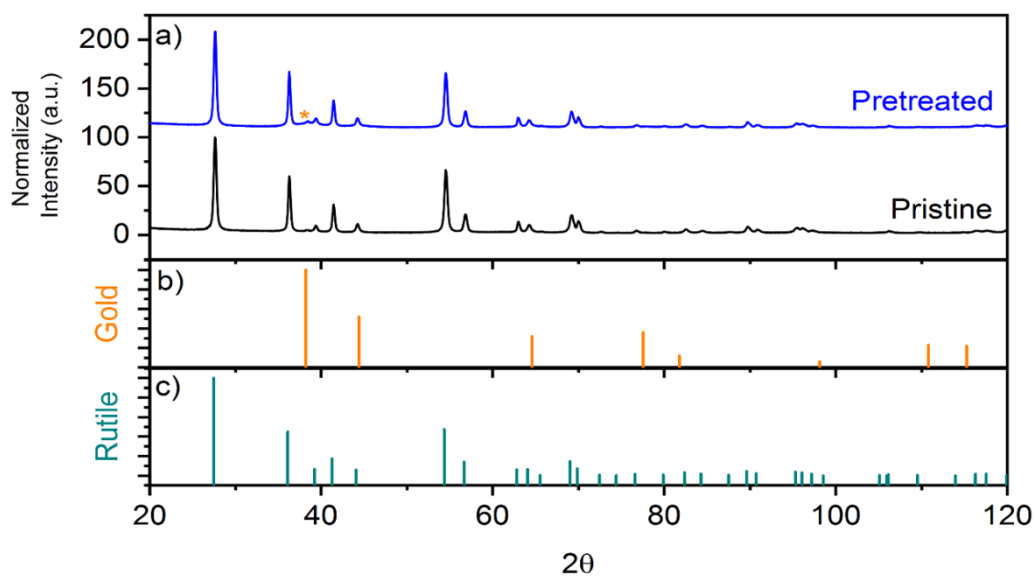


Figure 93. (a) XRD powder patterns of Au/rutile after pretreatment (blue) and pristine after the synthesis (black). The orange star marks the small gold peak in the pretreated sample. b) and c) show the reference peaks of gold (00-004-0784) and rutile (01-072-4817), respectively.

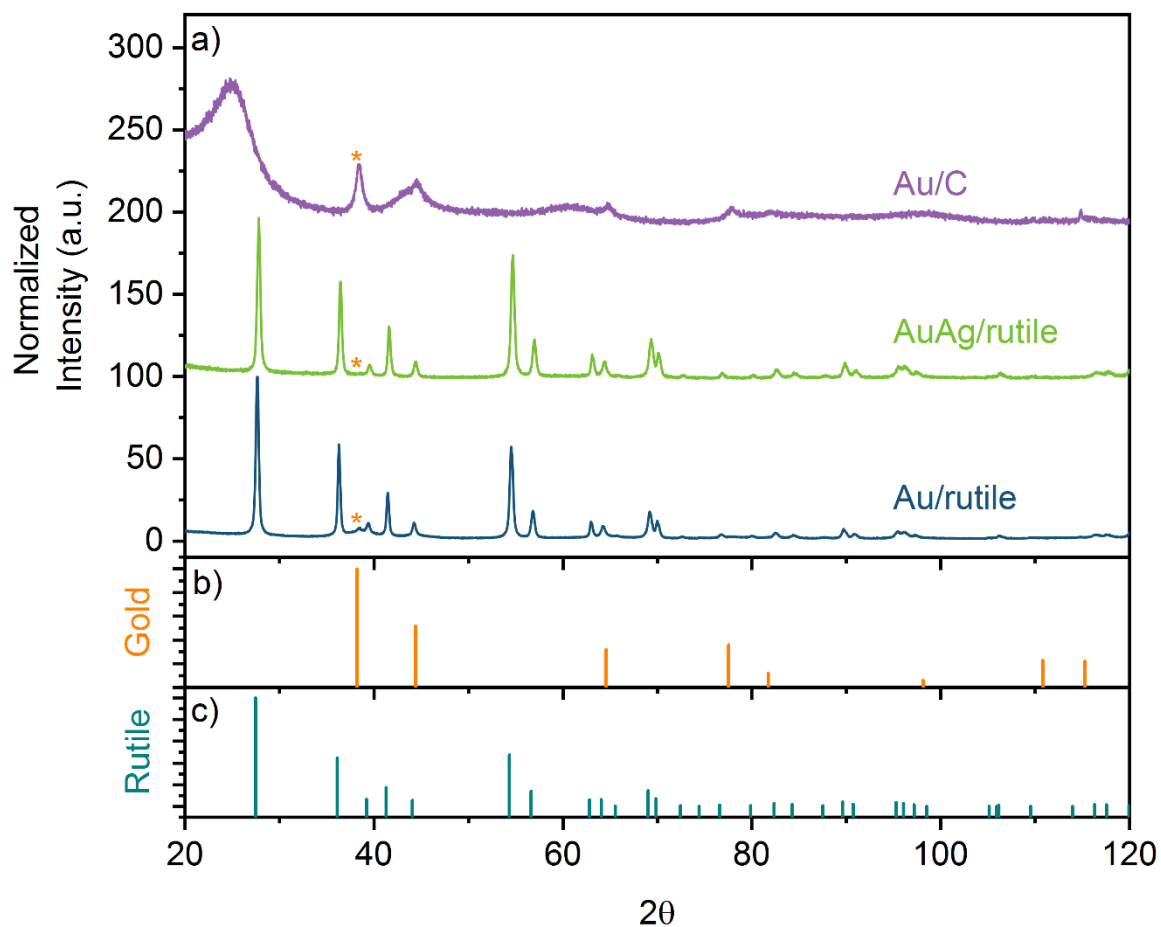


Figure 94. a) XRD powder patterns of Au/C (purple), AuAg/rutile (green) and Au/rutile (blue), always after pretreatment. The orange star marks the small gold peak in the pretreated sample. b) and c) show the reference peaks of gold (00-004-0784) and rutile (01-072-4817), respectively.

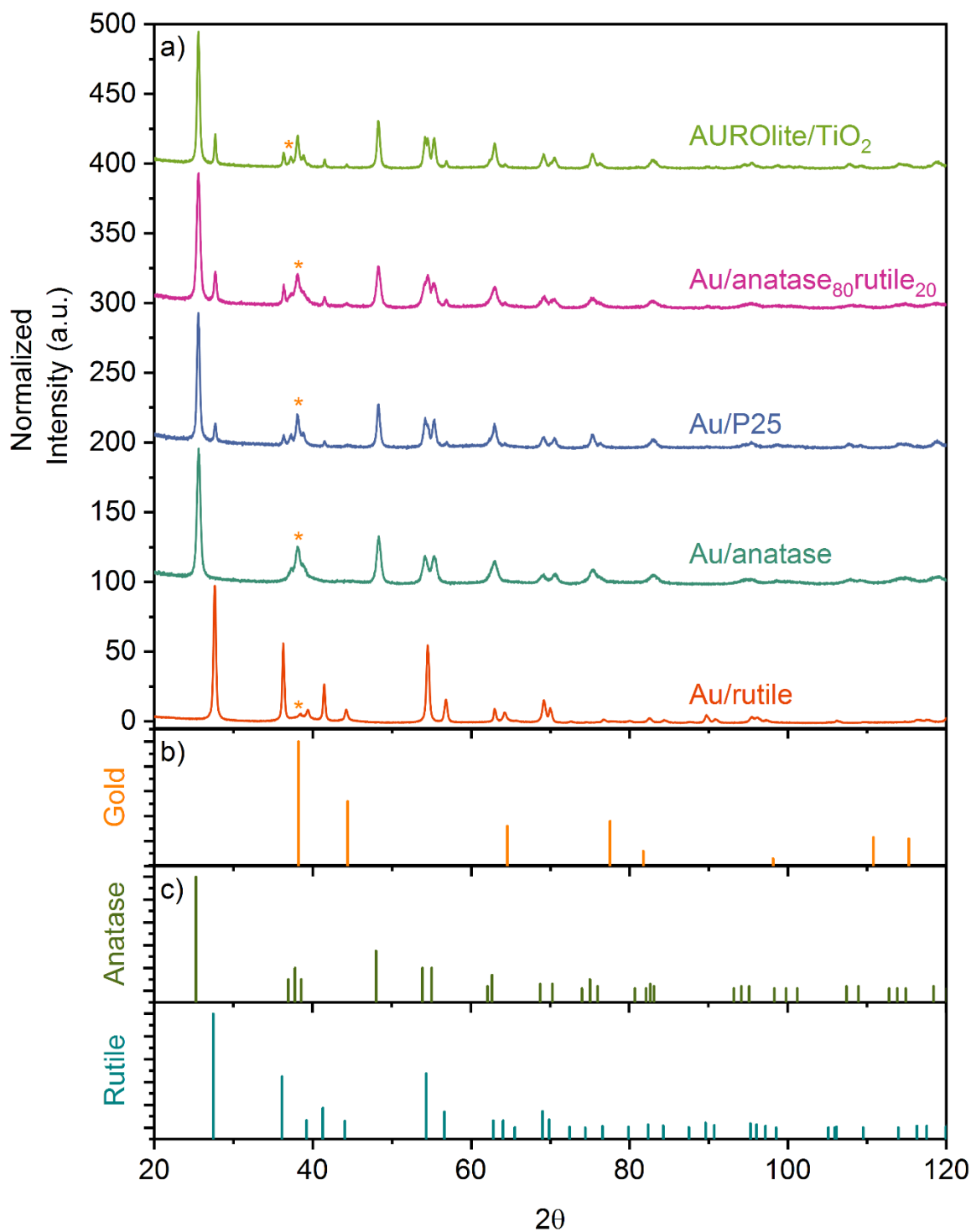


Figure 95. a) XRD powder patterns of AUROLite/TiO₂, Au/anatase₈₀rutile₂₀, Au/P25, Au/anatase and Au/rutile, always after pretreatment. The orange star marks the small gold peak in the pretreated sample. b), c) and d) show the reference peaks of gold (00-004-0784), anatase (00-021-1272) and rutile (01-072-4817), respectively.

The Rietveld refinements are shown in the following figures:

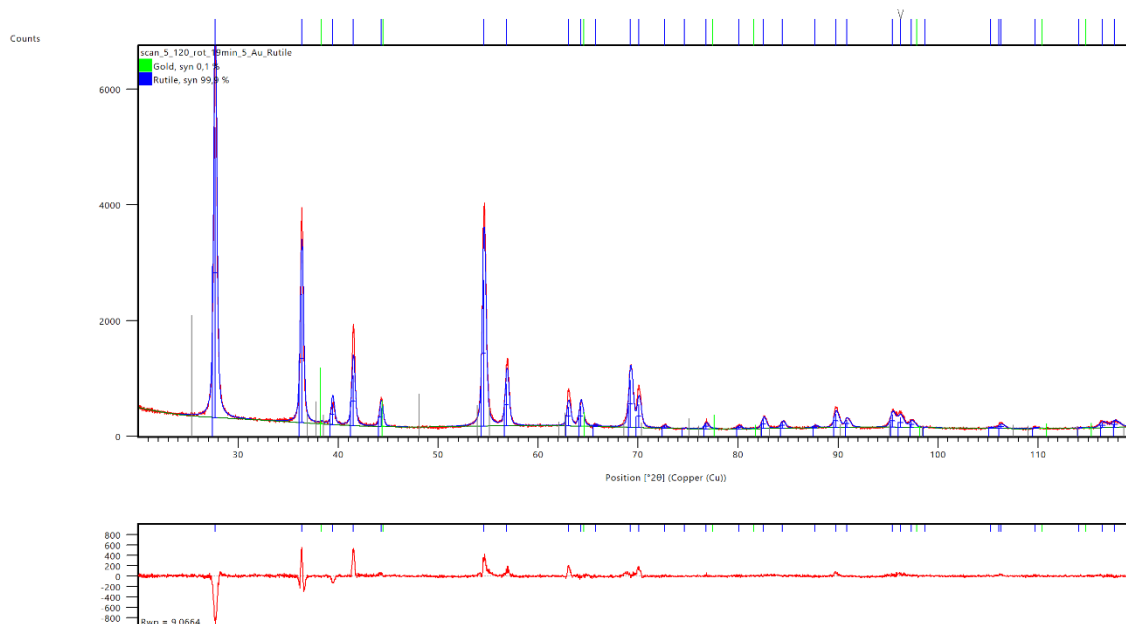


Figure 96. Rietveld refinement (including the difference plot) for Au/rutile (batch 3), after pretreatment. Due to the nanocrystalline character, 99.9% rutile and 0.1% Au have been found.

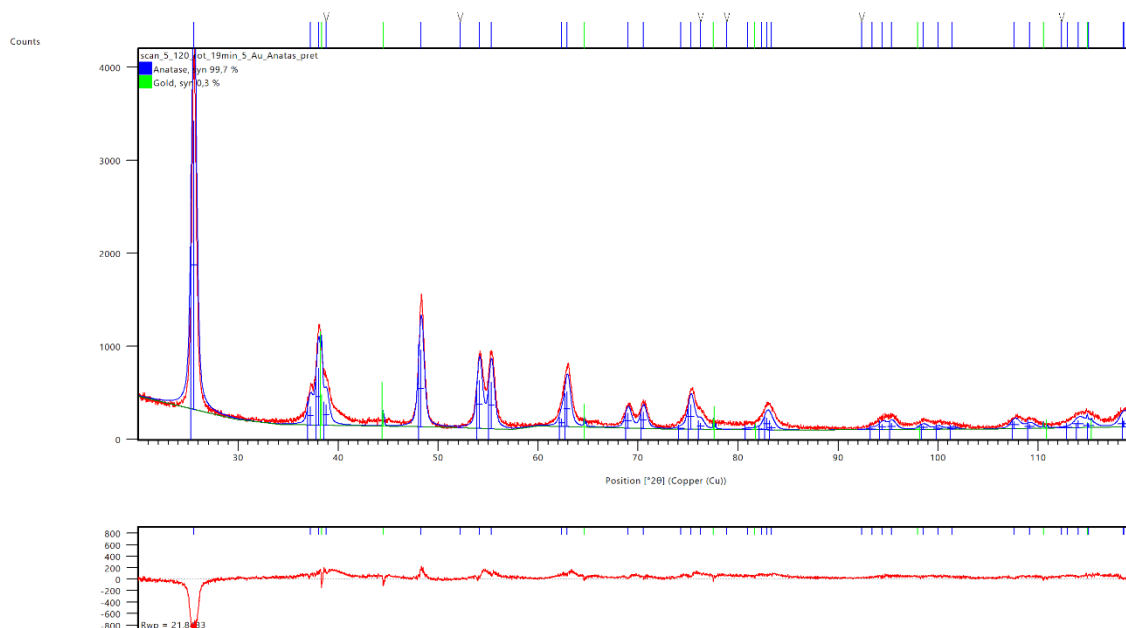


Figure 97. Rietveld refinement (including the difference plot) for Au/anatase, after pretreatment. Due to the nanocrystalline character, 99.7% anatase and 0.3% Au have been found.

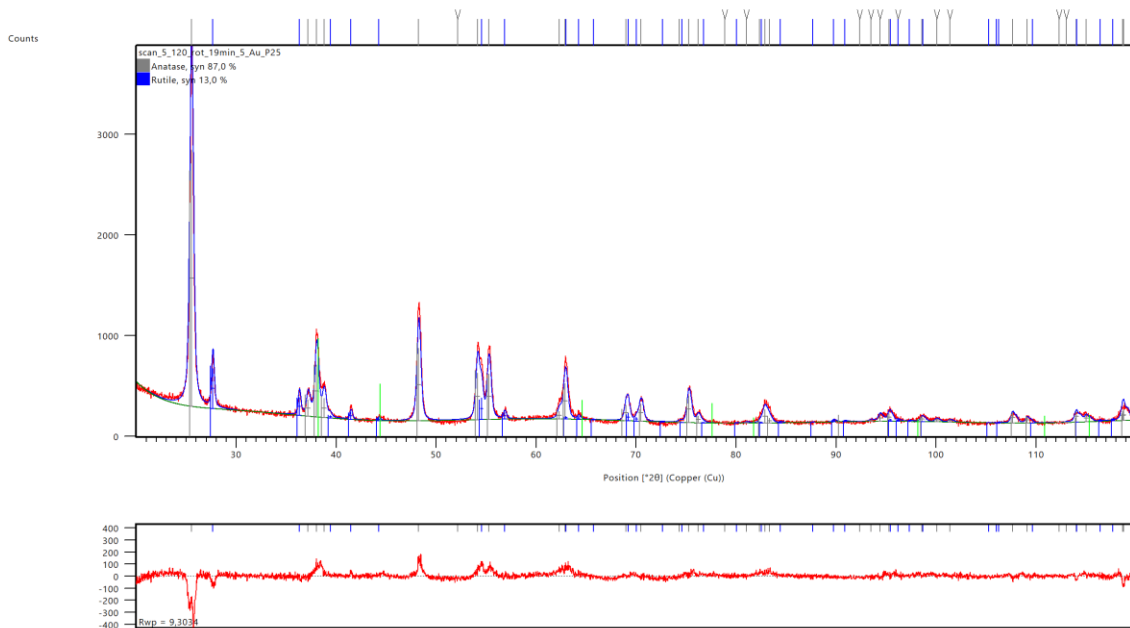


Figure 98. Rietveld refinement (including the difference plot) for Au/P25, after pretreatment. 87.0% anatase and 13.0% rutile have been found. Due to the nanocrystalline character of gold, no peak associated with Au could be found.

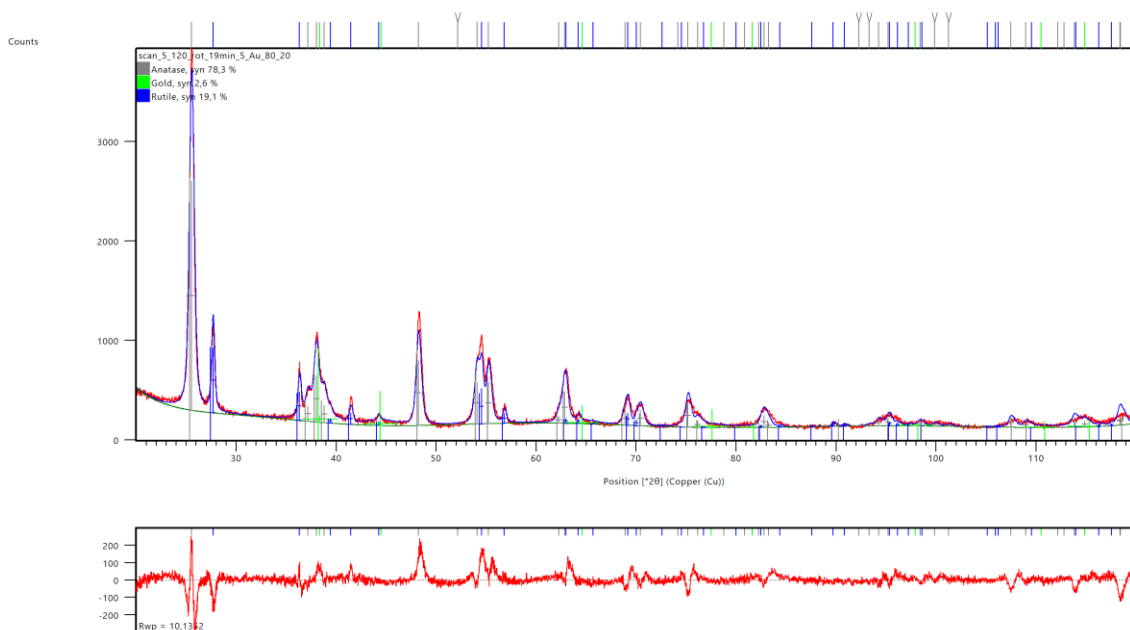


Figure 99. Rietveld refinement (including the difference plot) for Au/anatase₈₀rutile₂₀, after pretreatment. 78.3% anatase, 19.1% rutile and 2.6% Au have been found.

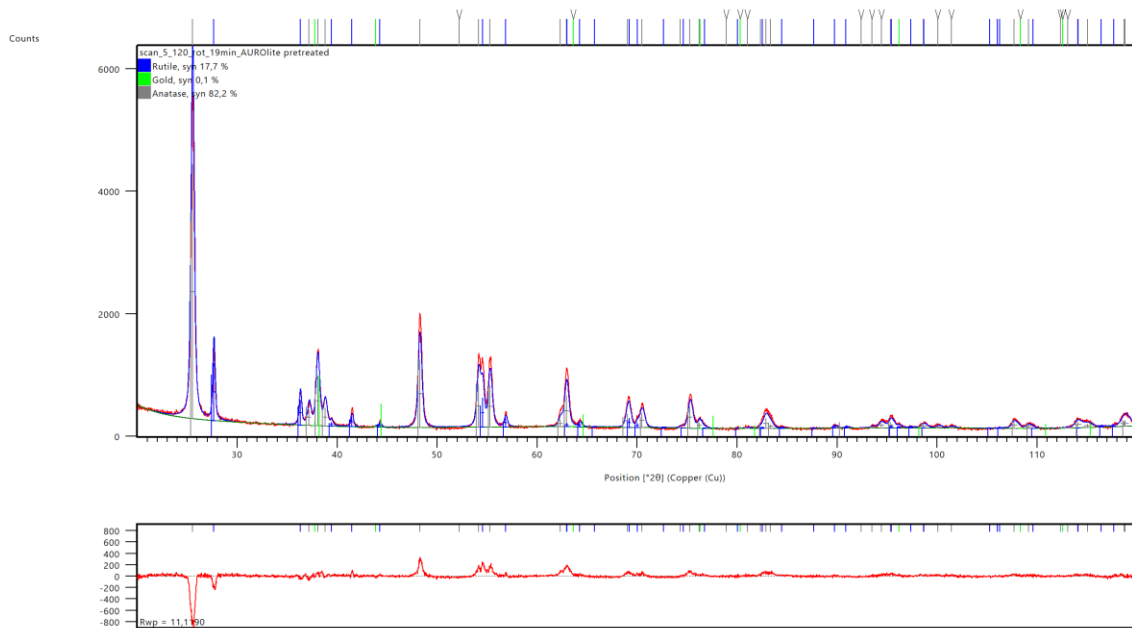


Figure 100 Rietveld refinement (including the difference plot) for AUROLite/TiO₂ after pretreatment. 82.2% anatase, 17.7% rutile and 0.1% Au have been found.

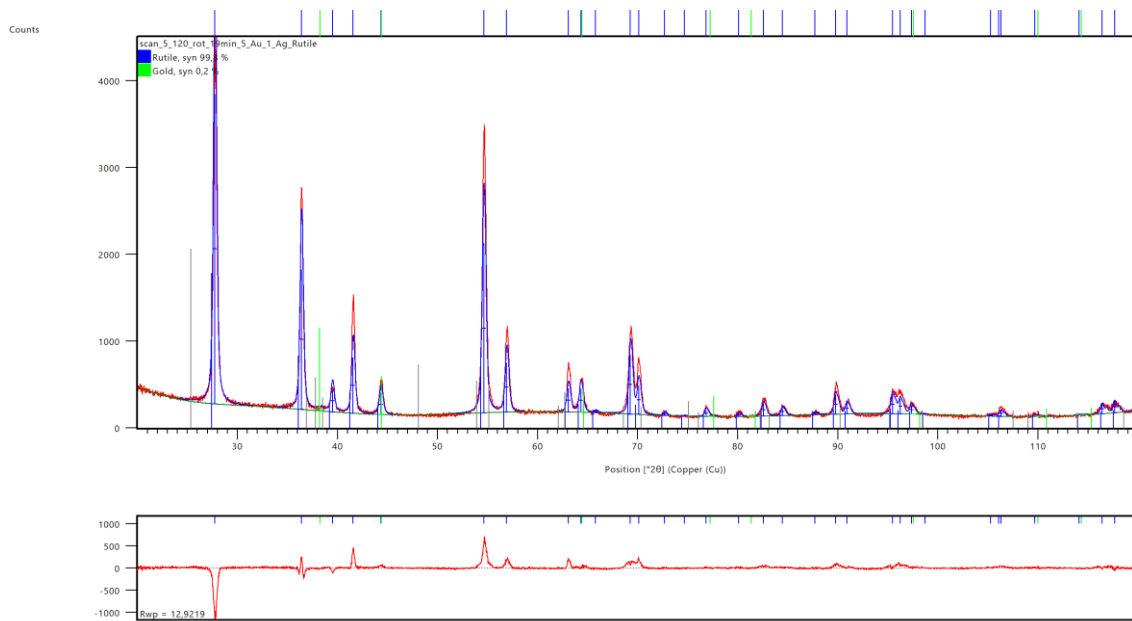


Figure 101 Rietveld refinement (including the difference plot) for AuAg/rutile after pretreatment. 0.2% Au has been found.

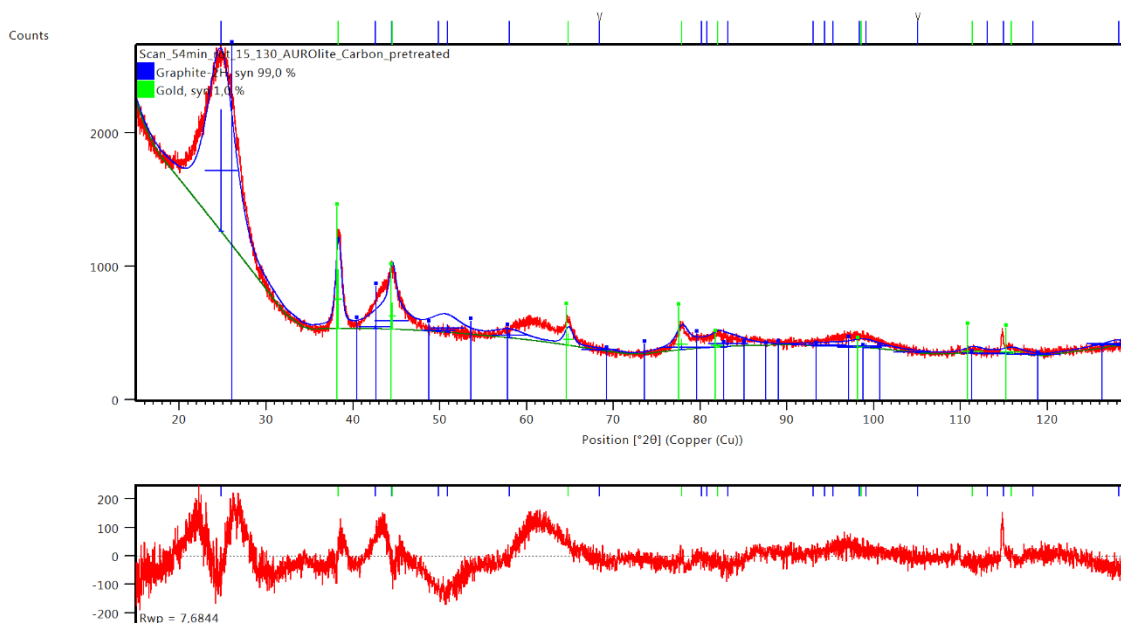


Figure 102. Rietveld refinement (including the difference plot) for AuC/rutile after pretreatment. 1.0% Au has been found.

9.3. Detailed LA-ICP-MS Parameters for the Determination of Metal Loadings

For the analysis a NWR213 (ESI, Fremont, CA) ns-Laser ablation (LA) system was hyphenated to an iCAP Q (Thermo Fisher Scientific, Bremen, Germany) quadrupol inductively coupled plasma mass spectrometer (Q-ICP-MS). The particles were dispersed in Ethanol and pipetted on a polycarbonate disk and individual particle clusters, as identified in the LA system, were subsequently ablated and analyzed in the ICP. Figure 103 shows exemplarily the metal loading for the individual particle clusters of the Au/rutile sample as analyzed by the LA-ICP-MS system, thus giving an estimate of the homogeneity of the catalyst. The parameters for the analysis are presented in Table 32 below.

Table 32. Detailed LA-ICP Parameters

He Gas Flow (Carrier gas)	850 mL/min
Ar Gas flow (Make-Up gas)	800 mL/min
Spot size	10 μm
Repetition rate	20 Hz
Shots per particle	20
Fluence	6.5 J/cm ²
Dwelltime per isotope	5 ms
Observed isotopes	Au-197, Ti-47, Ti-48

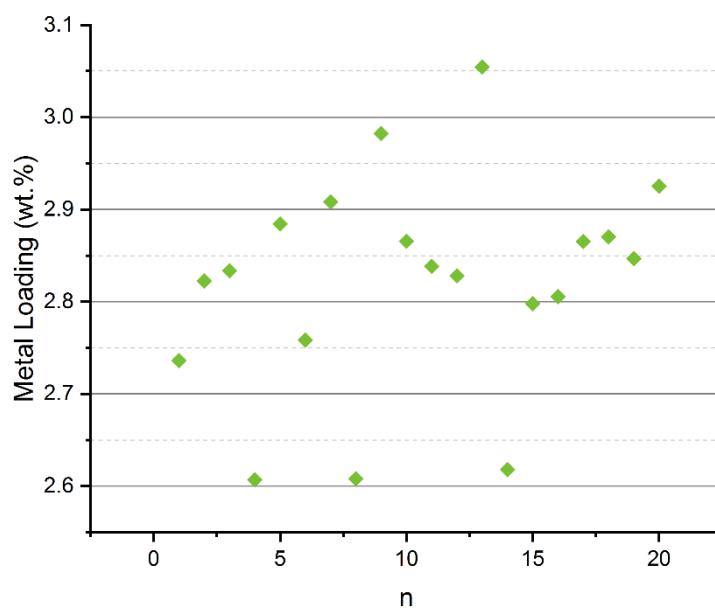


Figure 103. Results of individual particle clusters of the Au/rutile sample as ablated by the LA-ICP-MS system.

9.4. Details for Kinetic Measurements

9.4.1. GC Settings

The product stream was on-line analyzed in an Agilent 7890A GC, equipped with an FID and a TCD detector. During the analysis, 1000 μL of sample were introduced at 110°C.

The inlet was operated in splitless mode. Carrier gas (He) flow on column was kept at 6 mL with the following method: 40 °C for 4.5 minutes. followed a rapid heating (100°C/min.)

to 200°C which was kept for 11 minutes. The FID Detector was set at 250 K with a 40 mL/min H₂ and 400 mL/min air flow. The TCD was set at 220°C with a 20 mL/min reference flow. The molar concentration of each component was determined using linear regression of calibration standards. This GC program was optimized for speed, allowing an injection every 23 minutes and, after a first screening of the reaction by-products (and their concentrations) optimized.

9.4.2. Exact Flow Settings for Reaction Order Measurements

Table 33. Exact flows for the O₂ reaction order measurements.

EtOH/O₂ ratio	O₂ flow (mL/min)	EtOH flow (mL/min)	Total flow (mL/min)	p_{EtOH} (kPa)	p_{O₂} (kPa)
1/0.5	0.55	1.10	50.64	2.2	1.1
1/1.0	1.10	1.10	51.18	2.2	2.2
1/1.5	1.70	1.10	51.79	2.1	3.3
1/1.8	1.98	1.10	52.07	2.1	3.9
1/2.0	2.20	1.10	52.29	2.1	4.3
1/2.5	2.70	1.10	52.79	2.1	5.2
1/4.0	4.40	1.10	54.49	2.0	8.2

The gas flows were thus deviating not more than +/- 2% from 51.8 mL/min, except for the last EtOH/O₂ ratio of 1/4.0, which represents a bigger deviation from the desired constant flow of the measurements (due to the available MFC controllers).

Table 34. Exact flows for the EtOH reaction order measurements.

O ₂ /EtOH ratio	O ₂ flow (mL/min)	EtOH flow (mL/min)	Total flow (mL/min)	p _{EtOH} (kPa)	p _{O₂} (kPa)
5/0.25	5	0.26	49.73	0.5	10
5/0.60	5	0.62	50.00	1.2	10
5/1.1	5	1.10	50.00	2.2	10
5/1.65	5	1.64	50.00	3.3	10
5/2.2	5	2.21	50.21	04.5	10

The gas flows were thus deviating not more than +/- 1% from 50.0 mL/min

9.4.3. Exact Flow Settings for the Measurement of the Water Influence

Table 35 Exact experimental setup, gas flow settings and saturator temperature.

Conditions	O ₂ Flow (mL/min)	EtOH Flow (mL/min)	H ₂ O Flow (mL/min)	Saturator Temperature (°C)	Total Flow
I	0.55	0.52	-	21	49.57
II	0.55	0.51	0.30	7	51.32
II	0.55	0.52	0.98	21	50.55

The gas flows were thus deviating not more than +/- 2% from 50.5 mL/min.

9.5. Details for DRIFTS Measurements

Detailed setup of the *operando* DRIFTS experiment:

Table 36. Exact gas flow for the *operando* DRIFTS measurements.

Conditions	O ₂ Flow (mL/min)	EtOH Flow (mL/min)	Total Flow
I+II	-	1.1	50.1
II	1.1	1.1	51.2
IV	1.1	-	50.1

For the measurements with H₂O, the same conditions as for the kinetic measurements, see annex section 9.4.3, were used.

9.6. Additional STEM Data

9.6.1. Additional STEM-EDX Data

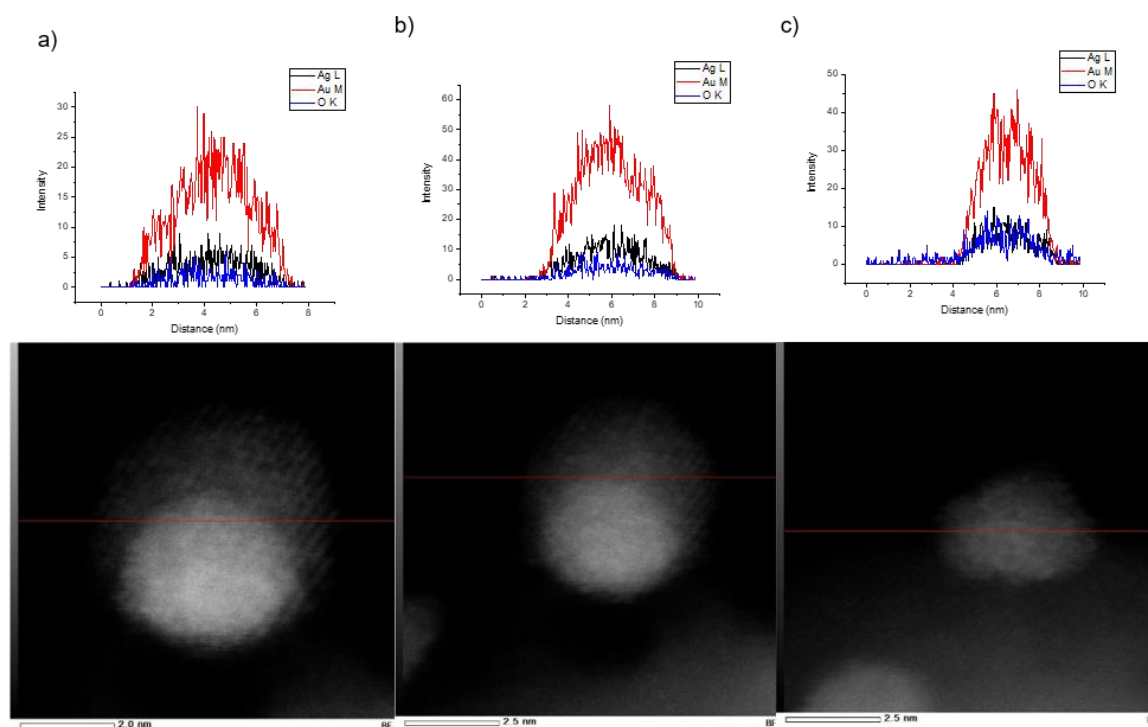


Figure 104. STEM-EDX line scans of selected AuAg nanoparticles, showing that there is no surface segregation of Ag. Measurements in cooperation with G. Dražič and A. Pintar, Department for Environmental Sciences and Engineering, National Institute of Chemistry, Ljubljana, Slovenia.

9.6.2. STEM-HAADF

Size distribution and STEM-HAADF micrographs of the Au/rutile used for synchrotron measurements (batch 4).

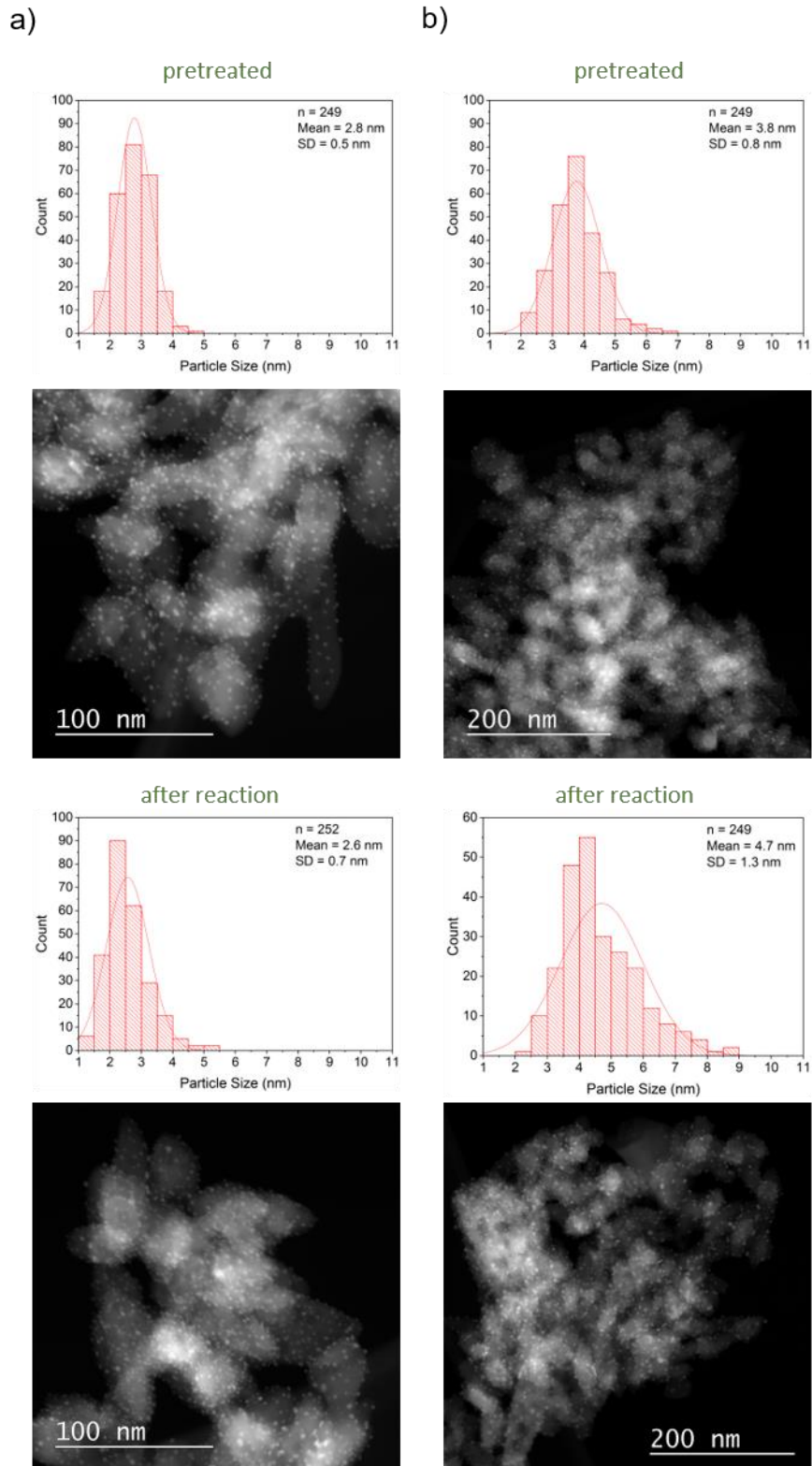


Figure 105. Size distributions obtained from STEM-HAADF and exemplary STEM-HAADF micrographs for (a) Au/rutile and (b) AuAg/rutile, both batch 4, which was used for the synchrotron beamtimes.

9.7. NAP-XPS

9.7.1. BESSY II

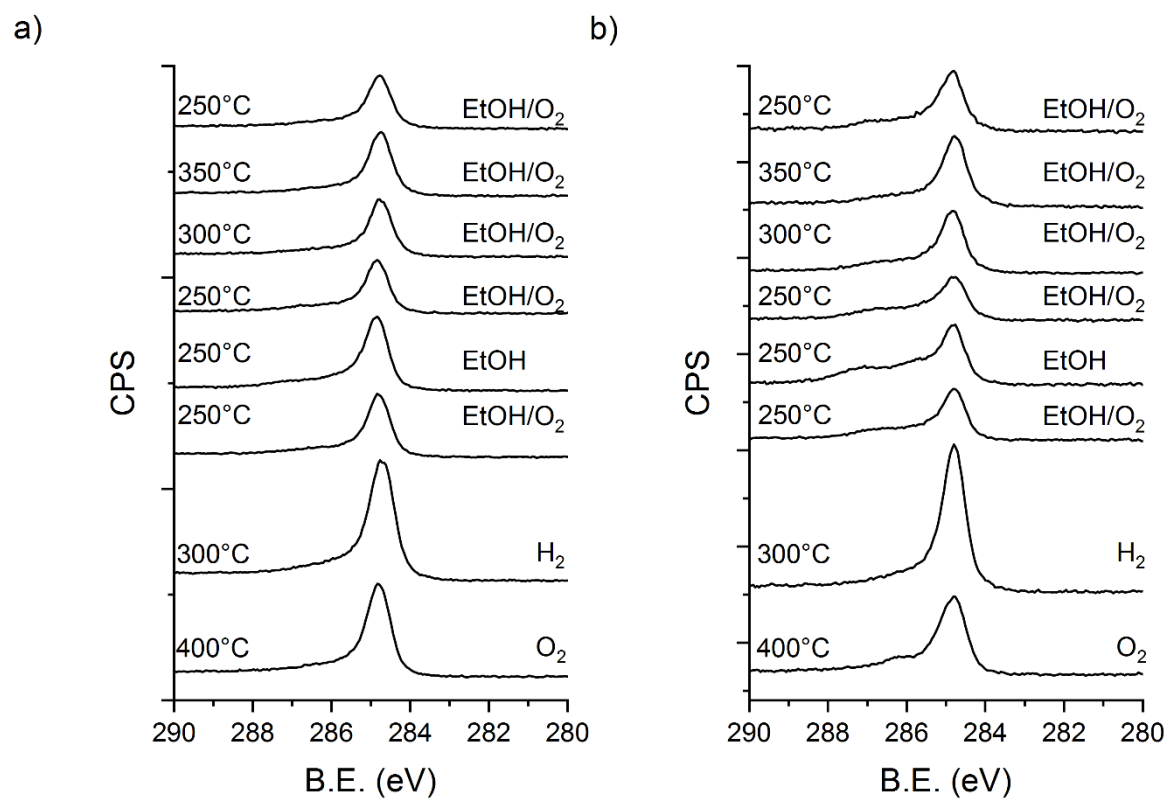


Figure 106. Cls spectra for (a) Au/rutile and (b) AuAg/rutile under different conditions: Pretreatment (5 mL/min O₂ at 400°C and H₂ at 300°C), oxidation with EtOH/O₂ (2.5 mL/min at temperatures from 250°C – 300°C) and EtOH only at 250°C. Spectra were taken at an E_{kin} = 310 eV.

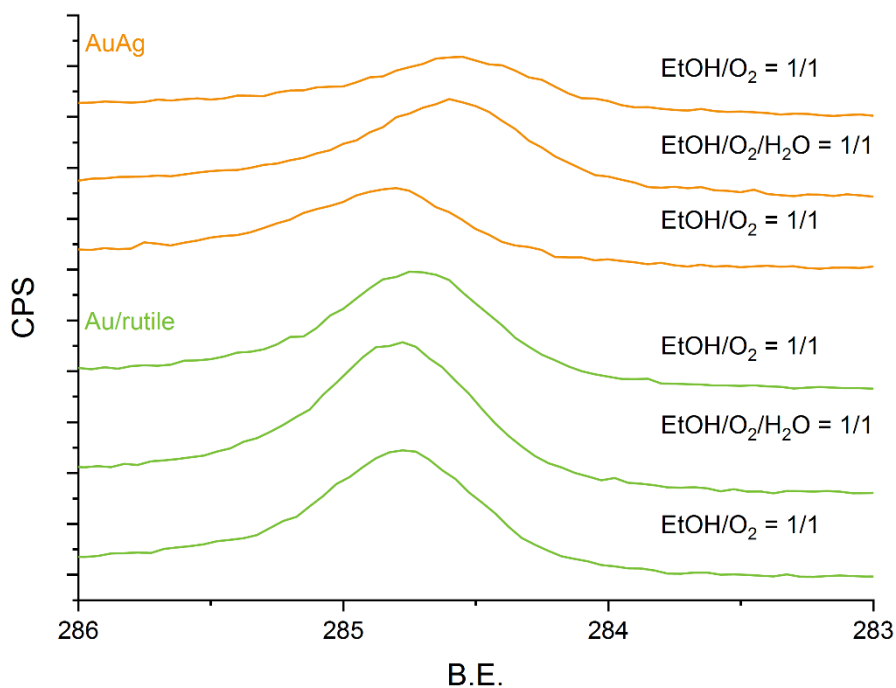


Figure 107. CIs detail spectra for Au/rutile (bottom) and AuAg/rutile (top) prior to H₂O introduction, during the reaction with EtOH/O₂/H₂O and after removing the H₂O from feed again. The feed consisted of 2.5 mL/min EtOH and O₂ (each, resulting in a ratio of 1/1) and, for the measurement of the water influence, 5 mL/min were added (resulting in an EtOH/O₂/H₂O of 1/1/2), always at total pressure of 0.5 mbar and a temperature of 250°C. The spectra were taken at a kinetic energy of 310 eV.

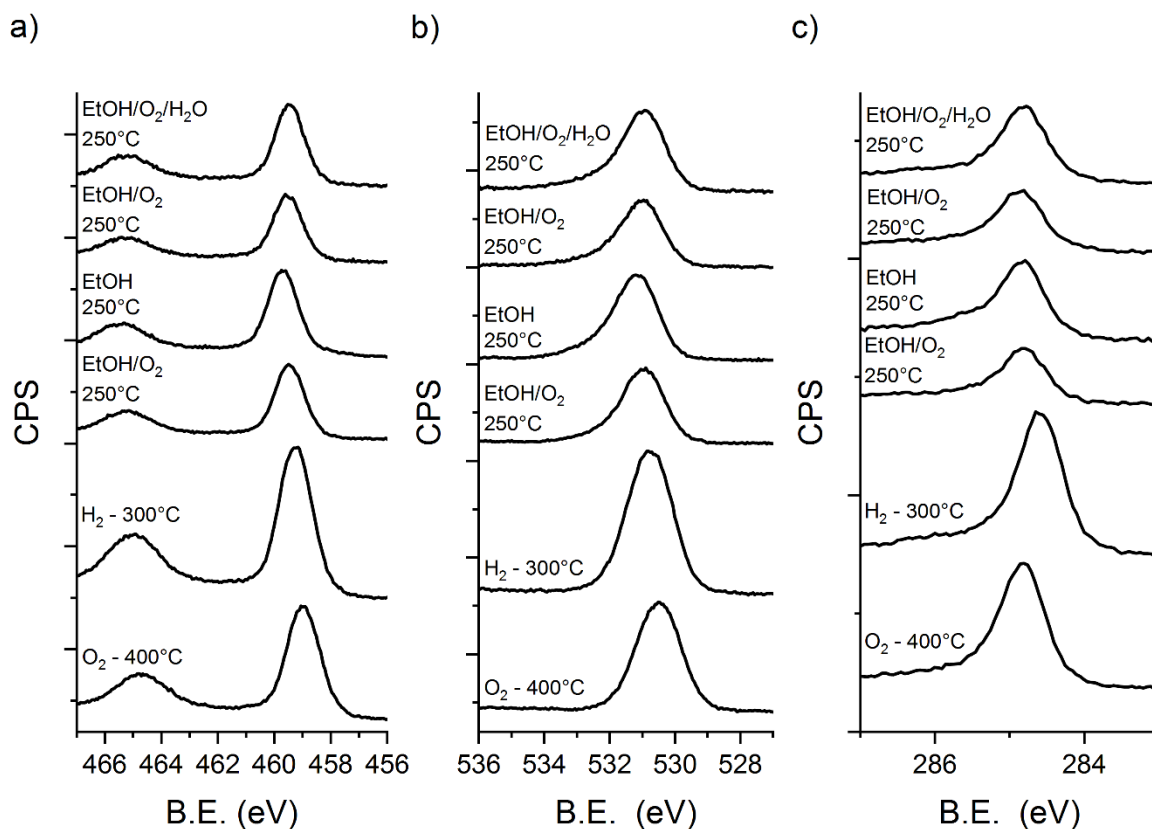


Figure 108. (a) Ti 2p, (b) O 1s and (c) C 1s details scans for the rutile reference sample under different conditions: Pretreatment (under O₂ and H₂ atmosphere) and under EtOH, EtOH/O₂ and EtOH/O₂/H₂O flow. Spectra were taken at a kinetic energy of 310 eV.

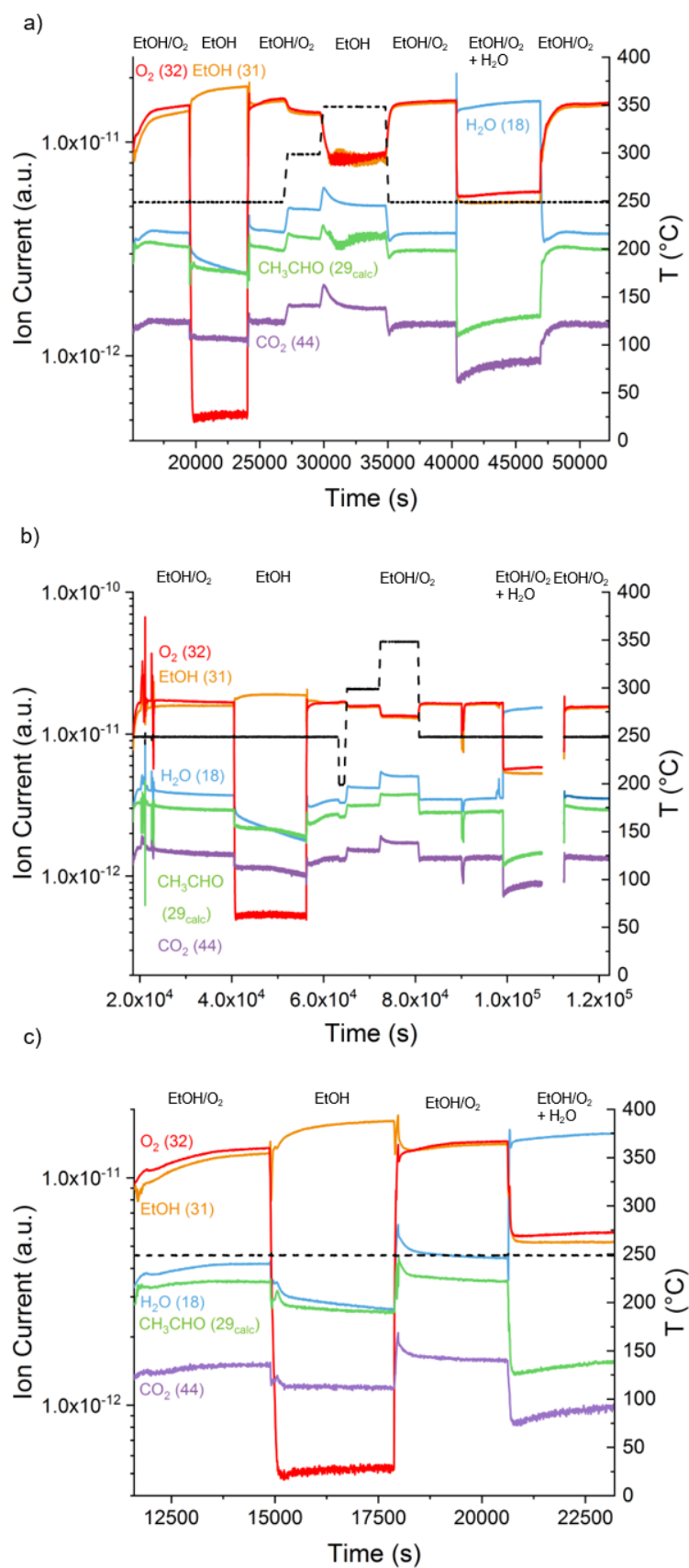


Figure 109. Mass data of the reaction, (a) Au/rutile, (b) AuAg/rutile and (c) rutile reference (data for the pretreatment not shown). As $m/z = 29$ not only the most intense peak for acetaldehyde, but also typical for EtOH, the signal of acetaldehyde was calculated using the known fragmentation as published by NIST. As the m/z of 44 is also present in acetaldehyde, CO₂ formation is unlikely.

9.7.2. ALBA

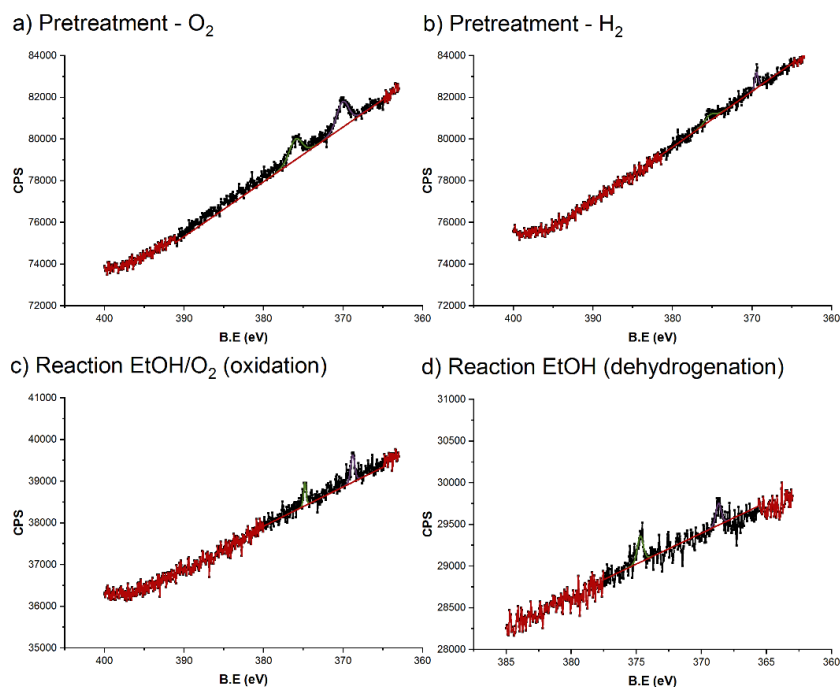


Figure 110. Ag 3d detail scans for the Ag/rutile sample obtained under different conditions, (a) pretreatment under O₂ (400°C), (b) pretreatment under H₂ (300°C), (c) oxidation with a ratio of EtOH/O₂ = 1/1 (250°C), (d) dehydrogenation conditions, EtOH only (250°C). During the pretreatment, under oxidative conditions, there is charging. After the pretreatment, however, depletion of Ag from the surface is observed (c, d), to a higher degree under oxidative conditions and to a lower degree during dehydrogenation.

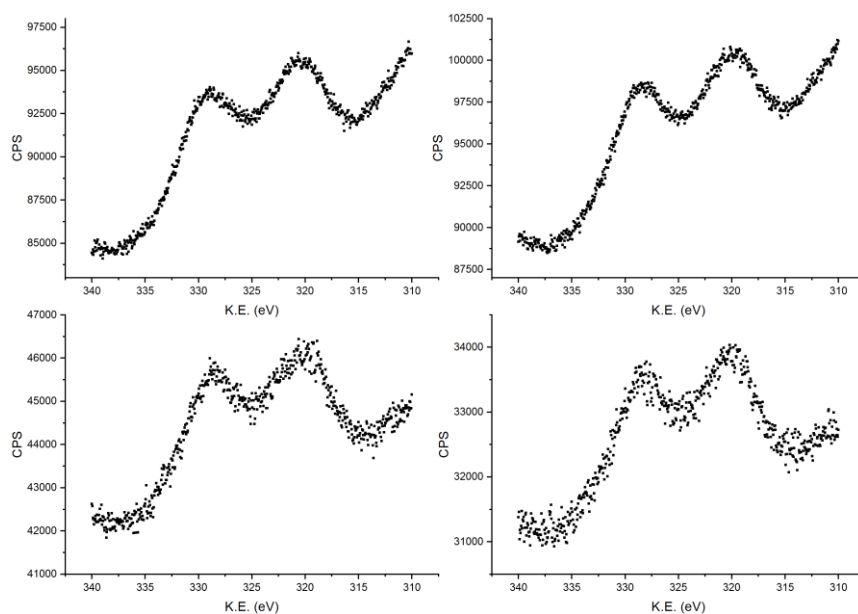


Figure 111. Ag MNN Auger signals for the Ag/rutile sample obtained under (a) pretreatment under H₂ (300°C), (b) oxidation with a ratio of EtOH/O₂ = 1/1 (250°C), (c) dehydrogenation conditions, EtOH only (250°C).

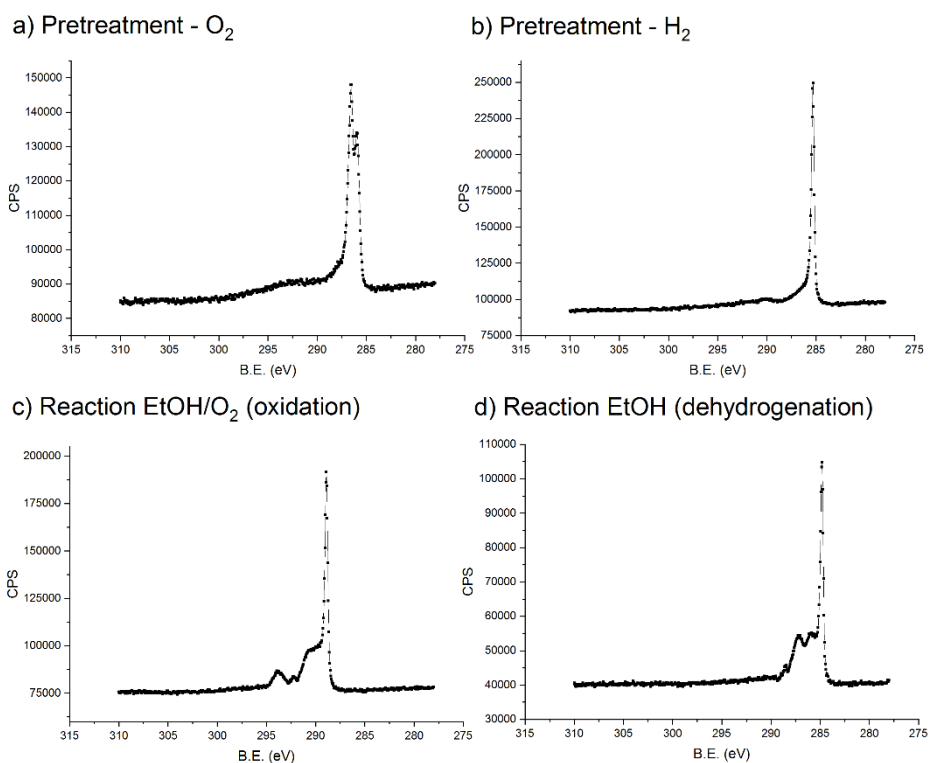


Figure 112. C 1s detail scans for the Ag/rutile sample obtained under different conditions, (a) pretreatment under O₂ (400°C), (b) pretreatment under H₂ (300°C), (c) oxidation with a ratio of EtOH/O₂ = 1/1 (250°C), (d) dehydrogenation conditions, EtOH only (250°C). The C 1s is visible right from the beginning, including the pretreatment, as the pellet was prepared with graphite as internal standard.

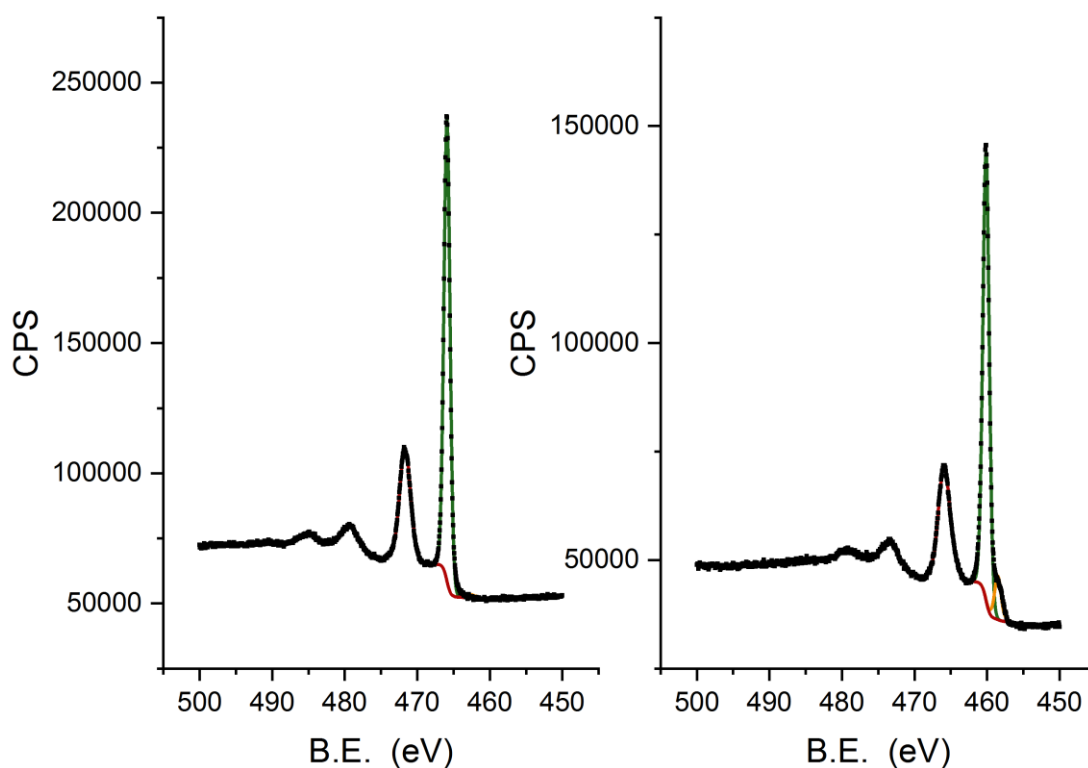


Figure 113. Ti 2p detail scans of the Ag/rutile catalyst at (a) oxidation conditions (EtOH/O₂ = 1/1) and (b) dehydrogenation conditions (EtOH only). The ratio of Ti³⁺ is 0.46 % for (a) and 9.33 % for (b). Spectra taken at 250°C.

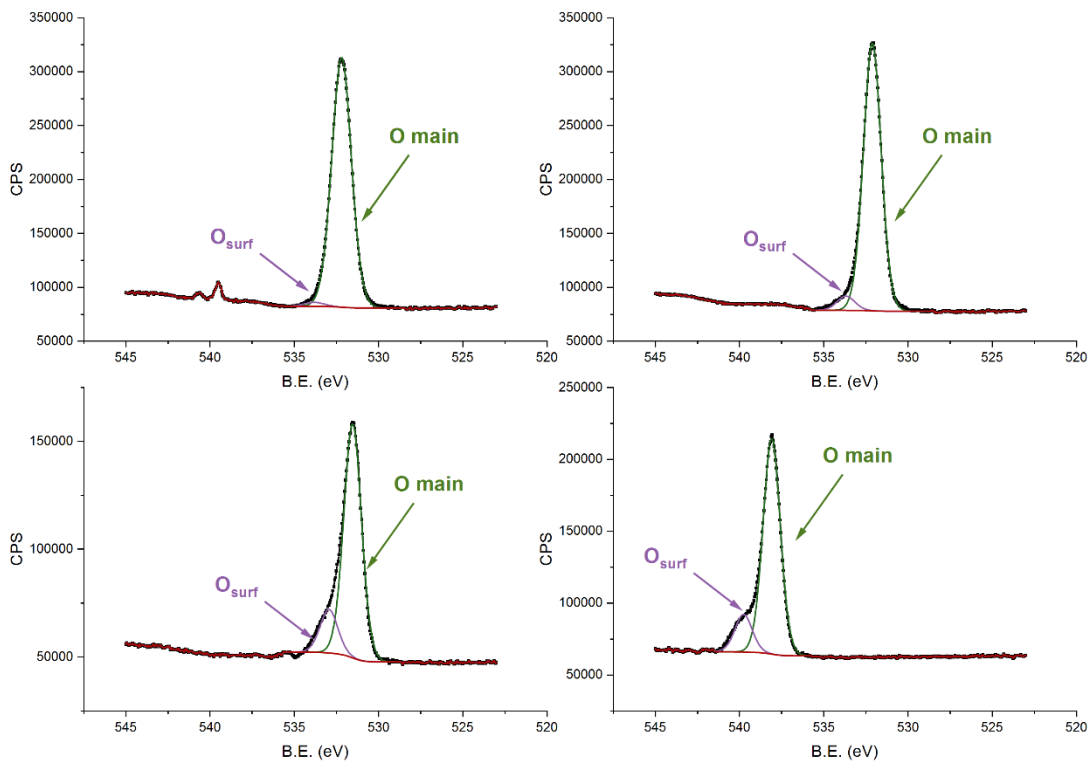


Figure 114. O 1s detail spectra of the Ag/rutile spectra, (a) under oxidative conditions during pretreatment (400°C), (b) reducing conditions during pretreatment (300°C) as well as (c) oxidation conditions (250°C, EtOH/O₂ = 1/1) and (d) dehydrogenation conditions (250°C, EtOH only). O_{surf} marks surface species such as OH, H₂O, ethoxy, acetate, etc.

9.8. Additional Information for the First Principles Microkinetic Model

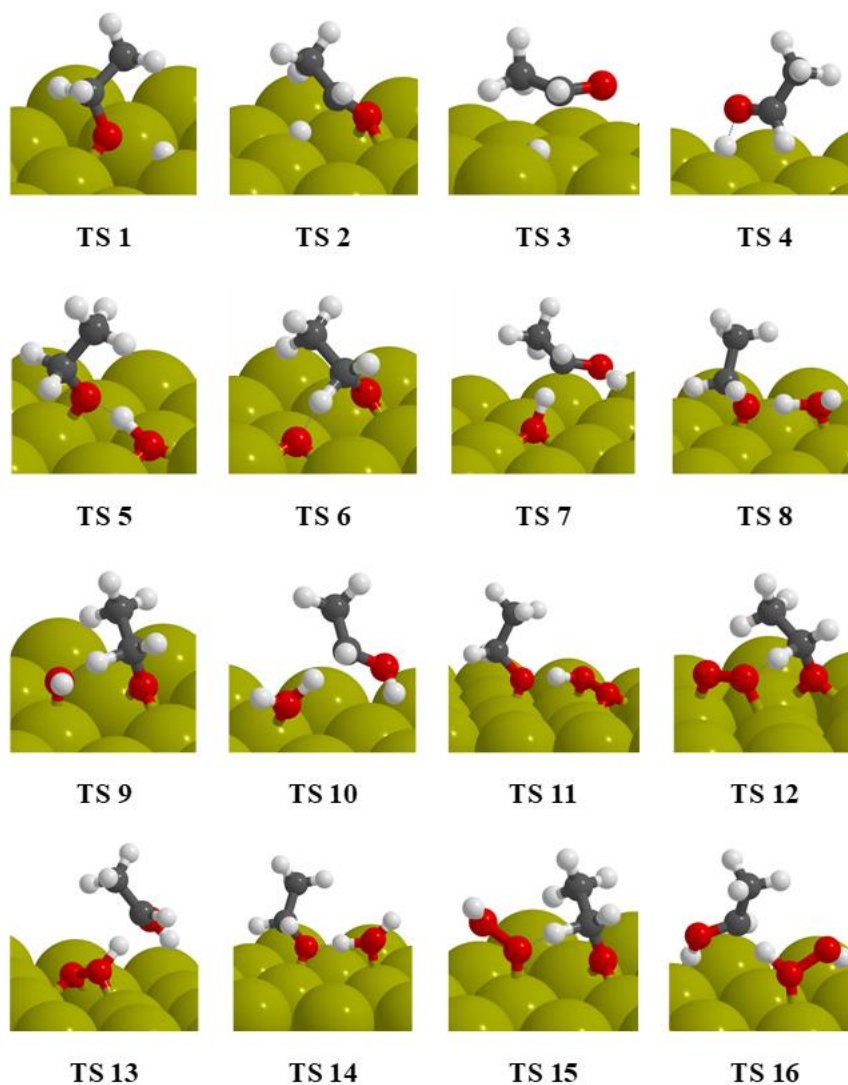


Figure 115. The transition states for ethanol oxidation via direct dehydrogenation and proton transfer to oxygen, hydroxyl, O₂ and OOH corresponding to the energy profiles in Figure 16.

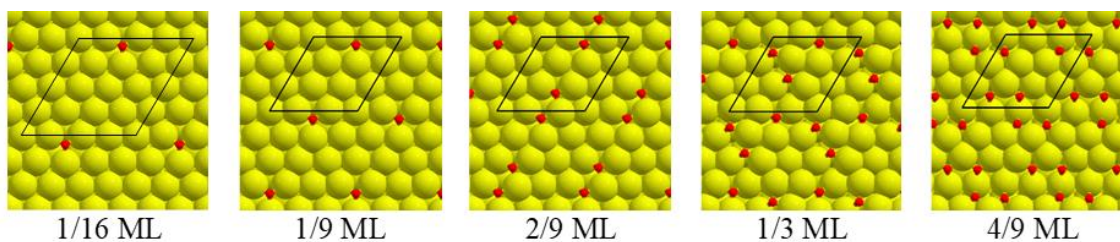


Figure 116. Oxygen adsorption structures at 1/16 ML, 1/9 ML, 2/9 ML, 1/3 ML and 4/9 ML coverage to calculate the oxygen intra-species repulsion.

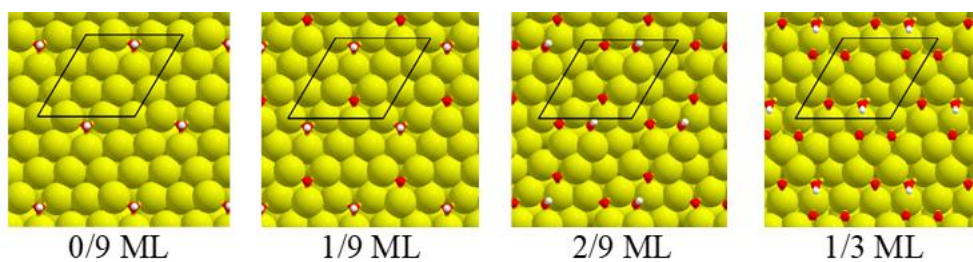


Figure 117. Oxygen – hydroxyl co-adsorption structures at 0/9 ML, 1/9 ML, 2/9 ML and 1/3 ML oxygen coverage to calculate the hydroxyl destabilization.

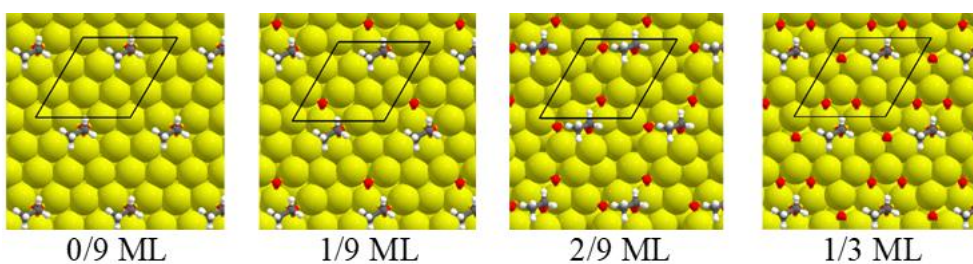


Figure 118. Oxygen – ethoxy co-adsorption structures at 0/9 ML, 1/9 ML, 2/9 ML and 1/3 ML oxygen coverage to calculate the ethoxy destabilization.

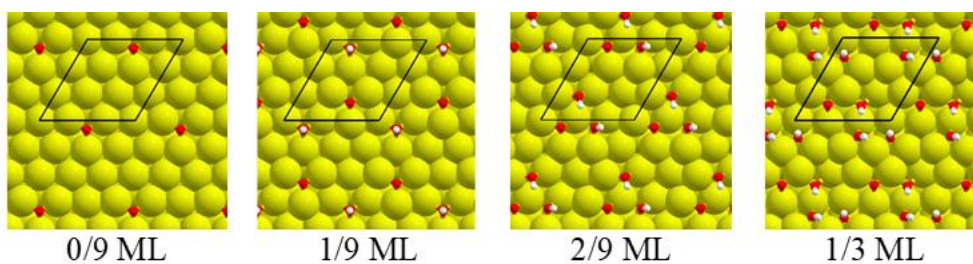


Figure 119. Hydroxyl – oxygen co-adsorption structures at 0/9 ML, 1/9 ML, 2/9 ML and 1/3 ML hydroxyl coverage to calculate the oxygen destabilization.

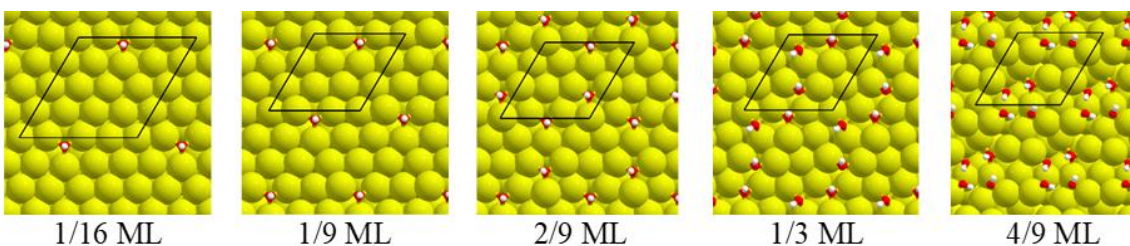


Figure 120. Hydroxyl adsorption structures at 1/16 ML, 1/9 ML, 2/9 ML, 1/3 ML and 4/9 ML coverage to calculate the hydroxyl intra-species repulsion.

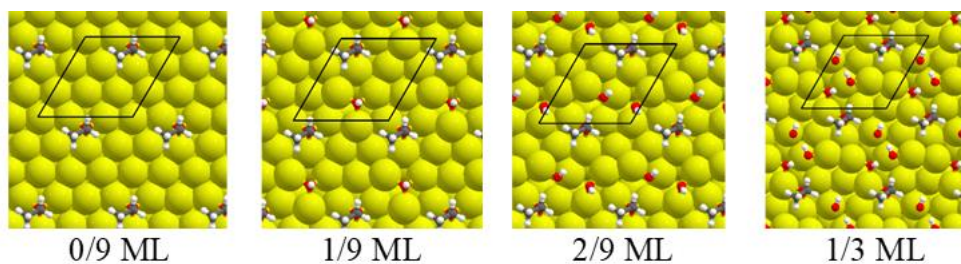


Figure 121. Hydroxyl – ethoxy co-adsorption structures at 0/9 ML, 1/9 ML, 2/9 ML and 1/3 ML hydroxyl coverage to calculate the ethoxy destabilization.

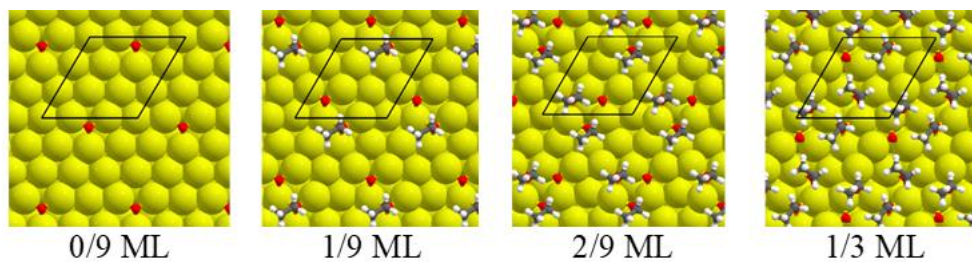


Figure 122. Ethoxy – oxygen co-adsorption structures at 0/9 ML, 1/9 ML, 2/9 ML and 1/3 ML ethoxy coverage to calculate the oxygen destabilization.

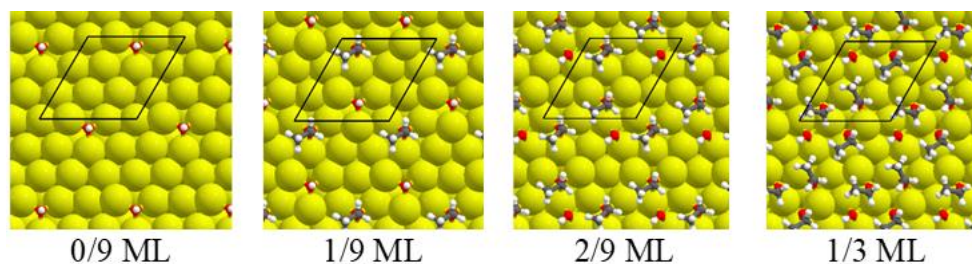


Figure 123. Ethoxy – hydroxyl co-adsorption structures at 0/9 ML, 1/9 ML, 2/9 ML and 1/3 ML ethoxy coverage to calculate the hydroxyl destabilization.

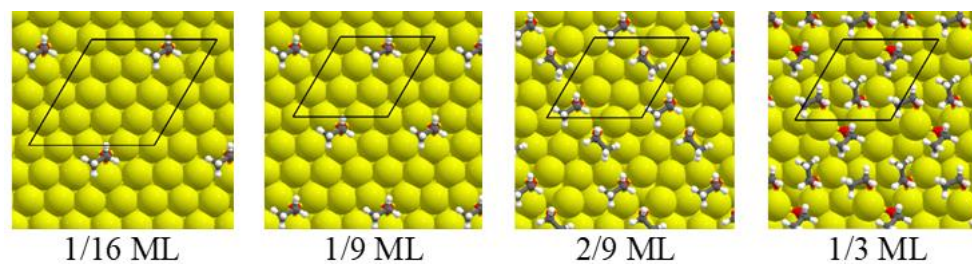


Figure 124. Ethoxy adsorption structures at 1/16 ML, 1/9 ML, 2/9 ML, 1/3 ML and 4/9 ML coverage to calculate the ethoxy intra-species repulsion.

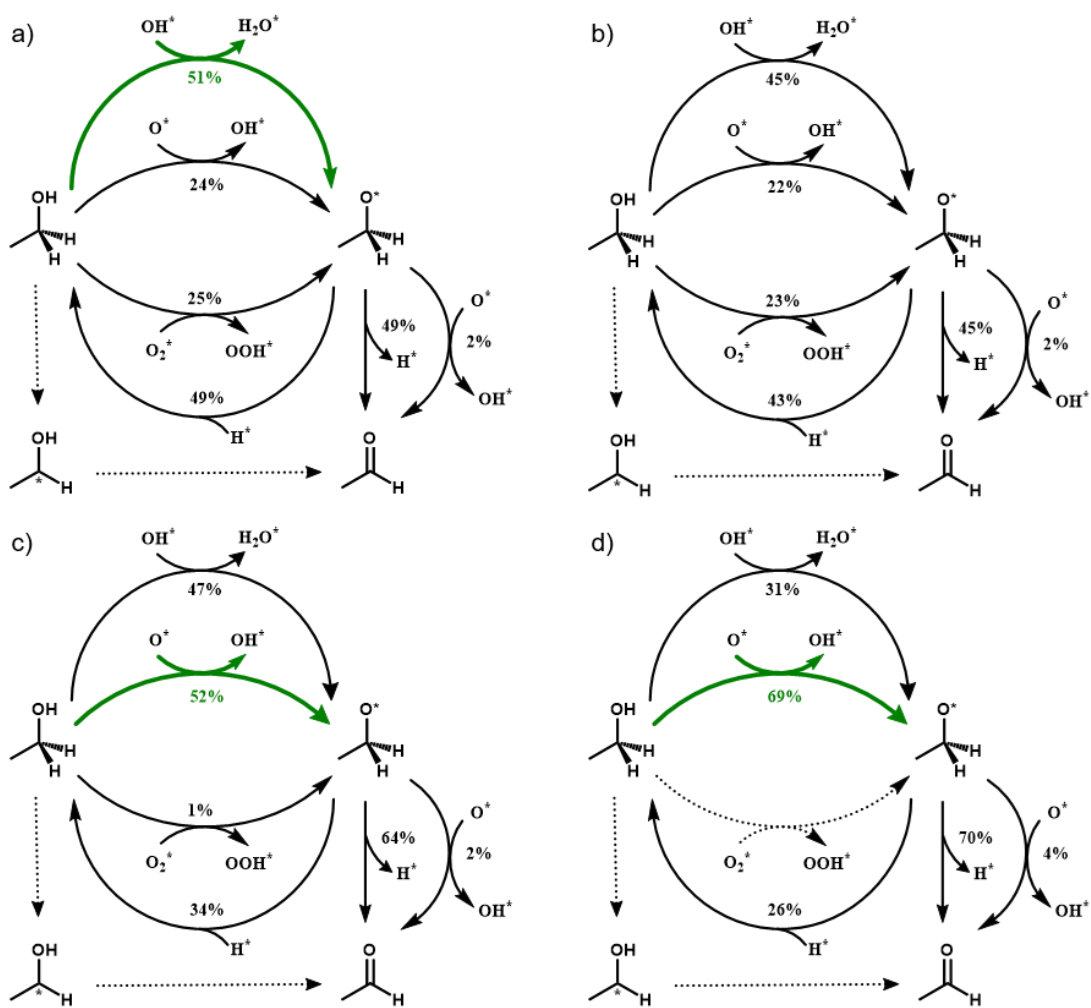


Figure 125. Reaction path analysis for the oxidation of ethanol to acetaldehyde at (a) 100 °C, (b) 150 °C, (c) 250 °C (d) and 300 °C. The numbers indicate the fraction of each component consumed in a particular reaction step. Dotted arrows indicate reaction steps with a fraction below 0.5%, while green arrows indicate reaction steps with a fraction equal to or above 50%. Conditions: 15 kg_{cat} s mol_{EtOH}⁻¹, p_{tot} = 0.05 bar, EtOH:O₂ = 1.

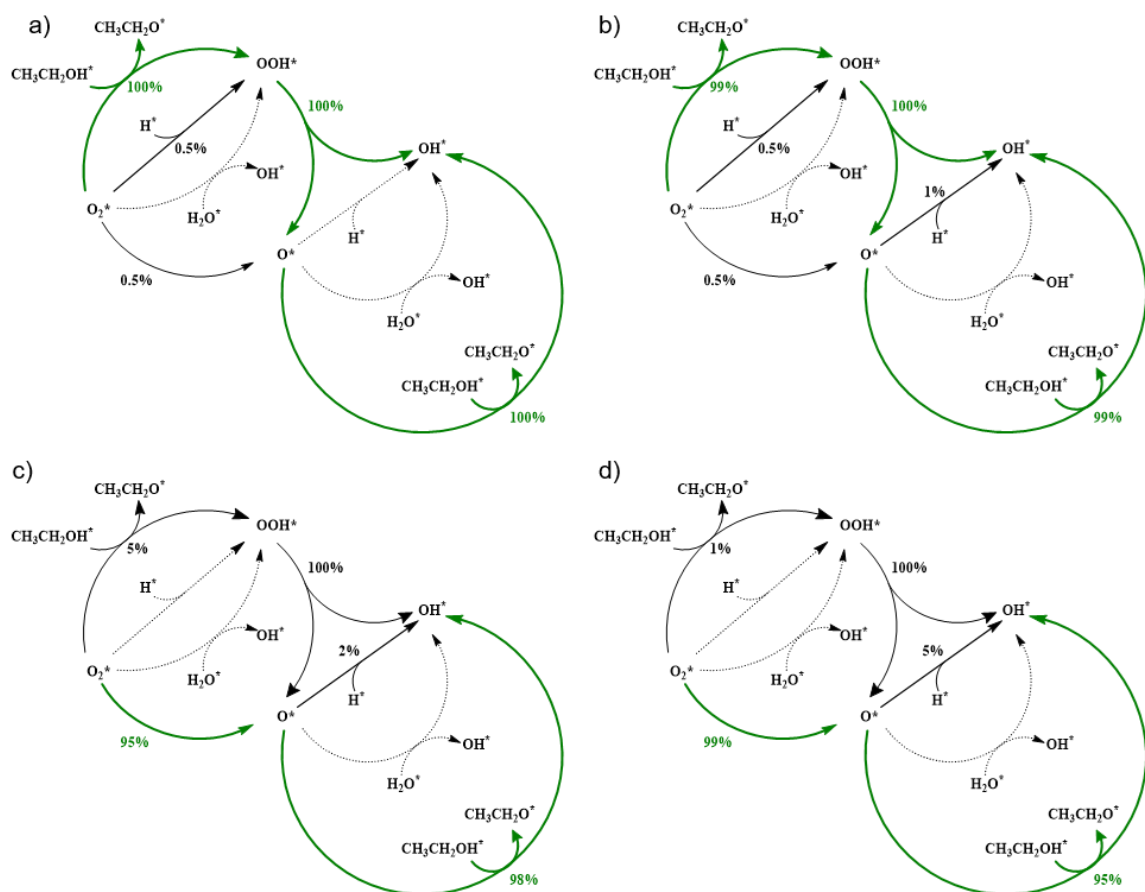


Figure 126. Reaction path analysis for the oxygen activation in ethanol oxidation to acetaldehyde at (a) 100 °C, (b) 150 °C, (c) 250 °C and (d) 300 °C. The numbers indicate the fraction of each component consumed in a particular reaction step. Dotted arrows indicate reaction steps with a fraction below 0.5%, while green arrows indicate reaction steps with a fraction equal to or above 50%. Conditions: $15 \text{ kg}_{\text{cat}} \text{ s mol}_{\text{EtOH}}^{-1}$, $p_{\text{tot}} = 0.05 \text{ bar}$, $\text{EtOH}:\text{O}_2 = 1$.

Publications

Peer-Reviewed Papers

1. S. Mostrou-Moser, S. Sipőcz, T. Fődi, B. Darvas, F. Nagl, A. Föttinger, K. van Bokhoven, J. A. Catalytic oxidation of aqueous bioethanol: an efficient upgrade from batch to flow *React. Chem. Eng.* 2018, doi: 10.1039/c8re00054a
2. Hemelaar, S. R., Nagl, A., Bigot, F., Rodríguez-García, M. M., de Vries, M. P., Chipaux, M. & Schirhagl, R. The interaction of fluorescent nanodiamond probes with cellular media. *Microchim. Acta* 2017, doi:10.1007/s00604-017-2086-6
3. Ong, Y., Chipaux, M., Nagl, A. & Schirhagl, R. Shape and crystallographic orientation of Nanodiamond for quantum sensing. *Phys. Chem. Chem. Phys.* 2017, doi:10.1039/C6CP07431F
4. Nagl, A., Hemelaar, S. R. & Schirhagl, R. Improving Surface and Defect Center Chemistry of Fluorescent Nano-Diamonds for Imaging Purposes – A Review. *Anal. Bioanal. Chem.* (2015). doi:10.1007/s00216-015-8849-1

In Preparation

1. De Vrieze, J., Nagl, A., Latschka, M., Mostrou-Moser, S., Teržan, S., Djinović, P., Horak, F., Limbeck, A., Pintar, A., van Bokhoven, J.A., Thybaut, J.W., Föttinger, K. & Saeys, M. Complex Kinetics for a Simple Reaction: Oxidative Dehydrogenation of Ethanol on Gold
2. Nagl, A., De Vrieze, J., Latschka, M., Mostrou-Moser, S., van Bokhoven, Saeys, M., & Föttinger, K. Bimetallic AuAg Catalysts: Promotional Effect of Silver in the Selective Oxidation of Ethanol. In preparation.

Talks and Poster Presentations

1. Nagl, A., Föttinger, K., Selective Oxidation of Ethanol on Modified Supported Au Catalysts, Talk: Catalysis Summit - 2018, Filzmoos - Gsenghof Alm; September 20-23, 2018.

2. Nagl, A., Mostrou-Moser, S., De Vrieze, J., Dražić, G., Saeys, M., van Bokhoven, J.A., Föttinger, K., Operando Studies of Ethanol Selective Oxidation on Supported Bimetallic Gold Catalysts, Poster: 14th Pannonian International Symposium on Catalysis, Stary Smokovec; September 3-7, 2018; in: "14th Pannonian International Symposium on Catalysis: Book of Abstracts", 2018, p. 114.
3. Pacholik, G., Nagl, A., Föttinger, K., Catalytic hydrogenation of CO₂ from flue gas to valuable compounds, Talk: 14th Pannonian International Symposium on Catalysis, Stary Smokovec; September 3-7, 2018; in: "Book of Abstracts", 2018, p. 42.
4. Nagl, A., Mostrou-Moser, S., De Vrieze, J., Dražić, G., Saeys, M., van Bokhoven, J.A., Föttinger, K., Operando Studies of Ethanol Selective Oxidation on Supported Bimetallic Gold Catalysts, Poster: 135th BASF International Summer Course, Ludwigshafen, Germany; August 19-25, 2018.
5. Horak, F., Nagl, A., Föttinger, K., Limbeck, A., Quantitative analysis of surface modified nano-particle catalyst materials using LA-ICP-MS, Poster: 14th European Workshop on Laser Ablation, Pau, France; June 26-29, 2018; in: "Book of Abstracts", 2018, p. 50.
6. Nagl, A., Mostrou-Moser, S., De Vrieze, J., Dražić, G., Saeys, M., van Bokhoven, J.A., Föttinger, K., Selective Ethanol Oxidation on Supported Bimetallic Gold Catalysts: Base Chemicals from "Green" Processes", Talk: VSS 2018 - Vienna Young Scientists Symposium, Vienna; June 7-8, 2018.
7. Nagl, A., Hradil, K., Terzan, J., Zabilskiy, M., Pintar, A., Mostrou-Moser, S., van Bokhoven, J.A., Föttinger, K., Operando Studies on Supported Bimetallic Gold Catalysts, Talk: OperandoVI - 6th International Congress on Operando Spectroscopy, Estepona, Malaga; April 15-19, 2018; in: "Operando VI 6th International Congress on Operando Spectroscopy", 2018, p. 44.
8. Horak, F., Nagl, A., Smetaczek, S., Föttinger, K., Limbeck, A., Quantitative elemental analysis of surface modified TiO₂ nanoparticles via LA-ICP-MS";Talk: 29th Mass Spec Forum Vienna, Vienna, Austria; February 20-21, 2018.
9. Nagl, A., Hradil, K., Terzan, J., Zabilskiy, M., Föttinger, K., Supported Bimetallic Au Catalysts: Structure-Performance Relationships, Talk: 17. Österreichische Chemietage 2017, Salzburg; September 25-28, 2017; at: "17. Österreichische Chemietage 2017", 2017

10. Nagl, A., Lukashuk, L., Yigit, N., Hradil, K., Föttinger, K., In-situ Pair Distribution Function (PDF) Analysis on Catalysts: CeO₂ promoted Co₃O₄ and Supported Bimetallic Au Catalysts., Poster: EUROPACAT 13th European Congress on Catalysis, Florence; August 27-31, 2017; in: "EUROPACAT 13th European Congress on Catalysis", 2017, p. 87.
11. Yigit, N., Lukashuk, L., Nagl, A., Hans, P., Leoni, M., Föttinger, K., Rupprechter, G., Operando Synchrotron X-Ray Absorption and Diffraction Study of Co-based catalysts: Insights into Structural and Microstructural Changes, Talk: XIII EuropaCat, Florence, Italy; August 27-31, 2017, in: "EUROPACAT 2017", 2017
12. Nagl, A., Rothensteiner, M., Föttinger, K., Selective oxidation of ethanol on modified supported Au catalysts, Talk: 13th Pannonian International Symposium on Catalysis, Siofok; September 19-23, 2016; in: "13th Pannonian International Symposium on Catalysis", Hungarian Chemical Society, 2016, ISBN: 978-963-9970-56-4; p. 68.
13. Nagl, A., Durán Outeiral, R., Rosenberg, E., Method Development for The Analysis of Acidic PAH Metabolites by GC/MS after TMSH Derivatisation, Poster: International Symposium on Capillary Chromatography (36th ISCC), Riva del Garda, Italy; May 27 June 1, 2012., Poster: 36th
14. Nagl, A., Durán Outeiral, R., Drozdova, S., Rosenberg, E., Development of a Screening Method for Acidic PAH Metabolites in Water and Soil Samples, Poster: IMA 2011 - Instrumental Methods of Analysis, Chania (Greece); September 18-22, 2011.
15. Rosenberg, E., Durán Outeiral, R., Nagl A., Bestimmung von PAH-Metaboliten in Umweltproben mittels LC/MS und GC/MS, Poster: Anakon 2011, Zürich; March 22-25, 2011.

Scientific Reports

1. Nagl, A., Föttinger, K., Experimental report for DESY: In-situ XAS Studies on Supported Bimetallic Au-Catalysts for Selective Ethanol Oxidation", 2018
2. Nagl, A., Föttinger, K., Experimental report for the Diamond Light Source: In-situ XAS Studies on Supported Bimetallic Au-Catalysts for Selective Ethanol Oxidation: Insights into Electronic and Geometric Structure of the Active Nanoparticles, 2018

3. Nagl, A., Föttinger, K, Experimental report for the ALBA Synchrotron: In-situ XAS Studies on Supported Bimetallic Au-Catalysts for Selective EtOH-Oxidation: Electronic/Geometric Structure for Tunable Catalysts", 2018
4. Nagl, A., Föttinger, K, Experimental report for the ALBA Synchrotron: NAPP-XPS Studies on Supported Bimetallic Au-Catalysts for Ethanol Oxidation: Unraveling the Electronic Structure of the Active Phase", 2018
5. Nagl, A., Yigit, N., Föttinger, K., Experimental report for the Diamond Light Source: Modulation Excitation Time-Resolved X-ray Total Scattering Study of Cobalt Oxide and Promoted Cobalt Oxide (Preferential) CO Oxidation Catalysts: Insights into the Dynamic of Local/Intermediate-Range Structure. Part II, 2016
6. Yigit, N., Nagl, A., Föttinger, K., Experimental report for the Diamond Light Source: Modulation Excitation Time-Resolved X-ray Diffraction Study of Cobalt Oxide and Promoted Cobalt Oxide (Preferential) CO Oxidation Catalysts: Insights into the Dynamic Structural and Microstructural Changes. Part I, 2016

Resume

Andreas Nagl

Kahlenberger Straße 1F/4, 1190 Vienna, Austria • Phone: +43 676 7164925 •

Email: andreas.nagl@gmail.com

Date of Birth: 16th Sept. 1988 • Nationality: Austrian

Education

- 10/2015 –** **PhD student in Prof. Föttinger’s group “Applied Catalysis”, Institute for Materials Chemistry, TU Wien, Austria**
Working title: “Selective oxidation of ethanol on modified supported Au catalysts “, joint project with Prof. van Bokhoven at the ETH Zurich

Methods: *in-situ* spectroscopy (DRIFTS, Raman, XAS, NAPP-XPS, UV-Vis), reaction kinetics/catalysis, chromatography, HR-(S)TEM, XRD/PDF, MATLAB
Expected graduation: 05/2019
- 10/2013 — 09/2015** **Master studies in Technical Chemistry (specialisation: Applied Physical and Analytical Chemistry), TU Wien. Graduated with distinction.**
Master Thesis: “Diamond Magnetometry for Biological Applications“, carried out in the group „Bioimaging and Bioanalysis“ in The Netherlands. Supervised by Prof. Schirhagl (Dep. of Biomedical Engineering, Rijksuniversiteit Groningen) and Prof. Lendl (Inst. for Chemical Technologies and Analytics, TU Wien)

Methods: Raman spectroscopy, TEM, nanoparticle modification, protein analysis
- 10/2008 — 10/2013** **Bachelor of Science in Technical Chemistry, TU Wien**
Bachelor Thesis: “Determination of Acidic PAH Metabolites by GC/MS after Derivatisation with TMSH”, in the group of Prof. Rosenberg (Inst. for Chemical Technologies and Analytics, TU Wien)
- 09/1999 — 07/2007** **Grammar school (Bundesgymnasium Werndlpark, Steyr, Austria)**

Professional Experience (Selection)

- 08/2013 — 02/2015** **Intern at Chemcon Technisches Büro für technische Chemie GmbH** (accredited laboratory, 8 hours/week). Responsibilities: Sample preparation, GC-MS, HPLC-MS, photometry
- 04/2013** **Stay at the Politechnika Gdańska/Gdańsk University of Technology** (Poland). Project: Membrane-SPME in the group of Prof. Namiesnik / Dr. Kloskowski

- 10/2011 — 07/2014** **Tutor at the Institute of Chemical Technologies and Analytics** (CTA, Vienna University of Technology). Lab Courses: “Qualitative Analysis” and “Instrumental and Bioanalytical Laboratory”
- 07/2012 — 08/2012** **Intern at the Department of Agrobiotechnology**, IFA-Tulln (Center for Analytical Chemistry, group “Mycotoxins” of Prof. Krska / Dr. Sulyok)
Responsibilities: Sample preparation, evaluation of HPLC-MS measurements
- 08/2007 – 04/2008** **Civil service, LKH Steyr (hospital)**

Awards and Scholarships

- 2018** Lion’s Sonderpreis 2018, awarded at the Vienna Young Scientist Symposium 2018
- 2018** ÖFG Travel Scholarship for the oral presentation at the Operando Conference 2018
- 2016** Erwin Wenzl Preis (for the Master Thesis)
- 2015 and 2016** Merit scholarship of the TU Wien
- 2014** Excellence Scholarship of the Federation of Austrian Industries (IV) in Carinthia, Austria
- 2010/11** “Stiftungsstipendium” of the TU Wien

Extracurricular Activities

- 04/2016 -03/2019** Participant of the McKinsey Capstone talent program
- 08/2018** Participation in the 135th BASF International Summer Course 2018, Ludwigshafen, Germany
- 05/2012 — 11/2015** Engaged in projects/initiatives of the Austrian Commission for UNESCO (e.g. Member of the Youth Advisory Panel, Delegate at the Muscat Youth Summit 2012 and the UNESCO Youth Forum 2013 in Paris)
- 02/2012 — 12/2014** Involved in various projects of the youth ÖJAB organization (independent of any political party or religious obligation), e.g. Assistant for Public Relations and Japan Youth Exchanges
- 11/2013** Participation in the UN Climate Conference in Warsaw 2013 as Youth Delegate of the Austrian Delegation

03/2009 — 03/2013 Member of the European student organization BEST (various activities and positions, e.g. Vice President of HR in 2010, hosting a student conference on „Education for Sustainable Development“ and establishment of the career event beWANTED at the Vienna University of Technology)

Related Experience and Skills

Languages German: native speaker; Hungarian: native speaker; English: excellent;
Dutch: basic; Spanish: basic

Technical Skills Programming (C#, Delphi, MATLAB), OriginPro, basics of Wolfram Mathematica
Methods: GC-MS, HPLC-MS, Raman-Microscopy/Spectroscopy, IR- Spectroscopy (*in-situ* DRIFTS) XRD (Rietveld and Pair Distribution Function Analysis) and (S)TEM. Experience at synchrotrons (e.g. NAPP-XPS at BESSY Berlin/ALBA Barcelona, XRD at MAX-lab in Sweden and EXAFS/XRD/PDF at Diamond Light Source UK; EXAFS at DESY in Hamburg, Diamond Light Source UK, ALBA Barcelona)